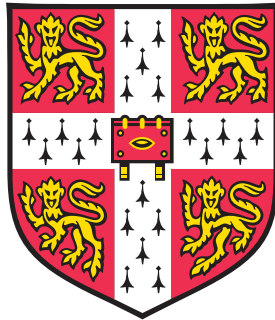


Rational Design of DNA-Based Lipid Membrane Pores



KERSTIN GÖPFRICH

CORPUS CHRISTI COLLEGE,
UNIVERSITY OF CAMBRIDGE

*This dissertation is submitted for the degree of Doctor of Philosophy
in October 2016.*

Rational Design of DNA-Based Lipid Membrane Pores

Kerstin Göpfrich

Abstract

DNA nanotechnology has revolutionised our capability to shape and control three-dimensional structures at sub-nanometre length scales. In this thesis, we use DNA to build synthetic membrane-inserting channels. Porphyrin and cholesterol tags serve as membrane anchors to facilitate insertion into the lipid membrane. With atomic force microscopy, confocal imaging and ionic current recordings we characterise our DNA nanochannels that mimic their natural protein-based counterparts in form and function. We find that they exhibit voltage-dependent conductance states. Amongst other architectures, we create the largest man-made pore in a lipid membrane to date approaching the electrical diameter of the nuclear pore complex. Pushing the boundaries on the other end of the spectrum, we demonstrate the ultimately smallest DNA membrane pore made from a single membrane-spanning DNA duplex. Thereby, we proof that ion conduction across lipid membranes does not always require a physical channel. With experiments and MD simulations we show that ions flow through a toroidal pore emerging at the DNA-lipid interface around the duplex. Our DNA pores spanning two orders of magnitude in conductance and molecular weight showcase the rational design of synthetic channels inspired by the diversity of nature – from ion channels to porins.



Declaration

This dissertation is the result of my own work and includes nothing which is the outcome of work done in collaboration except as specified in the text. I declare that no part of this work has been submitted for a degree or other qualification at this or any other university. This thesis does not exceed the word limit of 60 000 words set by the Physics and Chemistry Degree Committee, including abstract, tables, footnotes and appendices.

Cambridge, 20th October 2016

A handwritten signature in blue ink, appearing to read 'K. Göpfrich', written in a cursive style.

Kerstin Göpfrich

To scientific curiosity. And to my family.

Acknowledgements

In my head I had written the introduction to my thesis three years ago. “In this thesis we set out to determine how many glass capillaries I need to get a PhD.” I had started a tally in the back of my lab book as a record. As of today, the count reached 314 – much less than I anticipated. When I started my PhD, I was imagining myself pulling capillaries for three years. In hindsight, my project became a lot more diverse than I had expected. This was largely due to my supervisor Prof. Dr. Ulrich F. Keyser, who pointed me towards new and exciting problems, always found time for discussion and supported me to develop as a scientist. Ulrich has the ability to bring together a nice group of people creating a fun and productive atmosphere inside and outside the lab.

I thank every member of the Keyser group – past and present – as I can honestly say that every single one of them has helped me at some point during my PhD. I especially want to thank Oliver Pambos, who gave me an extremely thorough introduction to the lipid nano bilayer setup when I first arrived. Silvia Hernández-Ainsa and Nicholas Bell taught me, amongst other things, how to make DNA origami and Catalin Chimerele kindly shared his expertise on the black lipid membranes. Maria Ricci did not only help me to image some of my DNA samples but also taught me a lot of details about AFM. Thanks to my long-standing office mates Michael and Karolis, and to Elisa, Vivek, Nadanai, Jehangir, Jinglin, Kareem, Alex and Stefano for help on various things.

Ulrich gave me the opportunity to work together with several bright students, which I really enjoyed. Thanks to Thomas Zettl and Anna Meijering for their work on the four-helix pore, Bertalan Gyenes for initial work on the DNA origami porin, Theresa Meier for a short explorative project on XNA pores, Tadas Kartanas for a joint project with the Theory of Condensed Matter group, Madhavi Duvuuri and Cristiana Bercea for work on cells and ion transport and Irene Henning for exploring possibilities with the TATA-binding protein.

Thanks to Ulrich, I also had the opportunity to benefit from a network of collaborators. First of all, I thank Satya Bhamidimarri and Prof. Mathias Winterhalter from International University Bremen for teaching me about solvent-containing membranes and for having me stay over in Bremen. The molecular dynamics simulations, kindly provided by Chen-Yu Li and Aleksei Aksimentiev, University of Illinois at Urbana-Champaign, gave an interesting new angle to my experimental work. Without the help of Iwona Mames and Prof. Eugen Stulz, University of Southampton, who prepared large amounts of porphyrin-tagged DNA, some of the most interesting insights of my PhD would not have been possible. I further thank Stefan Howorka and Jonathan Burns, University College London, for a fruitful collaboration on the porphyrin-tagged six-helix pore and Oxford Nanopore Technologies for letting me visit a few times. Thanks to Thomas Zettl and Prof. Tim Liedl, Ludwigs-Maximilian-University Munich, for introducing me to DNA tile assembly.

Foremost, I owe gratitude to my family, who supported me in all my decisions and let me go abroad for such a long time. Special thanks to my partner Karl, for the past 7+ years and for teaching me many useful things, including Inkscape and Blender. Looking back, it seems almost impossible that we both got funding to do our PhDs here in Cambridge.

Therefore, I am extremely grateful for the support I received from Gates Cambridge, Oppenheimer and the Winton Programme for the Physics of Sustainability for my PhD. I owe gratitude to CambridgeShorts, who gave me the possibility to make a short film about DNA-based membrane pores.

Finally, I thank Karolis Misiunas, Clare Fitzgerald, Jehangir Cama, Silvia Hernández-Ainsa and Karl Gödel for proofreading chapters of this thesis and Alexander Ohmann for continuing the work on DNA-based membrane pores whilst exploring new directions. I am looking forward to see where it goes.

Contents

List of Publications	16
List of Abbreviations	19
1 Motivation	21
Bibliography	25
2 Self-assembly with DNA	27
2.1 DNA lattices and tiles	29
2.2 DNA origami	29
2.3 Considerations for design and assembly of DNA nanostructures	32
2.3.1 Conceiving the target shape	32
2.3.2 Crossover rules for DNA nanostructures	34
2.3.3 Computational tools for DNA nanotechnology	35
2.3.4 Assembly and stability of DNA nanostructures	37
2.3.5 Experimental characterisation of DNA nanostructures	38
2.4 Functionalisation of DNA	43
Bibliography	45
3 DNA sensors and nanopores	55
3.1 Nanomechanical DNA-based sensors	56
3.2 Nanopores for single-molecule detection	58
3.3 DNA nanotechnology for enhanced nanopore sensing	61
3.4 DNA origami hybrid nanopores	62
Bibliography	67
4 Synthetic membrane nanopores	75
4.1 Membrane pores in nature	76
4.2 Milestones of synthetic membrane pores	77

4.3	DNA-based membrane pores	78
4.3.1	Thermodynamics of membrane insertion	79
4.3.2	Estimating the nanopore conductance	81
4.4	Ionic current characterisation	83
4.4.1	Lipid nano bilayers	84
4.4.2	Experimental procedure and troubleshooting	86
4.4.3	Solvent-containing bilayers	91
	Bibliography	92
5	Prototyping DNA-based membrane pores	97
5.1	Introduction	98
5.2	Materials and methods	100
5.3	Results and discussion	103
5.3.1	Design, assembly and characterisation	103
5.3.2	Probing membrane anchoring	105
5.3.3	Ionic current recordings	107
5.3.4	Voltage-dependent conductance levels	109
5.4	Conclusion	113
	Bibliography	114
6	DNA tile-based ion channels	117
6.1	Introduction	118
6.2	Materials and methods	119
6.3	Results and discussion	121
6.3.1	Design, assembly and characterisation	121
6.3.2	Rapid low-cost assembly	124
6.3.3	Confocal fluorescent imaging	126
6.3.4	Ionic current recordings	128
6.4	Conclusion	133
	Bibliography	135
7	DNA origami-based porins	139
7.1	Introduction	140
7.2	Materials and methods	141
7.3	Results and discussion	143
7.3.1	Design, assembly and characterisation	143
7.3.2	Confocal fluorescent imaging	146

7.3.3	Ionic current recordings	147
7.3.4	Molecular dynamics simulations	151
7.4	Conclusion	155
	Bibliography	156
8	DNA-lipid channels	159
8.1	Introduction	160
8.2	Materials and methods	161
8.3	Results and discussion	163
8.3.1	Design and characterisation	163
8.3.2	Confocal fluorescent imaging	165
8.3.3	Ionic current recordings	165
8.3.4	Molecular dynamics simulations	168
8.4	Conclusion	173
	Bibliography	175
9	Conclusion	180
9.1	Comparative account of DNA membrane pores	181
9.2	Outlook	186
	Bibliography	188
Appendix		192
A1.	Methods for coarse-grained simulation of lipid pore formation	192
A2.	Pathways of scaffold and staple strands of the DNA origami porin	193
A3.	DNA sequences for the DNA origami porin	196
A4.	Methods for the molecular dynamics simulations	201
	Bibliography	204

List of Publications

Peer-reviewed publications

Göpfrich, K., Li, C.-J., Ricci, M., Bhamidimarri, S. P., Yoo, J., Geynes, B., Ohmann, A., Winterhalter, M., Aksimentiev, A. & Keyser, U. F. Large-conductance transmembrane porin made from DNA origami. *ACS Nano* **10**, 8207–8214 (2016).

Göpfrich, K., Li, C.-Y., Mames, I., Bhamidimarri, S. P., Ricci, M., Yoo, J., Mames, A., Ohmann, A., Winterhalter, M., Stulz, E., Aksimentiev, A. & Keyser, U. F. Ion channels made from a single membrane-spanning DNA duplex. *Nano Letters* **16**, 4665–4669 (2016).

Tesoro, S., **Göpfrich, K.**, Kartanas, T., Keyser, U. F. & Ahnert, S. E. Non-deterministic self-assembly with asymmetric interactions can lead to tunable self-limiting cluster growth. *Physical Review E* **94**, 022404 (2016).

Göpfrich, K., Zettl, T., Meijering, A. E. C., Hernández-Ainsa, S., Kocabey, S., Liedl, T. & Keyser, U. F. DNA-tile structures lead to ionic currents through lipid membranes. *Nano Letters* **15**, 3134–3138 (2015).

Seifert, A.* , **Göpfrich, K.***, Burns, J. R., Fertig, N., Keyser, U. F. & Howorka, S. Bilayer-Spanning DNA nanopores with voltage-switching between open and closed state. *ACS Nano* **9**, 1117–1126 (2014). *Equal contribution, front cover.

Burns, J. R., **Göpfrich, K.**, Wood, J. W., Thacker, V. V., Stulz, E., Keyser, U. F. & Howorka, S. Lipid-bilayer-spanning DNA nanopores with a bifunctional porphyrin anchor. *Angewandte Chemie International Edition* **52**, 12069–72 (2013). Front cover.

Göpfrich, K., Kulkarni, C. V., Pambos, O. J. & Keyser, U. F. Lipid nanobilayers to host biological nanopores for DNA translocations. *Langmuir* **29**, 355–364 (2013).

Hernández-Ainsa, S., Bell, N. A. W., Thacker, V. V., **Göpfrich, K.**, Misiunas, K., Fuentes-Perez, M. E., Moreno-Herrero, F. & Keyser, U. F. DNA origami nanopores for controlling DNA translocation. *ACS Nano* **7**, 6024–6030 (2013).

Conference papers

Göpfrich, K., Ohmann, A., Bhamidimarri, S. P., Duvvuri, M. V. S. V., Bercea, C. I., Gyenes, B., Winterhalter, M. & Keyser, U. F. From Ion-Channels to Porins: Engineering DNA-Based Synthetic Counterparts. *Biophysical Journal* **110**, 351a (2016).

Pambos, O. J., **Göpfrich, K.**, Mahendran, R., Gornall, J. L., Otto, O., Steinbock, L., Chimere, C., Winterhalter, M. & Keyser, U. F. Towards simultaneous force and resistive pulse sensing in protein nanopores using optical tweezers. *RSC Proceedings* 72–75 (2012).

Book chapters

Göpfrich, K. & Keyser, U. F. DNA Sensors, Nanopores and Ion Channels, in *Biological and Bio-inspired Nanomaterials: Assembly Mechanisms and Properties*, Advances in Experimental Medicine and Biology (eds. T. Knowles, A. Buell & S. Perrett), Springer Nature (2017).

List of Abbreviations

AFM	Atomic force microscopy
bp	Base pair
DLC	DNA-lipid channel
DLS	Dynamic light scattering
DNA	Deoxyribonucleic acid
DOPC	1,2-Dioleoyl- <i>sn</i> -glycero-3-phosphocholine
DphPC	1,2-Diphytanoyl- <i>sn</i> -glycero-3-phosphatidylcholine
EDTA	Ethylenediaminetetraacetic acid
FRET	Förster resonance energy transfer
GUV	Giant unilammelar vesicle
ITO	Indium tin oxide
I-V	Current-voltage
MD	Molecular dynamics
MES	2-(<i>N</i> -morpholino)ethanesulfonic acid
MWCO	Molecular weight cut-off
PAGE	Polyacrylamide gel electrophoresis
PEG	Polyethylene glycol
RNA	Ribonucleic acid
SEM	Scanning electron microscopy
SUV	Small unilamellar vesicle
TBE	Tris-borate EDTA
TEM	Transmission electron microscopy
UV-vis	Ultraviolet-visible

Chapter 1

Motivation

What I cannot create, I do not understand.

Richard Feynman, American physicist, written on his blackboard, 1988

Unser Begreifen ist Schaffen. – Our comprehension is creation.

Christian Morgenstern, German author and poet, 1871-1904

Man begreift nur, was man selber machen kann. – You only understand what you are able to create by yourself.

Johann Wolfgang von Goethe, German author and poet, in: Briefe. An Carl Friedrich Zelter, 1804

The intrinsic motivation of human endeavour is to understand the world around us. Many great minds, including writers and philosophers, like Goethe and Morgenstern, as well as scientists, like Feynman, concluded that without recreating a system it is impossible to truly understand it. The scope of this doctoral thesis was to recreate membrane pores inspired by the diversity of their natural counterparts. The motivation is in the first instance a purely scientific one: if we strive to understand a living system, we have to study molecular transport, and molecular transport is mediated by nanometre-sized membrane pores. Realising that fifty percent of the currently approved drugs target membrane pores [1] quickly adds another dimension to the research, one that is based on the hope that a better understanding of membrane pores will lead to the design of better drugs. It fuels the hope that designer pores could replace defective channels in cells and thereby potentially offer a cure to the numerous diseases related to ion-channel malfunction – from cystic fibrosis [2] to autoimmune diseases [3]. Since toxins are of-

ten protein nanopores themselves or destabilise the membrane, pore-forming synthetic compounds may be used as antimicrobial agents. The synthetic channel could act as a therapeutic itself or it could be coupled to a pharmaceutically active compound which is directly released into the target cell upon membrane insertion. Drug permeation into the cell, and specifically selective permeation into the diseased cell, is often a challenge. Synthetic membrane pores as drug carriers would be a step away from the current small-molecule drugs towards macro-molecular delivery machines with the ability to recognise the target cell, perforate its membrane and release the molecular payload. A quest for synthetic pores could also come from the rising field of synthetic bottom-up biology: an artificial cell built from molecular components will eventually require structures for membrane transport [4]. Many other, more remotely bio-inspired applications of synthetic pores fall into the broad category of sensing. Biological nanopores have successfully been employed for label-free single molecule sensing and even for DNA sequencing. A future purposefully designed synthetic pore with tailored chemical functionality could outperform current nanopore sensors. Synthetic membrane channels have been proposed as voltage sensors, filters or as components of artificial photosystems.

With such a diverse range of envisioned applications, we require versatile and adaptable nanopores custom-made for specific purposes. The synthetic pores have to be made with great precision and reproducibility, ideally from a biocompatible material, at high yield. Changing the nanopore architecture, size and functionality has to be straight forward relying on common design principles. A conceptually innovative approach is required to meet all these demands. With the recent advances in DNA nanotechnology, we have the tools at hand to employ DNA as a new material for the design and construction of transmembrane pores. Just as nature uses diverse folds of amino acids, the scope of this doctoral thesis was to fold DNA into functional membrane pores.

In this thesis, we introduce basic concepts and review relevant literature for the creation of synthetic membrane pores from DNA (Chapters 2-4), present the experimental results for four different DNA pore architectures (Chapters 5-8) and outline conclusions, challenges and perspectives for future work (Chapter 9).

In Chapter 2, we first lay the foundations by introducing the basic concepts in DNA nanotechnology. We discuss its scientific development and milestone achievements, including DNA origami, and give guidance on design, assembly and characterisation of DNA nanostructures. We further present possibilities for site-directed chemical functionalisation.

Chapter 3 leads from fundamentals to applications of DNA nanotechnology, highlighting

DNA sensors as a prominent area of interest. We distinguish nanomechanical sensors and nanopore sensors, and introduce nanopore sensing as a label-free technique for the detection of single molecules. We further discuss how DNA nanotechnology can enhance nanopore sensing, which directly leads to DNA origami nanopores. We present previous work on DNA nanopores inserted into solid state supports and discuss their advantages and disadvantages compared to conventional types of nanopores.

Chapter 4 describes the state of the art of synthetic membrane channels. Having laid out the characteristics of natural membrane components as the gold standards for the creation of artificial ones, we review relevant achievements. We finally discuss the potential of synthetic DNA-based membrane pores by considering theoretical models to evaluate the thermodynamics of membrane insertion and to estimate their conductance. We provide detailed experimental protocols for the ionic current characterisation of membrane pores.

Having discussed DNA nanotechnology, nanopores and synthetic membrane channels in the previous three chapters, we combine these concepts to create our first synthetic DNA-based membrane nanopore in Chapter 5. We present a prototype architecture composed of six concentrically arranged DNA duplexes encompassing a channel with a nominal diameter of 2 nm. We establish strategies for membrane anchoring, characterise the DNA pore and confirm its attachment to lipid membranes via confocal imaging. We carry out single-channel ionic current recordings revealing voltage-dependent conductance states.

Since voltage-gating is a typical property of ion channels, we were inspired to create a smaller channel with dimensions comparable to natural ion channels. In Chapter 6, we thus present and characterise a DNA nanostructure composed of four DNA duplexes arranged on a square lattice resulting in a sub-nanometre inner diameter. We demonstrate that the assembly and membrane attachment of this simple structure happens within a minute. Our four-helix bundle induces ionic currents across lipid membranes and exhibits voltage-dependent fluctuations as the larger six-helix pore.

We then push the boundaries on the other end of the spectrum in Chapter 7, by designing a DNA origami porin with a nominal constriction of 6 nm diameter. With dimensions approaching the size of the nuclear pore complex, our DNA porin is the largest man-made membrane pore to date. We validate its high ionic conductance in the range of tens of nanosiemens with experiments and molecular dynamics simulations¹.

A remaining open question concerns the microscopic ion conduction pathway of DNA

¹Simulations were carried out by C.-Y. Li and A. Aksimentiev, University of Illinois at Urbana-Champaign.

pores. In Chapter 8, we provide physical insights into conduction mechanism by studying a single membrane-spanning DNA duplex. Experiments and molecular dynamics simulations show that this construct without hollow interior induces stable transmembrane currents. This can be attributed to the formation of a toroidal DNA-lipid channel at the duplex circumference. We thus demonstrate that ion conduction across lipid membranes does not require the presence of a physical pore. For larger architectures, we conclude that ions flow through the central channel as well as at the DNA-lipid interface.

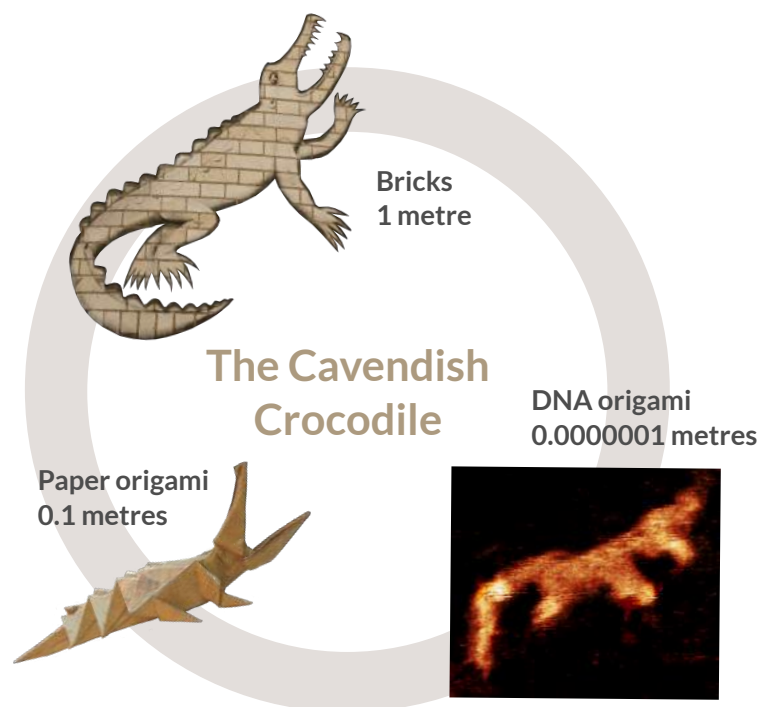
In Chapter 9, we summarise the findings of this thesis. We compare the different channel architectures with protein pores as the gold standards for synthetic pores and give an outlook for future work. We highlight potential applications of DNA-based membrane pores as well as pending challenges.

Bibliography

- [1] M. Baker. “Making membrane proteins for structures: a trillion tiny tweaks.” *Nature Methods* 7.6 (**2010**), pp. 429–34. DOI: 10.1038/nmeth0610-429.
- [2] M. R. Knowles, M. J. Stutts, A. Spock, N. Fischer, J. T. Gatzky, and R. C. Boucher. “Abnormal Ion Permeation through Cystic Fibrosis”. *Science* 221.4615 (**1983**), pp. 1067–70.
- [3] S. Feske. “Calcium signalling in lymphocyte activation and disease.” *Nature Reviews: Immunology* 7.9 (**2007**), pp. 690–702. DOI: 10.1038/nri2152.
- [4] A. Czogalla, H. G. Franquelim, and P. Schwillle. “DNA Nanostructures on Membranes as Tools for Synthetic Biology”. *Biophysical Journal* 110.8 (**2016**), pp. 1698–1707. DOI: 10.1016/j.bpj.2016.03.015.

Chapter 2

Self-assembly with DNA



Parts of this chapter will be reprinted in:

K. Göpfrich & U. F. Keyser, DNA Sensors, Nanopores and Ion Channels, in Biological and Bio-inspired Nanomaterials: Assembly Mechanisms and Properties, Advances in Experimental Medicine and Biology (eds. T. Knowles, A. Buell & S. Perrett), Springer Nature (2017).

Abstract Desoxyribonucleic acid (DNA) is predominantly known as the molecule that carries genetic information. Two complementary DNA strands are held together by the hydrophobic interactions and the Watson-Crick base-pairing of adenine (A) with thymine (T) and cytosine (C) with guanine (G) forming the iconic double helix [1]. While nature exploits the base pairing in the replication and expression of genetic information, the same property makes DNA an excellent material for molecular self-assembly. With a pitch of 3.3 nm and an unhydrated diameter of 2 nm, the dimensions of the DNA double helix are inherently suited for precise architectural control on the nanometre length scale. A linear DNA double helix, however, is of not much use for construction. Transient branched DNA structures have been found in nature, for instance as intermediates occurring during the process of genetic recombination (Holiday junctions) [2, 3]. But the realisation that it is possible to engineer stable DNA branches through intelligent sequence matching opened up the possibility to use DNA beyond its natural purpose as a nanomaterial for design and construction [4, 5]. Over the past thirty years, structural DNA nanotechnology, the science of building with DNA, has progressed tremendously and applied to research questions across disciplines thanks to multiple developments:

1. Due to the development of polymerase chain reaction (PCR), convenient and accurate in vitro DNA synthesis is available at low cost.
2. Off-the-shelf and custom-made chemical modifications of DNA have been developed broadening the scope of DNA nanostructures.
3. The self-assembly of DNA nanostructures does not require specialised equipment.
4. Computer-aided design tools specifically developed for DNA nanotechnology make prototyping quick and accessible.

The following sections will give an overview of some of the most relevant achievements in the field of DNA nanotechnology, including DNA origami, and provide guidance for the design and characterisation of DNA nanostructures. We will further discuss possibilities for the site-directed functionalisation of DNA.

2.1 DNA lattices and tiles

In 1982, Ned Seeman laid the intellectual foundation for the creation of two- and three-dimensional lattices from DNA. He realised the possibility to create immobile nucleic acid junctions by intelligent sequence design as shown in Figure 2.1A. If complementary single-stranded DNA overhangs, so-called sticky ends, are extended from this branched structure, it should be possible to link them up as illustrated in Figure 2.1B, and eventually to construct crystalline “macromolecular valence clusters” from DNA [4]. This idea has in the meantime been employed to construct two-dimensional DNA lattices characterised with atomic force microscopy (AFM) [6, 8–10], see Figure 2.1C. It has fully been realised with a DNA-based crystal structure at 4 Å resolution [7] of an earlier DNA tensegrity triangle [11], see Figure 2.1D. Since the location of an individual DNA sequence within the lattice is known, positions are addressable with near atomic precision and DNA strands with functional groups like proteins [6, 10] can be incorporated as required, see Section 2.4. Additionally, self-assembly of branched DNA structures with a controllable number of binding sites is a powerful tool to probe theories on algorithmic cluster growth and emergence of fractal patterns [9, 12].

Apart from branched junctions, single-stranded DNA bricks or tiles are popular motives in DNA nanotechnology. 32-42 base long single-strands, divided into four domains as shown in Figure 2.2A bind to their local neighbours, Figure 2.2B. Such DNA tiles have been used like LEGO bricks to programme DNA tube circumferences [13] or to construct complex finite-size two- [14] or three-dimensional architectures [15] as shown in Figure 2.2C and D.

2.2 DNA origami

The basic element of most common forms of structural DNA nanotechnology is the four-way DNA junction that allows for the construction of complex objects. One of the most promising techniques for creating large finite-size structures was invented by realising that a long DNA single-strand can be forced into almost any configuration by using short complementary DNA strands. Inspired by previous work [16, 17], Paul Rothemund folded a seven kilobase long single-strand of DNA into a predefined shape by choosing around 200 short complementary oligonucleotide “staples”. The DNA origami concept is illustrated in Figure 2.3A and B. The long scaffold is normally obtained by extracting the genomic DNA of a virus, often the M13mp18 phage with its single-stranded genome,

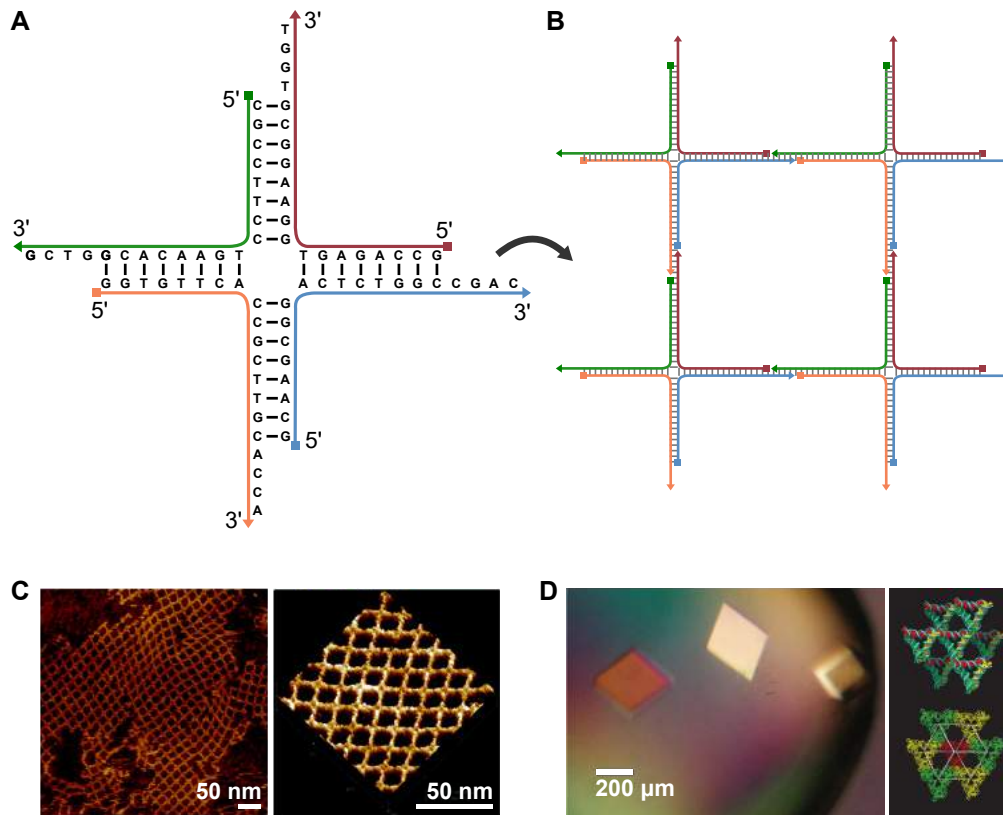


Figure 2.1: Milestone achievements implementing DNA lattices and crystals. A) Schematic drawing of an immobile nucleic acid junction of rank four as proposed by Seeman [4]. Each of the four single-strands (green, red, blue and orange) is partially complementary to two others, single-stranded “sticky ends” induce multimerisation as sketched in (B). Squares indicate 5’ ends of the DNA, triangles indicate 3’ ends. B) DNA lattice formed from the interconnected nucleic acid junctions from (A). By changing the rank of the junction, it should in principle be possible to create versatile two-dimensional lattices and three-dimensional crystals from DNA [4]. C) AFM images of a DNA lattice by Yan *et al.* Each section consists of two parallel double-strands of DNA, the nodes were functionalised with proteins. From [6]. Reprinted with permission from AAAS. D) DNA crystal at 4 Å resolution based on a DNA tensegrity triangle. Adapted by permission from Macmillan Publishers Ltd: Nature [7], copyright 2009.

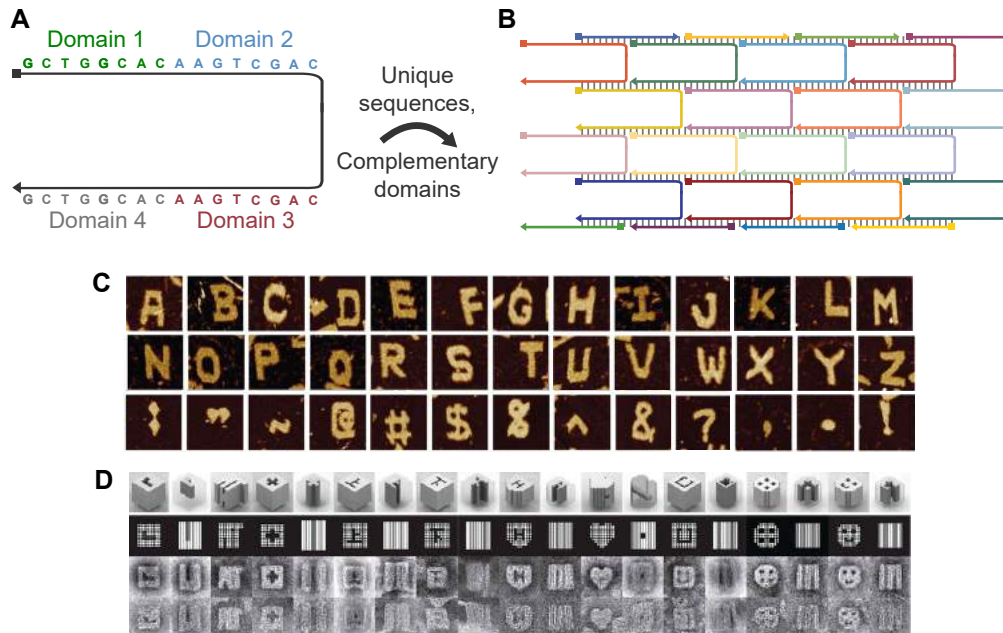


Figure 2.2: Self-assembly from single-stranded DNA tiles. A) Single-stranded DNA tile motive with four modular domains as proposed by Yin *et al.* [13]. A square indicates the 5' end, a triangle the 3' end. B) Unique tiles assemble into the designed secondary structure, whereby each tile binds a complementary domain of four neighbouring tiles. Base pairs are indicated as grey bars. C) AFM images of two-dimensional DNA tile assemblies designed by Wei *et al.* Adapted by permission from Macmillan Publishers Ltd: Nature [14], copyright 2012. D) Ke *et al.* used single-stranded tiles to construct modular three-dimensional DNA bricks. From [15]. Reprinted with permission from AAAS.

while the short staples can be synthesised as required. Both scaffold and staples are commercially available, making DNA origami accessible to a broad community of scientists.

The development of computer-aided design tools for DNA origami described in detail in Section 2.3, streamlined the process of prototyping making it achievable in four simple steps: In the first step, the desired shape is approximated by a lattice-based scaffold path. Secondly, staple pathways complementary to the scaffold are assigned in such a way that the target structure is the single most stable configuration, see Figure 2.3B. Since the base sequence of the scaffold is known, this step defines the staple sequences. Thirdly, these 18-50 bases long sequences are synthesised, often using commercial services. As a last step, the scaffold is mixed with an excess of staples and exposed to a distinct temperature gradient to enable correct hybridisation. This process reliably allows for the creation of billions of identical nanostructures in a simple and robust one-pot reaction. With all these tools at hand, it is not surprising that the DNA origami community grew quickly, contributing to new developments and notable achievements. Paul Rothemund invented DNA origami in 2006, famously exemplified with the nanoscale smiley face shown in Figure 2.3C [18]. Douglas *et al.* were the first to create three-dimensional structures from DNA origami, Figure 2.3D [19]. Possible DNA geometries were expanded further by Dietz *et al.* who designed the curved DNA structures in Figure 2.3E [20], and Benson *et al.* who demonstrated a general method for rendering of polyhedral meshes with DNA origami, Figure 2.3F [21].

2.3 Considerations for design and assembly of DNA nanostructures

In this section, we discuss the design rules for creating DNA nanostructures, introduce computational frameworks that facilitate the prototyping process and discuss conditions for assembly and storage.

2.3.1 Conceiving the target shape

The design of a new DNA nanostructure will depend on the functional requirements for its envisioned application. The first decision to make is whether to use scaffolded DNA origami, see Section 2.2, or a DNA tile approach where the structure is assembled from short single-strands as described in Section 2.1. When using a kilobase long scaffold,

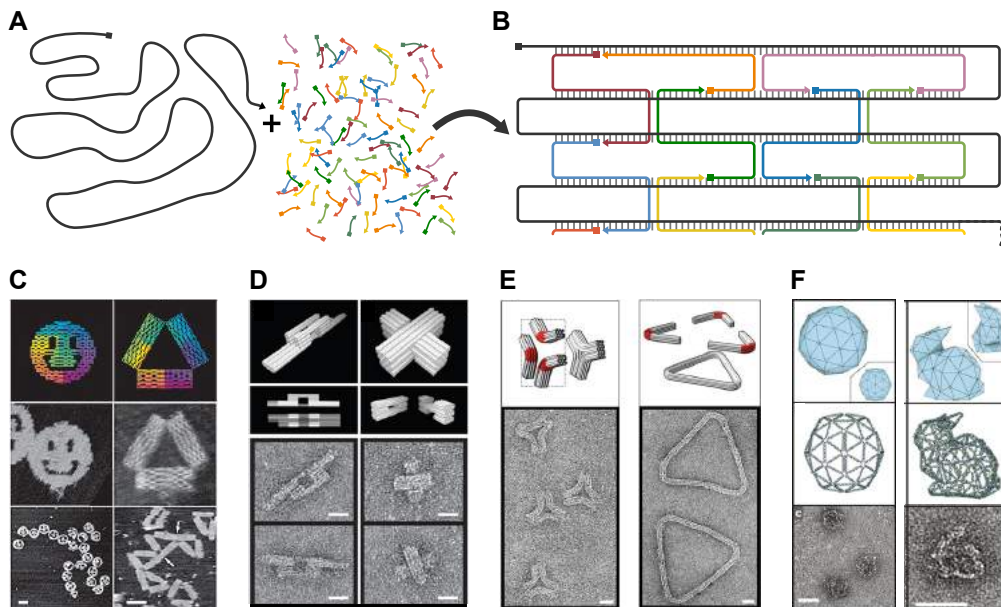


Figure 2.3: Self-assembly of DNA origami. A) A Viral single-strand of DNA (“scaffold”, grey) is mixed with an excess of short synthetic oligonucleotides (“staples”, multicoloured). B) Via complementary base pairing, the staples fold the scaffold into the pre-designed shape. Base pairs are indicated as grey bars. Only a small section of the DNA origami is shown. To fold the entire scaffold, around 200 staples are required. C) Paul Rothemund’s first demonstration of two-dimensional DNA origami. Adapted by permission from Macmillan Publishers Ltd: Nature [18], copyright 2006. D) First three-dimensional DNA origami nanostructures by Douglas *et al.* Adapted by permission from Macmillan Publishers Ltd: Nature [19], copyright 2009. E) Extension to curved DNA origami by Dietz *et al.* From [20]. Reprinted with permission from AAAS. F) Rendering of arbitrary polyhedral meshes from DNA origami by Benson *et al.* Adapted by permission from Macmillan Publishers Ltd: Nature [21], copyright 2015. All structures are tens of nanometres across.

the size of the DNA nanostructure immediately falls into the megadalton regime. The achievable concentrations are limited by the scaffold concentration and placing modifications on the scaffold strand is challenging. Therefore, assembly from short single-strands is useful when the target structure is smaller or has repeating structural units like lattices [10] or tubes [13]. Assembly from single-strands, however, becomes less efficient for large finite-size assemblies (12-17% yield [14]), which is why scaffolded DNA origami is then often the method of choice. Additionally, many of the software tools described in Section 2.3.3 have been developed specifically for DNA origami making its design relatively straightforward. The final yield of a DNA origami structure will depend on the design, the assembly conditions and the chosen scaffold. A good scaffold should have little internal sequence complementarity and secondary structure, like the M13mp18 viral DNA [18]. An additional benefit of selecting one of a few commonly used scaffolds is that they can be purchased from vendors like New England Biolabs or Tilibit. To obtain smaller structures, one can either cut the scaffold to the desired length using restriction enzymes [22, 23] or rely on the synthesis of a long custom DNA sequence (e.g. Ultramers from Integrated DNA Technologies).

2.3.2 Crossover rules for DNA nanostructures

The natural geometry of B-form DNA sets several rules for the design of DNA nanostructures, specifically for the placement of crossovers interconnecting adjacent DNA helices. 10.5 base pairs complete a full helical turn meaning that the angle between two base pairs is approximately 34.3° . If arranged on a hexagonal lattice, there is a 240° angle between neighbouring helices. In order to avoid twist and axial strain [20], a crossover should be placed where the base is pointing in the direction of the neighbour. This happens in constant intervals of 240° or equivalently seven base pairs as illustrated in Figure 2.4A. On a square lattice, where each helix has four immediate neighbours, crossover positions occur every 270° or 7.875 base pairs, see Figure 2.4B. For convenience, a constant eight base pair crossover spacing is often chosen. Global twisting torques can be avoided by either deviating from constant crossover spacing or by introducing base skips leaving one base of the scaffold unpaired [24]. For other helical geometries similar considerations have to be made. By violating crossover spacing rules on purpose, one can create twisted and curved structures from DNA [20].

Both scaffold and staple strands are available for crossovers. A common approach is to interconnect helices with a high density of staple crossovers and reduce the number of scaffold crossovers. Generally, scaffold crossovers should be shifted by 180° or five

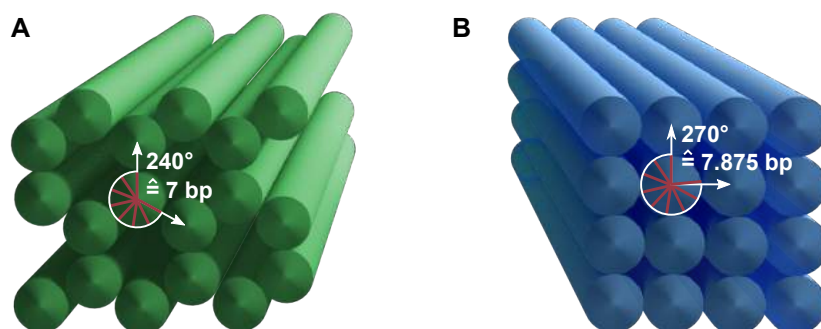


Figure 2.4: Illustration of crossover rules for structural DNA nanotechnology. A) Cross-sectional view of a three-dimensional DNA origami object with hexagonal packing. Suitable crossover positions exist every 7 base pairs along the helical axis, interconnecting a duplex with its three nearest neighbours. B) Cross-sectional view of a three-dimensional DNA origami object on a square lattice. Crossover positions to the four nearest neighbours can be found every 7.875 base pairs. Equidistant crossover spacing will hence induce a global twist.

to six bases relative to the staple crossovers [25]. It is possible that staples interconnect more than two DNA helices while undergoing multiple crossovers, as long as their length is roughly between 18-50 bases. While the lower limit ensures stable binding at room temperature, convenient synthesis at low cost and high purity set the upper limit. Equally, scaffold or staple regions within the structure can be left single-stranded, for instance for the later attachment of functionalised oligomers, to serve as flexible hinges [26, 27], to support tensegrity structures [28] or, most commonly, to prevent unwanted base stacking interactions between structures [18, 29]. An overview of useful values for structural DNA nanotechnology is presented in Table 6.4.

2.3.3 Computational tools for DNA nanotechnology

Multiple software tools have been developed to aid the design of DNA nanostructures. Without any claim to completeness, the following paragraphs describe some of them.

caDNAno caDNAno is an open-source DNA origami design software developed by Douglas *et al.*, available at <http://cadnano.org/> [19]. Multiple online tutorials offer guidance for inexperienced users and template designs are available for download. caDNAno exists as a stand-alone programme as well as a plug-in for Autodesk Maya providing

Table 2.1: Overview of geometrical and molecular features of B-DNA for structural DNA nanotechnology.

Geometry attribute	Approximate value for B-DNA
Helix sense	right-handed
Rotation per base pair	34.3°
Rise per base pair	3.32 Å
Basepairs per helical turn	10.5
Width of unhydrated DNA duplex	2 nm
Average weight of nucleotide (phosphate group + sugar + base)	325 Da
Persistence length	35 nm
Absorbance maximum	260 nm
Ratio of absorbance at 260 and 280 nm ($A_{260/280}$)	1.8
Charge of nucleotide	-e ($-1.6 \cdot 10^{-19}$ C)

an interface for three-dimensional visualisation. Possible DNA geometries are limited to hexagonal and square lattices. While caDNAno has been developed for scaffolded DNA origami, the scaffold path can later be broken up into short strands if the target structure is scaffold-free. Once a known DNA sequence has been assigned to the scaffold, a set of complementary staples is generated upon a single mouse-click. Having placed crossovers by following the embedded rules, the staple sequences can be exported as a spreadsheet and the design-file can be submitted to CanDo for structural analysis.

SARSE SARSE is an earlier software package available at <http://www.cdna.dk/index.php/software.html> for the automatic generation of two-dimensional DNA origami structures [30]. It includes a bitmap reader to import any shape as a design object and generates an atomic model. Conveniently, it tracks the design history and has a fully extendible toolbox.

Tiamat Tiamat is a graphical user interface for efficient modelling of large DNA nanostructures beyond DNA origami [31]. DNA duplexes can be placed freely in the three-dimensional space offering more flexibility than caDNAno. It includes a convenient visualisation tool.

CanDo CanDo, <http://cando-dna-origami.org/>, is a free online tool to predict the three-dimensional shape and flexibility of scaffolded and scaffold-free DNA nanostructures

in solution using finite-element analysis [25]. It can thus help to make design choices before the more cost- and time-intensive DNA synthesis. The structural predictions are regularly improved and updated [32]. Combining caDNAno and CanDo, one can be relatively certain that a new DNA origami design will assemble as designed – merely the yield remains uncertain.

NUPACK NUPACK, <http://www.nupack.org/>, is a free online tool for the analysis and the design of secondary structures of one or more interacting DNA sequences [33]. It is especially useful to inform the choice of DNA sequences for small scaffold-free DNA nanostructures. For such structures, NUPACK’s thermodynamic analysis can help select sequences without stable secondary structures and unwanted complementarities with other strands. A favourable set of DNA sequences will reduce the assembly times and produce a higher yield of the target structure.

vHelix vHelix, <http://www.vhelix.net/>, is a free plug-in for Autodesk Maya, similar to caDNAno, which enables straightforward rendering of polyhedral meshes from DNA [21].

2.3.4 Assembly and stability of DNA nanostructures

Design and assembly conditions are equally important to obtain uniform DNA nanostructures at high yield. Once a structure has been designed, the DNA needs to be synthesised, often relying on commercial services which include purification – standard-desalting is sufficient for unmodified staples, e.g. from Integrated DNA Technologies or Biomers. The first step in the assembly process is the preparation of a staple mix with equimolar concentrations of all constituent DNA staples. For scaffolded DNA origami, staples are added to the scaffold strand in five to tenfold excess. Excess staples can displace unwanted secondary structure by strand invasion helping to prevent misfolding [18] or cross-linking of two scaffolds. For the folding reaction, the DNA mix is supplemented with magnesium chloride and pH-stabilising buffer, often 40 mM Tris-HCl, 45 mM boric acid, 1 mM EDTA, pH 8.2 (0.5× TBE). The magnesium chloride acts as a charge-screening agent to reduce electrostatic repulsion between the densely packed DNA duplexes. The required magnesium chloride concentration will depend on the architecture of the DNA nanostructure. It is advisable to assemble a new structure at a range of magnesium chloride concentrations and determine the optimum concentration via gel electrophoresis as described in Section 2.3.5. For small simple DNA tiles,

2 mM MgCl₂ can be sufficient, whereas multilayer DNA origami often requires 10-20 mM. Magnesium chloride be replaced with increased concentrations of monovalent salts which have a lower affinity to the DNA duplex [34]. Assembly of DNA nanostructures is normally achieved via thermal annealing. The folding mix is heated to 80 °C to melt any secondary structures and subsequently cooled to room temperature over a few hours [18] or days [29]. UV melting profiles can help to optimize the annealing protocol, see Section 2.3.5. Simple scaffold-free designs with well-chosen sequences can be assembled at room temperature within minutes [35]. Isothermal assembly is also achievable for more complex structures under the right conditions in the presence of formamide [36, 37]. After assembly, buffer conditions are less crucial than during the folding process. DNA nanostructures are often stable in a range of buffer conditions, including cell culture medium or acidic buffers of pH 2.0 [25], increasing the possibilities for applications. Unmodified DNA nanostructures can normally be stored at 4 °C for weeks. For longer time periods, it is beneficial to freeze a sample whilst avoiding too many freeze-thaw cycles.

For most applications, scaffolded DNA origami requires purification from excess staples and from potentially misfolded structures. This can be achieved in many different ways, for instance via ultrafiltration, gel extraction, PEG precipitation or magnetic bead capture. Shaw *et al.* provide guidance to obtain the best recovery yield depending on the target structure and its functionalisations [38].

2.3.5 Experimental characterisation of DNA nanostructures

After assembly, it is essential to assess and to quantify the quality of the DNA product. While the level of detail of the characterisation will depend on the target application, there are a number of experimental techniques to demonstrate successful folding, including ultraviolet-visible (UV-vis) spectroscopy, UV melting profiles, gel electrophoresis, imaging and dynamic light scattering (DLS). These techniques will be discussed in the following paragraphs.

UV-vis spectroscopy

After purification of the DNA origami, the UV-vis spectrum gives a first insight into the obtained yield and the purity of the sample. DNA has an absorption maximum at 260 nm [39], a typical UV spectrum is shown in Figure 2.5A. Using the Beer-Lambert law [40], one can directly relate the amount of light absorbed to the concentration of the absorbing

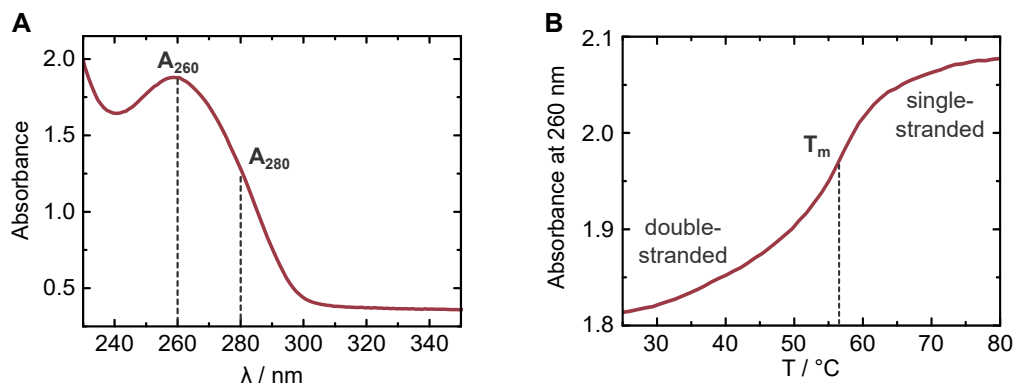


Figure 2.5: A) Typical UV-vis spectrum of a DNA sample with its absorbance maximum at $A = 260$ nm. A_{260} is used to quantify the DNA concentration, for a sample without impurities $A_{260/280} = 1.8$. B) UV melting profile, obtained by applying a linear heating ramp and monitoring the absorbance at 260 nm. The melting temperature T_m is defined as the inflection point of the melting profile. The displayed data was obtained from the four-helix DNA tile structure presented in Chapter 6.

molecule. At a wavelength of 260 nm, double-stranded DNA has an average extinction coefficient of $0.020 (\mu\text{g/ml})^{-1} \text{cm}^{-1}$. Thus, an Absorbance of $A = 1$ corresponds to a DNA concentration of $50 \mu\text{g/ml}$. This method for the determination of concentration is valid up to at least $A \leq 2$ [41]. Low-volume UV-vis spectrophotometers can reliably detect DNA at low concentrations down to a few $\text{ng}/\mu\text{L}$. Since the light is absorbed by the aromatic bases, the extinction coefficient of single-stranded DNA with unpaired bases is higher, approximately $0.027 (\mu\text{g/ml})^{-1} \text{cm}^{-1}$. This number is affected by the length and the base composition for short oligonucleotides [41]. When preparing a DNA sample, it is possible to introduce impurities, like proteins or other organic molecules. While good laboratory practice will help minimise the risk of contamination, the UV spectrum offers a useful control measure. The 260/280 absorbance ratio, $A_{260/280}$, of pure DNA lies around 1.8 [39]. Protein contamination, for instance, can be detected in the UV spectrum because it will result in $A_{260/280} < 1.8$. UV spectroscopy should be repeated every time a DNA nanostructure is assembled, as it is a convenient way of obtaining some information about a DNA sample. It does, however, not give any insights about the shape of the DNA nanostructures or the homogeneity of the sample.

UV melting profile

On a UV spectrophotometer with temperature control, a measurement of the melting profile can directly follow the determination of the UV spectrum. While increasing the temperature, typically at a rate of around $0.25\text{ }^{\circ}\text{C}/\text{min}$ to allow for equilibration inside the measurement cuvette, the absorption at 260 nm is determined. At a certain temperature, when the double-stranded DNA melts into its constituent single-strands, a sudden increase in absorption can be observed. A typical melting profile is shown in Figure 2.5B. The melting temperature T_m is defined as the inflection point of the melting curve, which is why it is common to plot the first derivative dA/dT . The melting temperature can then directly be determined via peak fitting. It typically lies between 50 and $65\text{ }^{\circ}\text{C}$ for DNA origami and other DNA nanostructures [25], which is below the melting temperature of the individual strands. This is caused by electrostatic repulsion and mechanical strain resulting from the tight packing.

Measuring the melting profile is useful for two reasons: First, a sharp melting transition is indicative of cooperative melting behaviour, which is expected for homogeneous and well-folded DNA nanostructures [42]. It can, however, not be understood as a definite proof for correct folding. Second, the melting point can inform the process of optimising the annealing protocol of DNA nanostructures to achieve better yield and shorter annealing times. The percentage of correctly folded structures can be increased by reducing the temperature gradient just before reaching the melting temperature, while the rest of the annealing process can be sped up [43].

Gel electrophoresis

As one of the most common experimental techniques in molecular biology, gel electrophoresis is a powerful and essential tool in the characterisation of new DNA nanostructures. The negatively charged DNA migrates across the porous gel against the direction of the applied electric field. The migration speed will depend on the applied voltage [44], the pore size of the gel [45, 46], the ion concentration and composition of the buffer as well as the size and the shape of the DNA nanostructure [47]. In order to gain the most useful information from a gel, the pore size has to be chosen according to the size of the DNA construct. Generally, two types of gels are used: Polyacrylamide gel electrophoresis (PAGE) is optimal to separate small DNA nanostructures of 5 - $1,000$ base pairs, whereas scaffolded DNA origami and nanostructures between 50 and $30,000$ base pairs, are studied in agarose gels. The polyacrylamide or agarose concentration will

determine the pore size of the gel [45, 46]. Table 2.2 offers guidance to select a suitable gel concentration for the designed nanostructure.

Table 2.2: Recommended gel percentages for optimal resolution of linear DNA. Adapted from: Agilent technologies.

Polyacrylamide gels		Agarose gels	
DNA size range	Gel percentage	DNA size range	Gel percentage
100 - 1,000 bp	3.5 %	1,000 - 30,000 bp	0.5 %
75 - 500 bp	5.0 %	800 - 12,000 bp	0.7 %
50 - 400 bp	8.0 %	500 - 10,000 bp	1.0 %
35 - 250 bp	12 %	400 - 7,000 bp	1.2 %
20 - 150 bp	15 %	200 - 3,000 bp	1.5 %
5 - 100 bp	20 %	50 - 2,000 bp	2.0 %

In a uniform sample, all DNA nanostructures are expected to migrate at the same speed, whereby small structures migrate faster than larger ones. After staining the gel in a bath solution supplemented with an UV-sensitive intercalating dye, the position of the DNA within the gel can be visualised using UV transillumination. Structures of similar size and shape are visible as a clear distinct band. Gels of DNA nanostructures sometimes show a second band at a slower migration speed, which can often be attributed to the formation of dimers due to base-stacking interactions. The relative intensity of the bands allows for conclusions on the abundance of different structures within a DNA sample. By cutting individual bands out of a gel and extracting the DNA from them, it is possible to purify a DNA sample from unwanted structures. It is essential to run gels in the presence of magnesium ions to ensure structural integrity of the sample. A DNA ladder with linear DNA fragments of different length can be used for reference. The gel should typically be loaded with 5 to 100 ng of DNA, whereby the optimum amount will depend on gel composition, running conditions and staining. For detailed advice and troubleshooting on gel electrophoresis of DNA samples see [41].

AFM and TEM

Due to the dimensions of DNA origami and other DNA nanostructures, only atomic force microscopy (AFM) and transmission electron microscopy (TEM) offer sufficient resolution to obtain precise structural information. At the same time, these imaging techniques are the most convincing and reliable evidence for the correct assembly. In AFM, a sample is raster-scanned with a cantilever, which gets displaced via its interac-

tion with the surface. This displacement is detected by collecting the reflection of a laser beam directed onto the cantilever. This information is used to reconstruct the surface topology. AFM imaging of DNA nanostructures is carried out in tapping mode, where the cantilever is driven to oscillate up and down near its resonance frequency. The height of the cantilever is controlled to maintain constant oscillation amplitude. The image is thus produced by determining the force of the intermittent contacts of the tip with the sample. It is possible to use a dry sample, where the DNA is deposited onto a mica surface. While this is often sufficient to confirm the structural integrity, it should be noted that hollow DNA structures can collapse during the drying process [48]. The apparent height of a DNA duplex imaged in air is only around 0.7 to 1 nm [49] likely because the DNA is immersed in a salt layer [50]. When imaging in liquid, DNA nanostructures are visualised in their native environment. Tip compression and tip deconvolution can still alter the observed dimensions. With high-speed AFM, dynamic processes can be monitored. Nanomechanical switching [51, 52], attachment of ligands to a DNA platform [6, 10] or cluster growth [53] have been studied using AFM imaging. A detailed protocol can be found in [54].

While the working principle of a TEM is completely different from an AFM, both imaging techniques obtain comparable resolution for DNA nanostructures [55]. In TEM, a focussed electron beam is transmitted through the sample and an image is generated by detecting the interaction of the transmitted electrons with the sample [56]. Due to the small de Broglie wavelength of electrons, the resolution is greatly enhanced compared to light microscopes. With high-resolution cryo-TEM images, it is possible to identify individual crossovers within a DNA origami structure [57] and to visualise DNA origami together with organic structures like lipid vesicles [58]. TEM is well-suited for hollow three-dimensional structures, as it circumvents problems with tip-compression in AFM. For two-dimensional structures, however, the contrast of TEM images is often not as good, which is why AFM is then the method of choice. Moreover, TEM cannot be used to image living cells, as it requires a vacuum. Details on TEM imaging can be found in [56].

DNA-PAINT

DNA-PAINT, or “DNA-based point accumulation for imaging in nanoscale topography”, is a super-resolution imaging method. Super-resolution is obtained by temporally switching each target between a fluorescence on-state and an off-state, and determining their respective positions with sub-diffraction limit precision. DNA-PAINT uses

transient binding of short fluorescently labelled single-strands of DNA to achieve a resolution down to 5 to 10 nm [59]. Unlike in AFM and TEM, DNA-PAINT offers chemical specificity due to the required hybridisation and even single-stranded DNA can be visualised [60].

Dynamic light scattering

Like gel electrophoresis, dynamic light scattering (DLS) allows for conclusions on the size distribution of DNA nanostructures in solution. It is mainly useful for small DNA structures, where direct imaging via AFM and TEM is more difficult and less conclusive. The hydrodynamic radius of particles is determined by shining a laser onto a sample, collecting the scattered light and analysing temporal fluctuations of the scattered intensity trace. The autocorrelation function in the time domain decays faster for smaller particles, because Brownian motion causes them to move faster than large particles. DLS does, however, not allow for conclusions regarding the shape of a DNA nanostructure, as all particles are approximated as spheres with a certain hydrodynamic radius. For details regarding DLS measurement and analysis see [61].

2.4 Functionalisation of DNA

With all the tools at hand, the creation of new shapes from DNA is no longer the main challenge in the field of structural DNA nanotechnology. We are experiencing a shift from mere structures to functional nano-objects with diverse applications. This is only achievable thanks to the possibility of site-directed chemical modification of DNA with functional groups. Commercially available amino- or thiol-modified oligonucleotides often serve as a starting point for the covalent attachment of the selected crosslinker. Proteins and aptamers have been attached to DNA nanostructures for biomimetic enzyme cascades [62], single molecule detection [63], cellular recognition [64, 65] or controlled substrate release [64, 66]. Gold [67–69] and silver nanoparticles [70, 71] and quantum dots [72] have been incorporated into DNA nanostructures for plasmonic applications [73]. DNA-based polyhedral meshes [21] have recently been used to assemble crystalline nanoparticle-DNA frameworks [74]. Attachment of carbon nanotubes [75] and metallisation of DNA structures [76] may lead to the fabrication of new nanomaterials for electronics. Responsive polymers offer scope for the creation of DNA nanostructures that reversibly change conformation as a response to external stimuli such as light [69, 77] or

pH [78]. Fluorescent dyes and quenchers are commonly incorporated for visualisation purposes or to monitor conformational changes of DNA nanostructures, see Section 3.1. They have also been used to study light harvesting on DNA platforms [79]. Fluorescently tagged DNA nanostructures have found commercial use as standards for super-resolution microscopy [80]. Lipophilic modifications, such as cholesterol or porphyrin tags, will be discussed throughout this thesis in the context of synthetic DNA-based membrane pores (Chapters 4-9). They have further been employed to promote cellular uptake, for two-dimensional assembly of DNA nanostructure arrays [53], or to scaffold [81] and bend vesicles [82]. Some functionalised custom oligomers, including fluorescent or lipophilic tags, can be purchased from vendors like Integrated DNA Technologies or Biomers. Combination of synthetic nucleic acids, like peptide nucleic acid (PNA) [83] or XNA [84], with DNA nanostructures may protect them from enzymatic degradation in living systems and offers control over the backbone charge [85]. Achieving a sufficient yield of the final purified product is still the main challenge for the integration of many heteroelements into DNA nanostructures. An additional challenge for some applications, like DNA-based synthetic light harvesting systems [79], is the lack of control over the orientation of the functional groups. Without chemical modification, dynamic motion of DNA nanostructures can be achieved by strand displacement, where the target strand is equipped with a single-stranded DNA toehold. The addition of a DNA strand which binds to the toehold and has higher sequence complementarity to the target strand will then replace a previously bound strand [86]. This mechanism has been employed for DNA-based logic gates [87], catalysed reaction circuits [88] or synthetic molecular motors [89].

The long-term prospects of structural DNA nanotechnology will depend on its success in constructing sophisticated nano-machines driving active and functional behaviour at a capacity that is unmatched by competing forms of nanotechnology. Until stability, scalability and cost issues are addressed, DNA nanotechnology will mainly be employed to address specific research questions. Yet thanks to the scope of chemical functionalisation, DNA sensors and nanopores have made remarkable progress towards viable applications beyond the research community. These will be discussed in the following chapter.

Bibliography

- [1] J. D. Watson and F. H. C. Crick. “Molecular structure of nucleic acids”. *Nature* 171.4356 (**1953**), pp. 737–8. DOI: 10.1097/BLO.0b013e3181468780.
- [2] R. Holliday. “A mechanism for gene conversion in fungi”. *Genetical Research* 5 (**1964**), pp. 282–304. DOI: 10.1017/S0016672308009476.
- [3] J. Doniger, R. C. Warner, and I. Tessma. “Role of circular dimer DNA in the primary recombination mechanism of bacteriophage S13”. *Nature: New Biology* 242.114 (**1973**), pp. 9–12.
- [4] N. C. Seeman. “Nucleic acid junctions and lattices”. *Journal of Theoretical Biology* 99.2 (**1982**), pp. 237–47. DOI: 10.1016/0022-5193(82)90002-9.
- [5] N. C. Seeman and N. R. Kallenbach. “Design of immobile nucleic acid junctions”. *Biophysical Journal* 44.2 (**1983**), pp. 201–9.
- [6] H. Yan, S. H. Park, G. Finkelstein, J. H. Reif, and T. H. Labean. “DNA-templated self-assembly of conductive nanowires”. *Science* 301 (**2003**), pp. 1882–4. DOI: 10.1126/science.1089389.
- [7] J. Zheng, J. J. Birktoft, Y. Chen, T. Wang, R. Sha, P. E. Constantinou, S. L. Ginell, C. Mao, and N. C. Seeman. “From molecular to macroscopic via the rational design of a self-assembled 3D DNA crystal.” *Nature* 461.7260 (**2009**), pp. 74–7.
- [8] E. Winfree, F. Liu, L. A. Wenzler, and N. C. Seeman. “Design and self-assembly of two-dimensional DNA crystals”. *Nature* 394 (**1998**), pp. 539–44. DOI: 10.1038/28998.
- [9] P. W. K. Rothemund, N. Papadakis, and E. Winfree. “Algorithmic self-assembly of DNA Sierpinski triangles”. *PLoS Biology* 2.12 (**2004**), pp. 2041–53. DOI: 10.1371/journal.pbio.0020424.
- [10] S. H. Park, C. Pistol, S. J. Ahn, J. H. Reif, A. R. Lebeck, C. Dwyer, and T. H. LaBean. “Finite-size, fully addressable DNA tile lattices formed by hierarchical assembly procedures.” *Angewandte Chemie International Edition* 45.5 (**2006**), pp. 735–9. DOI: 10.1002/anie.200503797.
- [11] D. Liu, M. Wang, Z. Deng, R. Walulu, and C. Mao. “Tensegrity: Construction of Rigid DNA Triangles with Flexible Four-Arm DNA Junctions”. *Journal of the American Chemical Society* 126.8 (**2004**), pp. 2324–5. DOI: 10.1021/ja031754r.

- [12] S. Tesoro, K. Göpfrich, T. Kartanas, U. F. Keyser, and S. E. Ahnert. “Non-deterministic self-assembly with asymmetric interactions”. *Physical Review E* 94.022404 (**2016**), pp. 1–8. DOI: 10.1103/PhysRevE.94.022404. arXiv: 1603.08874.
- [13] P. Yin, R. F. Hariadi, S. Sahu, H. M. T. Choi, S. H. Park, T. H. Labean, and J. H. Reif. “Programming DNA tube circumferences.” *Science* 321.5890 (**2008**), pp. 824–6. DOI: 10.1126/science.1157312.
- [14] B. Wei, M. Dai, and P. Yin. “Complex shapes self-assembled from single-stranded DNA tiles.” *Nature* 485.7400 (**2012**), pp. 623–7. DOI: 10.1038/nature11075.
- [15] Y. Ke, L. L. Ong, W. M. Shih, and P. Yin. “Three-Dimensional Structures Self-Assembled from DNA Bricks”. *Science* 338.6111 (**2012**), pp. 1177–83. DOI: 10.1126/science.1227268. arXiv: NIHMS150003.
- [16] H. Yan, T. H. LaBean, L. Feng, and J. H. Reif. “Directed nucleation assembly of DNA tile complexes for barcode-patterned lattices.” *Proceedings of the National Academy of Sciences* 100.14 (**2003**), pp. 8103–8. DOI: 10.1073/pnas.1032954100.
- [17] W. M. Shih, J. D. Quispe, and G. F. Joyce. “A 1.7-kilobase single-stranded DNA that folds into a nanoscale octahedron.” *Nature* 427.6975 (**2004**), pp. 618–21. DOI: 10.1038/nature02310.1..
- [18] P. W. K. Rothemund. “Folding DNA to create nanoscale shapes and patterns.” *Nature* 440.7082 (**2006**), pp. 297–302.
- [19] S. M. Douglas, A. H. Marblestone, S. Teerapittayanon, A. Vazquez, G. M. Church, and W. M. Shih. “Rapid prototyping of 3D DNA-origami shapes with caDNAno.” *Nucleic Acids Research* 37.15 (**2009**), pp. 5001–6. DOI: 10.1093/nar/gkp436.
- [20] H. Dietz, S. M. Douglas, and W. M. Shih. “Folding DNA into twisted and curved nanoscale shapes.” *Science* 325.5941 (**2009**), pp. 725–30. DOI: 10.1126/science.1174251.
- [21] E. Benson, A. Mohammed, J. Gardell, S. Masich, E. Czeizler, P. Orponen, and B. Högberg. “DNA rendering of polyhedral meshes at the nanoscale”. *Nature* 523.7561 (**2015**), pp. 441–44. DOI: 10.1038/nature14586.
- [22] H. Said, V. J. Schüller, F. J. Eber, C. Wege, T. Liedl, and C. Richert. “M1.3 - a small scaffold for DNA origami .” *Nanoscale* 5.1 (**2013**), pp. 284–90. DOI: 10.1039/c2nr32393a.
- [23] S. Brown, J. Majikes, A. Martínez, T. M. Girón, H. Fennell, E. C. Samano, and T. H. LaBean. “An easy-to-prepare mini-scaffold for DNA origami”. *Nanoscale* 7 (**2015**), pp. 16621–24. DOI: 10.1039/C5NR04921K.

- [24] Y. Ke, S. M. Douglas, M. Liu, J. Sharma, A. Cheng, A. Leung, Y. Liu, W. M. Shih, and H. Yan. “Multilayer DNA origami packed on a square lattice”. *Journal of the American Chemical Society* 131.43 (2009), pp. 15903–8. DOI: 10.1021/ja906381y.
- [25] C. E. Castro, F. Kilchherr, D.-N. Kim, E. L. Shiao, T. Wauer, P. Wortmann, M. Bathe, and H. Dietz. “A primer to scaffolded DNA origami.” *Nature Methods* 8.3 (2011), pp. 221–29. DOI: 10.1038/nmeth.1570.
- [26] J. List, M. Weber, and F. C. Simmel. “Hydrophobic Actuation of a DNA Origami Bilayer Structure”. *Angewandte Chemie International Edition* 53.16 (2014), pp. 4236–9. DOI: 10.1002/anie.201310259.
- [27] J. J. Funke and H. Dietz. “Placing molecules with Bohr radius resolution using DNA origami”. *Nature Nanotechnology* 11 (2015), pp. 47–52. DOI: 10.1038/nnano.2015.240.
- [28] T. Liedl, B. Högberg, J. Tytell, D. E. Ingber, and W. M. Shih. “Self-assembly of three-dimensional prestressed tensegrity structures from DNA.” *Nature Nanotechnology* 5.7 (2010), pp. 520–4. DOI: 10.1038/nnano.2010.107.
- [29] S. M. Douglas, H. Dietz, T. Liedl, B. Högberg, F. Graf, and W. M. Shih. “Self-assembly of DNA into nanoscale three-dimensional shapes.” *Nature* 459.7245 (2009), pp. 414–8.
- [30] E. S. Andersen, M. Dong, M. M. Nielsen, K. Jahn, A. Lind-Thomsen, W. Mamdoh, K. V. Gothelf, F. Besenbacher, and J. Kjems. “DNA origami design of dolphin-shaped structures with flexible tails”. *ACS Nano* 2.6 (2008), pp. 1213–18. DOI: 10.1021/nm800215j.
- [31] S. Williams, K. Lund, C. Lin, P. Wonka, S. Lindsay, and H. Yan. *Tiamat: A three-dimensional editing tool for complex DNA structures*. Ed. by A. Goel, F. Simmel, and P. Sosik. Heidelberg: Springer, 2009, pp. 90–101. DOI: 10.1007/978-3-642-03076-5_8.
- [32] K. Pan, D.-N. Kim, F. Zhang, M. R. Adendorff, H. Yan, and M. Bathe. “Lattice-free prediction of three-dimensional structure of programmed DNA assemblies”. *Nature Communications* 5 (2014), p. 5578. DOI: 10.1038/ncomms6578.
- [33] C. Steffen, K. Thomas, U. Huniar, A. Hellweg, O. Rubner, and A. Schroer. “TmoleX—a graphical user interface for TURBOMOLE.” *Journal of Computational Chemistry* 31.16 (2010), pp. 2967–70. DOI: 10.1002/jcc. arXiv: NIHMS150003.
- [34] T. G. Martin and H. Dietz. “Magnesium-free self-assembly of multi-layer DNA objects”. *Nature Communications* 3 (2012), p. 1103. DOI: 10.1038/ncomms2095.

- [35] K. Göpfrich, T. Zettl, A. E. C. Meijering, S. Hernández-Ainsa, S. Kocabey, T. Liedl, and U. F. Keyser. “DNA-tile structures lead to ionic currents through lipid membranes”. *Nano Letters* 15 (2015), pp. 3134–8. DOI: 10.1021/acs.nanolett.5b00189.
- [36] R. Jungmann, T. Liedl, T. L. Sobey, W. Shih, and F. C. Simmel. “Isothermal assembly of DNA origami structures using denaturing agents”. *Journal of the American Chemical Society* 130.31 (2008), pp. 10062–3. DOI: 10.1021/ja8030196.
- [37] J.-P. J. Sobczak, T. G. Martin, T. Gerling, and H. Dietz. “Rapid Folding of DNA into Nanoscale Shapes at Constant Temperature”. *Science* 338.6113 (2012), pp. 1458–61. DOI: 10.1126/science.1229919.
- [38] A. Shaw, E. Benson, and B. Högberg. “Purification of Functionalized DNA Origami Nanostructures”. *ACS Nano* 9.5 (2015), pp. 4968–75. DOI: 10.1021/nm507035g.
- [39] J. Glasel. “Validity of Nucleic Acid Purities Monitored by A260/A280 Absorbance Ratios”. *Biotechniques* 18.1 (1995), pp. 62–63.
- [40] Beer. “Bestimmung der Absorption des rothen Lichts in farbigen Flüssigkeiten”. *Annalen der Physik und Chemie* 86 (1852), pp. 78–88.
- [41] M. R. Green and J. Sambrook. *Molecular Cloning: A Laboratory Manual*. 4. New York: Cold Spring Harbor Laboratory Press, 2012.
- [42] J. R. Burns, K. Göpfrich, J. W. Wood, V. V. Thacker, E. Stulz, U. F. Keyser, and S. Howorka. “Lipid-bilayer-spanning DNA nanopores with a bifunctional porphyrin anchor.” *Angewandte Chemie International Edition* 52.46 (2013), pp. 12069–72. DOI: 10.1002/anie.201305765.
- [43] K. E. Dunn, F. Dannenberg, T. E. Ouldrige, M. Kwiatkowska, A. J. Turberfield, and J. Bath. “Guiding the folding pathway of DNA origami”. *Nature* 525 (2015), pp. 82–6. DOI: 10.1038/nature14860.
- [44] D. L. Holmes and N. C. Stellwagen. “The electric field dependence of DNA mobilities in agarose gels: a reinvestigation.” *Electrophoresis* 11.1 (1990), pp. 5–15. DOI: 10.1002/elps.1150110103.
- [45] D. L. Holmes and N. C. Stellwagen. “Estimation of polyacrylamide gel pore size from Ferguson plots of linear DNA fragments. II. Comparison of gels with different crosslinker concentrations, added agarose and added linear polyacrylamide.” *Electrophoresis* 12.9 (1991), pp. 612–9. DOI: 10.1002/elps.1150120903.
- [46] N. Pernodet, M. Maaloum, and B. Tinland. “Pore size of agarose gels by atomic force microscopy”. *Electrophoresis* 18.1 (1997), pp. 55–8. DOI: 10.1002/elps.1150180111.

- [47] A. Pluen, P. A. Netti, R. K. Jain, and D. A. Berk. “Diffusion of macromolecules in agarose gels: comparison of linear and globular configurations.” *Biophysical Journal* 77.1 (1999), pp. 542–52. DOI: 10.1016/S0006-3495(99)76911-0.
- [48] K. Göpfrich, C.-Y. Li, M. Ricci, S. P. Bhamidimarri, J. Yoo, B. Geynes, A. Ohmann, M. Winterhalter, A. Aksimentiev, and U. F. Keyser. “Large-Conductance Transmembrane Porin Made from DNA Origami”. *ACS Nano* (2016). DOI: 10.1021/acsnano.6b03759.
- [49] H. G. Hansma, I. Revenko, K. Kim, and D. E. Laney. “Atomic force microscopy of long and short double-stranded, single-stranded and triple-stranded nucleic acids”. *Nucleic Acids Research* 24.4 (1996), pp. 713–20. DOI: 10.1093/nar/24.4.713.
- [50] F. Moreno-Herrero, J. Colchero, and A. M. Baró. “DNA height in scanning force microscopy”. *Ultramicroscopy* 96.2 (2003), pp. 167–74. DOI: 10.1016/S0304-3991(03)00004-4.
- [51] A. Kuzuya, Y. Sakai, T. Yamazaki, Y. Xu, and M. Komiyama. “Nanomechanical DNA origami ‘single-molecule beacons’ directly imaged by atomic force microscopy.” *Nature Communications* 2 (2011), p. 449. DOI: 10.1038/ncomms1452.
- [52] R. Arivazhagan, M. Endo, K. Hidaka, P. L. Tao Tran, M.-P. Teulade-Fichou, J.-L. Mergny, and H. Sugiyama. “G-quadruplex-binding ligand-induced DNA synapsis inside a DNA origami frame”. *RSC Advances* 4 (2014), pp. 6346–55. DOI: 10.1039/c3ra45676e.
- [53] S. Kocabey, S. Kempter, J. List, Y. Xing, W. Bae, D. Schiffels, W. Shih, F. Simmel, and T. Liedl. “Membrane-Assisted Growth of DNA Origami Nanostructure Arrays”. *ACS Nano* 9 (2015), pp. 3530–9. DOI: 10.1021/acsnano.5b00161.
- [54] Y. Lyubchenko, L. Shlyakhtenko, and T. Ando. “Imaging of nucleic acids with atomic force microscopy”. *Methods* 54.2 (2011), pp. 274–83. DOI: 10.1016/j.ymeth.2011.02.001.Imaging.
- [55] D. Han, S. Pal, Y. Liu, and H. Yan. “Folding and cutting DNA into reconfigurable topological nanostructures.” *Nature Nanotechnology* 5.10 (2010), pp. 712–7. DOI: 10.1038/nnano.2010.193. arXiv: NIHMS150003.
- [56] D. B. Williams and C. B. Carter. *Transmission electron microscopy*. New York: Plenum Press, 1996.
- [57] X.-C. Bai, T. G. Martin, S. H. W. Scheres, and H. Dietz. “Cryo-EM structure of a 3D DNA-origami object.” *Proceedings of the National Academy of Sciences* 109 (2012), pp. 20012–7. DOI: 10.1073/pnas.1215713109. arXiv: arXiv:1408.1149.

- [58] M. Langecker, V. Arnaut, T. G. Martin, J. List, S. Renner, M. Mayer, H. Dietz, and F. C. Simmel. “Synthetic lipid membrane channels formed by designed DNA nanostructures.” *Science* 338.6109 (**2012**), pp. 932–6. DOI: 10.1126/science.1225624.
- [59] R. Jungmann, M. S. Avendaño, J. B. Woehrstein, M. Dai, W. M. Shih, and P. Yin. “Multiplexed 3D cellular super-resolution imaging with DNA-PAINT and Exchange-PAINT.” *Nature methods* 11.3 (**2014**), pp. 313–8. DOI: 10.1038/nmeth.2835. arXiv: NIHMS150003.
- [60] M. Dai. “DNA-PAINT Super-Resolution Imaging for Nucleic Acid Nanostructures”. *3D DNA Nanostructure: Methods and Protocols*. Ed. by Y. Ke and P. Wang. New York: Humana Press, **2017**, pp. 185–202.
- [61] B. J. Berne and R. Pecora. *Dynamic light scattering*. 2. New York: Dover Publications, Inc., **2000**.
- [62] J. Fu, Y. R. Yang, A. Johnson-Buck, M. Liu, Y. Liu, N. G. Walter, N. W. Woodbury, and H. Yan. “Multi-enzyme complexes on DNA scaffolds capable of substrate channelling with an artificial swinging arm.” *Nature Nanotechnology* 9 (**2014**), pp. 531–36. DOI: 10.1038/nnano.2014.100.
- [63] N. A. W. Bell and U. F. Keyser. “Digitally encoded DNA nanostructures for multiplexed, single-molecule protein sensing with nanopores”. *Nature Nanotechnology* 11 (**2016**), pp. 645–51. DOI: 10.1038/nnano.2016.50.
- [64] Y.-J. Chen, B. Groves, R. A. Muscat, and G. Seelig. “DNA nanotechnology from the test tube to the cell.” *Nature Nanotechnology* 10.9 (**2015**), pp. 748–60. DOI: 10.1038/nnano.2015.195.
- [65] N. Stephanopoulos, R. Freeman, H. A. North, S. Sur, S. J. Jeong, F. Tantakitti, J. A. Kessler, and S. I. Stupp. “Bioactive DNA-Peptide Nanotubes Enhance the Differentiation of Neural Stem Cells Into Neurons”. *Nano Letters* 15 (**2015**), pp. 603–9. DOI: 10.1021/nl504079q.
- [66] S. M. Douglas, I. Bachelet, and G. M. Church. “A logic-gated nanorobot for targeted transport of molecular payloads.” *Science* 335.6070 (**2012**), pp. 831–4. DOI: 10.1126/science.1214081.
- [67] A. Kuzyk, R. Schreiber, Z. Fan, G. Pardatscher, E.-M. Roller, A. Högele, F. C. Simmel, A. O. Govorov, and T. Liedl. “DNA-based self-assembly of chiral plasmonic nanostructures with tailored optical response”. *Nature* 483.7389 (**2012**), pp. 311–4. DOI: 10.1038/nature10889. arXiv: 1108.3752.

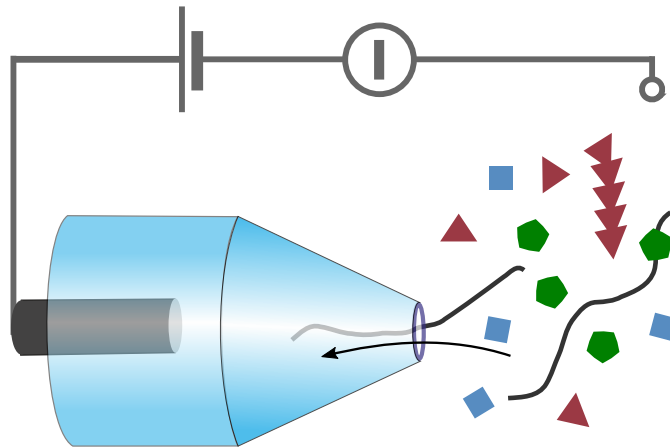
- [68] V. V. Thacker, L. O. Herrmann, D. O. Sigle, T. Zhang, T. Liedl, J. J. Baumberg, and U. F. Keyser. “DNA origami based assembly of gold nanoparticle dimers for surface-enhanced Raman scattering.” *Nature Communications* 5 (2014), p. 3448. DOI: 10.1038/ncomms4448.
- [69] A. Kuzyk, Y. Yang, X. Duan, S. Stoll, A. O. Govorov, H. Sugiyama, M. Endo, and N. Liu. “A light-driven three-dimensional plasmonic nanosystem that translates molecular motion into reversible chiroptical function.” *Nature Communications* 7 (2016), p. 10591. DOI: 10.1038/ncomms10591.
- [70] L. Weller, V. V. Thacker, L. O. Herrmann, E. A. Hemmig, A. Lombardi, U. F. Keyser, and J. J. Baumberg. “Gap-dependent coupling of Ag-Au nanoparticle heterodimers using DNA origami-based self-assembly”. *ACS Photonics* (2016). DOI: 10.1021/acsp Photonics.6b00062.
- [71] S. Pal, Z. Deng, B. Ding, H. Yan, and Y. Liu. “DNA-origami-directed self-assembly of discrete silver-nanoparticle architectures”. *Angewandte Chemie International Edition* 49.15 (2010), pp. 2700–4. DOI: 10.1002/anie.201000330.
- [72] R. Schreiber, J. Do, E.-M. Roller, T. Zhang, V. J. Schüller, P. C. Nickels, J. Feldmann, and T. Liedl. “Hierarchical assembly of metal nanoparticles, quantum dots and organic dyes using DNA origami scaffolds.” *Nature Nanotechnology* 9.1 (2014), pp. 74–8. DOI: 10.1038/nnano.2013.253.
- [73] S. J. Tan, M. J. Campolongo, D. Luo, and W. Cheng. “Building plasmonic nanostructures with DNA”. *Nature Nanotechnology* 6.5 (2011), pp. 268–76. DOI: 10.1038/nnano.2011.49.
- [74] Y. Tian, Y. Zhang, T. Wang, H. L. Xin, H. Li, and O. Gang. “Lattice engineering through nanoparticle–DNA frameworks”. *Nature Materials* 15 (2016), pp. 654–61. DOI: 10.1038/nmat4571.
- [75] H. T. Maune, S.-P. Han, R. D. Barish, M. Bockrath, W. A. G. III, P. W. K. Rothmund, and E. Winfree. “Self-assembly of carbon nanotubes into two-dimensional geometries using DNA origami templates”. *Nature Nanotechnology* 5.1 (2010), pp. 61–6. DOI: 10.1038/nnano.2009.311.
- [76] J. Liu, Y. Geng, E. Pound, S. Gyawali, J. R. Ashton, J. Hickey, A. T. Woolley, and J. N. Harb. “Metallization of branched DNA origami for nanoelectronic circuit fabrication”. *ACS Nano* 5.3 (2011), pp. 2240–7. DOI: 10.1021/nn1035075.

-
- [77] S. Hernández-Ainsa, M. Ricci, L. Hilton, A. Aviñó, R. Eritja, and U.F. Keyser. “Controlling the Reversible Assembly of Liposomes through a Multistimuli Responsive Anchored DNA”. *Nano Letters* 16 (2016), pp. 4462–6. DOI: 10.1021/acs.nanolett.6b01618.
- [78] D. Yao, H. Li, Y. Guo, X. Zhou, S. Xiao, and H. Liang. “A pH-responsive DNA nanomachine controlled catalytic assembly of gold nanoparticles”. *Chemical Communications* 52 (2016), pp. 7556–9. DOI: 10.1039/C6CC03089K.
- [79] E. A. Hemmig, C. Creatore, B. Wünsch, L. Hecker, P. Mair, M. A. Parker, S. Emmott, P. Tinnefeld, U.F. Keyser, and A.W. Chin. “Programming Light-Harvesting Efficiency Using DNA Origami”. *Nano Letters* 16.4 (2016), pp. 2369–74. DOI: 10.1021/acs.nanolett.5b05139.
- [80] J.J. Schmied, M. Raab, C. Forthmann, E. Pibiri, B. Wünsch, T. Dammeyer, and P. Tinnefeld. “DNA origami-based standards for quantitative fluorescence microscopy.” *Nature Protocols* 9.6 (2014), pp. 1367–91. DOI: 10.1038/nprot.2014.079.
- [81] Y. Yang, J. Wang, H. Shigematsu, W. Xu, W.M. Shih, J.E. Rothman, and C. Lin. “Self-assembly of size-controlled liposomes on DNA nanotemplates”. *Nature Chemistry* 8.5 (2016), pp. 476–83. DOI: 10.1038/nchem.2472.
- [82] A. Czogalla, D.J. Kauert, H.G. Franquelim, V. Uzunova, Y. Zhang, R. Seidel, and P. Schwille. “Amphiphathic DNA Origami Nanoparticles to Scaffold and Deform Lipid Membrane Vesicles”. *Angewandte Chemie International Edition* 54 (2015), pp. 6501–5. DOI: 10.1002/anie.201501173.
- [83] R. O. Pedersen, J. Kong, C. Achim, and T.H. LaBean. “Comparative incorporation of PNA into DNA nanostructures”. *Molecules* 20.9 (2015), pp. 17645–58. DOI: 10.3390/molecules200917645.
- [84] V.B. Pinheiro et al. *Synthetic Genetic Polymers Capable of Heredity and Evolution*. 2012. DOI: 10.1126/science.1217622.
- [85] V.B. Pinheiro and P. Holliger. “Towards XNA nanotechnology: new materials from synthetic genetic polymers”. *Trends in Biotechnology* 32 (2014), pp. 321–8. DOI: 10.1016/j.tibtech.2014.03.010.
- [86] B. Yurke, A.J. Turberfield, A.P. Mills, F.C. Simmel, and J.L. Neumann. “A DNA-fulled molecular machine made of DNA”. *Nature* 428.3 (2006), pp. 10092–102. DOI: 10.1021/ja0576738. arXiv: 0202466 [cond-mat].

- [87] Y. Benenson, T. Paz-Elizur, R. Adar, E. Keinan, Z. Livneh, and E. Shapiro. “Programmable and autonomous computing machine made of biomolecules.” *Nature* 414.6862 (**2001**), pp. 430–4. DOI: 10.1038/35106533.
- [88] D. Y. Zhang, A. J. Turberfield, B. Yurke, and E. Winfree. “Engineering Entropy-Driven Reactions and Networks Catalyzed by DNA”. *Science* 318.5853 (**2007**), pp. 1121–5. DOI: 10.1126/science.1148532.
- [89] J. Bath and A. J. Turberfield. “DNA nanomachines.” *Nature Nanotechnology* 2.5 (**2007**), pp. 275–84. DOI: 10.1038/nnano.2007.104.

Chapter 3

DNA sensors and nanopores



Parts of this chapter will be reprinted in:

K. Göpfrich & U. F. Keyser, DNA Sensors, Nanopores and Ion Channels, in Biological and Bio-inspired Nanomaterials: Assembly Mechanisms and Properties, Advances in Experimental Medicine and Biology (eds. T. Knowles, A. Buell & S. Perrett), Springer Nature (2017).

Abstract Living cells have developed an intriguingly complex sensory machinery to detect changes in their environment. Molecular control circuits help convert the sensor information into a reliable motor response adapting to environmental factors. Remarkably, in vitro DNA nanotechnology has made progress towards constructing molecular sensory devices. Applications of DNA sensors range from disease diagnostics to environmental screening or fundamental research. Single-molecule resolution can be achieved and is highly desirable for precise quantification and when a sample is scarce. As of today, DNA-based sensors are one of the most successful applications of structural DNA nanotechnology. They are either based on nanomechanical actuation or nanopores for biosensing. In this chapter, we will describe the working principle of nanomechanical DNA sensors, review existing devices and discuss the potential for future ones. We will then introduce nanopore sensors as a label-free single-molecule sensing technique and discuss how DNA nanotechnology can enhance this type of sensors. DNA origami nanopores are finally presented as an addition to existing types of nanopores. Liu *et al.* [1] and Chandrasekaran *et al.* [2] have written detailed and comprehensive overviews on DNA-based sensors. We just aim to give a brief overview.

3.1 Nanomechanical DNA-based sensors

In a common approach for the fabrication of DNA-based sensors, the DNA nanostructure is designed to undergo a detectable conformation change in response to a signal. This requires a shift from static structures towards dynamic DNA nanotechnology achieved by chemical functionalisation or strand displacement, see Section 2.4 [3]. Sections of single-stranded DNA can serve as flexible hinges interconnecting stiff regions of double-stranded DNA. Since the DNA nanostructure can only amplify the signal, a detection mechanism is still required. But observing the conformation change of a larger DNA structure in AFM and TEM is straight forward as described in Section 2.3.5. Alternatively, a FRET (Förster resonance energy transfer) pair of fluorescent dyes can be placed on the DNA construct. The donor fluorophore is excited and emits light at the right wavelength to excite the acceptor. The Stoke-shifted longer-wavelength emission of the acceptor is then detected. Since the energy transfer efficiency between the two fluorophores depends on their distance, the fluorophore emission is a sensitive measure for the conformation of a DNA nanostructure if the dyes are placed appropriately. Using this approach, a

straightforward bulk measurement of the emission spectrum is sufficient to detect conformational changes, surface immobilisation is not required. Single-molecule FRET can be carried out in addition. Other detection methods for nanomechanical DNA switches involve fluorescent quenchers [4], nanoparticles, colorimetric and electrochemical sensing techniques, gel electrophoresis [5], microfluidics, optical tweezers [6] or magnetic resonance imaging (MRI) contrast agents. DNA sensors with picomolar detection limits and over million-fold selectivity have been reported [4]. Nanomechanical DNA sensors can be based on large DNA origami structures or small functional nucleic acids. Regarding their functionality, they can broadly be divided into two classes: sensors that detect molecules or ions and sensors that detect environmental factors, like temperature or pH.

Molecular sensors Proteins, DNA and ribonucleic acid (RNA) have been detected employing variations of DNA origami or smaller nucleic acid-based sensors [7, 8]. The mechanical response of a DNA nanostructure has also been used to assess DNA repair activity [9] or to detect single-base polymorphisms in double-stranded genomic DNA [10]. Not just molecules, also ions have been detected, employing salt-dependent sequence motifs, like the G-quadruplex or metal-ion-bridged duplex nucleic acids structures [7, 8, 11–13]. A mercury sensor based on functional nucleic acids was integrated into dip-stick tests, making it practical for point-of-care diagnostics [4]. Some DNA sensors have been employed *in vivo* for the detection of messenger RNA as disease markers [14] or cell surface markers [8, 15]. These approaches may lead to the development of “smart drugs” capable of making autonomous decisions and releasing a molecular payload if appropriate. The cancer-targeting DNA origami drug delivery vehicle by Douglas *et al.* [16] and the DNA logic gates for drug release tested in living animals [17] can be seen as proof of principle for such devices.

Environmental sensors Environmental factors, such as temperature, pH, light or electric field can directly affect the conformation of DNA nanostructures or indirectly prompt a mechanical response mediated by functional groups. DNA-based sensors with pH-sensitive i-motives have successfully been used to map pH changes inside living cells [18, 19].

All sensors described until now can be classified as nanomechanical sensors, where the sensing molecule triggers a mechanical switch. The sensing mechanism of nanopores, described in the next section, does not rely on such a conformation change.

3.2 Nanopores for single-molecule detection

In the first instance, a nanopore is nothing but a nanometre-sized hole in an insulating material. But by applying a voltage across a nanopore immersed in an electrolyte solution, one employs it as a powerful albeit simple single-molecule sensor. The applied voltage induces an ionic current. Charged analytes are driven through the pore via electrophoresis, stochastically blocking part of the passage for ions. The current blockade signal can be used to detect the analyte, while its duration and depth provide information about charge, length and conformation of the molecule [20]. In this way, nanopores can achieve label-free detection of nanometre-sized particles, but the sensing mechanism is applicable across scales – as long as the size of the pore matches the size of the analyte. A Coulter counter, invented by Wallace H. Coulter in 1953 [21], uses this principle to detect, size and count cells and other particles between 400 nm and 1 mm [22]. The brilliantly simple and broadly applicable sensing mechanism based on this resistive pulse principle is illustrated in Figure 3.1A and B. A big advantage of nanopore sensors compared to the nanomechanical sensors described in Section 3.1 is that they can be employed as multi-purpose sensors. Whereas previous sensors had to be designed for a specific molecule, nanopores can in principle detect a broad range of different molecules in solution.

Bezrukov *et al.* were the first to demonstrate that a molecular-scale Coulter counter can indeed detect single polymers (polyethylene glycol) in solution [23]. The sensing nanopore itself was taken from nature, where nanopores are ubiquitous as molecular gatekeepers of cellular function. Biological protein nanopores are embedded in the membrane of all cells, where they control the selective transport of ions and biomolecules, see Section 4.1. The challenge for the field of nanopore sensing was to find a protein nanopore which is large enough for the passage of macromolecules and remains open for a sufficiently long period of time. Most protein pores show stochastic opening and closing which could potentially be misinterpreted as molecular translocation events. The bacterial toxin α -hemolysin, however, proved to be ideally suited for the purpose of nanopore sensing and became the most widely used sensing pore [20]. Its crystal structure showed a 10 nm long solvent-filled channel with a constriction of 1.4 nm diameter [24]. Kasianowicz *et al.* demonstrated that α -hemolysin can be used to detect single-stranded DNA and RNA [25]. This result quickly inspired researchers to refine the technology for the purpose of rapid DNA sequencing [26–28], even though the idea of nanopore sequencing had already been sketched out much earlier by David Deamer [29]. The assumption here is that the interaction between the nanopore and the DNA is base-specific [26]. While

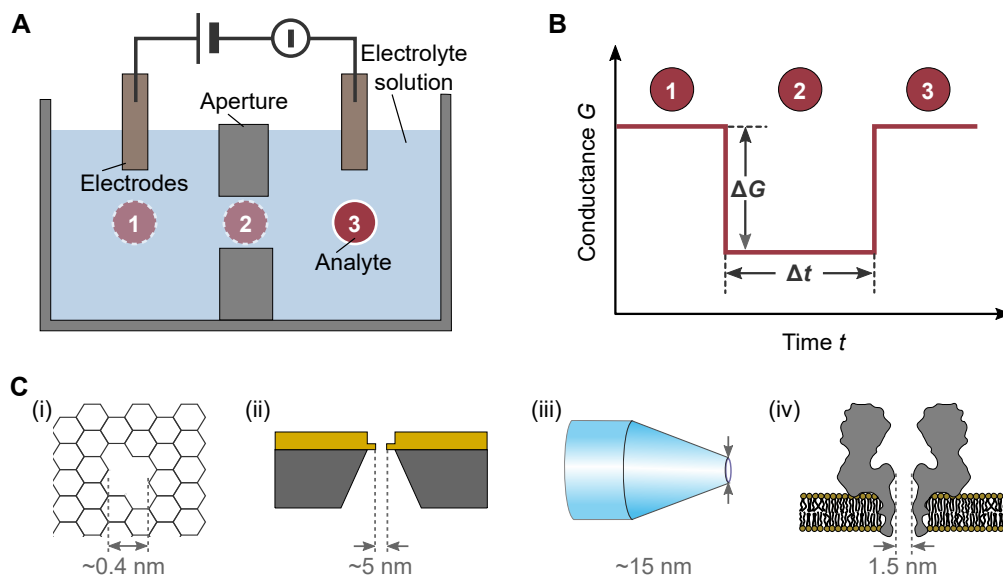


Figure 3.1: Resistive pulse sensing. A) Schematic illustration of a general Coulter counter and its key components. Two reservoirs containing the analyte species, immersed in an electrolyte solution, are connected via an aperture. A voltage is applied across the aperture while the ionic conductance is recorded. B) The passage of an analyte across the aperture via the positions 1, 2 and 3 causes a characteristic resistive pulse signal. The conductance drop ΔG and the passage time Δt contain information about the dimensions and the charge of the analyte. C) Engineered solid-state nanopores, like graphene (i), silicon nitride (ii) or glass (iii) nanopores, and natural protein pores, like α -hemolysin (iv), have been employed for resistive pulse sensing on the nanoscale to detect single molecules.

different oligonucleotides could indeed be distinguished [30], single-base resolution required mechanisms for slowing down and controlling the translocation process. Genetic engineering of the protein pore proved to be a promising approach [31]. The attachment of DNA polymerases [32, 33] and exonucleases [34] to the pore were major steps towards nanopore sequencing. Today, nanopore arrays for real-time sequencing are commercially available [35–37] and have been employed for several sequencing tasks [38–40]. While competing technologies remain the state of the art, the advantages of portable real-time sequencing devices have been demonstrated media-effectively for Ebola surveillance [40] and aboard the International Space Station [41]. While nanopore-based DNA sequencing has attracted a lot of attention, the native or genetically engineered α -hemolysin has also been used to detect many other analytes including small organic molecules [42] or even ions [43].

Apart from protein nanopores, pores in solid-state materials have expanded the field of nanopore sensing. Using nanofabrication techniques, such as ion or electron-beam lithography, single pores can be obtained in materials like silicon nitride [44, 45]. Nanopores in graphene, reducing the material thickness down to a single atomic layer, promise high sensitivity [46, 47]. Even simple low-cost glass capillaries have been employed to detect DNA [48] and proteins [49]. By combining ionic current measurements with force measurements using optical tweezers, one can gain additional information about the translocating molecule [50]. The advantage of solid-state pores are their high stability under a wide range of conditions and their tunable diameters. Even though surface modification with polymers [51], DNA [52] or proteins [53] offers routes to control translocation, the atomic precision and reproducibility of protein pores with the possibility of site-specific mutation remains unmatched. Protein sequencing with nanopores remains an interesting challenge in the field [54].

To design nanopore experiments and interpret the results, one should consider the expected conductance change ΔG due to the passage of the analyte. Let's assume double-stranded DNA is translocating through a solid-state pore. Three effects determine the magnitude of ΔG : First, and most obvious, the conductance is reduced due to the blockade of the ion pathway by the translocating molecule. Second, the counter ions from the electrolyte solution moving along the DNA increase the overall conductance. This is why the nanopore conductance can, counter-intuitively, increase due to the passage of a molecule at low salt concentrations [55]. Third, the passage of the charged DNA itself increases the total conductance. The following equation by Smeets *et al.* takes these

three effects into account to estimate the conductance change ΔG [55]:

$$\Delta G = \frac{e}{L_{\text{Pore}}} \left\{ -\frac{\pi}{4} \cdot d_{\text{DNA}}^2 (\mu_{\text{K}} + \mu_{\text{Cl}}) \cdot n_{\text{KCl}} + 2 \frac{\mu_{\text{K}}^*}{a} + 2 \frac{\mu_{\text{DNA}}}{a} \right\}. \quad (3.1)$$

L_{Pore} denotes the length of the pore, n_{KCl} the bulk concentration of ions and d_{DNA} the diameter of the translocating DNA molecule. μ_{K}^* is the effective electrophoretic mobility of potassium ions moving along the DNA, μ_{K} , μ_{Cl} and μ_{DNA} the mobility of ions and DNA. This equation gives a good estimate for the conductance change under simple conditions without major interactions between the translocating molecule and the pore [55].

3.3 DNA nanotechnology for enhanced nanopore sensing

In principle, nanopores are ideally suited as general-purpose sensors capable of identifying a range of different molecules, beyond DNA, in minimal sample volumes [56]. Yet despite all achievements in the field of nanopore sensing, detecting a molecule in a mixture of others remains challenging. Given that even an isolated molecule can exhibit different current signatures depending on its folding state in the moment of translocation [48], a multitude of similar complexes becomes virtually indistinguishable. This challenge is sketched out in Figure 3.2A and B. While receptor-modified sensing pores offer molecular specificity [42], the pore can then no longer be used as a general sensor for simultaneous detection of a variety of analytes.

Structural DNA nanotechnology offers a route to enhance the capabilities of nanopores while maintaining the simplicity of the sensing technique [56]. As discussed in Section 2.4, DNA nanostructures can be functionalised to bind a range of proteins or other molecules of interest. Before translocating through the pore, a DNA carrier can then fish out analytes in solution. Empty carriers show different current signatures than loaded ones, indicating the presence or absence of the molecule of interest. This concept has been demonstrated with a linear DNA carrier containing aptamer binding sites for proteins at predefined positions along the DNA [58, 59]. Different positions could encode for different proteins. The fabrication of the linear carrier relies on a simplified version of DNA origami: The kilobase-long DNA scaffold is hybridised with hundreds of short addressable staples without crossovers. Bell & Keyser designed a library of DNA nanostructures, where each member has a binding site for a specific antibody and produces a unique current signal due to a barcode of DNA hairpins [57]. This way, nanopore

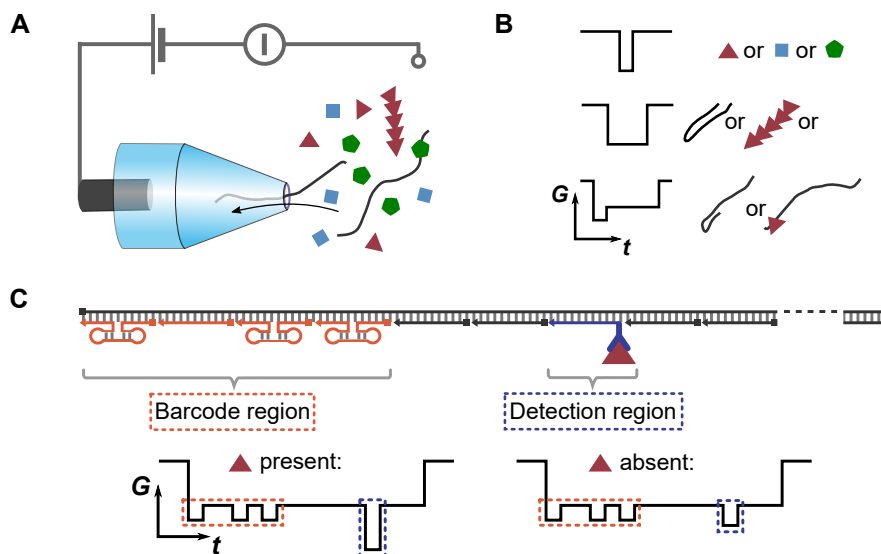


Figure 3.2: A) Schematic illustration of a glass capillary-based nanopore sensor. Various molecules can be driven through the pore via electrophoresis. B) Resistive pulse signals for the passage of different molecules and their ambiguous interpretation. Different proteins (square, triangle, pentagon) are often indistinguishable, signals of protein complexes or DNA-bound proteins may be mistaken for DNA translocating in a non-linear conformation. C) DNA carrier idea demonstrated by Bell & Keyser. The molecule of interest binds to a specific binding site on the DNA carrier, different carriers for different molecules can be identified via their barcode made from protrusions of DNA. The resistive pulse signal now gives a read-out for the barcode and the presence or absence of the target molecule [57].

sensing gained unprecedented specificity: An occupied or unoccupied binding site on the DNA carrier indicates the presence or absence of the protein, while the barcode provides information on the type of protein as illustrated in Figure 3.2C. Relying on DNA nanotechnology, more complex DNA origami carriers for nanopore sensing will contribute to the development of highly portable general-purpose lab-on-the-chip devices.

3.4 DNA origami hybrid nanopores

Another route to enhance nanopore sensing with DNA nanotechnology is to use the DNA nanostructure itself as the sensing pore. Relying on the ability to create arbitrary three-dimensional structures from DNA [60], it should be comparably easy to model

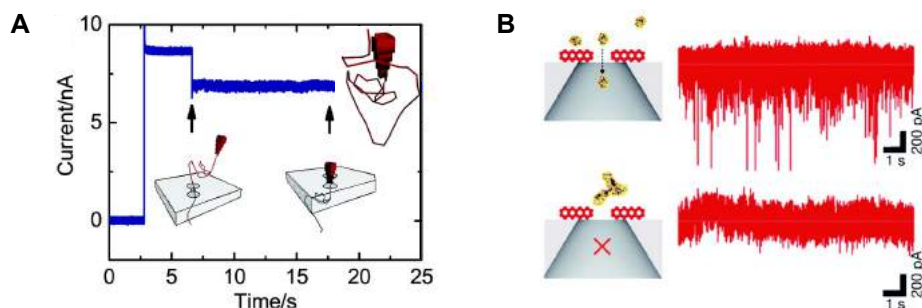


Figure 3.3: DNA origami hybrid nanopores. A) The funnel-shaped DNA origami nanopore by Bell *et al.* was inserted into a solid-state support. The long leash helped guide the voltage-driven formation of the hybrid nanopore. A recorded current trace is shown in blue. The formation of the hybrid pore can be detected as a drop in current (at around $t = 6$ s). Adapted with permission from [61]. Copyright 2012 American Chemical Society. B) Wei *et al.* used a flat DNA origami nanopore to demonstrate size-selective transport of proteins. The smaller streptavidin (top) can translocate through the DNA pore, visible as downward spikes in the current trace (right). The larger immunoglobulin G (bottom) does not fit through the hybrid nanopore. The bare solid-state pore, however, would have transported both species. Reprinted with permission from WILEY [62], copyright 2012.

the shape of a nanopore. DNA origami nanopores have indeed been created and used for sensing purposes by integrating them into solid-state nanopore systems [61, 62]. An appropriate electric field is applied across the solid-state pore in the presence of the DNA origami pores. The negatively charged DNA origami is thus driven towards the pore via electrophoresis, where it is trapped if its diameter is too large for translocation. A double-stranded leash on the DNA origami helps guide the entrance into the solid-state support and to achieve correct positioning. The formation of a hybrid nanopore can be monitored with the standard resistive-pulse measurement. If a DNA origami nanopore is trapped, it partially blocks the flow of ions resulting in a long-lasting stepwise decrease in the ionic current accompanied by a variable increase in noise, see Figure 3.3A. A similar method was previously used to trap α -hemolysin in a solid-state support [63], highlighting the applicability of the approach for a range of different pore geometries. By reversing the voltage, the DNA origami pore can subsequently be ejected and the solid-state support is available for further trapping cycles. The reversibility allows us to obtain statistical information about the inherent variability of the process, caused by different trapping orientations, mechanical conformations or structural damage [64]. Conical glass

nanopores [65] as well as silicon nitride nanopores [61, 62] have been used as solid-state supports capable of trapping DNA origami funnels, Figure 3.3B [61], or flat DNA origami plates, Figure 3.3B [62, 65]. The compatibility with glass capillaries is advantageous, as they can be combined with optical techniques to monitor the trapping [65], they allow for multiplexing [66] and their fabrication is straight-forward [67]. In addition to double-stranded DNA [61, 68], single-stranded DNA [62, 65] and proteins [62] were detected in DNA origami nanopore systems, whereby the voltage required to keep the DNA origami trapped is also used to drive the translocation of the analyte, see Figure 3.3B. Since the detection of all these molecules has been achieved before, without DNA origami, one is prompted to ask what the DNA origami hybrid system adds to the existing technologies. Its advantages are listed below.

Nanopore architecture by design First of all, the diversity of possible pore architectures achievable with DNA origami is unmatched by the conventional types of nanopores. Nanofabrication of solid-state pores offers limited control on the atomic level, especially regarding the pore geometry. Genetic engineering allows us to adapt the shape of a protein pore to some extent, but not in the same way as *de novo* design with DNA nanotechnology. Due to the specific base pairing interactions, DNA pores can be made reproducibly with high precision if the same DNA sequences are used – just like the amino acid sequence determines the shape of proteins.

Tunable pore diameter Precise control over the pore geometry obviously allows for control over the pore size. The diameter of α -hemolysin is well suited for the translocation of single-stranded DNA, yet detection of double-stranded DNA or folded proteins would require a larger pore. Large protein pores which are at the same time stable under high salt conditions and remain open for extended periods of time are rare in nature. While double-stranded DNA has been translocated through the phi29 pore [69], a protein pore large enough for the passage of kilodalton-sized protein complexes has not yet been found. The diameters of DNA-based nanopores, on the other hand, can easily be designed to match the size of the analyte, from ions to macromolecules. Published DNA nanopores span over one order of magnitude in diameter from sub-nanometre pores embedded in lipid membranes, see Chapter 6, to 15 nm pores in solid-state supports [65]. They are thus ideally suited for size-selective sensing. DNA origami nanopores with different diameters have for instance been used to sort two proteins of different sizes, Figure 3.3B [62] and to control the conformation of a linear double-strand of DNA [65].

High specificity Probably the most notable advantage of DNA nanopores are the diverse possibilities to add chemical functionality to the pore. The DNA structure is thereby used as an addressable skeleton, which can be functionalised as described in Section 2.4. Specific binding sites inside a nanopore can help to obtain information about the chemical identity of a molecule. While proteins or DNA hairpins have been used to functionalise solid-state nanopores, controlling the number and the exact location of these modifications within the sensing volume remains challenging. Genetic engineering solves this problem in the case of protein pores – yet only DNA pores have tunable diameters and come with the convenience of commercial synthesis for a wide range of chemical tags. Binding sites obtained by extending single-stranded DNA overhangs into the mouth of the pore have been used for the sequence-specific detection of complementary single-stranded DNA [62, 65]. Attachment of gold or silver nanoparticles to a DNA origami pore offer the possibility of plasmonic sensing in addition to the resistive pulse signal [70].

Stimuli response Chemical functionalisation further allows for the creation of stimuli responsive DNA origami nanopores. This offers a route to generalise DNA-based nanopore sensors beyond the detection of molecules. Responsive polymers attached to the DNA nanopore could trigger a resistive pulse signal in response to a change in physical environment. Light, temperature, pressure or pH could induce a conformation change of the DNA nanopore, similar to gating of natural ion channels. While these opportunities have not yet been fully exploited, voltage-response of DNA nanopores has been reported even without added chemical functionality in solid-state supports [68] and in lipid bilayers, see Chapter 5.

Ease of fabrication With the recent advances in DNA nanotechnology, we can access an elaborate toolbox for the design, assembly and modification of DNA nanopores as described in Chapter 2. While solid-state pores usually have to be fabricated one by one, billions of DNA nanostructures are obtained from a simple one-pot reaction. All components can be purchased off the shelf and the structural characterisation of the pores is straightforward.

DNA origami hybrid nanopores thus possess advantageous properties of both, protein and solid-state nanopores. But to make them really competitive, a few challenges have to be addressed – a major one being the leakage currents reducing the signal-to-noise

ratio for the detection of translocating molecules. Comparing the experimental conductance values of the hybrid pore with simple geometrical models, it is obvious that the DNA structures are permeable to ions [71]. To address this issue, Li *et al.* carried out molecular dynamics (MD) simulations and showed that the permeability can be reduced by increasing the concentration of magnesium ions in solution. Due to better charge screening, the DNA duplexes are more densely packed. They verified their results experimentally [72]. A DNA origami plate designed on a hexagonal lattice showed lower ion permeability than a square lattice plate [73]. Strategies to chemically attach the DNA nanopore to its solid-state support and thus tighten the seal will reduce leakage on the one hand, but make repeated trapping and ejection more difficult. Major groove binders [71] or hydrophobic coating [64] have been suggested as additional strategies. If DNA nanopores are inserted into lipid membranes, the leakage should be reduced further and it should in principle be possible to study passive transport, because the trapping voltage is no longer required.

A second concern is the mechanical stability of the DNA origami. MD simulations have shown bending and reversible layer-separation for DNA origami nanoplates [72]. Also experiments showed buckling and voltage-dependent conformational changes [68, 73]. This may not be surprising given the high electric field strength of around 10^7 V/m in typical nanopore experiments [71].

While the established types of nanopores are unlikely to be replaced entirely, DNA origami nanopores are useful for more challenging sensing applications where precise control over surface chemistry and geometry is an absolute necessity.

Bibliography

- [1] J. Liu, Z. Cao, and Y. Lu. *Functional nucleic acid sensors*. Vol. 109. 5. **2009**, pp. 1948–98. DOI: 10.1021/cr030183i.
- [2] A. R. Chandrasekaran, H. Wady, and H. K. K. Subramanian. “Nucleic Acid Nanostructures for Chemical and Biological Sensing”. *Small* 12 (**2016**), pp. 2689–700. DOI: 10.1002/sml.201503854.
- [3] J. Bath and A. J. Turberfield. “DNA nanomachines.” *Nature Nanotechnology* 2.5 (**2007**), pp. 275–84. DOI: 10.1038/nnano.2007.104.
- [4] S.-F. Torabi and Y. Lu. “Small-molecule diagnostics based on functional DNA nanotechnology: a dipstick test for mercury.” *Faraday Discussions* 149 (**2011**), pp. 125–135. DOI: 10.1039/c005404f.
- [5] A. R. Chandrasekaran, J. Zavala, and K. Halvorsen. “Programmable DNA Nanoswitches for Detection of Nucleic Acid Sequences”. *ACS Sensors* 1.2 (**2016**), pp. 120–123. DOI: 10.1021/acssensors.5b00178.
- [6] D. Koirala, P. Shrestha, T. Emura, K. Hidaka, S. Mandal, M. Endo, H. Sugiyama, and H. Mao. “Single-molecule mechanochemical sensing using DNA origami nanostructures”. *Angewandte Chemie International Edition* 53.31 (**2014**), pp. 8137–41. DOI: 10.1002/anie.201404043.
- [7] Y. Ke, T. Meyer, W. M. Shih, and G. Bellot. “Regulation at a distance of biomolecular interactions using a DNA origami nanoactuator.” *Nature Communications* 7 (**2016**), p. 10935. DOI: 10.1038/ncomms10935.
- [8] M. You, L. Peng, N. Shao, L. Zhang, L. Qiu, C. Cui, and W. Tan. “DNA ”nanoclave”: Logic-based autonomous cancer targeting and therapy”. *Journal of the American Chemical Society* 136.4 (**2014**), pp. 1256–9. DOI: 10.1021/ja4114903.
- [9] M. Tintore, I. Gallego, B. Manning, R. Eritja, and C. Fabrega. “DNA origami as a DNA repair nanosensor at the single-molecule level”. *Angewandte Chemie International Edition* 52.30 (**2013**), pp. 7747–50. DOI: 10.1002/anie.201301293.
- [10] S. X. Chen, D. Y. Zhang, and G. Seelig. “Conditionally fluorescent molecular probes for detecting single base changes in double-stranded DNA.” *Nature Chemistry* 5.9 (**2013**), pp. 782–9. DOI: 10.1038/nchem.1713. arXiv: NIHMS150003.

-
- [11] Y. Sannohe, M. Endo, Y. Katsuda, K. Hidaka, and H. Sugiyama. “Visualization of Dynamic Conformational Switching of the G-Quadruplex in a DNA Nanostructure”. *Journal of the American Chemical Society* 132.46 (2010), pp. 16311–3. DOI: 10.1021/ja1058907.
- [12] Y. Miyake et al. “MercuryII-mediated formation of thymine-HgII-thymine base pairs in DNA duplexes”. *Journal of the American Chemical Society* 128.7 (2006), pp. 2172–3. DOI: 10.1021/ja056354d.
- [13] X. Wang, C. Yang, S. Zhu, M. Yan, S. Ge, and J. Yu. “3D origami electrochemical device for sensitive Pb²⁺ testing based on DNA functionalized iron-porphyrinic metal-organic framework”. *Biosensors and Bioelectronics* 87 (2016), pp. 108–15. DOI: 10.1016/j.bios.2016.08.016.
- [14] Y. Benenson, B. Gil, U. Ben-Dor, R. Adar, and E. Shapiro. “An autonomous molecular computer for logical control of gene expression”. *Nature* 429 (2004), pp. 423–29. DOI: 10.1038/nature02517.1..
- [15] M. Rudchenko, S. Taylor, P. Pallavi, A. Dechkovskaia, S. Khan, V. P. Butler, S. Rudchenko, and M. N. Stojanovic. “Autonomous molecular cascades for evaluation of cell surfaces.” *Nature Nanotechnology* 8.8 (2013), pp. 580–6. DOI: 10.1038/nnano.2013.142.
- [16] S. M. Douglas, I. Bachelet, and G. M. Church. “A logic-gated nanorobot for targeted transport of molecular payloads.” *Science* 335.6070 (2012), pp. 831–4. DOI: 10.1126/science.1214081.
- [17] Y. Amir, E. Ben-Ishay, D. Levner, S. Ittah, A. Abu-Horowitz, and I. Bachelet. “Universal computing by DNA origami robots in a living animal.” *Nature Nanotechnology* 9 (2014), pp. 353–7. DOI: 10.1038/nnano.2014.58.
- [18] S. Modi, C. Nizak, S. Surana, S. Halder, and Y. Krishnan. “Two DNA nanomachines map pH changes along intersecting endocytic pathways inside the same cell.” *Nature Nanotechnology* 8.6 (2013), pp. 459–67. DOI: 10.1038/nnano.2013.92.
- [19] S. Modi, S. M G, D. Goswami, G. D. Gupta, S. Mayor, and Y. Krishnan. “A DNA nanomachine that maps spatial and temporal pH changes inside living cells.” *Nature Nanotechnology* 4.5 (2009), pp. 325–30. DOI: 10.1038/nnano.2009.83.
- [20] U. F. Keyser. “Controlling molecular transport through nanopores.” *Journal of the Royal Society* 8.63 (2011), pp. 1369–78. DOI: 10.1098/rsif.2011.0222.
- [21] W. H. Coulter. *Patent US2656508 A: Means for counting particles suspended in a fluid.* 1953.

- [22] H. E. Kubitschek. “Electronic Counting and Sizing of Bacteria”. *Nature* 182.4630 (1958), pp. 234–5. DOI: 10.1038/182234a0.
- [23] S. M. Bezrukov, I. Vodyanoy, and V. A. Parsegian. *Counting polymers moving through a single ion channel*. 1994. DOI: 10.1038/370279a0.
- [24] L. Song, M. R. Hobaugh, C. Shustak, S. Cheley, H. Bayley, and J. E. Gouaux. “Structure of staphylococcal alpha-hemolysin, a heptameric transmembrane pore.” *Science* 274.5294 (1996), pp. 1859–66. DOI: 10.1126/science.274.5294.1859. arXiv: VY200.
- [25] J. J. Kasianowicz, E. Brandin, D. Branton, and D. W. Deamer. “Characterization of individual polynucleotide molecules using a membrane channel.” *Proceedings of the National Academy of Sciences* 93.24 (1996), pp. 13770–3.
- [26] D. Branton et al. “The potential and challenges of nanopore sequencing.” *Nature Biotechnology* 26.10 (2008), pp. 1146–53. DOI: 10.1038/nbt.1495.
- [27] B. M. Venkatesan and R. Bashir. “Nanopore sensors for nucleic acid analysis.” *Nature Nanotechnology* 6.10 (2011), pp. 615–24. DOI: 10.1038/nnano.2011.129. arXiv: arXiv:1210.1987v2.
- [28] M. Wanunu. “Nanopores: A journey towards DNA sequencing.” *Physics of Life Reviews* 9.2 (2012), pp. 125–58. DOI: 10.1016/j.plrev.2012.05.010.
- [29] E. Pennisi. “Search for Pore-fection”. *Science* 336.6081 (2012), pp. 534–7. DOI: 10.1126/science.336.6081.534.
- [30] A. Meller, L. Nivon, E. Brandin, J. Golovchenko, and D. Branton. “Rapid nanopore discrimination between single polynucleotide molecules.” *Proceedings of the National Academy of Sciences* 97.3 (2000), pp. 1079–84.
- [31] H. Bayley and P. S. Cremer. “Stochastic sensors inspired by biology.” *Nature* 413.6852 (2001), pp. 226–30. DOI: 10.1038/35093038.
- [32] G. M. Cherf, K. R. Lieberman, H. Rashid, C. E. Lam, K. Karplus, and M. Akeson. “Automated Forward and Reverse Ratcheting of DNA in a Nanopore at Five Angstrom Precision”. *Nature Biotechnology* 30.4 (2012), pp. 344–8. DOI: 10.1038/nbt.2147.Automated.
- [33] B. R. Fonslow, B. D. Stein, K. J. Webb, T. Xu, J. Choi, S. Kyu, and J. R. Y. Iii. “Reading DNA at single-nucleotide resolution with a mutant MspA nanopore and phi29 DNA polymerase”. *Nature Biotechnology* 10.1 (2013), pp. 54–6. DOI: 10.1038/nmeth.2250.Digestion. arXiv: NIHMS150003.

- [34] J. Clarke, H.-C. Wu, L. Jayasinghe, A. Patel, S. Reid, and H. Bayley. “Continuous base identification for single-molecule nanopore DNA sequencing”. *Nature Nanotechnology* 4.4 (2009), pp. 265–70. DOI: 10.1038/nnano.2009.12.
- [35] Y. Feng, Y. Zhang, C. Ying, D. Wang, and C. Du. “Nanopore-based fourth-generation DNA sequencing technology”. *Genomics, Proteomics and Bioinformatics* 13.1 (2015), pp. 4–16. DOI: 10.1016/j.gpb.2015.01.009.
- [36] M. Loose, S. Malla, and M. Stout. “Real time selective sequencing using nanopore technology.” *Nature Methods* 13 (2016), pp. 751–4. DOI: 10.1101/038760.
- [37] T. Szalay and J. A. Golovchenko. “De novo sequencing and variant calling with nanopores using PoreSeq”. *Nature Biotechnology* 33.September (2015), pp. 1–7. DOI: 10.1038/nbt.3360.
- [38] N. J. Loman, J. Quick, and J. T. Simpson. “A complete bacterial genome assembled de novo using only nanopore sequencing data”. *Nature Methods* 12.8 (2015), pp. 733–5. DOI: 10.1038/nmeth.3444. arXiv: 015552 [10.1101].
- [39] H. Daims et al. “Complete nitrification by *Nitrospira* bacteria”. *Nature* 528.7583 (2015), pp. 504–9. DOI: 10.1038/nature16461.
- [40] J. Quick et al. “Real-time, portable genome sequencing for Ebola surveillance.” *Nature* 530.7589 (2016), pp. 228–32. DOI: 10.1038/nature16996.
- [41] A. Dunn. *Sequencing DNA in the Palm of Your Hand*. 2016.
- [42] L. Q. Gu, O. Braha, S. Conlan, S. Cheley, and H. Bayley. “Stochastic sensing of organic analytes by a pore-forming protein containing a molecular adapter.” *Nature* 398.6729 (1999), pp. 686–90. DOI: 10.1038/19491.
- [43] O. Braha, L. Q. Gu, L. Zhou, X. Lu, S. Cheley, and H. Bayley. “Simultaneous stochastic sensing of divalent metal ions.” *Nature Biotechnology* 18.9 (2000), pp. 1005–7. DOI: 10.1038/79275.
- [44] A. J. Storm, J. H. Chen, X. S. Ling, H. W. Zandbergen, and C. Dekker. “Fabrication of solid-state nanopores with single-nanometre precision.” *Nature Materials* 2.8 (2003), pp. 537–40. DOI: 10.1038/nmat941.
- [45] J. Li, D. Stein, C. McMullan, D. Branton, M. J. Aziz, and J. a. Golovchenko. “Ion-beam sculpting at nanometre length scales.” *Nature* 412.6843 (2001), pp. 166–9. DOI: 10.1038/35084037.

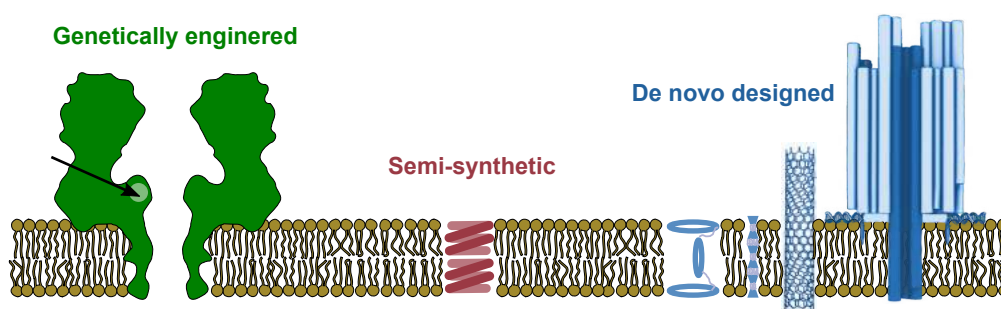
-
- [46] S. Garaj, W. Hubbard, A. Reina, J. Kong, D. Branton, and J. a. Golovchenko. “Graphene as a subnanometre trans-electrode membrane.” *Nature* 467.7312 (2010), pp. 190–3. DOI: 10.1038/nature09379. arXiv: 1006.3518.
- [47] S. J. Heerema and C. Dekker. “Graphene nanodevices for DNA sequencing”. *Nature Nanotechnology* 11.2 (2016), pp. 127–36. DOI: 10.1038/nnano.2015.307.
- [48] L. J. Steinbock, O. Otto, C. Chimerele, J. Gornall, and U.F. Keyser. “Detecting DNA folding with nanocapillaries”. *Nano Letters* 10.7 (2010), pp. 2493–7. DOI: 10.1021/nl100997s.
- [49] W. Li, N. A. W. Bell, S. Herna, R. Bujdoso, and U.F. Keyser. “Single Protein Molecule Detection by Glass Nanopores”. *ACS Nano* 7.5 (2013), pp. 4129–34.
- [50] U.F. Keyser, B.N. Koeleman, S. van Dorp, D. Krapf, R. M. M. Smeets, S. G. Lemay, N.H. Dekker, and C. Dekker. “Direct force measurements on DNA in a solid-state nanopore”. *Nature Physics* 2.7 (2006), pp. 473–7. DOI: 10.1038/nphys344.
- [51] M. Wanunu and A. Meller. “Chemically modified solid-state nanopores”. *Nano Letters* 7.6 (2007), pp. 1580–5. DOI: 10.1021/nl070462b.
- [52] P. Kohli, C. C. Harrell, Z. Cao, R. Gasparac, W. Tan, and C. R. Martin. “DNA-functionalized nanotube membranes with single-base mismatch selectivity”. *Science* 305.5686 (2004), pp. 984–6. DOI: 10.1126/science.1100024.
- [53] T. Jovanovic-Talisman, J. Tetenbaum-Novatt, A. S. McKenney, A. Zilman, R. Peters, M. P. Rout, and B. T. Chait. “Artificial nanopores that mimic the transport selectivity of the nuclear pore complex.” *Nature* 457.7232 (2009), pp. 1023–7. DOI: 10.1038/nature07600.
- [54] L. Movileanu. “Interrogating single proteins through nanopores: challenges and opportunities”. *Trends in Biotechnology* 27.6 (2009), pp. 333–41. DOI: 10.1016/j.tibtech.2009.02.008.
- [55] R. Smeets, U. Keyser, D. Krapf, M. Wu, N.H. Dekker, and C. Dekker. “Salt-dependence of ion transport and DNA translocation through solid-state nanopores”. *Nano Letters* 6.1 (2006), pp. 89–95. DOI: 10.1021/nl052107w.
- [56] U.F. Keyser. “Enhancing nanopore sensing with DNA nanotechnology”. *Nature Nanotechnology* 11.2 (2016), pp. 106–8. DOI: 10.1038/nnano.2016.2.
- [57] N. A. W. Bell and U. F. Keyser. “Digitally encoded DNA nanostructures for multiplexed , single-molecule protein sensing with nanopores”. *Nature Nanotechnology* 11.7 (2016), pp. 1–28. DOI: 10.1038/NNANO.2016.50.

- [58] N. A. W. Bell and U. F. Keyser. “Specific protein detection using designed DNA carriers and nanopores”. *Journal of the American Chemical Society* 137.5 (2015), pp. 2035–41. DOI: 10.1021/ja512521w.
- [59] J. Kong, N. A. W. Bell, and U. F. Keyser. “Quantifying Nanomolar Protein Concentrations Using Designed DNA Carriers and Solid-State Nanopores”. *Nano Letters* 16 (2016), pp. 3557–62. DOI: 10.1021/acs.nanolett.6b00627.
- [60] P. W. K. Rothemund. “Folding DNA to create nanoscale shapes and patterns.” *Nature* 440.7082 (2006), pp. 297–302.
- [61] N. A. W. Bell, C. R. Engst, M. Ablay, G. Divitini, C. Ducati, T. Liedl, and U. F. Keyser. “DNA origami nanopores.” *Nano Letters* 12.1 (2012), pp. 512–7. DOI: 10.1021/nl204098n.
- [62] R. Wei, T. G. Martin, U. Rant, and H. Dietz. “DNA Origami Gatekeepers for Solid-State Nanopores”. *Angewandte Chemie International Edition* 124.20 (2012), pp. 4948–51. DOI: 10.1002/ange.201200688.
- [63] A. R. Hall, A. Scott, D. Rotem, K. K. Mehta, H. Bayley, and C. Dekker. “Hybrid pore formation by directed insertion of α -haemolysin into solid-state nanopores.” *Nature Nanotechnology* 5.12 (2010), pp. 874–7. DOI: 10.1038/nnano.2010.237.
- [64] S. Hernández-Ainsa and U. F. Keyser. “DNA origami nanopores: developments, challenges and perspectives.” *Nanoscale* 6.23 (2014), pp. 14121–32. DOI: 10.1039/c4nr04094e.
- [65] S. Hernández-Ainsa, N. A. W. Bell, V. V. Thacker, K. Göpfrich, K. Misiunas, M. E. Fuentes-Perez, F. Moreno-Herrero, and U. F. Keyser. “DNA origami nanopores for controlling DNA translocation.” *ACS Nano* 7.7 (2013), pp. 6024–30. DOI: 10.1021/nm401759r.
- [66] N. a. W. Bell, V. V. Thacker, S. Hernández-Ainsa, M. E. Fuentes-Perez, F. Moreno-Herrero, T. Liedl, and U. F. Keyser. “Multiplexed ionic current sensing with glass nanopores.” *Lab on a Chip* 13.10 (2013), pp. 1859–62. DOI: 10.1039/c3lc50069a.
- [67] L. J. Steinbock, O. Otto, D. R. Skarstam, S. Jahn, C. Chimere, J. L. Gornall, and U. F. Keyser. “Probing DNA with micro- and nanocapillaries and optical tweezers.” *Journal of Physics: Condensed Matter* 22.45 (2010), p. 454113. DOI: 10.1088/0953-8984/22/45/454113.
- [68] S. Hernández-Ainsa, K. Misiunas, V. V. Thacker, E. a. Hemmig, and U. F. Keyser. “Voltage-Dependent Properties of DNA Origami Nanopores.” *Nano Letters* 14 (2014), pp. 1270–4. DOI: 10.1021/nl404183t.

- [69] F. Haque, S. Wang, C. Stites, L. Chen, C. Wang, and P. Guo. “Single pore translocation of folded, double-stranded, and tetra-stranded DNA through channel of bacteriophage phi29 DNA packaging motor”. *Biomaterials* 53 (2015), pp. 744–52. DOI: 10.1016/j.biomaterials.2015.02.104.
- [70] V. V. Thacker, L. O. Herrmann, D. O. Sigle, T. Zhang, T. Liedl, J. J. Baumberg, and U. F. Keyser. “DNA origami based assembly of gold nanoparticle dimers for surface-enhanced Raman scattering.” *Nature Communications* 5 (2014), p. 3448. DOI: 10.1038/ncomms4448.
- [71] N. A. W. Bell and U. F. Keyser. “Nanopores formed by DNA origami: A review.” *FEBS Letters* 588.19 (2014), pp. 3564–70. DOI: 10.1016/j.febslet.2014.06.013.
- [72] C. Y. Li, E. A. Hemmig, J. Kong, J. Yoo, U. F. Keyser, and A. Aksimentiev. “Ionic Conductivity , Structural Deformation and Programmable Anisotropy of DNA Origami in Electric Field”. *ACS Nano* 9.2 (2015), pp. 1420–33.
- [73] C. Plesa, A. N. Ananth, V. Linko, C. Gulcher, A. Katan, H. Dietz, and C. Dekker. “Ionic Permeability and Mechanical Properties of DNA Origami Nanoplates”. *ACS Nano* 8.1 (2014), pp. 35–43. DOI: 10.1021/nn405045x. arXiv: arXiv:1408.1149.

Chapter 4

Synthetic membrane nanopores



Parts of this chapter will be reprinted in:

K. Göpfrich & U. F. Keyser, DNA Sensors, Nanopores and Ion Channels, in *Biological and Bio-inspired Nanomaterials: Assembly Mechanisms and Properties*, Advances in Experimental Medicine and Biology (eds. T. Knowles, A. Buell & S. Perrett), Springer Nature (2017).

Parts of this chapter previously appeared in:

K. Göpfrich, C.-Y. Li, M. Ricci, S. P. Bhamidimarri, J. Yoo, B. Gyenes, A. Ohmann, M. Winterhalter, A. Aksimentiev, U. F. Keyser. Large-conductance transmembrane porin made from DNA origami. *ACS Nano* (2016). doi:10.1021/acsnano.6b03759

Abstract In the previous chapter, we presented synthetic nanopores in solid state materials as well as biological nanopores in organic lipid membranes. Now, we want to go one step further and ask if it is possible to create an entirely organic nanopore system from scratch, where a man-made pore self-assembles into a lipid bilayer membrane. The scope of synthetic membrane pores reaches from nanopore sensing to biomimicry and beyond, offering broader possibilities for biomedical applications. We first present characteristics of natural membrane pores as gold-standards for creating artificial ones. Having reviewed milestone achievements in the history of synthetic pores, we will discuss the potential of structural DNA nanotechnology for man-made transmembrane pores. We include theoretical estimates for the nanopore conductance and consider the thermodynamics of membrane insertion.

4.1 Membrane pores in nature

Before creating a synthetic membrane pore, a closer look at their natural counterparts, protein membrane pores, is illuminating. Their functions in living organisms are as diverse as their architectures. Small kilodalton ion channels control the selective transport of ions across the lipid membrane and are thus key players in electrically excitable tissue, like neurons or muscles [1]. While ion channels rely on passive transport of ions following an electrochemical or a concentration gradient, ion pumps are active, fuelled by the hydrolysis of adenosine triphosphate (ATP) [1]. Larger porins, found in many prokaryotes and the mitochondria of eukaryotic cells, open selective transmembrane pathways for polar solutes, like sugars or water molecules [2]. The megadalton-sized nuclear pore complex, embedded in the nuclear envelope, can be considered the most sophisticated among all membrane pores. It enables the spacial separation of transcription and translation in eukaryotic cells. The transport of larger substrates is highly selective. For instance, only correctly processed messenger RNA can exit the nucleus, while proteins and lipids are imported [3]. Protein membrane pores span one order of magnitude in diameter and three orders of magnitude in ionic conductance and molecular weight. The common feature of all these protein pores is that they span the lipid bilayer membrane, which defines the cell relative to its environment and divides it into functional compartments to sequester biochemical processes. This membrane is made from amphiphilic

phospholipids forming an approximately 4 nm thick bilayer sheet. Hydrophilic lipid head groups face the cytoplasmic environment and shield the hydrophobic tails from polar water molecules creating a semipermeable barrier. While small apolar molecules like O₂ can pass via free diffusion, the membrane is highly impermeable to ions and polar biomolecules, like sugars, DNA or proteins. The energy cost for ions to cross the lipid membrane via free diffusion lies in the range of hundreds of kT. This process is thus by far not efficient enough to maintain metabolic function requiring efficient molecular exchange mechanisms between membranous compartments [4]. Membrane proteins serve as catalysts of translocation, often switching conformation as a response to external stimuli like membrane potential [5], tension [6] or specific ligands [7]. For some ion channels, the existence of an open and a closed state has been demonstrated with the corresponding crystal structures [8]. Generally, X-ray crystallography of membrane proteins is challenging because of their hydrophobicity and structural flexibility [9]. As of July 2016, only about 600 membrane protein structures were known [10], although 30% of human genes encode for them [11]. Therefore, functional studies via ionic current recordings, described in Section 4.4, can provide crucial insights.

To summarise, protein membrane pores show four main characteristics [12]:

1. They can have a variety of function-dependent structures.
2. They span the lipid bilayer membrane.
3. They mediate the rapid flux of ions without moving themselves.
4. They are often responsive to physical or chemical stimulation.

These are the benchmark criteria which a synthetic pore should fulfil and which we have to test for in experiments.

4.2 Milestones of synthetic membrane pores

Early attempts to mimic the behaviour of protein pores relied on synthetic ionophores, carriers which encapsulated ions before diffusing across the membrane. Prominent ionophores are based on cryptands, calixarenes and crown ethers [13]. Even though this approach mimics some of the biological functions, carrier-mediated transport is orders of magnitude slower compared to the passage through an ion channel and does not fulfil our criteria for the classification as a synthetic pore presented in Section 4.1.

Nevertheless, natural ionophores, like indole, play an important role in biological systems [14]. Real ion channel activity has first been reported for a synthetic peptide in 1977 [15]. Synthetic pore-forming peptides remain an active field of research [16], but when using nature's own building blocks, a channel can only be called semi-synthetic. The first purely synthetic de novo designed channel is commonly attributed to Tabushi *et al.* [17]. The dimer of amphiphilic cyclic oligosaccharides (β -cyclodextrins) still inspires current research [18]. In 1998, Fyles *et al.* created the first stimuli-responsive artificial nanopore: a voltage-sensitive channel [19]. The voltage sensitivity emerged from the asymmetrically positioned charges. The pore design was based on an earlier crown-ether based pore, which can be considered as a milestone achievement itself because of its excellent single-channel activity [20]. Tanaka *et al.* were the first to report ion selectivity for their artificial membrane pore [21]. Moving away from the traditional chemical synthesis approaches for synthetic pores, ion channel behaviour has also been reported for membrane-piercing carbon nanotubes [22]. While all these accounts of synthetic ion channels still fall behind their natural counterparts in terms of structural complexity and specificity of function, it is striking that they achieve the same high ion flux. Catalysis of translocation seems easier to achieve compared to synthetic enzymes, which still fall orders of magnitude behind their natural benchmarks [4].

There are several key challenges to address in taking the field of synthetic membrane pores forward: All synthetic pores presented above are minuscule in size compared to natural protein pores. Their molecular weight falls one to two orders of magnitude behind protein pores which typically have a molecular weight in the range of megadalton. Chemical synthesis of large constructs is hard to achieve and inefficient. While all natural pores are based on polypeptides, independent of their size and function, synthetic pores do not yet have a common molecular basis. This makes it more difficult to compare different synthetic pores and to make functional adaptations. The preparation of many of the described constructs is labour-intensive, often not scalable and requires expert knowledge.

4.3 DNA-based membrane pores

We set out to address the challenges in the creation of synthetic pores by approaching the field from a conceptually different angle. With the recent advances in structural DNA nanotechnology described in Chapter 2, the creation of megadalton sized structures from a single chemical building block is no longer a challenge. The preparation of DNA nanos-

structures is quick and accessible and DNA is an abundant and inherently biocompatible material. DNA origami nanopores have previously been made and inserted into solid-state supports, see Section 3.4. The groundwork for the creation of DNA-based synthetic membrane pores has thus already been carried out. The main remaining challenge was to achieve stable membrane insertion of the DNA construct. To address this challenge, it makes sense to take inspiration from natural protein pores. Some protein pores like the widely used sensing pore α -hemolysin have a large hydrophilic head group allowing the pore to diffuse in the cytoplasmic environment of a cell. The membrane-embedded part of the protein has a hydrophobic belt to lower the energy barrier for membrane insertion. A DNA-based pore is initially hydrophilic due to the negatively charged phosphate groups on the DNA backbone. Chemical hydrophobic modifications, covalently bound to the DNA, could however mimic the hydrophobic belt of membrane proteins. There are numerous candidates for such modifications, such as cholesterol, tocopherol, porphyrin or ethane, some of which are commercially available. Membrane insertion of a DNA-based nanopore has first been demonstrated by Langecker *et al.* who overcame the energy barrier for membrane insertion by attaching 26 cholesterol tags to their pore. TEM images gave convincing visual evidence of successful membrane insertion, ionic current recordings gave an average conductance of 0.9 nS. In this thesis, we aim to expand the design space of synthetic DNA membrane pores by creating significantly smaller and larger, albeit overall simpler pores.

4.3.1 Thermodynamics of membrane insertion

To assess whether it is plausible to anchor a DNA construct in the lipid bilayer membrane, one should first consider the thermodynamics of membrane insertion. Membrane insertion certainly is a complex process and in this section we do not aim to describe the molecular mechanisms. We only estimate the energy cost of pore formation relative to the energy gain for the insertion of hydrophobic tags. This gives a rough idea about the number of hydrophobic tags one would require to insert a DNA pore into the membrane and what pore sizes are achievable.

Membrane insertion involves the formation of a cylindrical hole of radius R_P in the lipid bilayer. A continuum model for the free energy cost F for such a hole in a lipid bilayer was proposed by Litster [23]:

$$F(R_P) = 2\pi\gamma_L R_P - \pi\gamma_S R_P^2. \quad (4.1)$$

Here, γ_L is the line tension and γ_S is the surface tension of the lipid membrane. The first term in Equation 4.1 corresponds to the free energy cost for an edge of length $2\pi R_P$, the second term is the free energy gain for reducing the membrane area by πR_P^2 . Pores in lipid membranes can form spontaneously by thermal fluctuations, but they will reseal unless they exceed a critical radius R_C :

$$R_C = \gamma_L / \gamma_S. \quad (4.2)$$

For a conservative estimate for the energy cost of pore formation, we keep only the linear term in Equation 4.1, which dominates for nanopores with $R_P \approx 10^{-9}$ m. Thus:

$$F(R_P) \approx 2\pi\gamma_L R_P. \quad (4.3)$$

Litster estimated the line tension of a lipid bilayer based on typical molecular interaction energies and gave $\gamma_L \approx 10$ pN. Later, experimental and theoretical values in the range of 5 pN to 40 pN have been published [24]. In this simple model, the energy cost for membrane insertion increases linearly with the outer pore diameter. Let's consider a simple DNA nanopore prototype composed of six concentrically arranged DNA duplexes on a hexagonal lattice. Assuming an anhydrated DNA diameter of 2 nm, this pore would have a channel diameter of 2 nm with an outer diameter of 6 nm. Insertion of this structure into a lipid bilayer would imply an energy cost between 85 pN nm and 690 pN nm or approximately 20 kT to 170 kT. This energy cost has to be compensated by an energy gain from the insertion of hydrophobic tags into the membrane. For cholesterol, the free energy gain for insertion into a lipid bilayer was estimated from continuum solvent models and is expected to lie around 25 kT [25]. Insertion of the DNA structure into the lipid membrane would thus require only a few cholesterol anchors, one to seven based on our rough estimates, making it seem plausible. A pore with the described dimensions was constructed as our prototype membrane pore in Chapter 5.

For a more precise estimate on whether the gain in free energy produced by incorporation of cholesterol anchors into a lipid bilayer membrane can compensate the free energy penalty associated with the formation of a lipid pore, C.-Y. Li and A. Aksimentiev, University of Illinois at Urbana-Champaign, carried out coarse-grained simulations [26] as described in Appendix A1. They estimated the free energy of pore formation using the MARTINI coarse-grained model [27], which is known to semi-quantitatively reproduce the mechanical properties of lipid bilayers [28, 29]. Starting from an equilibrated lipid

bilayer system, a pore of radius R_P was created by applying a cylindrical half-harmonic wall potential to lipid molecules as shown in Figure 4.1A [29]. Figure 4.1B plots the average pressure exerted by the lipid molecules on the potential wall as a function of the pore radius R_P . The pressure was computed by dividing the total force applied by the potential wall to the lipid molecules by the surface area, $2\pi R_P L_P$, where $L_P = 4$ nm is the lipid bilayer thickness. The pressure increases initially reaching 300 bar for a critical radius of $R_P = 0.5$ nm, then decreases monotonically as R_P increases, levelling off at approximately 20 bar. The work required to form a pore of radius R_P can be determined by integrating the pressure-volume (pV) work [26]:

$$W_P(R_P) = \int_0^{R_P} p_P(r) \times 2\pi r L_P dr. \quad (4.4)$$

Previous MD studies estimated the insertion free energy of a single cholesterol molecule into a lipid bilayer at $\Delta F_{\text{Chol}} = -75$ kJ/mol [30]. For the DNA porin insertion to be favourable, the sum of the pore formation work, $W_P(R_P)$, and the insertion free energy ΔF_{Chol} of N cholesterol anchors must be negative:

$$W_P(R_P) + N\Delta F_{\text{Chol}} < 0. \quad (4.5)$$

Figure 4.1C shows the value of the sum as a function of the pore radius and the number of cholesterol anchors. These coarse-grained simulations can give guidance when planning a new DNA membrane pore design. It should be noted, however, that the pore radius of the pore in the lipid membrane, R_P , is not necessarily identical with the outer pore radius of the DNA pore. In fact, MD simulations have shown that there are gaps at the DNA-lipid interface resulting in a larger effective lipid pore diameter, see Chapters 7 and 8. Nevertheless, even large pores seem plausible with a realistic number of cholesterol tags, as we will demonstrate in Chapter 7.

4.3.2 Estimating the nanopore conductance

In the simplest model, an ion channel can be treated as an aqueous, cylindrical resistor without internal electric field within an otherwise impermeable membrane. The Hille equation then gives an estimate for the resistance predicting the maximal possible flux of ions [1]:

$$R_{\text{Cyl}} = \frac{1}{\sigma} \cdot \frac{l}{\pi r^2}. \quad (4.6)$$

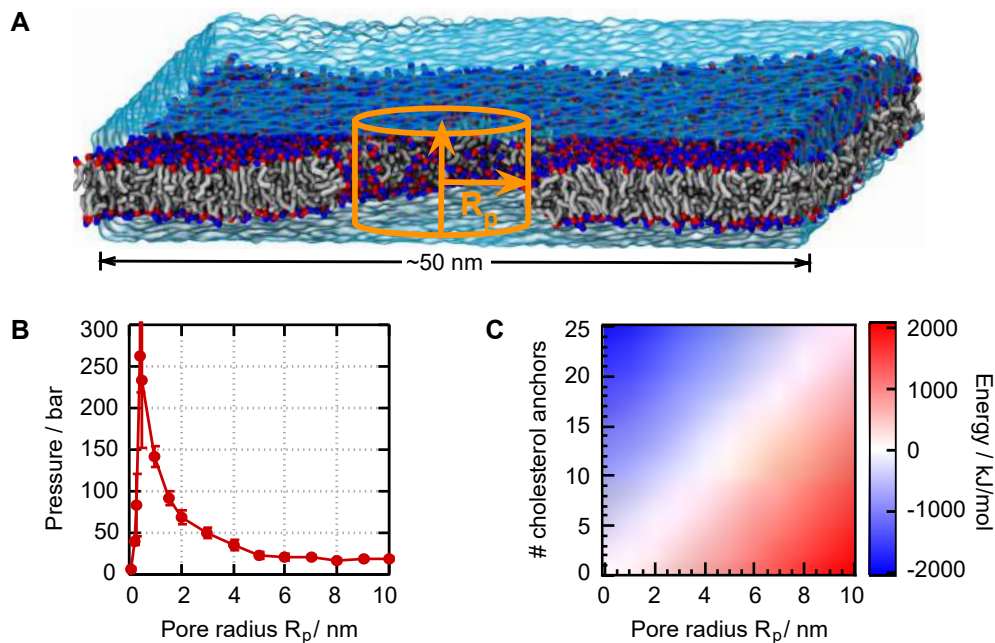


Figure 4.1: Coarse-grained simulations of the energetics of pore formation carried out by C.-Y. Li and A. Aksimentiev, University of Illinois at Urbana-Champaign. A) Setup of the simulation. Cut-away view of a 50 nm patch of a lipid bilayer membrane containing a single cylindrical pore of radius R_p submerged in a rectangular volume of water (blue semi-transparent surface). The coarse-grained beads representing lipid hydrocarbon, phosphate, and choline are shown in grey, red and blue, respectively. The orange cylinder indicates the half-harmonic potential wall that stabilises the pore. B) Pressure exerted on the half-harmonic potential wall by the lipid molecules, p_p , as a function of the pore radius, R_p . C) Free energy of DNA porin insertion as a function of the pore radius and the number of cholesterol anchors. The free energy was computed as the sum of the work required to create a pore of radius R_p , $W_P(R_p)$, and the insertion free energy of N cholesterol anchors, $N \times \Delta F_{\text{Chol}}(N)$. $W_P(R_p)$ was computed from Equation 4.4.

Here, σ is the conductance of the electrolyte solution and l and r specify the length and the radius of the pore. In addition to the resistance of the cylinder, the access resistance R_{Access} caused by limited diffusion and entrance into the pore has to be taken into account [1]:

$$R_{Access} = \frac{1}{\sigma} \cdot \frac{1}{2r}. \quad (4.7)$$

Thus, the total conductance G of a nanopore can be approximated as

$$G = \frac{1}{R_{Cyl} + R_{Access}} = \sigma \cdot \frac{2\pi r^2}{2l + \pi r}. \quad (4.8)$$

The conductance of 1 M KCl, a standard electrolyte solution for lipid bilayer recordings, is $\sigma = 11$ S/m at room temperature [31]. For reference, for a 15 nm long pore with an inner diameter of 2 nm Equation 4.8 predicts a conductance of 2 nS. We will present a DNA pore with these dimensions in the following chapter. The crude approximation based on the ohmic conduction model works best for highly conductive channels, but becomes less reliable as the channel dimensions decrease, where charge and dehydration effects are dominant. These effects can only be modelled with continuum equations or MD. From experiments with protein pores with conductances above 150 pS, the Hille equation typically overestimates the conductance by 30-50 % [32]. An additional shortcoming of the Hille equation is that it predicts the same conductivity for all types of ions in a mixture. For a highly negatively charged DNA pore a certain degree of selectivity for cations is to be expected, which would reduce its conductance. In our study of DNA-based membrane pores, we find that their conductance behaviour is even more complex. The contributing factors are detailed in the following chapters. To describe the conductance behaviour more adequately, we also present MD simulations carried out in collaboration with the group of Aleksei Aksimentiev, University of Illinois at Urbana-Champaign.

4.4 Ionic current characterisation

Single-channel ionic current recordings are at the core of membrane pore characterisation – for natural pores and thus also for synthetic pores. The ionic current passing through a single channel has for the first time been recorded by Neher and Sackman using their Nobel Prize-winning patch-clamp method [33]. Forming a tight seal between

a glass pipette and the cell membrane, one can electrically isolate a membrane patch small enough to contain one or a few ion channels. With an appropriate amplifier, ionic currents in the picoampere range are recorded. These currents often exhibit stochastic fluctuations between distinct states, attributed to channels switching between conformations.

A range of techniques have been developed to study membrane proteins *ex vivo* in synthetic membranes providing a simpler environment in which uncharacterised channels can be studied in isolation. All of them rely on the same measurement principle: A lipid membrane is supported across an aperture and an electric field is applied across the membrane inducing an ionic current. Magnitude, noise and fluctuations in the recorded ionic current allow for conclusions on the presence or absence of membrane pores, their size, their stability and their functional properties like gating, ligand-binding or ion selectivity [34].

Every lipid bilayer experiment starts with the formation of a lipid membrane. Since the membrane is a gigaohm resistor reducing the flow of ions across the aperture, its formation can be observed as a sudden decrease in the ionic current. The insertion of a membrane pore, on the other hand, opens a transmembrane passage for ions and thus causes a stepwise increase in ionic current. Amongst others, commercial supported membrane systems have been used for the characterisation of DNA pores, see Section 5.3.4 [35]. As a general rule for the characterisation of unknown pores – synthetic or natural – it is always advisable to use at least two different techniques to verify pore insertion and nanopore conductance. This is especially crucial because the properties of the membrane can influence the single-channel behaviour as we will discuss in Chapter 5. We found two methods, lipid nano bilayers and solvent containing membranes, especially useful for the characterisation of synthetic DNA pores. These two techniques, and their advantages for our purpose, are described below.

4.4.1 Lipid nano bilayers

Lipid nano bilayers are supported membrane patches of only around 200 nm in diameter that are formed by bursting vesicles across the tip of a glass capillary. This method has been developed by Gornall *et al.* [36] and tested on biological membrane proteins such as the porin OmpF [36] and α -hemolysin [37]. A sketch of the setup is shown in Figure 4.2A. The glass capillary tips are fabricated in a similar way as the much larger patch-pipettes for ionic current recordings on cells [33]. By adjusting the pulling parameters on a conventional laser pipette puller, one can reduce the tip diameter down to

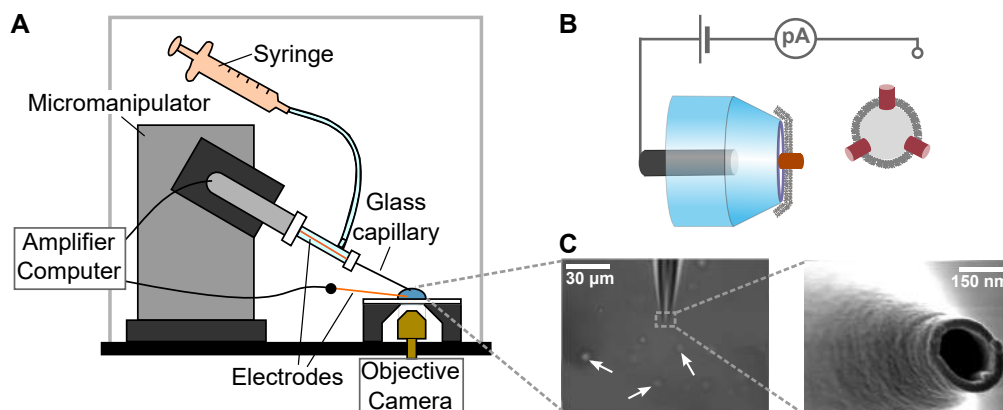


Figure 4.2: The lipid nano bilayer setup for ionic current recordings of membrane pores. A) Sketch of the setup and its components. A bilayer patch is formed by bursting a *GUV* onto the glass capillary when applying a negative pressure with the syringe. *GUVs* are monitored on screen via an inverted microscope with a $60\times$ objective. The position of the glass capillary within the bath solution can be adjusted via a micromanipulator. The ionic current is amplified and recorded. B) Schematic close-up of the glass capillary tip (not drawn to scale), showing the bilayer patch supported across a glass capillary and illustrating the ionic current recording principle. C) Left: Microscope image showing the glass capillary immersed in the bath solution and surrounded by *GUVs* (indicated by white arrows). Right: SEM image of the glass capillary tip coated with a 10 nm thick Pd/Au layer to prevent charging effects. Adapted with permission from [36]. Copyright 2011 American Chemical Society.

the nanometre scale as visible in the scanning electron microscope (SEM) image in Figure 4.2C (right). Details on the pulling parameters for the fabrication of the tips can be found in the protocol in the following section. Without further modification, the tips are connected to a plastic syringe via a pipette holder. One Ag/AgCl electrode is inserted into the back of the capillary, while the ground electrode is placed in the bath solution, see Figure 4.2A. Giant unilamellar vesicles (*GUVs*) are prepared via electroformation as described in the following section and added to the bath solution. They can be monitored via a microscope with a $60\times$ objective, see microscope image in Figure 4.2C (left). A supported membrane can simply be formed by applying a suction at the back of the glass capillary using the syringe. When applying a suction, *GUVs* are drawn towards the tip and burst when in contact, forming a supported lipid membrane. Lipid bilayers can be broken by applying a positive pressure and reformed rapidly without replacing

the tip [36, 37].

Lipid nano bilayers have several advantages for current recordings of new synthetic DNA membrane pores. Due to the membrane curvature, insertion into lipid vesicles is energetically favourable compared to planar lipid bilayers [38]. This can help compensate for a low insertion rate. Moreover, a large number of vesicles can be screened for pore incorporation within a very short time. This enables us to obtain a reasonable amount of ionic current data even if the insertion rate of the pore is not yet optimised. The second advantage lies in the increased bilayer stability. Due to their small diameter, lipid nano bilayers can be stable up to 400 mV for longer time periods [36] and withstand short high voltage pulses up to 1 V. Such pulses facilitate membrane insertion via electroporation [38]. These properties make our nano bilayer system ideally suited to study ionic current characteristics of uncharacterised membrane pores and pores with low insertion rates. The main disadvantage of the lipid nano bilayer method is that the membrane pores are already inserted prior to the ionic current recording. One can thus not directly observe the stepwise increase in current attributed to the insertion of a membrane pore. The presence of membrane pores can rather be deduced from lower average resistances of the membrane patches and due to typical pore behaviour, such as gating. This is why it is ideal to use a second, independent technique to verify the results from the lipid nano bilayer recordings, like the solvent-containing bilayers described in Section 4.4.3.

4.4.2 Experimental procedure and troubleshooting

In this section, we aim to provide details on the experimental procedure for lipid nano bilayer recordings and guidance for troubleshooting. Before the actual ionic current recording, glass capillaries and GUVs have to be prepared as described below.

Fabrication of glass capillaries for the lipid nano bilayer setup

Reagents & materials: Borosilicate glass capillaries with filament and 0.5 mm outer diameter, 0.062 mm wall thickness (Hilgenberg GmbH); for cleaning: acetone, ethanol, pressurised nitrogen

Equipment: Laser pipette puller (Sutter Instruments, P-2000)

Fabrication of glass capillaries for the lipid nano bilayer setup – *Timing:*
45 min

PROCEDURE:

1. Sonicate capillaries in acetone for 15 min, then dry with pressurised nitrogen.
2. Sonicate in ethanol for 15 min, then dry thoroughly with pressurised nitrogen.
3. Attach ends of the capillary to the pulling slides of the pipette puller.
4. *Critical step:* Choose appropriate pulling parameters to obtain tip sizes of 150 nm to 250 nm, e.g.: HEAT = 180, FIL = 2, VEL = 19, DEL = 130, PUL = 125, typical pulling times: ~ 1.3 s.
5. After pulling, remove capillaries carefully using tweezers and store in box for up to four weeks at room temperature (or until they cannot be backfilled any more).

TROUBLESHOOTING:

Inconsistent, too small or too large tip diameters, noticeable as a change in pulling times, looping of the pulling programme and decreased or increased resistances on lipid nano bilayer setup

- Clean pipette puller as described in manual.
- Work at consistent lab temperatures.
- Make sure capillaries are dry before pulling.
- If none of above works: adjust pulling parameters (laser power or capillary properties may have changed), increasing HEAT, VEL, DEL and PUL will increase capillary resistances.
- Pull 5 pairs of capillaries, note their pulling times and measure resistances on lipid nano bilayer setup until suitable set of parameters found.

The critical step in obtaining glass capillary tips for the formation of lipid nano bilayers is to set the correct pulling parameters. The pulling process on the laser puller consists of two stages: While a CO₂ laser heats the middle of the capillary, its ends are pulled apart. As a result, the glass diameter shrinks in the heated area. A second stronger pull tears the capillary apart in the middle. This gives two nearly identically shaped tips [39]. The pulling parameters determine the size of the obtained nanocapillary tips. HEAT (0-999) sets the power of the laser, FIL (0-15) the size of the heated spot on the capillary and VEL (0-255) the velocity of the pull. DEL (0-255) defines the delay time after which the laser is switched off and PUL (0-255) the strength of the pull [40].

Lipid vesicle formation

Reagents & materials: 1,2-diphytanoyl-sn-glycero-3-phosphatidylcholine (DphPC) lipids (Avanti Polar Lipids), chloroform (Sigma-Aldrich), cholesterol (Sigma-Aldrich), two indium tin oxide (ITO)-coated glass slides (Nanion Technologies GmbH), rubber ring as spacer, 1 M sorbitol solution (Sigma-Aldrich); for cleaning: acetone, isopropanol, ethanol, pressurised nitrogen

Equipment: Electroformation unit (Vesicle Prep Pro, Nanion Technologies GmbH)

Preparation of GUVs via electroformation – *Timing: 3 h*

PROCEDURE:

1. Dissolve DphPC in chloroform to a final concentration of 50 mg/ml.
2. Mix with cholesterol, 10 % by weight.
3. Clean ITO slides by sonicating them in acetone first, then in isopropanol and ethanol for 10 min each.
4. *Crucial step:* Spread 10 μ l of the lipid mix on conducting side of each slide using a clean glass coverslip. Spreading should look even, without empty spots, and shimmer in green or purple colours.
5. Place in desiccator for 10 min.
6. Press rubber ring onto one of the slides, enclosing the area where the lipid was spread.
7. Place this cover slide in the electroformation unit and fill with 1 M sorbitol.
8. Put the second slide on top so that the two coated sides are facing one another with the rubber ring in between.
9. Apply an AC-current of 3 V_{p-p} and a frequency of 5 Hz for 2 h.
10. Remove vesicles with large-diameter pipette tip immediately after the 2 h and store at 4 °C.

TROUBLESHOOTING:

Low yield of GUVs, GUVs appear to be multilammellar

- Remove GUVs immediately after the electroformation is finished, else they fuse with the glass slides again.
- Use GUVs 2-5 days after electroformation for lipid nano bilayer recordings.
- Prepare fresh lipid stocks, sorbitol solution, use new ITO slides and then make a fresh batch of GUVs.
- Try different lipid spreading techniques and spread smaller/larger volumes (temperature and humidity can alter the optimum procedure).

Lipid nano bilayer recordings

Reagents & materials: 200 nm-diameter borosilicate glass capillary tips, GUVs, buffer solution (1 M KCl, 10 mM 2-(N-morpholino)ethanesulfonic acid (MES), pH 6.0), DNA membrane pores, glass coverslip, silver wire for electrodes, microfil needles (World Precision Instruments), plastic syringe

Equipment: Custom-made lipid nano bilayer setup, see Section 4.4.1

Lipid nano bilayer recordings – *Timing: 2 h, ideally 1 day*

PROCEDURE:

1. Prepare Ag/AgCl electrodes, backfill capillary tip with buffer solution using a microfil needle, check for air bubbles.
2. Insert electrode into the back of the capillary, place in capillary holder and connect to micromanipulator.
3. Put 50 μL droplet of buffer solution on coverslip and place above objective, insert ground electrode.
4. Move capillary into droplet and focus on the tip by adjusting its position with the micromanipulator while monitoring it via the inverted microscope.
5. Measure open resistance of the capillary, should be ohmic and around 3 M Ω .
6. Add 1-2 μL GUVs, should be visible in the microscope image.
7. Apply a low voltage to obtain a current of approximately 200 pA.
8. Apply a suction at the back of the capillary with the plastic syringe to burst vesicles onto the tip.
9. After bilayer formation was observed (sudden drop in current to the low pA regime), wait for approximately 30 s, then record I - V curve of bilayer, typically between ± 100 mV.
10. Remove bilayer by applying pressure.
11. *Crucial step:* Repeat procedure to sample a large number of GUVs before adding pores to obtain statistics on the conductance behaviour. Bilayers should have an ohmic resistance of around 10 G Ω .
12. *Crucial step:* Only proceed if the GUVs show uniform resistances, then add DNA membrane pores to GUVs and repeat the measurements.
13. *Crucial step:* Compare membrane patches of GUVs with and without pores, e.g. using all-point conductance histograms.

TROUBLESHOOTING:

No bilayers are formed, bilayers have too low or too high resistances

- Move capillary in and out of solution a few times, apply 1 V pulse to remove trapped lipids.
- Check if GUVs are visible in solution and if they flow towards the tip as suction is applied.
- If there is no flow, tips are too small or clogged, hence replace the capillary tip, if necessary adjust pulling parameters.
- Prepare a new batch of vesicles – not every batch works reliably due to the inherent variability of the electroformation process.

4.4.3 Solvent-containing bilayers

The solvent-containing bilayer was developed by Mueller *et al.* in 1962 as the first supported lipid bilayer techniques [41]. The lipids are dissolved in an organic solvent, often n-decane, and then smeared across one side of the approximately 1 mm wide aperture of the measurement cuvette shown in Figure 4.3. The chamber is then filled with electrolyte solution and lipids are spread across the other side of the aperture as well. This procedure will form a multilayer membrane which thins out to form a bilayer within a few minutes. The quality of the membrane can be assessed optically by monitoring it through a 10× light microscope objective. A multilamellar membrane shows colourful reflections whereas the bilayer reflection is black [41]. Once a bilayer membrane has been formed, the membrane pores are added to the chamber while recording the ionic current until a spontaneous insertion is observed.

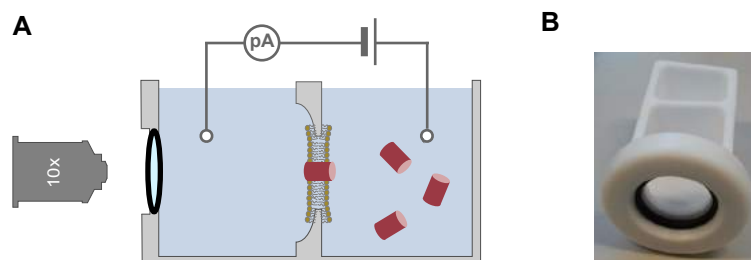


Figure 4.3: The solvent-containing membrane setup for ionic current recordings of membrane pores. A) Sketch of measurement cuvette (not drawn to scale). The lipid bilayer is supported across an approximately 1 mm wide aperture, its formation can be monitored via a 10× objective. Membrane pores (red) are added to the bath solution and spontaneously insert into the membrane. B) Photographic image of a typical measurement cuvette made from PTFE.

Solvent-containing bilayers are often the method of choice when studying the potential channel-forming activity of uncharacterised proteins [34, 42]. They are soft, flexible and have a variable hydrophobic thickness depending on the amount of solvent inside it. Solvent-containing membranes thus simulate a broad spectrum of natural membranes [34]. Additionally, the large membrane area increases the chances of pore insertion. Compared to lipid nano bilayers, the membrane area is about 25 million times larger. For the functional characterisation of DNA pores, which follows in the next chapters, we are going to use lipid nano bilayers as well as solvent-containing membranes.

Bibliography

- [1] B. Hille. *Ion Channels of Excitable Membranes*. Sunderland: Palgrave Macmillan, **2001**.
- [2] R. Benz, ed. *Bacterial and Eukaryotic Porins*. Weinheim: WILEY-VCH Verlag GmbH & Co KGaA, **2004**. DOI: 10.1002/3527603875.
- [3] M. P. Rout, J. D. Aitchison, A. Suprapto, K. Hjertaas, Y. Zhao, and B. T. Chait. “The Yeast Nuclear Pore Complex”. *The Journal of Cell Biology* 148.4 (**2000**), pp. 635–52. DOI: 10.1083/jcb.148.4.635.
- [4] T. M. Fyles. “Synthetic ion channels in bilayer membranes”. *Chemical Society Reviews* 36.2 (**2007**), pp. 335–47. DOI: 10.1039/B603256G.
- [5] D. A. Doyle, J. Morais Cabral, R. A. Pfuetzner, A. Kuo, J. M. Gulbis, S. L. Cohen, B. T. Chait, and R. MacKinnon. “The structure of the potassium channel: Molecular basis of K⁺ conduction and selectivity.” *Science* 280.5360 (**1998**), pp. 69–77. DOI: 10.1126/science.280.5360.69.
- [6] E. S. Haswell, R. Phillips, and D. C. Rees. “Mechanosensitive channels: What can they do and how do they do it?” *Structure* 19.10 (**2011**), pp. 1356–69. DOI: 10.1016/j.str.2011.09.005. arXiv: NIHMS150003.
- [7] F. Hucho and C. Weise. “Ligand-Gated Ion Channels”. *Angewandte Chemie International Edition* 40.17 (**2001**), pp. 3100–16. DOI: 10.1002/1521-3773(20010903)40:17<3100::AID-ANIE3100>3.0.CO;2-A.
- [8] Y. Jiang, A. Lee, J. Chen, M. Cadene, B. T. Chait, and R. MacKinnon. “The open pore conformation of potassium channels.” *Nature* 417.6888 (**2002**), pp. 523–46. DOI: 10.1038/417523a.
- [9] E. P. Carpenter, K. Beis, A. D. Cameron, and S. Iwata. “Overcoming the challenges of membrane protein crystallography”. *Current Opinion in Structural Biology* 18.5 (**2008**), pp. 581–6. DOI: 10.1016/j.sbi.2008.07.001.
- [10] S. White. *Membrane Proteins of Known 3D Structure*. **2016**.
- [11] M. Baker. “Making membrane proteins for structures: a trillion tiny tweaks.” *Nature Methods* 7.6 (**2010**), pp. 429–34. DOI: 10.1038/nmeth0610-429.
- [12] N. Sakai and S. Matile. “Synthetic Ion Channels.” *Langmuir* 29.29 (**2013**), pp. 9031–40. DOI: 10.1021/la400716c.

-
- [13] C. J. Pedersen. “The discovery of crown ethers (Nobel address)”. *Angewandte Chemie International Edition* 27 (1988), pp. 1021–7. DOI: 10.1002/anie.198810211.
- [14] C. Chimerele, C. M. Field, S. Piñero-Fernandez, U. F. Keyser, and D. K. Summers. “Indole prevents *Escherichia coli* cell division by modulating membrane potential”. *Biochimica et Biophysica Acta - Biomembranes* 1818.7 (2012), pp. 1590–4. DOI: 10.1016/j.bbamem.2012.02.022.
- [15] S. J. Kennedy, R. W. Roeske, A. R. Freeman, A. M. Watanabe, and H. R. Besche. “Synthetic peptides form ion channels in artificial lipid bilayer membranes.” *Science* 196.4296 (1977), pp. 1341–2.
- [16] D. P. Wallace, J. M. Tomich, J. W. Eppler, T. Iwamoto, J. J. Grantham, and L. P. Sullivan. “A synthetic channel-forming peptide induces Cl⁻ secretion: Modulation by Ca²⁺-dependent K⁺ channels”. *Biochimica et Biophysica Acta - Biomembranes* 1464.1 (2000), pp. 69–82. DOI: 10.1016/S0005-2736(99)00248-5.
- [17] I. Tabushi, Y. Kuroda, and K. Yokota. “A,B,D,F-tetrasubstituted β -cyclodextrin as artificial channel compound”. *Tetrahedron Letters* 23.44 (1982), pp. 4601–4. DOI: 10.1016/S0040-4039(00)85664-6.
- [18] H. Mamad-Hemouch et al. “Biomimetic nanotubes based on cyclodextrins for ion-channel applications”. *Nano Letters* 15.11 (2015), pp. 7748–54. DOI: 10.1021/acs.nanolett.5b03938.
- [19] T. M. Fyles, D. Loock, and X. Zhou. “A Voltage-Gated Ion Channel Based on a Bis-Macrocyclic Bolaamphiphile”. *Journal of the American Chemical Society* 7863.10 (1998), pp. 2997–3003.
- [20] V. E. Carmichael, P. J. Dutton, T. M. Fyles, T. D. James, J. A. Swan, and M. Zojaji. “Biomimetic Ion Transport: A Functional Model of a Unimolecular Ion Channel”. *Journal of the American Chemical Society* 24 (1989), pp. 767–9.
- [21] Y. Tanaka, Y. Kobuke, and M. Sokabe. “A Non-Peptidic Ion Channel with K⁺ Selectivity”. *Angewandte Chemie International Edition* 34.6 (1995), pp. 693–4. DOI: 10.1002/anie.199506931.
- [22] J. Geng et al. “Stochastic transport through carbon nanotubes in lipid bilayers and live cell membranes”. *Nature* 514.7524 (2014), pp. 612–5. DOI: 10.1038/nature13817.
- [23] J. D. Litster. “Stability of lipid bilayers and red blood cell membranes”. *Physics Letters A* 53.3 (1975), pp. 193–4. DOI: [http://dx.doi.org/10.1016/0375-9601\(75\)90402-8](http://dx.doi.org/10.1016/0375-9601(75)90402-8).

- [24] J. Wohlert, W. K. den Otter, O. Edholm, and W. J. Briels. “Free energy of a transmembrane pore calculated from atomistic molecular dynamics simulations.” *The Journal of Chemical Physics* 124.15 (2006), p. 154905. DOI: 10.1063/1.2171965.
- [25] A. Kessel, N. Ben-Tal, and S. May. “Interactions of cholesterol with lipid bilayers: the preferred configuration and fluctuations.” *Biophysical Journal* 81.2 (2001), pp. 643–58. DOI: 10.1016/S0006-3495(01)75729-3.
- [26] K. Göpflich, C.-Y. Li, M. Ricci, S. P. Bhamidimarri, J. Yoo, B. Gyenes, A. Ohmann, M. Winterhalter, A. Aksimentiev, and U. F. Keyser. “Large-Conductance Transmembrane Porin Made from DNA Origami”. *ACS Nano* 10.9 (2016), pp. 8207–14. DOI: 10.1021/acs.nano.6b03759.
- [27] L. Monticelli, S. Kandasamy, X. Periole, R. Larson, D. P. Tieleman, and S. J. Marrink. “The MARTINI Coarse Grained Force Field: Extension to Proteins”. *Journal of Chemical Theory and Computation* 4 (2008), pp. 819–834. DOI: 10.1021/ct700324x.
- [28] O. H. S. Ollila, H. J. Risselada, M. Louhivuori, E. Lindahl, I. Vattulainen, and S. J. Marrink. “3D Pressure Field in Lipid Membranes and Membrane-Protein Complexes”. *Physical Review Letters* 102.7 (2009), p. 078101.
- [29] J. Yoo, M. B. Jackson, and Q. Cui. “A Comparison of Coarse-Grained and Continuum Models for Membrane Bending in Lipid Bilayer Fusion Pores”. *Biophysical Journal* 104.4 (2013), pp. 841–852. DOI: 10.1016/j.bpj.2012.12.043.
- [30] W. F. D. Bennett and D. P. Tieleman. “Molecular Simulation of Rapid Translocation of Cholesterol, Diacylglycerol, and Ceramide in Model Raft and Nonraft Membranes”. *Journal of Lipid Research* 53.3 (2012), pp. 421–429. DOI: 10.1194/jlr.M022491. eprint: <http://www.jlr.org/content/53/3/421.full.pdf+html>.
- [31] K. Pratt, W. Koch, Y. C. Wu, and P. Berezansky. “Molality-based primary standards of electrolytic conductivity (IUPAC Technical Report)”. *Pure and Applied Chemistry* 73.11 (2001), pp. 1783–93. DOI: 10.1351/pac200173111783.
- [32] J. K. W. Chui and T. M. Fyles. “Ionic conductance of synthetic channels: analysis, lessons, and recommendations.” *Chemical Society Reviews* 41.1 (2012), pp. 148–75. DOI: 10.1039/c1cs15099e.
- [33] E. Neher and B. Sakmann. “Single-channel currents recorded from membrane of denervated frog muscle fibres.” *Nature* 260.5554 (1976), pp. 799–802. DOI: 10.1038/260799a0.

-
- [34] T. Gutsmann, T. Heimburg, U. Keyser, K.R. Mahendran, and M. Winterhalter. “Protein reconstitution into freestanding planar lipid membranes for electrophysiological characterization.” *Nature Protocols* 10.1 (2015), pp. 188–98. DOI: 10.1038/nprot.2015.003.
- [35] A. Seifert, K. Göpfrich, J.R. Burns, N. Fertig, U.F. Keyser, and S. Howorka. “Bilayer-Spanning DNA Nanopores with Voltage-Switching between Open and Closed State.” *ACS Nano* 9.2 (2014), pp. 1117–26. DOI: 10.1021/nm5039433.
- [36] J.L. Gornall, K.R. Mahendran, O.J. Pambos, L.J. Steinbock, O. Otto, C. Chimerele, M. Winterhalter, and U.F. Keyser. “Simple reconstitution of protein pores in nano lipid bilayers.” *Nano Letters* 11.8 (2011), pp. 3334–40. DOI: 10.1021/nl201707d.
- [37] K. Göpfrich, C.V. Kulkarni, O.J. Pambos, and U.F. Keyser. “Lipid Nanobilayers to Host Biological Nanopores for DNA Translocations”. *Langmuir* 29.1 (2013), pp. 355–64. DOI: 10.1021/la3041506.
- [38] S.J. Marrink, A.H. de Vries, and D.P. Tieleman. “Lipids on the move: simulations of membrane pores, domains, stalks and curves.” *Biochimica et Biophysica Acta* 1788.1 (2009), pp. 149–68. DOI: 10.1016/j.bbamem.2008.10.006.
- [39] L.J. Steinbock, O. Otto, D.R. Skarstam, S. Jahn, C. Chimerele, J.L. Gornall, and U.F. Keyser. “Probing DNA with micro- and nanocapillaries and optical tweezers.” *Journal of Physics: Condensed Matter* 22.45 (2010), p. 454113. DOI: 10.1088/0953-8984/22/45/454113.
- [40] Lorenz J. Steinbock. “Micro- and nanocapillaries for resistive pulse analysis of microparticles and single molecules”. PhD thesis. 2011.
- [41] P. Mueller, D.O. Rudin, H.T. Tien, and W.C. Wescott. “Reconstitution of cell membrane structure in vitro and its transformation into an excitable system.” *Nature* 194 (1962), pp. 979–80. DOI: 10.1038/194979a0.
- [42] S. Nekolla, C. Andersen, and R. Benz. “Noise analysis of ion current through the open and the sugar-induced closed state of the LamB channel of Escherichia coli outer membrane: evaluation of the sugar binding kinetics to the channel interior.” *Biophysical Journal* 66.5 (1994), pp. 1388–97. DOI: 10.1016/S0006-3495(94)80929-4.

Chapter 5

Prototyping DNA-based membrane pores



Parts of this work previously appeared in:

J. R. Burns, **K. Göpfrich**, J. W. Wood, V. V. Thacker, E. Stulz, U. F. Keyser, S. Howorka. Lipid-bilayer-spanning DNA nanopores with a bifunctional porphyrin anchor. *Angewandte Chemie International Edition* **52**, 12069–72 (2013).

A. Seifert*, **K. Göpfrich***, J. R. Burns, N. Fertig, U. F. Keyser, S. Howorka. Bilayer-spanning DNA nanopores with voltage-switching between open and closed state. *ACS Nano* **9**, 1117–26 (2014). *Equal contribution.

Abstract In this chapter, we lay the foundations for the rational design of versatile DNA membrane pores by studying a six-helix DNA bundle with a nominal diameter of 2 nm as a prototype. We discuss strategies for anchoring it in the lipid membrane and show that only two porphyrin-based tags achieve the otherwise energetically unfavourable insertion of the highly charged DNA nanostructure into hydrophobic lipid bilayers. The fluorescent properties of the porphyrin tags additionally facilitate microscopic visualisation of membrane attachment. We carry out in-depth ionic current characterisation comparing data from two different lipid membrane systems. We observe and discuss the voltage-dependent conductance levels of our DNA pores.

5.1 Introduction

In the previous chapters, we reviewed recent developments in the fields of DNA nanotechnology, nanopore sensors and synthetic membrane pores. In this chapter, we combine these three concepts to demonstrate synthetic DNA-based membrane pores. While DNA nanotechnology in principle allows for the creation of diverse nanopore architectures, a six-helix bundle arranged on a hexagonal lattice is an obvious choice for prototyping DNA pores. In this arrangement, the naturally emerging gap between the DNA helices has a nominal diameter of 2 nm and is thus comparable to the widely studied protein pore α -hemolysin [1]. The very first DNA membrane pore by Langecker *et al.*, shown in Figure 5.1A, was based on this six-helix bundle architecture [2] and we will adhere to it while simplifying the overall architecture of the pore. Figure 5.1B shows our first DNA membrane pore. With a length of 40 nm it is comparable to the central channel of the pore by Langecker *et al.* Yet instead of folding the entire 7249 base-long M13mp18 scaffold, we reduced the scaffold length to 704 bases (“M1.3” scaffold) using restriction enzymes and a published protocol [5]. While our approach yielded functional pores which induced transmembrane currents [3], their production is labour-intensive. Furthermore, the design was suboptimal because the flexible linkers for the attachment of cholesterol were long enough to allow for the insertion of all six cholesterol tags even if the pore is not in the desired perpendicular orientation. Design, assembly and ionic current characterisation of this pore were presented in my MPhil thesis [3]. In collaboration with S. Howorka and J. R. Burns, University College London, we thus pursued a different approach based on scaffold-free assemblies. The DNA membrane pore in Figure 5.1C uses fourteen syn-

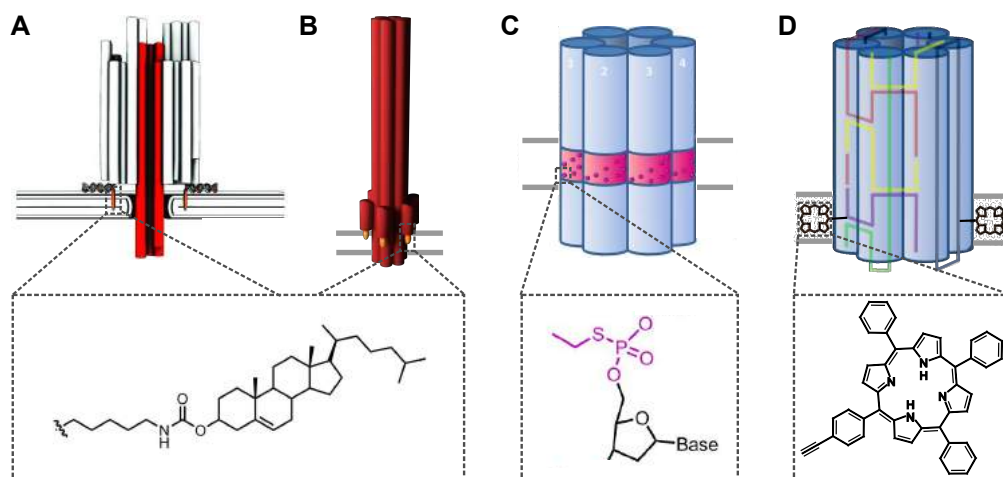


Figure 5.1: Six-helix bundles as prototypes of DNA membrane pores and their hydrophobic membrane anchors based on cholesterol, ethane-phosphorothioate and tetra-phenyl porphyrin. A) The first DNA membrane pore by Langecker *et al.* based on scaffolded DNA origami featuring 26 cholesterol tags for membrane anchoring and a 40 nm long channel (highlighted in red). From [2]. Reprinted with permission from AAAS. B) A 40 nm long DNA membrane pore made from the enzymatically cut 704 base-long M1.3 scaffold, anchored via six cholesterol tags. For details on this pore see [3]. C) The first scaffold-free DNA membrane pore by Burns *et al.* made of 14 synthetic oligonucleotides. This 14 nm long pore has a hydrophobic belt of 72 ethane-phosphorothioates replacing the phosphate groups on the DNA. Adapted with permission from [4]. Copyright 2013 American Chemical Society. D) A 15 nm long scaffold-free six-helix pore made of six synthetic oligonucleotides. Only two porphyrins serve for membrane anchoring and visualisation at the same time. This pore will be studied in this chapter.

thetic oligomers and features a hydrophobic belt of ethane-phosphorothioates replacing the charged phosphate groups on the DNA backbone [4]. The design in Figure 5.1D, composed of only six synthetic oligomers, will be studied in this chapter. With a length of 15 nm, the scaffold-free assemblies (C, D) have a nominally lower sensing volume than the previous 40 nm long DNA origami-based membrane pores making them in principle better suited for nanopores sensing applications. Since they are made from a small number of DNA strands, they are cheaper and quicker to produce, while sacrificing attachment sites for hydrophobic tags and limiting the possibilities for direct visualisation with AFM and TEM. We thus explored possibilities to insert scaffold-free DNA pores with a small number of strongly hydrophobic tags for minimal chemical intervention and simplified design. With its large aromatic core and high van-der-Waals surface area, a porphyrin derivative should satisfy the criterion of strong hydrophobicity. It offers the possibility to attach additional aromatic substituents if required. Conveniently, porphyrin is a fluorophore with an emission maximum at 656 nm and can thereby act as a powerful visualisation tag. In previous DNA nanopore designs, fluorophores had to be incorporated in addition to the hydrophobic tags [2, 4]. Moreover, inserting porphyrin into lipid bilayers leads to a characteristic shift in the fluorescence spectrum offering an independent experimental handle to confirm membrane anchoring [6].

5.2 Materials and methods

Design of the porphyrin-tagged six-helix DNA nanopore. The six-helix DNA nanopore was designed using the computer-aided DNA origami design software caDNAo [7] described in Section 2.3.3. Only six scaffold and staple strands were terminally linked for stabilisation and interconnected as shown in Figure 5.2. The DNA sequences, purchased from Integrated DNA Technologies, are listed in Table 5.1. Using a molecular model generated with Macromodel, the positions for attaching porphyrins were selected to be pointing outwards on two opposite duplexes.

Synthesis and purification of porphyrin-DNA. Tetra-phenyl porphyrin deoxy-uridine was synthesised and incorporated into DNA oligonucleotides as previously described [8, 9], see also Supplementary Information in [10]. The modified oligomers were purified using size-exclusion chromatography and NAP-25 columns to remove cleaved protecting groups, followed by neutralisation of the porphyrin-containing fractions via bubbling with ammonia gas and concentration to a dry red solid under vacuum. After dissolving

in ddH₂O, the DNA material was purified by gel electrophoresis, see Section 2.3.5. The crushed gel slices were incubated with 1 mL of ddH₂O while shaking for 30 min at 50 °C, followed by removal of the DNA-containing liquid. The process was repeated three times. The collected fractions were concentrated to dryness under vacuum followed by NAP-25 purification [8, 9]. The purity of the strands was confirmed by RP-HPLC while yield was determined via UV-vis spectroscopy as described in Section 2.3.5¹.

Assembly of the six-helix DNA nanopore. The six-helix pore was assembled by heating an equimolar mixture of all six strands, including the porphyrin-tagged strands, at 1 μM each dissolved in buffer A (1 M KCl, 50 mM Tris, pH 8.0, total volume 1 mL) to 95 °C for 5 min, followed by cooling to 16 °C at a rate of 0.25 °C/min in a Varian Cary 300 Bio UV-vis spectrophotometer equipped with a Peltier cooling element.

Characterisation of the six-helix pore with gel electrophoresis, UV-vis spectroscopy and DLS. The assembled DNA pores were analysed using 0.8% agarose gel electrophoresis in standard TBE buffer (Sigma-Aldrich) supplemented with 11 mM MgCl₂ and running conditions of 80 V, 80 min, 8 °C, see Section 2.3.5. The bands were visualised by staining in ethidium bromide solution and UV transillumination². The melting point analysis was performed on samples with a concentration of 0.2 μM dissolved in buffer A using a heating rate of 0.5 °C/min on a Cary spectrophotometer as described in Section 2.3.5. DLS experiments were conducted on a Zetasizer Nano S from Malvern [11], see Section 2.3.5, using DNA samples with a concentration of 0.25 μM in buffer A.

AFM imaging. For AFM analysis, see Section 2.3.5, DNA pores were first adsorbed onto mica, following a modified version of a published procedure [12]. Freshly cleaned mica was incubated with a solution of 3 mM MgCl₂ for 5 min and then repeatedly washed with ddH₂O. The surface was then incubated with a 20 nM solution of the DNA nanopore solution. AFM images were acquired in situ at room temperature with a Multimode AFM as described in [4]³.

¹Porphyrin-DNA was synthesised by J. R. Burns, University College London, and E. Stulz, University of Southampton.

²Gel electrophoresis was carried out by J. R. Burns, University College London.

³AFM was carried out by J. R. Burns, University College London.

Lipid vesicle formation. DphPC (Avanti Polar Lipids), 10% cholesterol (Sigma Aldrich) GUVs for imaging and current recordings on the lipid nano bilayer setup were prepared as described in the detailed protocol in Section 4.4.2.

Fluorescent confocal imaging. For confocal imaging, we took advantage of the fluorescent properties of porphyrin itself. A porphyrin-free Cy3-tagged DNA nanopore (Integrated DNA Technologies) served as a control. GUVs were suspended in buffer A in an incubation chamber (Grace Biolabs) and imaged using a Confocal Leica TCS SP5 microscope with a 60× oil immersion objective in bright field and fluorescence mode. The DNA pore was added at a concentration of 5 nM. Porphyrin and Cy3 were excited at 514 nm using an argon laser and emission was collected above 530 nm. Images were processed in ImageJ.

Ionic current recordings on the lipid nano bilayer setup. The ionic recordings were performed using the lipid nano bilayer setup as described in the detailed protocol in Section 4.4.2. GUVs were incubated with 30 nM DNA nanopores for 1 h at room temperature in buffer A. Bilayer formation was detected as a drop in current. Bilayers that held DNA nanopores were identified due to their lowered seal resistances. Nanopore incorporation was optionally triggered by applying a voltage pulse. Ionic current data was acquired using an Axopatch 200B amplifier and analysed as described earlier [13, 14].

Ionic current recordings on the planar lipid bilayer setup. A commercial integrated chip-based, parallel bilayer recording setup (Orbit 16, Nanion Technologies) with multi-electrode-cavity-array (MECA) chips (IONERA) was used for planar bilayer recordings. Bilayers were automatically formed by remotely actuated spreading DphPC (Avanti Polar Lipids) dissolved in octane (10 mg/mL). 1 M KCl, 10 mM HEPES, pH 8.0 was used as an electrolyte solution. For pore insertion, a 2:1 mixture of porphyrin-tagged DNA nanopores and 0.5% n-octyl-oligo-oxyethylene (OPOE, in 150 mM KCl, 10 mM HEPES, pH 8.0) was added to the cis side of the bilayer to a final concentration of 10 nM nanopores. A positive voltage of 40 mV was applied to facilitate pore insertion. Successful incorporation was observed by detecting the current steps to distinct levels. The data were Bessel filtered at 2.873 kHz and acquired at 10 kHz with an EPC-10 patch-clamp amplifier (HEKA Elektronik) with the PATCHMASTER software (HEKA Elektronik). Single channel analysis was performed using Clampfit (Molecular Devices)⁴.

⁴Planar lipid bilayer current measurements were carried out by A. Seifert at Nanion Technologies.

5.3 Results and discussion

5.3.1 Design, assembly and characterisation

For the creation of membrane-spanning DNA nanopores, we selected the tetra-phenyl porphyrin tag, which can be easily coupled to DNA [15]. Its chemical structure is shown in Figure 5.2A. Acetylene tetra-phenyl porphyrin was attached to deoxy-uridine via Sonogashira coupling to achieve a rigid linkage. The site-specific insertion of the modified nucleoside into oligo-deoxy-nucleotides was accomplished using standard phosphoramidite chemistry as described previously [8, 9, 15, 16]. For details on the synthesis, purification and analysis of the porphyrin-tagged DNA see [10]. In our nanopore design, six single-strands of DNA interconnect the six DNA duplexes as shown in Figure 5.2B. Crucially, two porphyrin-tags are incorporated in the design to facilitate membrane insertion. The resulting six-helix bundle has a nominal width of 6 nm, a length of 15 nm, and an inner channel diameter of 2 nm. For comparability with a previous six-helix bundle [4], two DNA strands carried several phosphothioate groups instead of the native phosphate groups on the DNA backbone. Their behaviour, however, is identical at our experimental condition of pH 8.0 [4]. The DNA nanopore was assembled by thermal annealing of an equimolar mixture all six DNA strands, for sequences see Table 5.1. The assembly process was followed by a structural characterisation of the DNA nanopore. As shown in Figure 5.3A, agarose gel electrophoresis of the six-helix pore without hy-

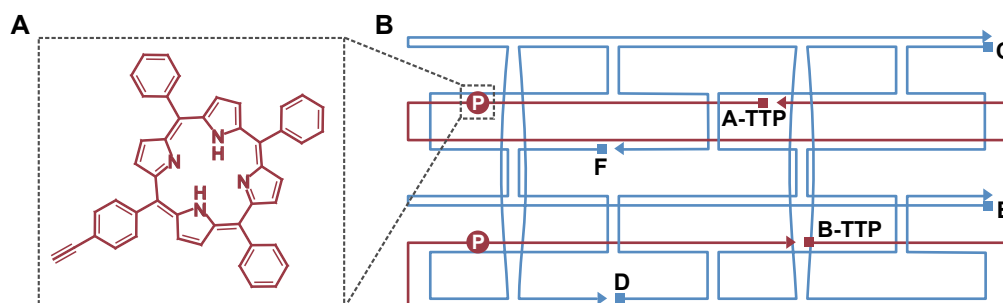


Figure 5.2: A) Chemical structure of the tetra-phenyl porphyrin tag. B) Pathways of the six DNA strands interconnecting the six duplexes forming the DNA nanopore. Porphyrin-tagged strands are shown in red, the positions of the porphyrins are indicated as red circles. The letters denominate the individual DNA sequences listed in Table 5.1. The DNA pore was designed by J. R. Burns and S. Howorka, University College London.

Table 5.1: DNA sequences used for the assembly of the six-helix bundle. **P** indicates a deoxy-uridine nucleotide carrying a tetra-phenyl porphyrin modification, (*) signifies a phosphorothioate modification. This modification behaves like a regular phosphate group at pH 8.0 and was included for reasons of comparability with the previous ethane-modified DNA nanopore by Burns *et al.* [4]. The porphyrin-tagged oligonucleotides were synthesised by J. R. Burns, University College London, and E. Stulz, University of Southampton.

Name	Sequence (5' to 3')
A-TPP	TTATAAGGGATTTTGCCGATTPGGAATTTTACAGGATTTTCGCCT GCTGGGGCAAACCAGCGTGGACCGCTTTTTTGGCTATTCTTTTGAT
B-TPP	GGCGCCAATACGCTTTTTCCCCGCGCGTTGGCCGATTCATTAATGC AGCTGGCACGACATTTTTCTCPCTGGTGAAAAGAAAACCACCT
C	TGTTCCAAATAGCCAAGCGGTCCACGCTCCCTGAGGGGCGCC AGGGTGGGAATCGGACAAGAGTCCACTAAAATCCCCCAGCA
D	CATTAATTTTTTCTCCTTCACCGCCTGGGGTTTGCTTATAAA TCAAAGGTTTGGACCAACGCGCGGGGAGCGTATTAGAGTTG CAACTCTCTCAGGGCCAGGCGGTGAAGGGCAATC*A*G*C*T*G*
E	TTGTTTTCAA* C*A*G*C*A*T*C*C*TGTTTC*C*G*A*A*A*TCG GCATTAAAG*A*C*CAGCTG
F	GGCGAA*A*T*GATTGCTTTCAC*C*A*G*T*G*AGATGT*C*G*T*G*A* C*G*T *GGATTTTTCC*A*C*G*T*T*CTTAATAGTGGACTCTTGTT CCAAACTGGAACA

drophobic groups, Lane 1, yields a single sharp band migrating as fast as the 500 base pair (bp) band of the DNA ladder, Lane 3. For the porphyrin-tagged structure, Lane 2, the band smears, potentially due to π - π stacking interactions between the porphyrin tags. Porphyrin-DNA has previously been shown to form distinct clusters in aqueous solutions. This, however, is suppressed in the presence of organic solvents [9, 16] and is thus not expected to happen within the hydrophobic lipid bilayer environment. Free single strands, which would migrate faster than the assembled structure, are not observed in the gel, indicating efficient assembly of the structure.

DLS measurements, yielded a single peak at a hydrodynamic radius of 5.5 ± 0.2 nm for the porphyrin-tagged DNA nanopore, consistent with its predominantly monomeric nature, see Figure 5.3B (red line). As expected, the porphyrin-free pore is marginally smaller with a hydrodynamic radius of 5.2 ± 0.2 nm (blue dashed line). The expected hydrodynamic radius was calculated using the software HYDROPRO [17]. The calculated value of 4.9 nm is smaller than the measured one, but still in accordance within the accuracy of DLS measurements for comparable DNA structures [18].

AFM imaging was performed on the DNA nanopore in solution in tapping mode⁵. The rod-shaped structure of the DNA nanopore is clearly visible in the AFM image in Figure 5.3C. The apparent height is 2.2 ± 0.25 nm, the length 20.4 ± 4.5 nm and the width 9.7 ± 2 nm ($n = 10$). The deviation from the actual dimensions of 6, 14 and 6 nm are likely to be caused by lateral tip-deconvolution and tip-compression of the hollow DNA nanostructure.

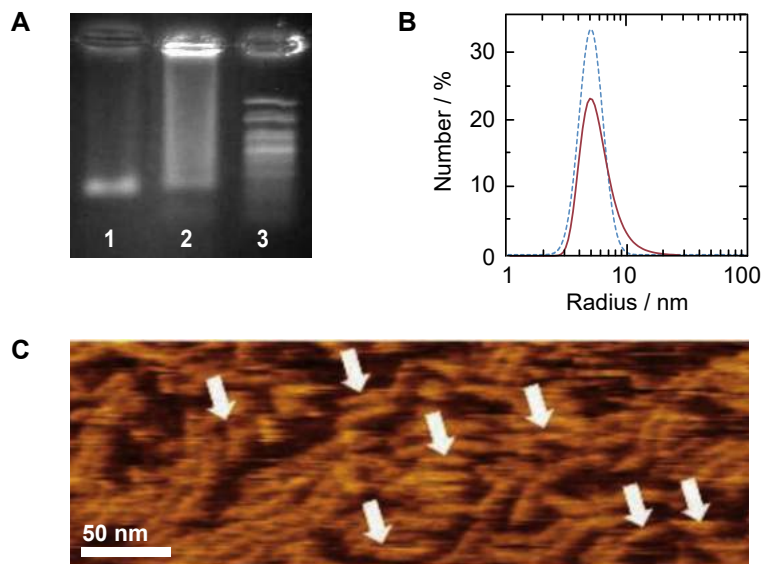


Figure 5.3: A) 1% agarose gel electrophoresis of DNA nanopores. Lane 1: Six-helix pore without porphyrin anchors; Lane 2: Porphyrin-tagged six-helix pore; Lane 3: 50 bp DNA ladder. Gel electrophoresis was carried out by J. R. Burns, University College London. B) DLS trace of the six-helix pore with (red line) and without (blue dashed line) porphyrin anchors featuring a hydrodynamic radius of 5.5 ± 0.2 nm and 5.2 ± 0.2 nm, respectively. C) AFM image of the six-helix DNA nanopore without porphyrin-tags imaged in solution in tapping mode. AFM images were taken by J. R. Burns, University College London.

5.3.2 Probing membrane anchoring

While ionic current recordings serve as the ultimate proof of membrane insertion, we first carried out three simple bulk measurements to probe the attachment of our DNA

⁵AFM images were taken by J. R. Burns, University College London.

constructs to lipid vesicles: fluorescence emission measurements, UV melting analysis and fluorescent confocal imaging.

Upon insertion into lipid membranes, the fluorescence emission spectrum of porphyrin is known to shift to shorter wavelengths [19]. As illustrated in Figure 5.4A, we observed this characteristic shift upon addition of small unilamellar lipid vesicles (SUVs)⁶. The fluorescence emission maxima at 605 nm and 653 nm were reduced by 2 nm and 1 nm, respectively, in line with previous studies on individual porphyrin-carrying DNA duplexes [19]. The shift could be enhanced by using zinc-porphyrin tags [19].

UV melting analysis can indicate structural uniformity as well as membrane insertion of DNA nanostructures, see Section 2.3.5. For our porphyrin-tagged six-helix DNA nanopore, UV melting profiles showed a single sharp melting transition at a temperature of $T_m = 53.7^\circ\text{C}$, Figure 5.4B (green line), indicative of cooperative melting and hence structural uniformity. When lipid vesicles were added to the porphyrin-tagged pores, the melting temperature increased by 6.5°C (grey line), consistent with a stabilisation of the structure inserted into the bilayer. An increase in the melting temperature upon addition to vesicles has also been reported for other DNA membrane pores with different hydrophobic membrane anchors [4, 20].

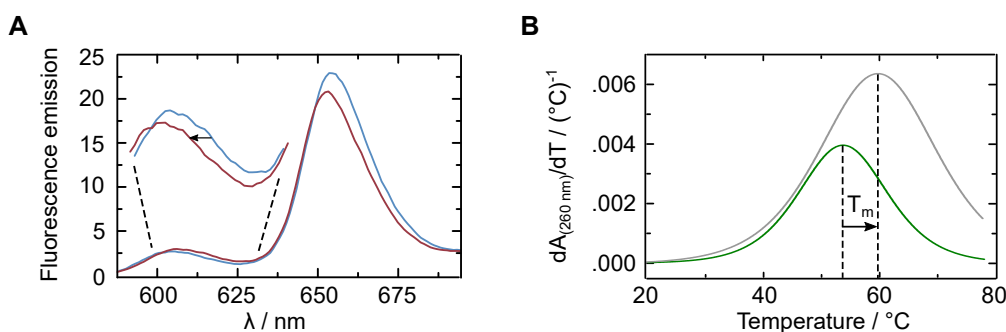


Figure 5.4: A) Fluorescence emission spectrum of the porphyrin-tagged six-helix DNA pore in the absence (blue) and in the presence (red) of DphPC lipid vesicles, $\lambda_{\text{ex}} = 424\text{ nm}$. In the presence of SUVs, the spectrum shows a characteristic shift to shorter wavelengths, indicative of membrane insertion of the porphyrin. Emission spectra were taken by J. R. Burns, University College London. B) UV melting analysis of the porphyrin-tagged six-helix pore in the absence (green) and the presence (grey) of DphPC lipid vesicles. The melting temperature T_m increases by 6.5°C in the presence of the GUVs.

⁶Emission spectra were taken by J. R. Burns, University College London.

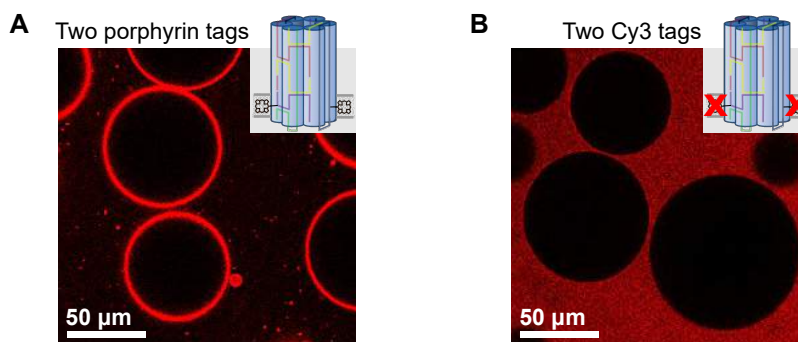


Figure 5.5: Fluorescent confocal imaging, $\lambda_{\text{ex}} = 514 \text{ nm}$, of DphPC lipid vesicles in the presence of A) the porphyrin-tagged six-helix DNA nanopores, $c = 5 \text{ nm}$ and B) the six-helix DNA nanopore with Cy3 tags instead of porphyrin membrane anchors, $c = 5 \text{ nm}$.

For fluorescent confocal imaging of membrane attachment, we could directly exploit the fluorescent properties of porphyrin. Prior to fluorescent imaging, GUVs were incubated with 1 nM of the DNA nanopores. Figure 5.5A clearly shows that the porphyrin-tagged DNA pores adhered to the surface of the circular vesicles. As a control, we prepared a DNA nanopore where we replaced the fluorescent hydrophobic porphyrins with terminal Cy3 tags. No membrane adhesion was observed in the confocal image in Figure 5.5B.

5.3.3 Ionic current recordings

To provide definite proof for the formation of functional transmembrane pores, we carried out ionic current recordings of our porphyrin-tagged six-helix DNA nanopores. Relying on previous observations indicating that our DNA pores attach to lipid vesicles, we decided to form supported membranes directly from those vesicles using our lipid nanobilayer setup described in Section 4.4. Lipid vesicles were incubated with porphyrin-tagged DNA nanopores and subjected to recordings whereby a vesicle was suctioned onto a nanocapillary. Porphyrin-free DNA nanopores served as a negative control given that confocal imaging confirmed that they do not attach to GUVs. By sampling a large number of vesicles, we could obtain information on the conductance and the behaviour of our six-helix pores. The vesicles that were incubated with functional porphyrin-tagged pores repeatedly showed higher conductances due to the presence of one or more transmembrane-spanning DNA nanopores. Representative current-voltage (I - V) traces

for membrane-inserted DNA pores are shown in Figure 5.6. We can broadly group the observed conductances into three categories: a frequently occurring low conductance level with a typical conductance between 0.25 nS and 0.50 nS (blue colour coding), a less probable high conductance level reaching more than double the conductance of the low level (red colour coding) and, as expected, the conductance of the plain bilayer with no pore inserted (grey colour coding). Assuming a cylinder with rigid walls, one would expect to observe just one well-defined conductance level. According to the Hille equation introduced in Section 4.3.2, an uncharged cylindrical channel with the dimensions of our DNA pore should have a conductance of 2 nS. It is not surprising that a membrane-embedded DNA pore with high surface charge and flexible walls exhibits more complex conductance behaviour. Possible molecular mechanisms causing the occurrence of multiple conductance levels include electric field-induced fraying of DNA duplexes [2], flipping of DNA loops at the pore entrances, conformational alterations in the overall DNA structure, hydrophobic gating, or repositioning of the pore with respect to the bilayer.

In line with previous reports of DNA nanopores [2, 4], our porphyrin-tagged pores exhibit ohmic I - V behaviour when looking at the conductance levels separately as shown in Figure 5.6A. In addition to stable ionic current traces, we repeatedly observed step-wise reductions in the ionic current. In the representative trace in Figure 5.6B, the current switched from the low conductance level to the level of the plain bilayer under an applied transmembrane bias of 60 mV. While the threshold voltage can vary, these permanent closures are generally observed when increasing the voltage. They could be caused by a DNA pore escaping from the membrane entirely. Alternatively, it could be flipping from an ion conducting into an inactive orientation where the pore is bound to the membrane without penetrating it. Apart from permanent closures, transient gating was a characteristic event observed in the presence of porphyrin-tagged DNA pores. Representative gating traces are shown in Figure 5.7. Gating occurred either between the low conductance level and the plain bilayer (A, B) or the high conductance level and the plain bilayer (C), or alternatively between low and high conductance level (D). The latter type of gating is rarely observed on the lipid nano bilayer setup, but occurs frequently in solvent-containing membranes. Switching typically happened on the millisecond to second time scale. Stochastic thermodynamic and electric-field induced fluctuations are expected on molecular length scales. MD simulations have indicated that the motion of flexible DNA loops at the end of the pore might cause the stochastic partial obstruction of the ion pathway [21].

The conductance behaviour of our DNA pores, exhibiting different conductance levels

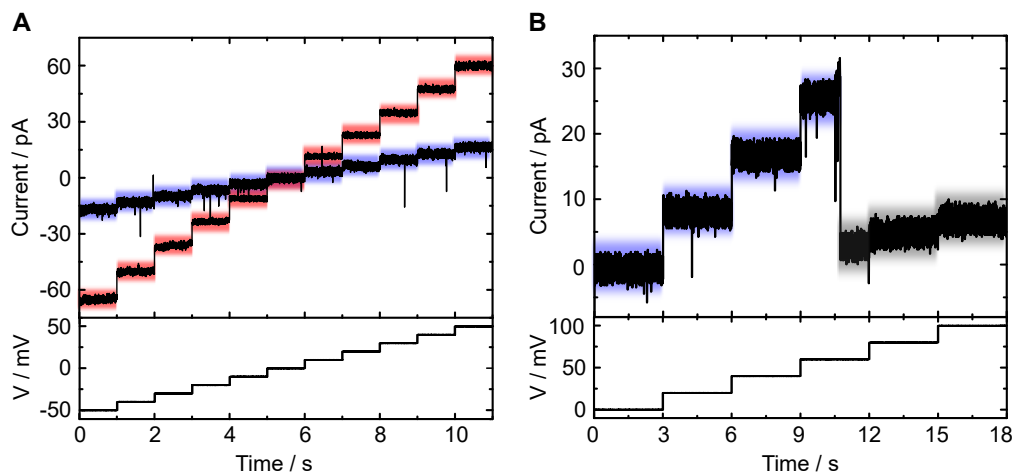


Figure 5.6: Ionic current traces for the porphyrin-tagged six-helix pore in 1 M KCl, 50 mM Tris, pH 8.0 recorded on the lipid nano bilayer setup. A) Exemplary I - V trace of a stable DNA pore in the high conductance level (red, 1.3 nS) and in the low conductance level (blue, 0.33 nS) recorded at voltages stepping up from -50 mV to $+50$ mV as indicated in the plot below. B) I - V trace recorded between 0 and 100 mV showing a complete and permanent DNA pore closure at 60 mV from the low-conductance level (blue, 0.39 nS) to the conductance level of the plain bilayer (grey, 0.07 nS).

and gating, appears to be complex and heterogeneous. To develop DNA membrane pores further, it is key to understand the parameters that cause the DNA pores to reside in a certain conductance level. In the following section, we thus carried out ionic current recordings on different membrane systems and as a function of transmembrane voltage to study the probabilistic occurrence of the conductance levels.

5.3.4 Voltage-dependent conductance levels

In nature, transmembrane voltage is a key parameter influencing the conductance of pores and ion channels embedded in electrically excitable tissue [22]. Our synthetic DNA pores are highly negatively charged, making it seem plausible that they, too, are susceptible to the applied voltage. We thus set out to explore the effect of transmembrane voltage on the conductance of our DNA pores.

Initially, we started all bilayer recordings by applying a high voltage of 100 mV to probe the incorporation of pores. Figure 5.8A shows a histogram compiled from the observed conductance steps which peaks at 0.25 pS and has a mean of 0.41 nS. Insertion, closure

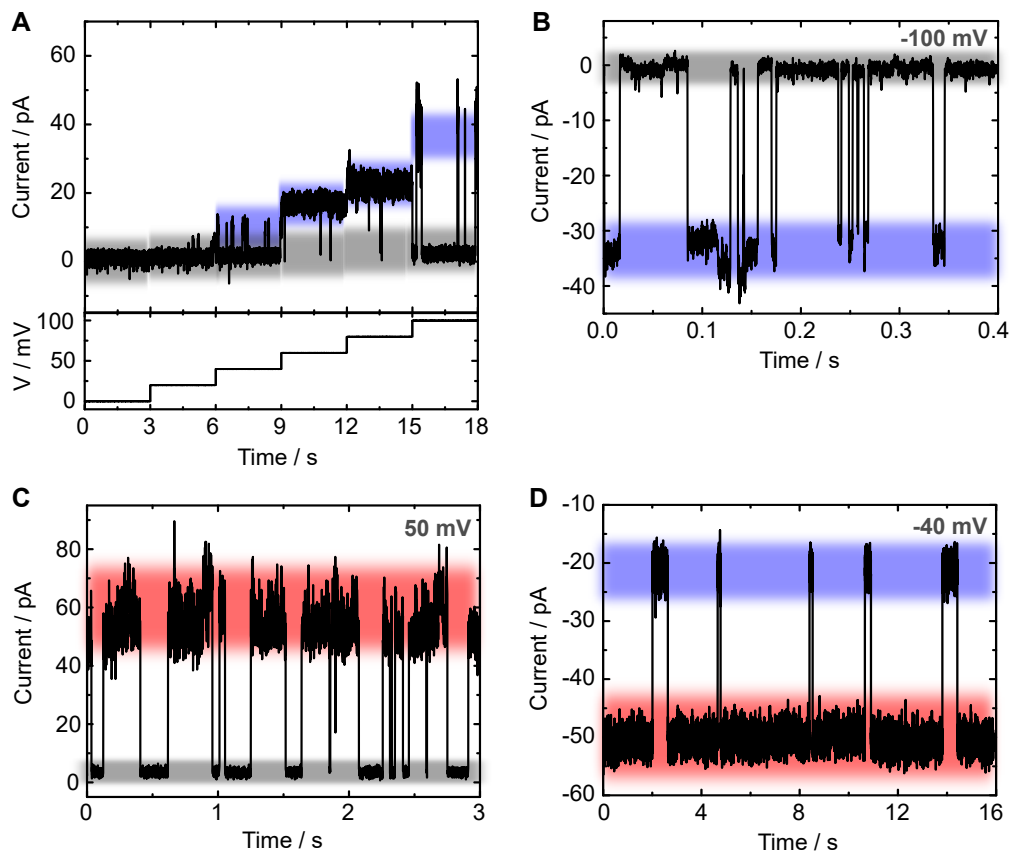


Figure 5.7: Gating of porphyrin-tagged 6-helix pores between different conductance levels. A) Voltage-dependent transient opening of a DNA pore. At 60 mV and 80 mV the low conductance level (blue, 0.30 nS) dominates, while the fully closed level dominates at 20 mV, 40 mV and 100 mV (grey, 0.03 nS). B) Gating between the fully closed level (grey, 0.01 nS) and the low conductance level (blue, 0.32 nS) at -100 mV. C) Gating between the fully closed level (grey, 0.07 nS) and the high conductance level (red, 1.1 nS) at 50 mV. D) Gating between the low (blue, 0.53 nS) and the high conductance level (red, 1.3 nS) at -40 mV.

and gating steps were all included in the histogram, contributing to its broad distribution. Less than 3 % of all steps have a conductance of over 1 nS. When reducing the initial applied voltage to 20 mV, we noticed that steps of over 1 nS in conductance occurred more frequently, now accounting for approximately 40 %. The inset in Figure 5.8A shows a histogram of these high conductance steps with a mean of 1.6 nS.

To quantify the influence of transmembrane voltage on the occurrence of the different conductance levels, a series of cumulative all-point histograms was plotted for applied voltages of 20 mV, 40 mV, 60 mV, 80 mV and 100 mV, see Figure 5.8B. Two main peaks for a higher and a lower conductance level were clearly visible. While the lower conductance level was dominant independent of the applied voltage, lower voltages shifted the distribution towards the higher conductance level.

With the applied transmembrane voltage, we clearly identified a parameter that influences the relative abundance of the different conductance levels. When comparing our own results with published conductances of DNA pores, we realise that the utilised membrane system might be an additional factor. Our collaborator A. Seifert at Nanion Technologies thus carried out additional current recordings in the presence of an organic solvent on a commercial setup using planar cholesterol-free membranes [23]. In this system, we also observed a lower and a higher conductance level at around 0.25 nS and 1.6 nS. As before, the distribution shifted to the higher conductance level as the voltage was reduced. Yet again the probability of observing the higher conductance level increased noticeably, especially at low voltages. Figure 5.8C compares the probability of observing the higher conductance level as a function of transmembrane voltage on the two membrane systems. The probabilities were extracted from the counts in the all-point histograms, setting an arbitrary threshold at 0.75 nS where the levels are well separated. While the probability of observing the high conductance level reaches 97 % on the planar bilayer system at 20 mV, it only goes up to 45 % on the lipid nano bilayer system. On planar membranes, where the DNA pores are more likely to remain open for extended periods of time, the pore diameter in the higher conductance level was probed with PEG-sizing experiments. The measured diameter of 1.9 nm is in excellent agreement with the expected diameter from geometric considerations [23]. It should be noted, however, that the microscopic structure of the pore is expected to deviate from idealistic geometric models. In these models, we approximate each DNA double-helix as a rod with a diameter of 2 nm. In reality, multiple factors alter the exact shape of the pore, most importantly the position of the crossovers. In our design, the crossover positions were selected to compromise between strain and structural integrity. In between the crossovers, the helices can move apart due to electrostatic repulsion causing buckling

of the structure. Additional strain comes from the surrounding lipid molecules and the applied electric field when the pore is inserted. The shape of a six-helix bundle in the lipid membrane can be appreciated from MD simulations by Yoo *et al.* [24].

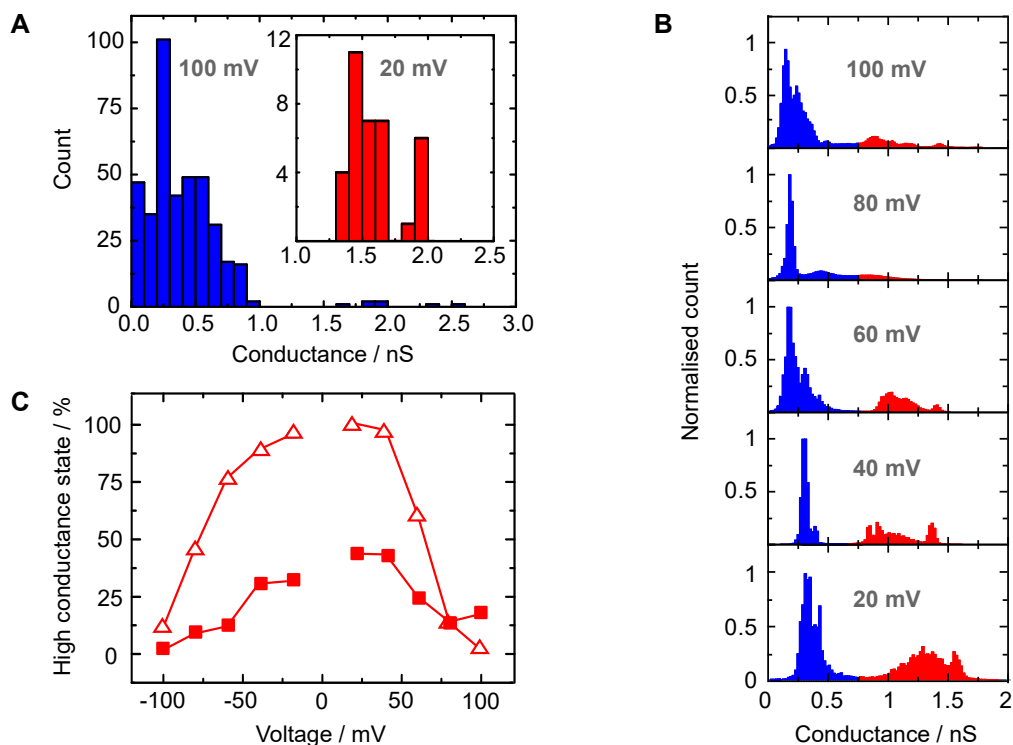


Figure 5.8: A) Conductance histogram derived from discrete conductance steps in multiple ionic current recordings with an initial applied voltage of 100 mV. The inset shows the region of the high conductance levels for experiments that were carried out under an initial applied voltage of only 20 mV, where the high conductance level occurs more frequently. B) Cumulative all-point conductance histograms recorded at 100 mV, 80 mV, 60 mV, 40 mV and 20 mV (from top to bottom), respectively, combining 21 independent recordings on the lipid nano bilayer setup. C) Probability of observing the high conductance level as a function of the applied voltage on the lipid nano bilayer system (filled squares) and on planar bilayers (empty triangles). The probabilities were derived from all-point histograms as presented in B. An arbitrary threshold dividing the conductances into low and high was set at 0.75 nS. Recordings on the planar bilayer system were carried out by A. Seifert, Nanion Technologies.

5.4 Conclusion

With the creation of a six-helix DNA nanopore with only two bi-functional porphyrin tags for visualisation and membrane insertion, we demonstrated a route to the design of versatile DNA membrane pores with minimal chemical intervention. Our results establish that the DNA pore exhibits multiple voltage-dependent conductance levels, whereby the probability of observing the lower conductance level increases with higher transmembrane potential. Voltage-dependent switching between different conductance levels is biologically highly relevant and hence an interesting property for a synthetic pore. We assume that multiple factors contribute to the complex conductance behaviour of DNA pores, including mechanical deformation induced by the electric field, lateral membrane pressure or thermodynamic fluctuations. It will be insightful to ascertain the origin of the gating in future work. Our observations help reconcile previously reported, conflicting conductance values by showing that the open level of our 14 nm long pore has, as expected, a higher conductance than a longer pore with the same six-helix bundle design [2]. We demonstrate the importance of considering different supported lipid membrane systems when characterising novel membrane pores. Conductances measured on lipid nano bilayers and planar bilayers were in agreement, yet the frequency of occurrence of different conductance levels was dependent on the membrane system. These differences could be caused by the system-specific lateral membrane pressure, which was later shown to affect the conductance of a six-helix pore in MD simulations [24]. The presence or absence of detergents and cholesterol can affect the membrane thickness and fluidity, which may influence the ion conduction pathway, the packing of the membrane-inserted DNA nanostructure or the orientation and depth of insertion of the hydrophobic tags. From the results of the present study, we already expect that not only the DNA pore itself but also the lipid membrane surrounding it influences the conductance behaviour. In Chapter 8, we will confirm this hypothesis by proving that a rearrangement in the lipid bilayer structure around the DNA pore opens up an additional ion pathway at the DNA-lipid interface.

If two membrane anchors are enough to insert the six-helix pore into lipid membranes, it should in principle be possible to create larger and more complex membrane-inserting DNA pores with higher-level functionality. At the same time, it opens up the possibility to create smaller ion channel-like DNA nanostructures which naturally have fewer possible attachment sites for chemical tags. The creation of smaller and larger DNA membrane pores inspired by the diversity of nature will be the scope of the following chapters.

Bibliography

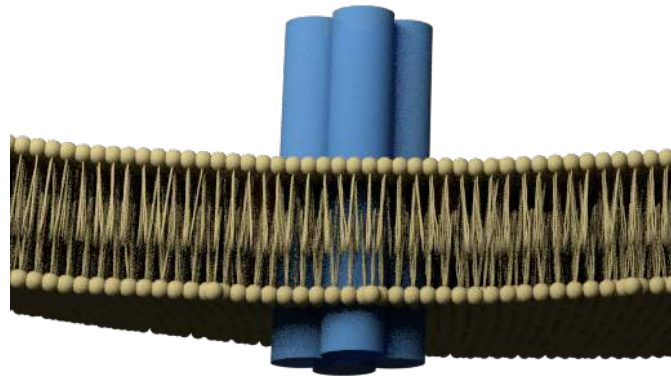
- [1] L. Song, M.R. Hobaugh, C. Shustak, S. Cheley, H. Bayley, and J.E. Gouaux. “Structure of staphylococcal alpha-hemolysin, a heptameric transmembrane pore.” *Science* 274.5294 (1996), pp. 1859–66. DOI: 10.1126/science.274.5294.1859. arXiv: VY200.
- [2] M. Langecker, V. Arnaut, T.G. Martin, J. List, S. Renner, M. Mayer, H. Dietz, and F. C. Simmel. “Synthetic Lipid Membrane Channels Formed by Designed DNA Nanostructures”. *Science* 338.6109 (2012), pp. 932–6. DOI: 10.1126/science.1225624.
- [3] K. Göpfrich. “Towards rational design of artificial membrane pores using DNA nanotechnology”. Master of Philosophy in Physics. University of Cambridge, 2013.
- [4] J. R. Burns, E. Stulz, and S. Howorka. “Self-Assembled DNA Nanopores That Span Lipid Bilayers.” *Nano Letters* 13.6 (2013), pp. 2351–6. DOI: 10.1021/nl304147f.
- [5] H. Said, V. J. Schüller, F. J. Eber, C. Wege, T. Liedl, and C. Richert. “M1.3 - a small scaffold for DNA origami .” *Nanoscale* 5.1 (2013), pp. 284–90. DOI: 10.1039/c2nr32393a.
- [6] J. G. Woller, K. Börjesson, S. Svedhem, and B. Albinsson. “Reversible hybridization of DNA anchored to a lipid membrane via porphyrin”. *Langmuir* 28.4 (2012), pp. 1944–53. DOI: 10.1021/la2039976.
- [7] S. M. Douglas, A. H. Marblestone, S. Teerapittayanon, A. Vazquez, G. M. Church, and W. M. Shih. “Rapid prototyping of 3D DNA-origami shapes with caDNAno.” *Nucleic Acids Research* 37.15 (2009), pp. 5001–6. DOI: 10.1093/nar/gkp436.
- [8] L. A. Fendt, I. Bouamaied, S. Thöni, N. Amiot, and E. Stulz. “DNA as supramolecular scaffold for porphyrin arrays on the nanometer scale”. *Journal of the American Chemical Society* 129 (2007), pp. 15319–29.
- [9] T. Nguyen, A. Brewer, and E. Stulz. “Duplex stabilization and energy transfer in zipper porphyrin-DNA”. *Angewandte Chemie International Edition* 48 (2009), pp. 1974–7.
- [10] J. R. Burns, K. Göpfrich, J. W. Wood, V. V. Thacker, E. Stulz, U. F. Keyser, and S. Howorka. “Lipid-bilayer-spanning DNA nanopores with a bifunctional porphyrin anchor.” *Angewandte Chemie International Edition* 52.46 (2013), pp. 12069–72. DOI: 10.1002/anie.201305765.

-
- [11] L. A. Clifton, M. R. Sanders, V. Castelletto, S. E. Rogers, R. K. Heenan, C. Neylon, R. A. Frazier, and R. J. Green. “Puroindoline-a, a lipid binding protein from common wheat, spontaneously forms prolate protein micelles in solution”. *Physical Chemistry Chemical Physics* 13.19 (2011), pp. 8881–8. DOI: 10.1039/c0cp02247k.
- [12] N. Mitchell, A. Ebner, P. Hinterdorfer, R. Tamp??, and S. Howorka. “Chemical tags mediate the orthogonal self-assembly of DNA duplexes into supramolecular structures”. *Small* 6.16 (2010), pp. 1732–5. DOI: 10.1002/sml.201000790.
- [13] J. L. Gornall, K. R. Mahendran, O. J. Pambos, L. J. Steinbock, O. Otto, C. Chimere, M. Winterhalter, and U. F. Keyser. “Simple reconstitution of protein pores in nano lipid bilayers.” *Nano Letters* 11.8 (2011), pp. 3334–40. DOI: 10.1021/nl201707d.
- [14] K. Göpfrich, C. V. Kulkarni, O. J. Pambos, and U. F. Keyser. “Lipid Nanobilayers to Host Biological Nanopores for DNA Translocations”. *Langmuir* 29.1 (2013), pp. 355–64. DOI: 10.1021/la3041506.
- [15] J. R. Burns, S. Preus, D. G. Singleton, and E. Stulz. “A DNA based five-state switch with programmed reversibility.” *Chemical Communications* 48.90 (2012), pp. 11088–90. DOI: 10.1039/c2cc35799b.
- [16] A. Brewer, G. Siligardi, C. Neylon, and E. Stulz. “Introducing structural flexibility into porphyrin-DNA zipper arrays”. *Organic & Biomolecular Chemistry* 9 (2011), pp. 777–82.
- [17] a. Ortega, D. Amorós, and J. García de la Torre. “Prediction of hydrodynamic and other solution properties of rigid proteins from atomic- and residue-level models.” *Biophysical Journal* 101.4 (2011), pp. 892–8. DOI: 10.1016/j.bpj.2011.06.046.
- [18] A. Kuzuya and M. Komiyama. “Design and construction of a box-shaped 3D-DNA origami.” *Chemical Communications* 28 (2009), pp. 4182–4. DOI: 10.1039/b907800b.
- [19] K. Börjesson, J. Wiberg, A. H. El-Sagheer, T. Ljungdahl, J. Mårtensson, T. Brown, B. Nordén, and B. Albinsson. “Functionalized nanostructures: Redox-active porphyrin anchors for supramolecular DNA assemblies”. *ACS Nano* 4.9 (2010), pp. 5037–46. DOI: 10.1021/nm100667b.
- [20] K. Göpfrich, T. Zettl, A. E. C. Meijering, S. Hernández-Ainsa, S. Kocabey, T. Liedl, and U. F. Keyser. “DNA-tile structures lead to ionic currents through lipid membranes”. *Nano Letters* 15 (2015), pp. 3134–8. DOI: 10.1021/acs.nanolett.5b00189.
- [21] V. Maingi, M. Lelimousi, S. Howorka, and M. S. P. Sansom. “Gating-like Motions and Wall Porosity in a DNA Nanopore Scaffold Revealed by Molecular Simulations.” *ACS Nano* 9.11 (2015), pp. 11209–17. DOI: 10.1021/acsnano.5b06357.

- [22] B. Hille. *Ion Channels of Excitable Membranes*. Sunderland: Palgrave Macmillan, **2001**.
- [23] A. Seifert, K. Göpfrich, J.R. Burns, N. Fertig, U.F. Keyser, and S. Howorka. “Bilayer-Spanning DNA Nanopores with Voltage-Switching between Open and Closed State.” *ACS Nano* 9.2 (**2014**), pp. 1117–26. DOI: 10.1021/nm5039433.
- [24] J. Yoo and A. Aksimentiev. “Molecular Dynamics of Membrane-Spanning DNA Channels: Conductance Mechanism, Electro-Osmotic Transport, and Mechanical Gating”. *Journal of Physical Chemistry Letters* 6.23 (**2015**), pp. 4680–7. DOI: 10.1021/acs.jpcllett.5b01964.

Chapter 6

DNA tile-based ion channels



Parts of this work previously appeared in:

K. Göpfrich, T. Zettl, A. E. C. Meijering, S. Hernández-Ainsa, S. Kocabey, T. Liedl & U. F. Keyser. DNA-tile structures lead to ionic currents through lipid membranes. *Nano Letters* **15**, 3134–3138 (2015).

Abstract In this chapter, we create the first DNA membrane channel that deviates from the archetypal six-helix bundle architecture. Using the DNA tile approach, we create a bundle of four DNA duplexes with a sub-nanometre channel and cholesterol tags for membrane anchoring. The dimensions of our synthetic nanostructure are comparable to biological ion channels. Due to its simple design, the four-helix bundle self-assembles within a minute, making its creation scalable for applications in biology. Ionic current recordings demonstrate that our four-helix bundle enables ion conduction across lipid bilayers and shows gating and voltage-switching behaviour like the larger six-helix DNA pore. By presenting a DNA-based membrane channel with a near molecular inner diameter, our work showcases the versatility of synthetic DNA pores inspired by the rich diversity of natural membrane components.

6.1 Introduction

In the previous chapter, we demonstrated the incorporation of DNA pores into lipid membranes via hydrophobic tags. While the DNA origami technique [1] has been employed to construct pores with a molecular weight of around 5 MDa [2], we presented a six-helix bundle made from only six interconnected DNA strands reducing the complexity and the molecular weight. The fact that DNA membrane pores exhibit gating reminiscent of natural ion channels inspired us to create much smaller, more ion channel-like pores from DNA.

In this chapter, we design a DNA tile-based nanostructure [3, 4] prototyping a novel channel architecture. It consists of only four helices arranged on a square lattice, whereas all previously published DNA membrane channels were formed from a bundle of six DNA duplexes arranged on a hexagonal lattice [2, 5–7]. We thus reduced the nominal channel width from 2 nm to 0.8 nm, reaching typical diameters of natural ion channels [8]. Due to its simple design, our DNA tile structure can readily be made within a minute at micro-molar concentrations and high yields avoiding complex heating protocols.

With a simple DNA channel we aim to inform the design pathway towards ion channel-like biomimetic DNA membrane pores. In biology, the transport of ions across lipid membranes is essential for a wide range of processes including signal transduction in electrically excitable tissue [8]. Synthetic membrane constructs can advance our fundamental understanding of the physical principles dictating functions of ion channels in cells, but they could also serve as stimuli-responsive biosensors [9], cytotoxic agents [10]

or drug carriers [11]. While larger DNA pores have initially been designed for the purpose of nanopore sensing, we shift the focus towards smaller synthetic channels opening up broad perspectives for their biotechnological and biomedical applications [11, 12].

6.2 Materials and methods

Design and assembly of the DNA tile structure. The four-helix structure was designed and visualised using the open source software caDNAno [13]. Eight single-stranded DNA tiles (Integrated DNA Technologies) were arranged on a square lattice to form a bundle of four interconnected DNA duplexes. Four randomly generated sequences were selected for minimal unwanted sequence complementarity and secondary structure using NUPACK [14], a software tool described in Section 2.3.3. On the ends of the structure, these sequences were extended by three terminal adenine bases per duplex to avoid multimerisation via base stacking (“non-sticky ends”, see Section 2.3). Complementary sequences were generated for the remaining four tiles. All DNA sequences are listed in Table 6.1. One, two or four strands were selected for cholesterol modifications, two others carried Cy3 tags. For assembly of the DNA tile structure, an equimolar mixture (1 μ M in 10 mM Tris-HCl, 1 mM EDTA, 20 mM MgCl₂, pH 8.0) of the unmodified strands were annealed using a standard protocol (heating to 80 °C for 5 min, cooling down to 65 °C using a linear cooling ramp over 75 min, subsequently cooling to 25 °C within 16 h in a thermocycler (BioRad)). Alternatively, rapid assembly protocols were used as described in Section 6.3.2. The cholesterol-modified strands (Integrated DNA Technologies) were first heated to 60 °C to dissolve aggregates and then added in 5 \times excess before each experiment.

Characterisation via AFM imaging, PAGE, DLS and UV melting. For AFM imaging, 5 μ L of DNA tile structures at a concentration of 100 nM in 10 mM Tris-HCl, 1 mM EDTA, 20 mM MgCl₂ were deposited on freshly cleaved mica and left for one minute to adsorb. The sample was then rinsed with ddH₂O three times to remove salts and dried with gaseous nitrogen. Imaging was performed using a Nanosurf Mobile S AFM in tapping mode. The DNA tile structures were further characterised using 10% PAGE in a solution containing 11 mM MgCl₂ buffered to pH 8.3 with 45 mM Tris-borate, 1 mM EDTA and running conditions of 100 V and 90 min. Bands were stained with GelRed and visualised using UV transillumination. DLS experiments were conducted on a Zetasizer Nano S (Malvern) using DNA tile structures at a concentration of 0.3 μ M in 10 mM

Tris, 1 mM EDTA, 20 mM MgCl₂. For UV melting experiments, 500 nM of the DNA tile structure were added to a quartz cuvette (Sigma Aldrich) either in presence or in absence of lipid vesicles. The mixture was subjected to heating and cooling cycles (25 °C to 80 °C) at a rate of 0.25 °C/min for the determination of the melting temperature and at 5 °C/min for estimating the required folding time in a Varian Cary 300 Bio UV-vis spectrophotometer while monitoring the absorption at 260 nm.

Lipid vesicle preparation. DphPC (Avanti Polar Lipids), 10% cholesterol (Sigma Aldrich) GUVs were prepared via electroformation using the Vesicle Prep Pro unit (Nanion Technologies) and the protocol described in Section 4.4.2. For confocal imaging, 1,2-Dioleoyl-sn-glycero-3-phosphocholine (DOPC; Avanti Polar Lipids), or DOPC supplemented with 1% of the fluorescent NBD-DphPE, was used following the same procedure.

Fluorescent imaging. Cy3-labelled DNA tile structures were added to GUVs and diluted to a final concentration of 5 nM or 100 nM in 10 mM Tris-HCl, 1 mM EDTA, 20 mM MgCl₂, pH 8.0 in an incubation chamber (Grace Biolabs). Imaging was performed using a Confocal Leica TCS SP5 microscope with a 40× objective and an excitation wavelength of 514 nm from an Argon laser. Fluorescence emission was collected above 530 nm. Images were processed using ImageJ.

Ionic current recordings on the lipid nano bilayer setup. DNA tile structures were incubated with GUVs at room temperature for 5 min and diluted to a final concentration of 50 nM in 1 M KCl, 10 mM MES, pH 6.0. Bilayers were formed by suctioning the GUVs onto nano capillaries as described the detailed protocol in Section 4.4.2. Each bilayer was subjected to a 33 s long *I-V* recording at a sampling rate of 10 kHz. Current data was acquired using an Axopatch 200B amplifier and filtered at 2 kHz.

6.3 Results and discussion

6.3.1 Design, assembly and characterisation

Our DNA tile structure consists of four 11 nm long DNA duplexes arranged on a square lattice as illustrated in the sketch in Figure 6.1A. In this arrangement, the naturally emerging gap between the helices gives rise to a central channel with a nominal diameter of 0.8 nm, assuming geometrical packing and an anhydrated helix diameter of 2 nm. The duplexes are formed from eight interconnected single-stranded DNA tiles, two of which carry terminal cholesterol modifications to allow for membrane anchoring. The DNA sequences of the tiles, listed in Table 6.1, were selected to have minimal unwanted complementarity and secondary structure to ensure efficient and fast assembly. Two additional tiles carry Cy3 tags for visualisation by fluorescence microscopy. The pathways of the DNA tiles linking neighbouring helices with two crossovers per helix are shown in Figure 6.1B. Terminal adenine repeats were introduced at both ends of the structure to avoid stacking of multiple structures [4]. It should be noted that the crossovers between neighbouring helices are ten or eleven base pairs apart. The design thus deviates from the recommended eight base pair spacing which reduces strain and twisting torques in DNA nanostructures. While this is very important for larger structures, the assembly of our small four-helix bundle is nonetheless efficient as shown in the following sections. The additional base pairs increase its thermal stability.

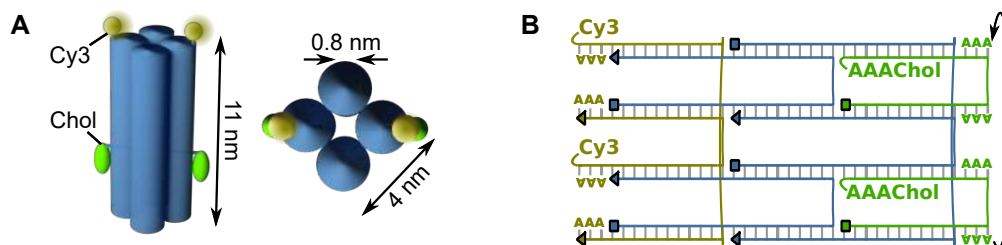


Figure 6.1: A) Schematic side view (left) and top view (right) of the DNA tile structure composed of four interconnected duplexes represented as blue cylinders. The two cholesterol anchors are shown in green, the Cy3 tags in yellow. B) Pathways of the eight single-stranded DNA tiles forming the four duplexes and positions of the Cy3 and cholesterol modifications. Squares represent the 5' ends, triangles the 3' ends, base pairs are indicated as vertical bars. The four-helix structure was designed in collaboration with T. Zettl, visiting Master student, and T. Liedl, LMU Munich.

Table 6.1: DNA sequences used for the assembly of the four-helix DNA tile structure.

Name	Sequence (5' to 3')
U1R1+Cy3	Cy3-AAAACGCTAAGCCACCTTTAGATCCAAA
U1R2	GGTCGTGCGGACTGTTCGAACACCAACGATGCCTGATAGAAGT
U2R1	GGATCTAAAGGACTTCTATCAAAGACGGGACGACTCCGGGAG
U2R2+Chol	GGCATCGTTGGAAAAAATTTTCGGATCCAAAA-Chol
U3R1+Cy3	Cy3-AAACTCCCGGAGTCCGCTGCTGATCCAAA
U3R2	GTCCCGTCTTTGGATCCGAAAGCCATAATATATCGAGACGGG
U4R1	GATCAGCAGCGCCCGTCTCGACCGCACGACCTGGCTTAGCGT
U4R2+Chol	TATATTATGGCAAAAAATGTTTCGACAGTAAA-Chol

Our design aims to mimic the complex behaviour of biological ion channels by increasing the structural flexibility and reducing the diameter to the molecular scale. MD simulations have suggested that free DNA at the pore entrance could cause the observed gating of the six-helix pore [15]. We therefore left the four-helix structure open at one terminus, while the other end was stabilised with terminal crossovers to aid membrane insertion, see Figure 6.1B. Fluctuations were deliberately enhanced further by choosing DNA tiles of short length and by placing the crossovers at symmetric positions.

The four-helix DNA tile structure was assembled by annealing equimolar concentrations of the six cholesterol-free tiles at a final concentration of 1 μM in 10 mM Tris-HCl, 1 mM EDTA, 20 mM MgCl_2 at pH 8.0. The two cholesterol-tagged tiles were added in 5 \times excess at room temperature directly before the experiment. Subsequently, the structure was characterised to probe its correct assembly. AFM imaging confirmed the monomeric nature and established that the dimensions fell within the expected bounds for such a small design, see Figure 6.2A. Gel electrophoresis of the DNA structure without the two cholesterol-tagged DNA tiles yielded a single band, see Figure 6.2B, Lane 5, whereas the migration in the gel of structures with the cholesterol-tagged tiles was hindered due to hydrophobic interactions causing aggregation in the gel pocket, Lane 2. This demonstrates that the cholesterol-modified DNA strands were successfully incorporated. As expected, a fully assembled structure with all eight tiles but no cholesterol tags migrated slower than the six-tile construct, Lane 4. DLS measurements, presented in Figure 6.2C, gave a mean hydrodynamic radius of 5.4 nm for the DNA construct missing the cholesterol-modified tiles and 8.5 nm for the complete structure with cholesterol, respectively. These values indicate the monomeric nature of the four-helix structures in the measurement buffer.

We subsequently performed UV melting experiments as described in Section 2.3.5. Table 6.2 lists the obtained melting temperatures for the four-helix structure with and

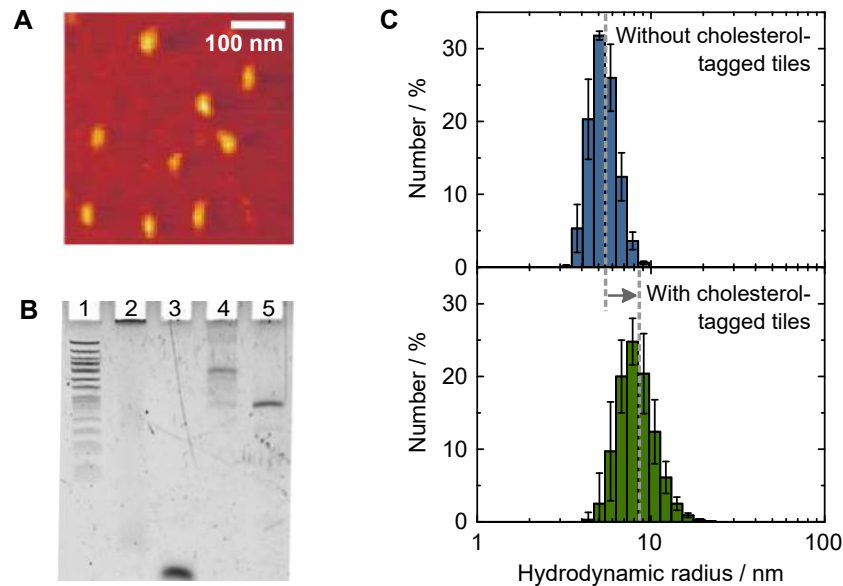


Figure 6.2: Characterisation of the four-helix DNA tile nanostructure. A) AFM image (in air, tapping mode) of the DNA tile structure. B) 10% PAGE. Lane 1: 50 bp DNA ladder; Lane 2: Complete DNA tile structure with two cholesterol tags; Lane 3: Individual 28 bp long single-stranded DNA tile; Lane 4: Complete DNA tile structure without cholesterol tags; Lane 5: DNA tile structure missing the two cholesterol-tagged strands. C) DLS trace of the incomplete DNA tile structure composed of six DNA oligomers (blue, top) and the complete structure with two cholesterol-modified oligomers (green, bottom). Both traces feature a single peak with a mean hydrodynamic radius of 5.4 nm and 8.5 nm, respectively. Error bars correspond to the standard deviation of eight independent measurements.

Table 6.2: Melting temperature of the four-helix structure measured at 260 nm in presence and absence of cholesterol-tagged DNA and GUVs (DphPC, 10% cholesterol), using a temperature gradient of 0.25 °C/min. The melting temperature increases for the four-helix structure with cholesterol anchors in the presence of GUVs.

	Without cholesterol-tagged DNA	With cholesterol-tagged DNA
Without GUVs	54 °C	54 °C
With GUVs	54 °C	61 °C

without cholesterol tags in the presence and the absence of GUVs. It lies at 54 °C for both the cholesterol-tagged and the cholesterol-free four-helix structure. If the UV melting experiments are performed in the presence of GUVs, the melting temperature of the fully assembled structure with cholesterol anchors increases by over 7 °C, while it stays almost constant for the construct without hydrophobic tags. This thermal stabilisation can be explained through a considerable interaction between GUVs and our DNA tile structures. We reported a similar increase in the melting temperature for the porphyrin-tagged six-helix pore in Chapter 5.

6.3.2 Rapid low-cost assembly

A major advantage of our tile-based four-helix design is its simplicity resulting in a significant cost reduction and minimal preparation times. In Table 6.3, we estimate the material cost for the production of 1 nmole DNA tile structures with two cholesterol anchors in a standard university setting. The total cost for 1 nmole assembled structures is 40 GBP. 1 nmole is sufficient for approximately 200 independent lipid nano bilayer or confocal imaging experiments. The DNA origami pore by Langecker *et al.* required a much higher number of DNA strands in addition to the scaffold increasing the cost for 1 nmole to around 200 GBP [2]. Our six-helix pore presented in Chapter 5 was made of longer single-strands which had to be PAGE-purified, reducing the yield and increasing the cost of their synthesis to around 240 GBP for 1 nmole [5–7, 10]. With our DNA tile structure, we hence achieved a considerable reduction in cost compared to previous DNA membrane pores. Large quantities of the four-helix structure can be prepared in less than 10 minutes. The preparation only involves mixing the six untagged single-strands of DNA at equimolar ratios and adding the cholesterol-tagged oligos directly before the

Table 6.3: Estimated cost for the production of 1 nmole DNA tile structures with two cholesterol anchors in a standard university setting.

Reagent	Quantity	Supplier	Cost
MgCl ₂	1.9 mg	Sigma-Aldrich	0.13 GBP
1 × Tris-EDTA	1 mL	Sigma-Aldrich	0.17 GBP
6 DNA oligomers	6 nmole	Integrated DNA Technologies	1.12 GBP
2 cholesterol-tagged DNA oligomers (HPLC-purified)	10 nmole	Integrated DNA Technologies	40.0 GBP

experiment to prevent aggregation. Premixed tiles can be frozen and thawed as required.

Additionally, we examined different annealing procedures and noticed that by choosing the DNA sequences carefully, time-consuming protocols were made redundant. We assembled the four-helix construct lacking the two cholesterol-modified tiles in 10 mM Tris-HCl, 1 mM EDTA, 20 mM MgCl₂, pH 8.0 using four different assembly protocols:

1. An 18 hour standard annealing protocol (heating to 80 °C for 5 min, cooling down to 65 °C using a linear cooling ramp over 75 min, subsequently cooling to 25 °C within 16 hours) as a benchmark procedure;
2. A 10 min thermocycler protocol (heating to 80 °C for 5 min, holding at 65 °C for 5 min);
3. A 10 min water-bath treatment (80 °C);
4. A 10 min incubation at room temperature.

To assess the feasibility and assembly yield for each protocol, we performed gel electrophoresis as shown in Figure 6.3A. We confirm that the structure has successfully been formed under all assembly conditions. The intensity of the bands is indicative of the obtained yield. Notably, the 10 min annealing (Protocol 2) still yields 85 % compared to the benchmark conditions (Protocol 1). The Protocols 3 and 4 without thermocycler result in 78 % and 76 % respectively.

To estimate an upper limit for the required assembly time, we performed UV melting experiments. Instead of using a slow heating rate as before when determining the melting temperature, we rapidly melted and subsequently re-annealed the DNA structure by heating and cooling it at a rate of 5 °C/min in a UV spectrophotometer. Figure 6.3B shows the corresponding melting curve for the absorption measured as a function of temperature. It should be noted that the inflection point here is not actually the melting temperature of the structure, as the sample inside the measurement cuvette is not fully

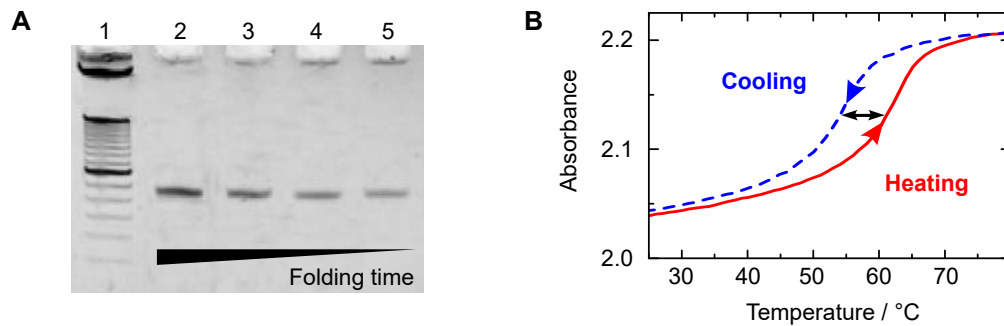


Figure 6.3: A) 10% PAGE. Lane 1: 50 bp DNA ladder; Subsequent lanes: DNA tile structure lacking the two cholesterol-modified tiles annealed for 18 h in the thermocycler (Lane 2), for 10 min in the thermocycler (Lane 3), for 10 min in a hot water bath (Lane 4) and for 10 min at room temperature (Lane 5). B) Absorption measured at 260 nm during a heating (red) and a subsequent cooling cycle (blue) in a UV melting experiment. At the cooling rate of $5^{\circ}\text{C}/\text{min}$ the shift in melting temperature gives an upper limit for the folding time of 2 min. UV melting experiments were carried out in collaboration with A. E. C. Meijering, visiting master student.

equilibrated. The sole purpose of this experiment was to determine an upper limit for the required assembly time. In the cooling cycle, we observed re-hybridisation of the structure, visible as a reduction in the absorbance. The shift in the inflection point gives a measure for the upper limit of the required assembly time. At the given cooling rate of $5^{\circ}\text{C}/\text{min}$, the observed shift of 8°C effectively corresponds to a maximum folding time of 2 min. The fact that the absorbance returns to its original value after the temperature cycle indicates that the number of correctly assembled structures remains at a similar level even for such short duration of the programme.

6.3.3 Confocal fluorescent imaging

To visualise the interaction of the four-helix structures with lipid vesicles, we carried out fluorescent confocal imaging. Figure 6.4 shows a bright-field (left) and a confocal (right) image of GUVs incubated with fluorescently labelled cholesterol-tagged DNA tile structures. The outlines of the GUVs of various sizes appears uniformly bright, indicating efficient coating of their membrane with DNA tile structures. Using confocal imaging, we could further demonstrate that the complete structure with cholesterol anchors assembles and attaches to GUVs within a minute. A mixture of all eight tiles was kept at

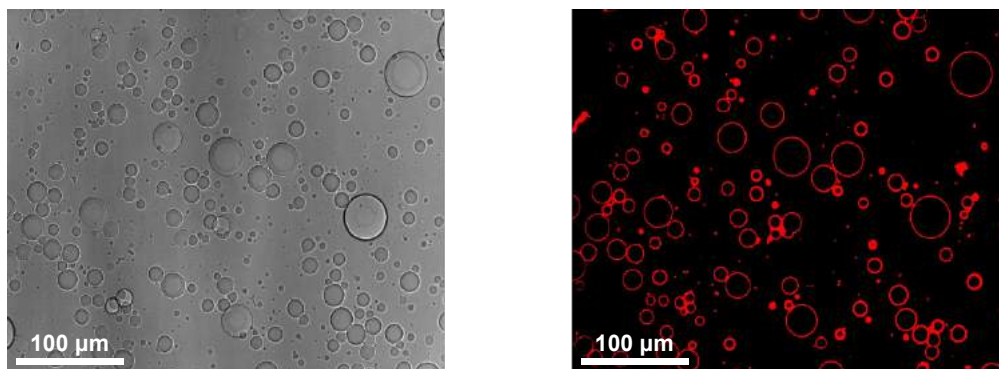


Figure 6.4: Confocal images, 40 \times , of GUVs (DphPC, 10% cholesterol) incubated with 100 nM Cy3-labelled DNA tile structures with two cholesterol anchors imaged in bright field (left) and fluorescence mode (right, excitation at 514 nm).

80 °C to prevent hybridisation before adding the sample to GUVs at room temperature. Figure 6.5 shows a GUV imaged in bright field (left) and fluorescence mode (middle) directly after addition of the sample containing the melted DNA tile mixture. After only 60 seconds, a bright ring around the same GUV (right) indicates the presence of then assembled DNA tile structures on the membrane of the vesicle. This proves that the DNA assembly was complete, since only a fully formed structure connects both the Cy3 tag and the cholesterol tag, see Figure 6.1B. Control experiments show that membrane attachment requires the presence of at least one cholesterol anchor. The uniform distribution of DNA tile structures around the GUV points towards minimal aggregation. Even though larger aggregates are sometimes visible in the fluorescent images, especially after long storage of the sample, we observed that aggregation is significantly reduced upon addition of GUVs.

Interestingly, high concentrations of DNA tile structures led to the formation of tubular lipid deformations up to several hundred micron in length as shown in Figure 6.6. Two lipid compositions were tested, DOPC and DphPC with 10% cholesterol, which both exhibit these deformations. Similar observations were previously made for high concentrations of certain membrane-binding proteins [16, 17]. Crowding of DNA structures on the membrane could lead to increased membrane pressure and competition for access to the membrane. This might help to overcome the energy barrier for bending of the membrane as has been proposed for specialised membrane proteins [16]. Alternatively, our DNA tile structures could behave like amphiphilic membrane-inserted α -helices that are hypothesised to cause membrane bending [17]. To test if the tubular structures are

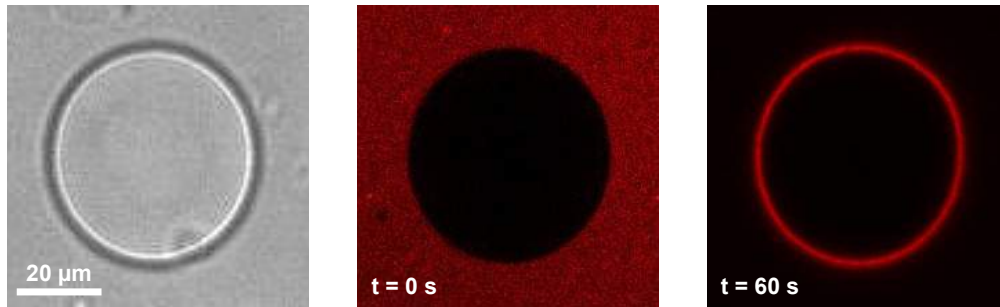


Figure 6.5: GUV imaged in bright field (left) and fluorescence mode (excitation at 514 nm). 60 seconds after addition of the DNA tile mixture, a bright ring forms around the vesicle, indicating rapid folding and membrane attachment of the structure.

indeed lipid deformations rather than aggregates of DNA tile constructs, we prepared a sample without Cy3 tags and added it to GUVs containing fluorescently labelled lipids (DOPC, 1% NBD-DphPE). The confocal image in Figure 6.6B confirms the hypothesis of lipid deformation. Importantly, addition of high concentrations of cholesterol-tagged DNA alone does not cause membrane bending, see Figure 6.6C. After we published our results [18], membrane tubulation was also reported for larger DNA nanostructures [19].

6.3.4 Ionic current recordings

This study set out to investigate whether a DNA nanostructure made of only four duplexes can induce ion flux across lipid membranes like natural ion channels. Since fluorescent imaging confirmed that the DNA tile structures strongly interact with lipid vesicles, we decided to form lipid bilayers for electro-physiological characterisation directly from these vesicles as we did for the six-helix pores in Chapter 5. We use our lipid nano bilayer system [7, 20, 21] which allows us to screen large numbers of vesicles for the incorporation of pores relatively quickly as described in Section 4.4.1 and 4.4.2. We incubated GUVs (DphPC, 10% cholesterol) with DNA tile structures in 1 M KCl, 10 mM MES, pH 6.0. As illustrated in Figure 6.7A, these vesicles were then suctioned onto the tip of a 200 nm diameter glass capillary (1), where they burst and form a bilayer. This bilayer is then subjected to a standardised I - V recording protocol (2), before it is removed from the capillary by applying a positive pressure (3). We repeated this process at least 100 times for each of the experimental conditions to obtain reasonable

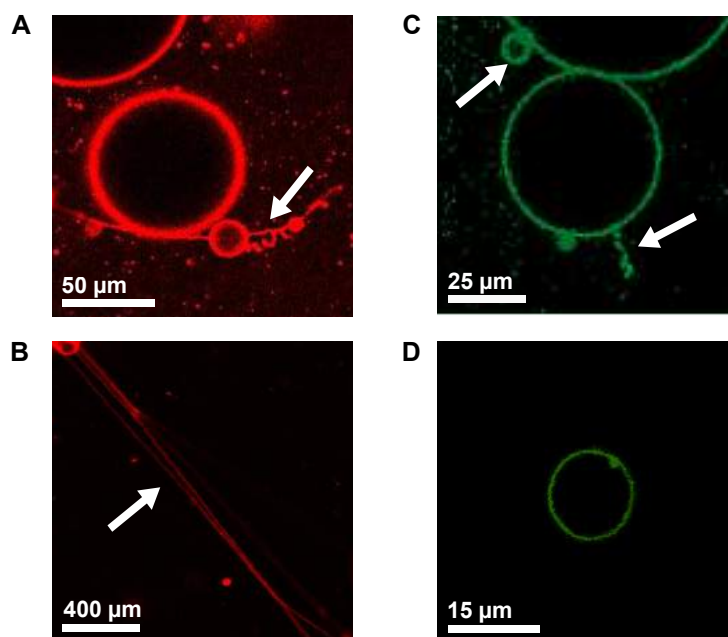


Figure 6.6: Confocal imaging of lipid tubulation of GUVs in presence of high concentrations of DNA tile structures. A) DOPC GUVs with 50 nM of Cy3-labelled cholesterol-tagged DNA tile structures, excitation at 514 nm. The white arrow points at lipid deformations. B) Tubules extended from GUVs (here: DphPC, 10% cholesterol) can reach several hundred microns in length. C) GUVs formed from fluorescently-labelled lipids (DOPC, 1% NBD-DphPE) with 50 nM of non-fluorescent DNA tile structures, excitation at 488 nm. D) Cholesterol-tagged single-stranded DNA only does not produce tubulation.

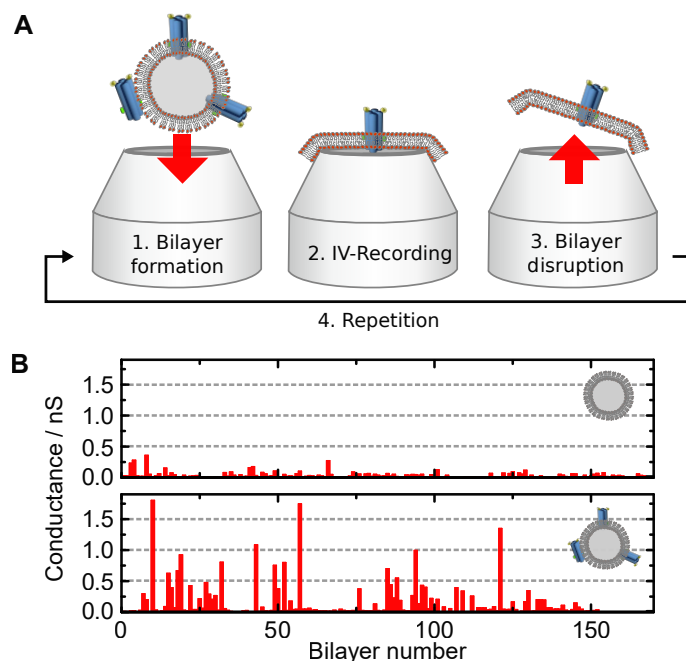


Figure 6.7: A) Illustration of the three-step ionic current measurement protocol on our lipid nano bilayer setup. The same protocol was used for GUVs without DNA tile structures. B) Conductances obtained for 170 independent I - V recordings of GUVs without (top) and with cholesterol-tagged DNA tile structures (bottom).

statistics. All GUVs are tested without DNA tile structures first to assess the bilayer quality. The GUVs are only used for recordings if they exhibit a consistent conductance in the range of tens of pS and no pore-like events are observed. Figure 6.7B shows the conductances of 170 independent I - V recordings for plain GUVs (top) and GUVs that have been incubated with DNA tile structures (bottom).

None of the bilayers formed from plain GUVs shows a conductance above 0.3 nS. In contrast, 12% of bilayers formed from GUVs with DNA structures exhibit higher conductances. Also the percentage of bilayers with conductances between 0.15 nS and 0.3 nS increases. Control experiments were carried out with GUVs that were incubated with the cholesterol-modified single-stranded DNA only, with DNA tile structures without cholesterol anchors, with a cholesterol-tagged DNA duplex, with only one cholesterol anchor and with four cholesterol anchors. Table 6.4 shows the percentage of bilayers with conductances above 0.15 nS for each of these conditions. This percentage is much higher in the presence of DNA tile structures with two or four cholesterol anchors, indi-

cating that only our fully assembled DNA tile structures are capable of producing ion conduction across lipid membranes. For the structure with four cholesterol, the additional modifications were placed at the 3' ends of U1R2 and U3R2, see Table 6.1. The duplex with a terminal cholesterol was made of two complementary strands of DNA with the exact sequence and length of one of the duplexes of the four-helix structure.

Table 6.4: Percentage of bilayers exhibiting a conductance G above 0.15 nS after addition of GUVs incubated with control samples and functional membrane-inserting four-helix structures. n denotes the number of bilayers that were formed and tested for each of the samples.

Sample	$G > 0.15$ nS	n
No DNA	3.7 %	170
Cholesterol-free four-helix structure	3.3 %	44
Cholesterol-tagged DNA strands only	3.3 %	99
DNA duplex with terminal cholesterol	3.1 %	27
Four-helix structure with 1 cholesterol	2.8 %	35
Four-helix structure with 2 cholesterol	26.1 %	170
Four-helix structure with 4 cholesterol	19.0 %	93

An increase in the conductance is not the only way in which bilayers holding functional four-helix structures are distinct from plain bilayers. We observe characteristic events that we can attribute to the presence of one or more DNA tile assemblies, like a stepwise increase or decrease in current at constant voltage. A typical event is shown in Figure 6.8A (top). It is likely to correspond to flipping of a DNA tile structure that was previously bound to the membrane into an ion conducting orientation. These insertion events are rarely observed on the lipid nano bilayer setup as the membrane area is very small and the pores are already pre-inserted into the GUVs. Additionally, we often observe gating as shown in Figure 6.8A (bottom). Looking at the design of the four-helix pore in Figure 6.1, this is not surprising as one end of the structure does not contain terminal cross-overs allowing for fluctuations in the electric field. In Figure 6.8B, we present typical ionic current traces obtained from I - V recordings in the presence of four-helix structures with cholesterol anchors. Although we sometimes obtain ohmic current traces (black), traces with reduced conductance at higher voltage (green) are very characteristic. It is interesting to note that comparable gating and voltage-switching behaviour from a higher to a lower conductance state has also been reported for the archetypal six-helix bundle in planar bilayers and lipid nano bilayers [7]. Taking all conductance steps into account, including insertions and closures, we

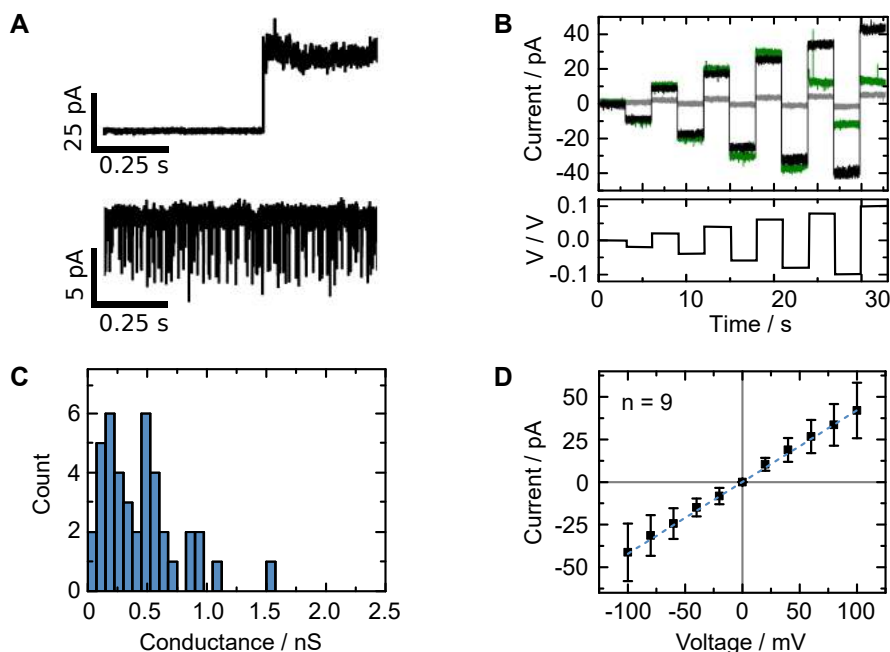


Figure 6.8: A) Characteristic ionic current events indicating the presence of a DNA tile structure in the membrane include insertion steps (top) and gating (bottom). B) Typical current traces obtained from an *I-V* recording in the presence of DNA tile structures with cholesterol anchors. Traces corresponding to plain bilayers (grey), ohmic traces (black) and traces with reduced conductance at higher voltage (green) are observed repeatedly. C) Histogram of conductance steps for the four-helix DNA tile structure. D) *I-V* curve of stable insertions. The error bars correspond to the standard deviation for nine independent recordings, the dashed line represents a linear fit with a gradient of 0.42 nS.

compiled the histogram in Figure 6.8C. The broad spread of the histogram captures the presence of multiple conductance states, with a higher conductance around 0.5 nS and a lower conductance around 0.25 nS occurring most frequently. The lower conductance state thus seems to agree with the lower conductance state of the six-helix bundle potentially pointing towards their similar nature. MD simulations attributed the partially obstructed ionic current pathway to fluctuations of the mouth region for the six-helix pore [15]. While we cannot make a definite statement about the nature of the conductance states, this explanation is conceivable for the four-helix pore as well.

For stable insertions, which did not gate at higher voltages, like the black trace (B), we obtained the *I-V* curve shown in Figure 6.8D. The linear fit has a gradient of 0.42 nS for this subset of stable insertions. This value is lower than the 1.6 nS high conductance

level of the six-helix pore reported in Chapter 5, in line with the smaller pore diameter. A channel with the nominal diameter of 0.8 nm should have a conductance of 0.45 nS in 1 M KCl according to the Hille equation (Equation 4.8), assuming a rigid cylindrical channel. However, the effective channel diameter in solution is expected to deviate from the nominal value. The hydrodynamic helical diameter has been estimated as 2.2 to 2.6 nm [22] (compared to 2 nm anhydrated). Electrostatic repulsion between the helices will increase the effective channel diameter further [23–25], while the Debye layer on the charged channel walls will reduce it. In addition, MD simulations have shown that lateral membrane pressure can influence the effective diameter of DNA pores [26]. A small and highly charged channel will exhibit charge selective transport. In line with our data, rigid channels with a uniform conductance are not expected at near molecular length scales. The relatively good agreement between the Hille equation and the experimental conductance is thus likely due to the cancellation of competing effects.

When reducing the pore diameter to molecular length scales, it is interesting to consider the ion conductance pathway and mechanism. Assuming our DNA tile structure is actually penetrating the membrane in the perpendicular orientation, the obvious ion pathway leads through its 0.8 nm wide interior. Assuming a rigid channel with uncharged walls this should provide enough space for potassium ions to pass with their hydration shell. In Chapter 8 of this thesis, we present a study demonstrating that ions do not only flow through the central channel of a DNA pore, but also through gaps at the DNA-lipid interface. We therefore now know for certain that ion conduction via the central channel is not the only contribution to the total conductance. Potentially, the membrane bending observed in the confocal images in Figure 6.6 and the resulting high membrane curvature could induce an additional ion conduction pathway due to flexoelectricity [27, 28]. On a related note, the DNA tile structures could be catalysts for the formation of lipid pores as has been proposed for membrane proteins [27]. While we believe that some of the current-inducing four-helix structures will be inserted perpendicular to the membrane, but other orientations are likely to induce additional conductance pathways contributing to the observed heterogeneity.

6.4 Conclusion

In this chapter we showcased the versatility of DNA nanotechnology by diversifying the design of membrane-inserted DNA structures beyond the archetypal six-helix bundle. Control over channel diameter and architecture is regarded as the main advantage of

DNA pores compared to other synthetic membrane channels [29], which we exploited here for the first time. We demonstrate that DNA tile assembly can be used to create ion-conducting structures with diameters comparable to biological ion channels within minutes. By reducing cost, time and required equipment for the large-scale creation of the DNA membrane channels, we make them accessible to a wider community. Not surprisingly, our structure exhibits complex conductance behaviour despite its apparent simplicity: the four duplexes are not connected at one end allowing for fluctuations of the highly charged structure in the electric field. We observe voltage-dependent conductance states as for the larger six-helix bundles, see Section 5.3.4. With this work, we shift the focus to smaller, highly flexible artificial ion channels constructed from DNA, whereas previous DNA membrane structures were preliminary designed for biosensing [2, 7]. Due to their simple design with defined geometry, we expect that DNA pores with near molecular inner diameters will help to understand gating and voltage-induced switching behaviour of DNA membrane pores. DNA nanotechnology in principle provides the exciting possibility to model the energy landscape inside a DNA pore by introducing synthetic nucleic acids with a different backbone charge or ion-responsive DNA motives like the G-quadruplex. Such approaches will be key to achieve sophisticated selectivity mechanisms as found in nature. Eventually this will lead to the creation of man-made ion channels with controlled ion-selectivity and stimuli response.

Bibliography

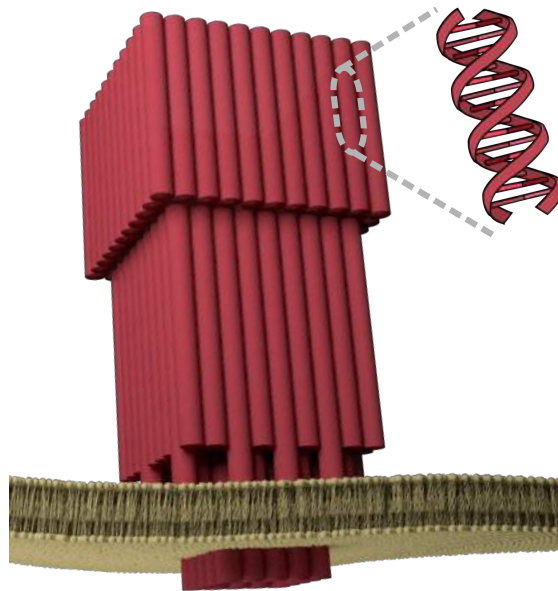
- [1] P. W. K. Rothemund. “Folding DNA to create nanoscale shapes and patterns.” *Nature* 440.7082 (2006), pp. 297–302.
- [2] M. Langecker, V. Arnaut, T. G. Martin, J. List, S. Renner, M. Mayer, H. Dietz, and F. C. Simmel. “Synthetic Lipid Membrane Channels Formed by Designed DNA Nanostructures”. *Science* 338.6109 (2012), pp. 932–6. DOI: 10.1126/science.1225624.
- [3] B. Wei, M. Dai, and P. Yin. “Complex shapes self-assembled from single-stranded DNA tiles.” *Nature* 485.7400 (2012), pp. 623–7. DOI: 10.1038/nature11075.
- [4] P. Yin, R. F. Hariadi, S. Sahu, H. M. T. Choi, S. H. Park, T. H. Labean, and J. H. Reif. “Programming DNA tube circumferences.” *Science* 321.5890 (2008), pp. 824–6. DOI: 10.1126/science.1157312.
- [5] J. R. Burns, K. Göpfrich, J. W. Wood, V. V. Thacker, E. Stulz, U. F. Keyser, and S. Howorka. “Lipid-bilayer-spanning DNA nanopores with a bifunctional porphyrin anchor.” *Angewandte Chemie International Edition* 52.46 (2013), pp. 12069–72. DOI: 10.1002/anie.201305765.
- [6] J. R. Burns, E. Stulz, and S. Howorka. “Self-Assembled DNA Nanopores That Span Lipid Bilayers.” *Nano Letters* 13.6 (2013), pp. 2351–6. DOI: 10.1021/nl304147f.
- [7] A. Seifert, K. Göpfrich, J. R. Burns, N. Fertig, U. F. Keyser, and S. Howorka. “Bilayer-Spanning DNA Nanopores with Voltage-Switching between Open and Closed State.” *ACS Nano* 9.2 (2014), pp. 1117–26. DOI: 10.1021/nm5039433.
- [8] B. Alberts, A. Johnson, J. Lewis, M. Raff, K. Roberts, and P. Walter. *Molecular Biology of the Cell*. 2002.
- [9] J. Clarke, H.-C. Wu, L. Jayasinghe, A. Patel, S. Reid, and H. Bayley. “Continuous base identification for single-molecule nanopore DNA sequencing”. *Nature Nanotechnology* 4.4 (2009), pp. 265–70. DOI: 10.1038/nnano.2009.12.
- [10] J. R. Burns, N. Al-Juffali, S. M. Janes, and S. Howorka. “Membrane-Spanning DNA Nanopores with Cytotoxic Effect”. *Angewandte Chemie International Edition* 53.46 (2014), pp. 12466–70. DOI: 10.1002/anie.201405719.
- [11] S. Hernández-Ainsa and U. F. Keyser. “DNA origami nanopores: an emerging tool in biomedicine.” *Nanomedicine* 8.10 (2013), pp. 1551–4. DOI: 10.2217/nmm.13.145.
- [12] S. Hernández-Ainsa and U. F. Keyser. “DNA origami nanopores: developments, challenges and perspectives.” *Nanoscale* 6.23 (2014), pp. 14121–32. DOI: 10.1039/c4nr04094e.

-
- [13] S. M. Douglas, A. H. Marblestone, S. Teerapittayanon, A. Vazquez, G. M. Church, and W. M. Shih. “Rapid prototyping of 3D DNA-origami shapes with caDNAno.” *Nucleic Acids Research* 37.15 (2009), pp. 5001–6. DOI: 10.1093/nar/gkp436.
- [14] C. Steffen, K. Thomas, U. Huniar, A. Hellweg, O. Rubner, and A. Schroer. “TmoleX—a graphical user interface for TURBOMOLE.” *Journal of Computational Chemistry* 31.16 (2010), pp. 2967–70. DOI: 10.1002/jcc. arXiv: NIHMS150003.
- [15] V. Maingi, M. Lelimousi, S. Howorka, and M. S. P. Sansom. “Gating-like Motions and Wall Porosity in a DNA Nanopore Scaffold Revealed by Molecular Simulations.” *ACS Nano* 9.11 (2015), pp. 11209–17. DOI: 10.1021/acsnano.5b06357.
- [16] J. C. Stachowiak, E. M. Schmid, C. J. Ryan, H. S. Ann, D. Y. Sasaki, M. B. Sherman, P. L. Geissler, D. A. Fletcher, and C. C. Hayden. “Membrane bending by protein-protein crowding.” *Nature Cell Biology* 14.9 (2012), pp. 944–9. DOI: 10.1038/ncb2561.
- [17] M. G. J. Ford, I. G. Mills, B. J. Peter, Y. Vallis, G. J. K. Praefcke, P. R. Evans, and H. T. McMahon. “Curvature of clathrin-coated pits driven by epsin”. *Nature* 419.6905 (2002), pp. 361–6. DOI: 10.1038/nature01020.
- [18] K. Göpfrich, T. Zettl, A. E. C. Meijering, S. Hernández-Ainsa, S. Kocabey, T. Liedl, and U. F. Keyser. “DNA-tile structures lead to ionic currents through lipid membranes”. *Nano Letters* 15 (2015), pp. 3134–8. DOI: 10.1021/acs.nanolett.5b00189.
- [19] A. Czogalla, D. J. Kauert, H. G. Franquelim, V. Uzunova, Y. Zhang, R. Seidel, and P. Schwille. “Amphiphathic DNA Origami Nanoparticles to Scaffold and Deform Lipid Membrane Vesicles”. *Angewandte Chemie International Edition* 54 (2015), pp. 6501–5. DOI: 10.1002/anie.201501173.
- [20] J. L. Gornall, K. R. Mahendran, O. J. Pambos, L. J. Steinbock, O. Otto, C. Chimere, M. Winterhalter, and U. F. Keyser. “Simple reconstitution of protein pores in nano lipid bilayers.” *Nano Letters* 11.8 (2011), pp. 3334–40. DOI: 10.1021/nl201707d.
- [21] K. Göpfrich, C. V. Kulkarni, O. J. Pambos, and U. F. Keyser. “Lipid Nanobilayers to Host Biological Nanopores for DNA Translocations”. *Langmuir* 29.1 (2013), pp. 355–64. DOI: 10.1021/la3041506.
- [22] M. Mandelkern, J. G. Elias, D. Eden, and D. M. Crothers. “The dimensions of DNA in solution”. *Journal of Molecular Biology* 152.1 (1981), pp. 153–161. DOI: 10.1016/0022-2836(81)90099-1.

- [23] Y. Ke, S. M. Douglas, M. Liu, J. Sharma, A. Cheng, A. Leung, Y. Liu, W. M. Shih, and H. Yan. “Multilayer DNA Origami Packed on a Square Lattice”. *Journal of the American Chemical Society* 131.43 (2009), pp. 15903–8.
- [24] D. Schiffels, T. Liedl, and D. K. Fygenson. “Nanoscale Structure and Microscale Stiffness of DNA Nanotubes”. *ACS Nano* 7.8 (2013), pp. 6700–10.
- [25] X.-C. Bai, T. G. Martin, S. H. W. Scheres, and H. Dietz. “Cryo-EM structure of a 3D DNA-origami object.” *Proceedings of the National Academy of Sciences* 109.49 (2012), pp. 20012–7. DOI: 10.1073/pnas.1215713109.
- [26] J. Yoo and A. Aksimentiev. “Molecular Dynamics of Membrane-Spanning DNA Channels: Conductance Mechanism, Electro-Osmotic Transport, and Mechanical Gating”. *Journal of Physical Chemistry Letters* 6.23 (2015), pp. 4680–7. DOI: 10.1021/acs.jpcllett.5b01964.
- [27] L. D. Mosgaard and T. Heimburg. “Lipid ion channels and the role of proteins.” *Accounts of Chemical Research* 46.12 (2013), pp. 2966–76. DOI: 10.1021/ar4000604.
- [28] A. Petrov. “Flexoelectric model for active transport”. *Physical and Chemical Basis of Information Transfer*. 1975, pp. 111–25.
- [29] N. Sakai and S. Matile. “Synthetic Ion Channels.” *Langmuir* 29.29 (2013), pp. 9031–40. DOI: 10.1021/la400716c.

Chapter 7

DNA origami-based porins



Parts of this work previously appeared in:

K. Göpfrich, C.-Y. Li, M. Ricci, S. P. Bhamidimarri, J. Yoo, B. Gyenes, A. Ohmann, M. Winterhalter, A. Aksimentiev, U. F. Keyser. Large-conductance transmembrane porin made from DNA origami. *ACS Nano* **10**, 8207–8214 (2016).

Abstract In this chapter, we use DNA to build the largest synthetic pore in a lipid membrane to date. Our DNA origami porin approaches the dimensions of the nuclear pore complex, increasing the pore-area and the conductance tenfold compared to previous man-made channels. In our design, nineteen cholesterol tags anchor a megadalton funnel-shaped DNA origami construct in a lipid bilayer membrane. Confocal imaging and ionic current recordings reveal spontaneous insertion of the DNA porin into the lipid membrane, creating a transmembrane pore of tens of nanosiemens in conductance. All-atom molecular dynamics simulations characterise the conductance mechanism at the atomic level and independently confirm the DNA porin’s large ionic conductance.

7.1 Introduction

In the previous chapters, we presented DNA as readily available chemical block for building transmembrane pores, but their architectures have so far been limited to two basic pore types: a bundle of six DNA duplexes with a nominal inner channel diameter of 2 nm presented in Chapter 5, and a bundle of four duplexes with a 0.8 nm channel in Chapter 6. Reported open conductances of these DNA channels range from 0.4 nS to 1.6 nS. In this chapter, we expand the design space of synthetic lipid membrane pores beyond these limits by creating a significantly larger funnel-shaped DNA origami porin made exclusively from off-the-shelf components. Previously, funnel-shaped large-diameter DNA origami nanopores were inserted into SiN apertures [1], however insertion of large-diameter nanopores into lipid membranes has not been achieved until now.

The motivation for creating large synthetic channels from DNA is twofold: First of all, we want to determine if membrane anchoring of large DNA pores is feasible, as the energy barrier for insertion increases with the pore diameter. Secondly, chemical synthesis methods for the creation of artificial membrane pores traditionally limit the achievable pore sizes [2]. Therefore, the architectural variability of biological membrane proteins, spanning one order of magnitude in channel diameter and three orders of magnitude in molecular weight and conductance, remains widely unexplored. With DNA nanotechnology, where the creation of megadalton constructs is straightforward [3], we are in a good position to address this challenge. Porins with large diameters are highly desirable for nanopore sensing, as they would allow for the passage of large biomolecules like proteins in their native state [4]. At the same time, we aim to mimic the diversity of nature’s own

membrane components encompassing small ion channels as well as large porins. Only by achieving architectural diversity, protein channels in natural lipid membranes are capable of fulfilling a variety of functions in living cells, from the recognition of substrates to the selective transport of ions or large biomolecules between cellular compartments [5].

7.2 Materials and methods

Design of the cholesterol-tagged DNA origami porin. The funnel-shaped DNA origami was designed on a square lattice adapted from an earlier design [1] using the open source software caDNAno [6]. The funnel shape is composed of three segments. On the middle segment, 19 single-strands of DNA are extended to allow for later hybridisation with the cholesterol tags. The position of these overhangs was chosen to compromise between even distribution and minimal disruption of the design. The pathways of scaffold and staple strands are shown in Appendix A2. Custom DNA oligomers (for sequences see Appendix A3) were purchased from Integrated DNA Technologies and Biomers.

Molecular self-assembly. 10 nM of the M13mp18 scaffold (New England Biolabs) were mixed with 100 nM of the 179 staples and annealed for 23 h in 40 mM Tris-HCl, 45 mM boric acid, 1 mM EDTA, 14 mM MgCl₂, pH 8.2 using a protocol described previously [7].

Purification. Structures were purified from excess staples using spin-filtration with 100 kDa molecular weight cut-off (MWCO) filters (Amicon) in 40 mM Tris-HCl, 45 mM boric acid, 1 mM EDTA, 2 mM MgCl₂, pH 8.2. The MgCl₂ concentration was reduced to prevent sticking to the filter membrane and re-adjusted to 14 mM after filtration. This protocol yielded approximately 65 ng/μL assembled structures as determined by UV-vis spectroscopy (NanoDrop 2000, Fisher Scientific). The concentration was then adjusted to 10 nM.

Gel electrophoresis. 1% agarose gel electrophoresis of the DNA origami porin was carried out in 11 mM MgCl₂ buffered to pH 8.2 with 45 mM Tris-borate, 1 mM EDTA under running conditions of 60 V for 3 h. Bands were stained with GelRed (Cambridge Bioscience) and visualised using UV transilluminaton.

Attachment of cholesterol anchors. The cholesterol-modified strands (3' cholesterol-TEG from Integrated DNA Technologies, 5' cholesterol-C6 from Biomers, for sequences see Appendix A3) were heated to 50 °C for 10 min to dissolve aggregates and incubated with the DNA origami for 10 min at room temperature in 5× excess and 40 mM Tris-HCl, 45 mM boric acid, 1 mM EDTA, 14 mM MgCl₂ directly before each experiment.

Atomic force microscopy. 5 μL of the DNA origami porin (10 nM) in 10 mM Tris-HCl, 1 mM EDTA, 20 mM MgCl₂, pH 8.0 were deposited on a freshly cleaved mica surface (Agar Scientific) and incubated for 90 seconds. Subsequently, the surface was rinsed three times with 1 mL of ddH₂O (Merck Millipore) to remove ions and excess DNA porins and blow-dried with nitrogen. Imaging was carried out using a Cypher S AFM (Oxford Instruments) in amplitude modulation in air and at room temperature using AC240TS cantilevers (Olympus) with a nominal spring constant of 2 N/m. The set-point to free amplitude ratio was generally kept around 70 % with a free oscillation amplitude of 20 nm. The frequency of excitation was set close to the resonance of the first flexural mode (around 70 kHz) and a repulsive mode was preferred. The scan speed was set to either 1 or 2 Hz obtaining an image of 256 × 256 pixels. The images were flattened and band-pass filtered using Gwyddion.

Lipid vesicle preparation. DphPC (Avanti Polar Lipids), 10 % cholesterol (Sigma-Aldrich) GUVs were prepared via electroformation using the Vesicle Prep Pro unit (Nanion technologies, Germany) and the protocol described in Section 4.4.2.

Confocal fluorescent imaging. For confocal imaging, three staples on the wider end of the DNA origami porin were replaced by Cy3-tagged ones (Integrated DNA Technologies, see Appendix A2 and A3). Vesicles were suspended in 500 mM KCl, 10 mM MES, pH 6.0 in an incubation chamber (Grace Biolabs) and imaged using a Confocal Leica TCS SP5 microscope with a 60× oil immersion objective in bright field and fluorescence mode. While imaging, the fluorescently labelled DNA origami porins were added at a concentration of 1 nM keeping the osmolarity balanced. The Cy3 tag was excited at 514 nm using an argon laser and emission was collected above 530 nm. Images were processed using ImageJ.

Ionic current recordings. Ionic current recordings were carried out using solvent (n-decane, Alexis) containing DphPC (Avanti Polar Lipids) membranes [8] following the

detailed protocol by Gutsman *et al.* [9]. The experimental technique is described in Section 4.4. Current data was acquired at a sampling rate of 1 kHz using an Axopatch 200B amplifier and analysed in Matlab and Clampfit. After a stable membrane was formed, the DNA porin (in 40 mM Tris-HCl, 45 mM boric acid, 1 mM EDTA, 14 mM MgCl₂, pH 8.2) was added to the cis side at concentrations between 0.5 nM and 1.0 nM in 1 M KCl, 10 mM MES, pH 6.0. Additional ionic current recordings were carried out on the lipid nano bilayer setup [10] under the same buffer conditions using the protocol from Section 4.4.2.

MD simulations. MD simulations were carried out by C.-Y. Li and A. Aksimentiev, University of Illinois at Urbana-Champaign. The details of the simulation methods are described in the Appendix A4.

7.3 Results and discussion

7.3.1 Design, assembly and characterisation

The design of our DNA origami porin as schematically shown in Figure 7.1 derives from that of the very first DNA nanopore [1]. It has been modified significantly by introducing a double-layered middle section which can accommodate nineteen cholesterol anchors to facilitate insertion into a lipid membrane. The square-shaped 6 nm × 6 nm constriction gives rise to a nominal inner diameter of 6.8 nm, making it wider than large natural porins [11] and comparable to the electrical diameter of the nuclear pore complex [12]. The 5 MDa DNA origami porin was assembled using the 7249 base-long M13mp18 scaffold and 179 single-stranded DNA staples. For the DNA origami layout and the DNA sequences see Appendices A2 and A3. The “top-heavy” funnel shape allows for future positioning of multiple binding sites along the pore axis, which has to be the ultimate goal of the creation of large DNA origami membrane pores. Furthermore, by moving the cholesterol anchors up segment by segment, it may be possible to study different pore diameters using the same design. The large hydrophilic head can further help reduce aggregation.

Agarose gel electrophoresis shown in Figure 7.2 yields a distinct sharp band for the assembled DNA origami porin (Lane 3). Due to its tight packing, the over 7 kbp large origami structure migrates at the same speed as the linear 2 kbp DNA fragment of the ladder. The M13mp18 scaffold with half the molecular weight runs marginally slower

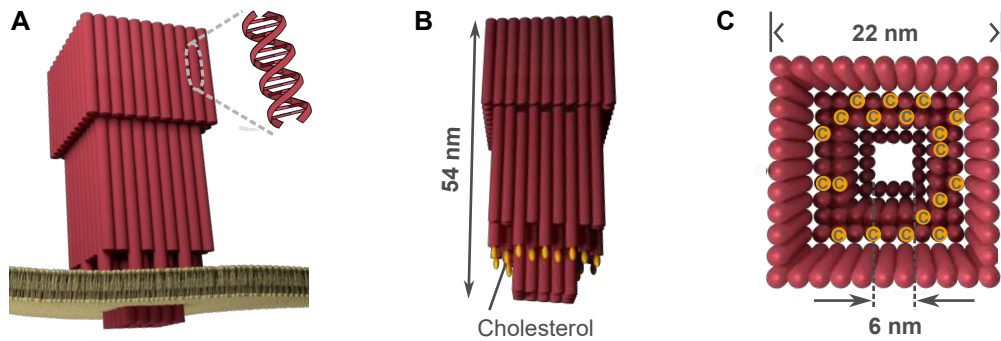


Figure 7.1: Design, shape and dimensions of the DNA origami porin. A) Envisioned positioning of the funnel-shaped DNA porin (red) in the lipid membrane (yellow), roughly drawn to scale. Each DNA duplex is represented as a red rod. B) Side view and C) top view and dimensions of the DNA porin with nineteen cholesterol tags (orange).

than the assembled DNA porin (Lane 2). Spin filtration proves to be an adequate method of purification from access staples (Lane 4), as the large cloud of access staples disappears in the gel. DNA porins that have been incubated in the measurement buffer migrate at the same speed as the original structure (Lane 5) confirming its structural integrity. The weaker slower migrating bands in Lanes 3-5 are likely to correspond to dimer formation. The possibility of dimer formation is intrinsic to the DNA origami folding process, as a staple can always bind to two scaffold strands and thereby interconnect them [13]. The dominating effect, however, are non-floppy ends at the narrow end of the DNA funnel, see Appendix A2, which can introduce end-to-end dimerisation via base-stacking interactions [14].

AFM measurements, presented in Figure 7.3, clearly resolve the funnel shape of the DNA origami porin, including its three segments with an average segment length of 20.8 ± 2.5 , 23.6 ± 2.1 and 11.0 ± 1.7 nm ($n = 10$) for the wide, the middle and the narrow sections of the porin structure, respectively, in good agreement with the designed dimensions (20, 24, 10 nm). Assuming geometrical packing and a helix 2 nm diameter [6], the designed segments have a width and height of 22×22 , 18×18 , 10×10 nm². The measured dimensions ($46.7 \pm 2.0 \times 2.67$, $35.8 \pm 2.0 \times 5.95$ and $18.9 \pm 2.0 \times 2.67$ nm²) show the collapse of the hollow funnel when imaged in air. Consequently, the middle segment of the funnel (which is made of two layers of DNA) is roughly twice as high as the other segments (which are made from a single DNA layer). Given the finite-size of the AFM tip (9 ± 2 nm nominal radius) and the anhydrated state of the DNA, the measured

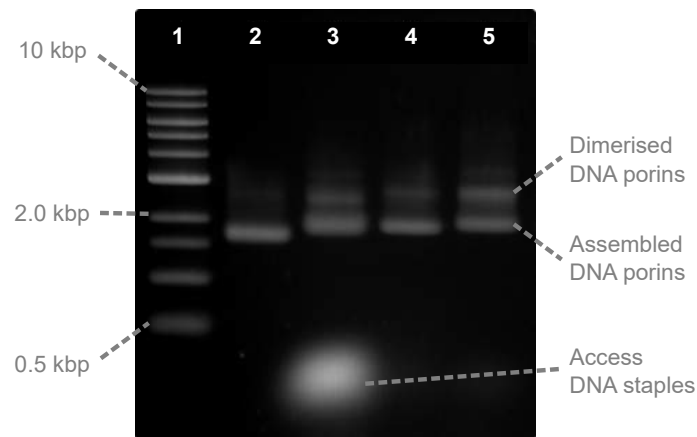


Figure 7.2: 1% agarose gel electrophoresis of the DNA origami porin. Lane 1: 1 kbp DNA ladder (New England Biolabs); Lane 2: 7249 base long M13mp18 single-stranded DNA scaffold (New England Biolabs); Lane 3: Assembled DNA origami porin before purification from access staples in 40 mM Tris-HCl, 45 mM boric acid, 1 mM EDTA, 14 mM MgCl₂, pH 8.2. The origami migrates marginally slower than the M13mp18 scaffold. The weaker slower migrating band is likely to correspond to dimer formation; Lane 4: Assembled DNA origami porin after purification by spin filtration with 100 kDa MWCO (Amicon) in 40 mM Tris-HCl, 45 mM boric acid, 1 mM EDTA, 14 mM MgCl₂, pH 8.2. Spin filtration proves to be an adequate method of purification from excess staples; Lane 5: Sample from Lane 4 after 20 h incubation in the measurement buffer (1 M KCl, 10 mM MES, pH 6.0) at room temperature.

dimensions only partially reflect the actual dimensions of the DNA origami in solution. The purpose of the AFM investigation was to ensure accurate folding, not to obtain precise and quantitative information on the dimensions of the structures. It should also be noted that the imaging was performed before the addition of cholesterol staples. The required excess of cholesterol staples would contaminate the background.

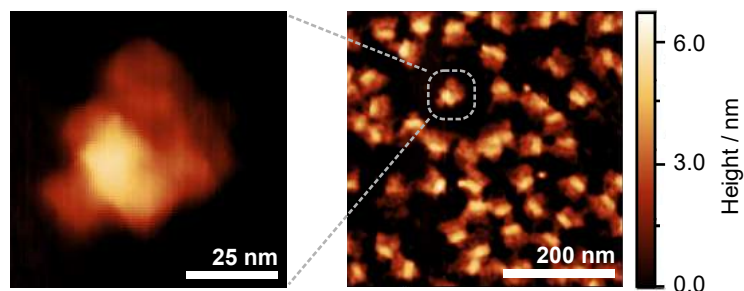


Figure 7.3: Zoom (left) and overview (right) AFM images confirming the correct assembly of the DNA origami porin. Since the structures were absorbed onto mica and imaged in air, the hollow funnel with its double-layered middle section is collapsed. AFM imaging was performed by M. Ricci.

7.3.2 Confocal fluorescent imaging

To probe effective attachment of the DNA origami porin to lipid membranes, we carried out confocal fluorescent imaging experiments. For this purpose, three Cy3-labelled fluorescent DNA oligomers were incorporated during assembly of the funnel-shaped DNA porin at its wider end. The same construct was prepared without the cholesterol membrane anchors as a negative control. After addition to GUVs, bright rings appeared around the vesicles in the confocal plane for the cholesterol-tagged sample, Figure 7.4A, whereas no membrane adhesion was observed for the control sample, Figure 7.4B. These observations confirm that also the large DNA origami construct can attach to lipid vesicles via its cholesterol anchors, but they do not allow for conclusions about successful membrane incorporation in the ion-conducting orientation.

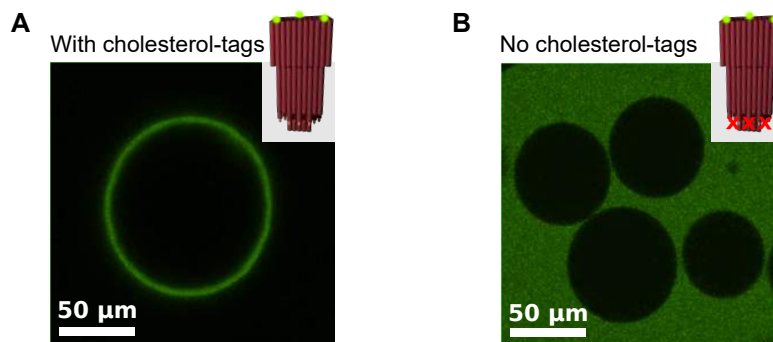


Figure 7.4: Fluorescent confocal images (excitation wavelength: 514 nm) of DphPC lipid vesicles after addition of the Cy3-labelled DNA origami porin, $c = 1$ nM, with A) 19 cholesterol tags and B) no hydrophobic tags (negative control).

7.3.3 Ionic current recordings

We subsequently carried out ionic current recordings in solvent-containing membranes [9] and on lipid nano bilayers to prove the membrane-insertion capabilities of the synthetic DNA porin and to determine its ionic conductance. As shown in Figure 7.5A, multiple insertion steps were observed repeatedly. Their high conductance in the range of tens of nanosiemens is striking. A stepwise decrease in conductance, see Figure 7.5B, could be caused by DNA porins escaping from the membrane. Such closures were repeatedly observed as a result of increasing the applied voltage. These results are remarkable, as it was previously unclear whether our membrane anchoring strategy for DNA pores would work for such large constructs. Figure 7.5C shows the rather broad histogram obtained from conductance steps. The mean conductance increase associated with a DNA porin insertion lies at 30 nS in 1 M KCl, 10 mM MES, pH 6.0. The wide spread of conductance values is likely to be caused by multiple factors. Previous MD simulations have suggested that the conductance of DNA pores can be influenced by membrane pressure [15]. Hence, a certain amount of variability is expected among experiments which involve breaking and reforming the membrane. Agarose gel electrophoresis, see Figure 7.2, showed a proportion of dimerised DNA origami porins ($\sim 15\%$), which could account for higher conductances if they are capable of inserting jointly. Deviations from perpendicular insertion orientation with respect to the lipid bilayer plane is likely to account for further variability.

Out of the 80 insertions shown in the histogram in Figure 7.5C, only six were stable

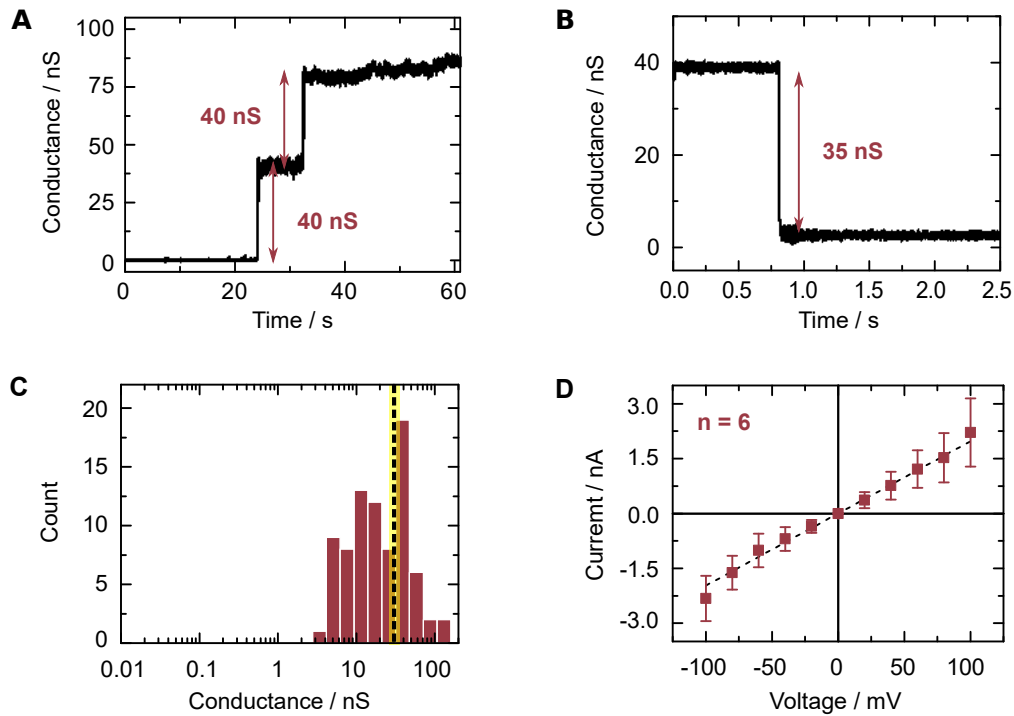


Figure 7.5: Ionic current recordings of the DNA origami porin in 1 M KCl, 10 mM MES, pH 6.0. A) Exemplary current traces showing two consecutive insertions, recorded at 10 mV, and B) a closure step, recorded at 20 mV. C) Histogram of conductance steps with logarithmic binning including stable insertions, closures as well as insertion attempts. The dashed line at 30 nS represents the mean of the histogram. D) I - V characteristics of stable insertions of the DNA porin. Error bars correspond to the standard deviation of six independent recordings. The dashed line represents a linear fit.

across the voltage range of ± 100 mV and for the duration of the I - V recording. To determine the I - V characteristics presented in Figure 7.5D, only this subset of stable insertions was taken into account. Their I - V curves were found to be largely ohmic with a gradient of 20 nS. This could indicate that porins with a conductance of around 20 nS are particularly stable and less prone to closures. It should be noted, however, that it was mainly the voltage-switching that destabilised the pores. If one keeps a constant voltage below 50 mV, the number of stable DNA porins is much higher. Deviations from the linear I - V behaviour are often observed above ± 50 mV: The DNA origami porins switch to lower conductance states or disappear entirely as the voltage is increased, in line with previous observations for smaller DNA-based membrane pores [16, 17]. Rarely, the conductance increases at higher voltages, see Figure 7.6B, while the current exhibits large fluctuations. Pores with high noise levels occur across the observed conductance range.

Although some insertions could be stable for tens of minutes as in the presented I - V traces in Figure 7.6A and B, transient insertions or attempts, see Figure 7.7A, prevail in ionic current recordings and contribute to the width of the reported conductance histogram. On the lipid nano bilayer setup, insertions could optionally be triggered by applying a short 1 V pulse, see Figure 7.7B. While the bilayer often breaks as a result of the voltage pulse, defect formation via electroporation could facilitate insertion of the DNA porin. High voltage pulses immediately break the large-diameter solvent-containing membranes, which is why this method can only be employed on the lipid nano bilayer setup with its much smaller membrane area (200 nm diameter).

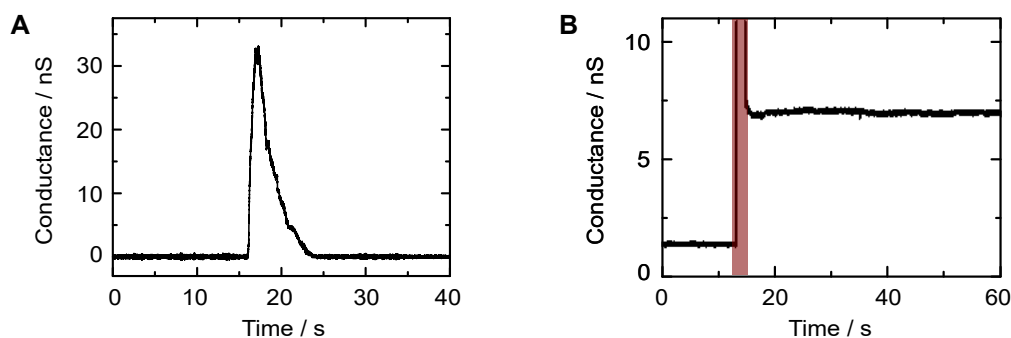


Figure 7.7: A) Transient insertions of this characteristic pattern were observed repeatedly in the presence of the DNA origami porins, recorded at 50 mV. B) Insertion triggered by a short voltage pulse (1 V) on the lipid nano bilayer setup, recorded at 100 mV.

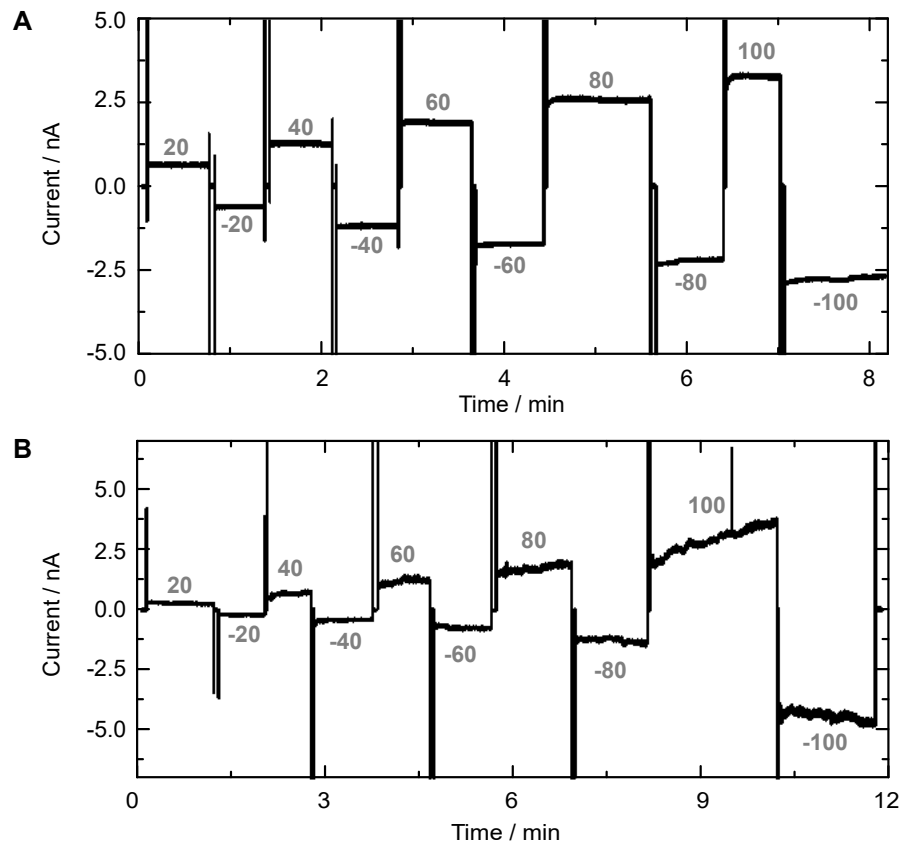


Figure 7.6: Example I - V traces of DNA porins which remain inserted for minutes, recorded after a clear insertion step was observed. A) Lower-noise DNA porin with a conductance of approximately 30 nS. B) DNA porin with increasing noise and conductance at higher voltage. Traces are recorded at 1 kHz, grey numbers indicate the applied voltage in mV.

7.3.4 Molecular dynamics simulations

To independently evaluate the ionic conductance of our synthetic DNA-based porin, we collaborated with C.-Y. Li and A. Aksimentiev to build an all-atom model including all components of the experimental system: the DNA origami porin itself, the DphPC lipid bilayer, ions and water molecules, Figure 7.8A, resulting in a system of 7,963,516 atoms. In the first 48 ns of the equilibration simulation, the DNA porin was restrained to its initial coordinates allowing the membrane and the solvent to adopt an equilibrium configuration. The restraints were gradually removed over 14.4 ns. The system was subsequently simulated in the absence of restraints for another 19.2 ns. During the equilibration simulation, lipid molecules rearranged around the transmembrane part of the DNA porin, forming a water-filled passage along the DNA porins' outer surface, Figure 7.8B. Approximately 900 water molecules, or 50 per 180 degree segment of each DNA duplex, surrounded the DNA porin within a 1 nm thick rectangular slab centred at the middle plane of the membrane. The interior volume of the channel was filled with solution as well. This gives rise to an effective electrical diameter of approximately 11 nm for the DNA porin, making it larger than the electrical diameter proposed for the nuclear pore complex (6 nm [12]).

To evaluate its ionic conductance, the DNA porin was simulated at +100 mV, +30 mV, -30 mV and -100 mV transmembrane biases, reproducing the experimental voltage range. The duration of each MD simulation was 19.2 ns at ± 100 mV and 48 ns at ± 30 mV which was sufficient to observe statistically significant displacement of ions within the MD trajectories [15, 18, 19].

A movie illustrating the MD trajectory of the system was appended to our publication [20]. From this movie, one can appreciate that a fraction of the ionic current is passing through gaps between the outside channel wall and the lipid membrane. Figure 7.8C-E shows the cross sections of the local densities of DNA (C), ions (D) and water molecules (E). The points with the highest density of DNA mark the positions of the 16 transmembrane DNA helices (each marked with a cross). The shape of the cross section of the DNA porin deviates from the designed square, highlighting that the DNA pore is not rigid. It can be deformed due to structural strains and buckling as well as due to the pressure exerted by the surrounding lipid molecules. The density of ions (B) and water molecules (C) peaks inside the channel. Nevertheless, a considerable fraction of both is passing on the outside of the DNA porin. Around 80% of ions flow through the central pore, while ion flow along the outside of the channel contributes 20% to the total conductance. The fact that a significant proportion of ions were also flowing through

gaps at the DNA-lipid interface prompted us to ask whether a single DNA duplex could induce transmembrane currents. The results of this experimental investigation will be presented in Chapter 8.

Figure 7.9A shows the histogram of the conductance obtained from the cumulative charge transmitted across the lipid bilayer over time. Its mean lies at 46.6 nS. Taking into account the systematic overestimation of the bulk conductivity of KCl solution in the MD simulation (16 S/m instead of 11 S/m [15]), the simulated conductance of 32 nS agrees almost exactly with the mean conductance from the experimentally obtained conductance histogram (30 nS). Although the width of the simulated conductance histogram is similar to that obtained from our experiments, the time scale of the MD simulation precludes us from making a definitive statement about the possible origin of broad conductance histograms. At the time scale of 50 ns, a considerable fraction of the ionic current noise is produced by thermal fluctuations [21]. Another factor is the deformation of the funnel structure and fluctuations of the toroidal lipid pore, which can be appreciated from the appended movie [20]. 32% of the experimentally recorded insertions steps fall outside the conductance range obtained from MD simulations. Assuming that the simulated range is correct, this could represent the fraction of pores that inserted in an orientation different from that considered in MD simulations. In absolute numbers, 23 of the experimentally obtained insertion steps had lower conductances, potentially due to angled insertion. Only three exhibited higher conductances, which could be attributed to the insertion of dimers. The I - V curve obtained from simulations, Figure 7.9B, is ohmic-like for the subset of stable insertions in the experiments. The linear fit yields an average conductance of 46.6 nS, in agreement with the simulated conductance histogram. Unlike in the experiments, the pores do not close or pop out of the membrane as a result of increasing voltage. This is likely to be due to the much shorter timescale of the MD simulation.

For reference, the Hille equation from Section 4.3.2 estimates the conductance of the DNA porin as 12 nS. While the order of magnitude is still correct, it is not surprising that the equation underestimates the conductance. It only takes conductance through the central channel of the DNA funnel into account ignoring the ion pathway at the DNA-lipid interface and the permeability of the pore walls. The MD simulation give a better prediction of the experimentally obtained conductance values.

Despite the clear experimental evidence, it may seem surprising that it is possible to anchor a construct as large as our DNA porin in the lipid membrane. To assess whether the insertion of the DNA porin is plausible despite its large diameter, let's consider the coarse grained model from Section 4.3.1. It is important to consider the radius of the

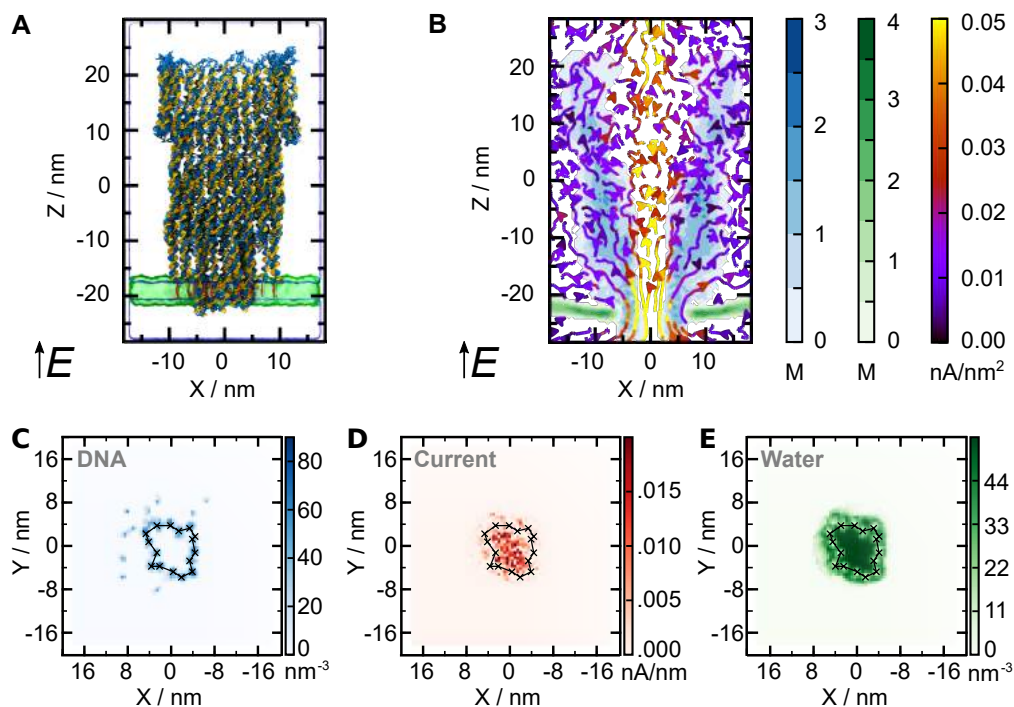


Figure 7.8: MD simulations of the DNA origami porin inserted into a DphPC lipid bilayer. A) All-atom model of the DNA porin (blue and yellow) with cholesterol tags (red) embedded in a lipid membrane (green) prior to the equilibration simulation. Total system size: 7,963,516 atoms. Electric field E in direction of positive transmembrane bias as indicated. B) Steady-state local densities of lipid tails (carbon atoms, green colour scale), DNA (phosphorus atoms, blue scale) and ionic current (streamlines, purple-red-yellow scale). The arrows indicate the direction of the local ionic current flux and the colour indicates the flux' magnitude. The maps were computed from 19.2 ns long MD trajectories at a +100 mV bias sampled with a frequency of 240 ps, radially averaged about the z -axis to improve the resolution. C-E) Cross sections of panel B across the lipid plane showing the local density of C) DNA, D) ionic current and E) water molecules. The data was averaged between $-24 \text{ nm} < Z < -21.5 \text{ nm}$ (corresponding to the height of the lipid bilayer, see B). The 16 cross marks indicate the positions of the highest DNA density, corresponding to the positions of the 16 membrane-piercing DNA duplexes of the narrow segment of the funnel-shaped DNA porin. Simulations were carried out by C.-Y. Li and A. Aksimentiev, University of Illinois at Urbana-Champaign.

hole in the lipid membrane (5.5 nm), not the nominal inner radius of the DNA porin (3.3 nm) as the pore radius R_P . With 19 cholesterol anchors, we obtain

$$W_P(5.5 \text{ nm}) + 19\Delta F_{\text{Chol}} \approx -400 \text{ kJ/mol}, \quad (7.1)$$

meaning a net energy gain for the membrane insertion of the DNA origami porin. Our experimental results seem plausible according to this coarse grained model. In the MD simulation, the DNA porin was initially placed into the membrane in the envisioned position. Conclusions regarding the insertion process, its energy cost and probability can therefore unfortunately not be drawn. From the appended MD movie [20], one can appreciate that the porin does not attempt to escape the membrane for the duration of the MD simulation. On the contrary, the system seems to be equilibrated with fluctuations reaching a constant level over time.

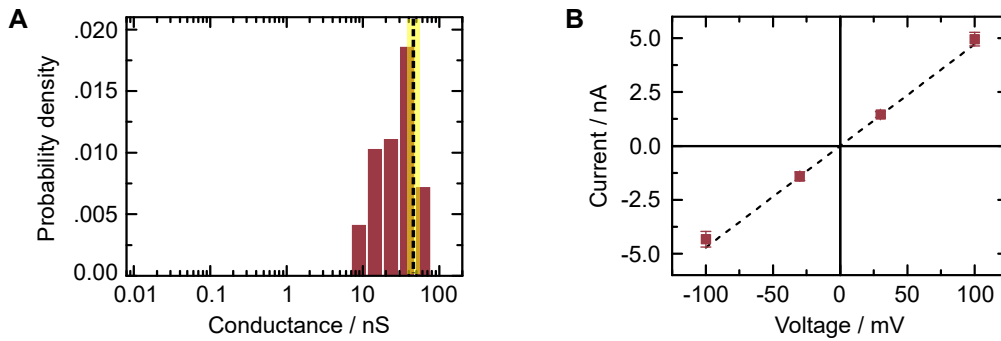


Figure 7.9: MD simulations of the cumulative charge transmitted across the lipid bilayer. A) All-point conductance histograms with logarithmic binning. The conductance histograms were computed using block averaged instantaneous currents at +100, +30, -30, and -100 mV transmembrane biases; the block average size was 2.88 ns. The dashed line indicates the mean conductance value (46.6 nS). B) I - V characteristics. The data is block averaged with a block size of 2.88 ns. Error bars indicate the standard error of the mean, the dashed line represents a linear fit. MD simulations were carried out by C.-Y. Li and A. Aksimentiev, University of Illinois at Urbana-Champaign.

7.4 Conclusion

In the present study, we have demonstrated a synthetic DNA membrane porin with the largest conductance known to date. Electrophysiological experiments and MD simulations have shown that the conductance of our DNA origami porin is over one order of magnitude larger compared to all previous DNA membrane pores. In nature, such high conductances are rare and have only been measured for few toxins [22, 23] or suggested for the nuclear pore complex. Our work demonstrates that cholesterol-based membrane anchoring is a viable method for creating larger DNA pores with diameters of several nanometres. The excellent quantitative agreement between experiments and MD simulations is promising for the future development of DNA-based membrane pores.

The choice of an appropriate nanopore architecture will ultimately depend on the target application. Large scaffold-based DNA nanopores like our DNA origami porin are ideally suited for functionalisation and can provide space for the passage of larger biomolecules. Such DNA pores are prime candidates for single-molecule sensing or as a research tool to study transport at the molecular level if the insertion stability can be increased further. Strategies to achieve this include the use of additional hydrophobic tags, cationic lipids or positively charged groove binders like tetrabutylammonium. For the field of nanopore sensing, it would be highly desirable to have a large diameter membrane pore matching the longevity of α -hemolysin. Since such pores are rare in nature, it makes sense to continue developing synthetic analogues. In biological environments, our synthetic DNA porins could mimic the behaviour of toxins. By creating an unspecific large-diameter membrane defect, it would disturb the tightly regulated cellular homeostasis. By positioning binding sites along the pore axis, it should eventually be possible to achieve complex function inspired by systems like the nuclear pore complex.

With our DNA origami porin expanding the design space of synthetic membrane pores, we envision custom-made pores to become a versatile toolbox for cross-disciplinary applications. From a methodological point of view, we showcase the potential of MD simulations for the design of future DNA pores. The results from this combined study, revealing a conductance pathway at the DNA-lipid interface, inspired us to employ a single membrane-spanning DNA duplex to induce transmembrane currents. The results will be presented in the following chapter.

Bibliography

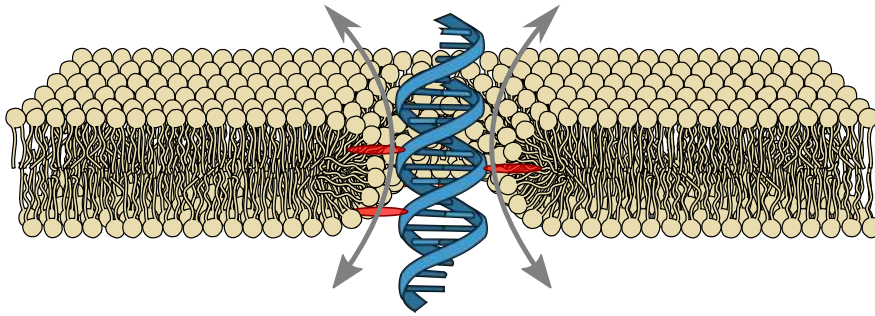
- [1] N. A. W. Bell, C. R. Engst, M. Ablay, G. Divitini, C. Ducati, T. Liedl, and U. F. Keyser. “DNA origami nanopores.” *Nano Letters* 12.1 (**2012**), pp. 512–7. DOI: 10.1021/nl204098n.
- [2] N. Sakai and S. Matile. “Synthetic Ion Channels.” *Langmuir* 29.29 (**2013**), pp. 9031–40. DOI: 10.1021/la400716c.
- [3] P. W. K. Rothmund. “Folding DNA to create nanoscale shapes and patterns.” *Nature* 440.7082 (**2006**), pp. 297–302.
- [4] U. F. Keyser. “Controlling molecular transport through nanopores.” *Journal of the Royal Society* 8.63 (**2011**), pp. 1369–78. DOI: 10.1098/rsif.2011.0222.
- [5] B. Alberts, A. Johnson, J. Lewis, M. Raff, K. Roberts, and P. Walter. *Molecular Biology of the Cell*. **2002**.
- [6] S. M. Douglas, H. Dietz, T. Liedl, B. Högberg, F. Graf, and W. M. Shih. “Self-assembly of DNA into nanoscale three-dimensional shapes.” *Nature* 459.7245 (**2009**), pp. 414–8.
- [7] S. Hernández-Ainsa, N. A. W. Bell, V. V. Thacker, K. Göpfrich, K. Misiunas, M. E. Fuentes-Perez, F. Moreno-Herrero, and U. F. Keyser. “DNA origami nanopores for controlling DNA translocation.” *ACS Nano* 7.7 (**2013**), pp. 6024–30. DOI: 10.1021/nm401759r.
- [8] P. Mueller, D. O. Rudin, H. T. Tien, and W. C. Wescott. “Reconstitution of cell membrane structure in vitro and its transformation into an excitable system.” *Nature* 194 (**1962**), pp. 979–80. DOI: 10.1038/194979a0.
- [9] T. Gutsmann, T. Heimburg, U. Keyser, K. R. Mahendran, and M. Winterhalter. “Protein reconstitution into freestanding planar lipid membranes for electrophysiological characterization.” *Nature Protocols* 10.1 (**2015**), pp. 188–98. DOI: 10.1038/nprot.2015.003.
- [10] K. Göpfrich, C. V. Kulkarni, O. J. Pambos, and U. F. Keyser. “Lipid Nanobilayers to Host Biological Nanopores for DNA Translocations”. *Langmuir* 29.1 (**2013**), pp. 355–64. DOI: 10.1021/la3041506.
- [11] R. Benz. “Biophysical properties of porin pores from mitochondrial outer membrane of eukaryotic cells”. *Experientia* 46.2 (**1990**), pp. 131–7.
- [12] M. Mazzanti, J. O. Bustamante, and H. Oberleithner. “Electrical dimension of the nuclear envelope.” *Physiological Reviews* 81.1 (**2001**), pp. 1–19.

-
- [13] K. E. Dunn, F. Dannenberg, T. E. Ouldridge, M. Kwiatkowska, A. J. Turberfield, and J. Bath. “Guiding the folding pathway of DNA origami”. *Nature* 525 (2015), pp. 82–6. DOI: 10.1038/nature14860.
- [14] F. Kilchherr, C. Wachauf, B. Pelz, M. Rief, M. H. Zacharias, and H. Dietz. “Single-molecule dissection of stacking forces in DNA”. *Science* 353.6304 (2016), aaf5508. DOI: 10.1126/science.aaf5508. arXiv: arXiv:1011.1669v3.
- [15] J. Yoo and A. Aksimentiev. “Molecular Dynamics of Membrane-Spanning DNA Channels: Conductance Mechanism, Electro-Osmotic Transport, and Mechanical Gating”. *Journal of Physical Chemistry Letters* 6.23 (2015), pp. 4680–7. DOI: 10.1021/acs.jpcllett.5b01964.
- [16] A. Seifert, K. Göpfrich, J. R. Burns, N. Fertig, U. F. Keyser, and S. Howorka. “Bilayer-Spanning DNA Nanopores with Voltage-Switching between Open and Closed State.” *ACS Nano* 9.2 (2014), pp. 1117–26. DOI: 10.1021/nm5039433.
- [17] K. Göpfrich, T. Zettl, A. E. C. Meijering, S. Hernández-Ainsa, S. Kocabey, T. Liedl, and U. F. Keyser. “DNA-tile structures lead to ionic currents through lipid membranes”. *Nano Letters* 15.5 (2015), pp. 3134–8. DOI: 10.1021/acs.nanolett.5b00189.
- [18] A. Aksimentiev. “Deciphering ionic current signatures of DNA transport through a nanopore”. *Nanoscale* 2 (2010), pp. 468–83.
- [19] C. Y. Li, E. A. Hemmig, J. Kong, J. Yoo, U. F. Keyser, and A. Aksimentiev. “Ionic Conductivity , Structural Deformation and Programmable Anisotropy of DNA Origami in Electric Field”. *ACS Nano* 9.2 (2015), pp. 1420–33.
- [20] K. Göpfrich, C.-Y. Li, M. Ricci, S. P. Bhamidimarri, J. Yoo, B. Gyenes, A. Ohmann, M. Winterhalter, A. Aksimentiev, and U. F. Keyser. “Large-Conductance Transmembrane Porin Made from DNA Origami”. *ACS Nano* 10.9 (2016), pp. 8207–14. DOI: 10.1021/acsnano.6b03759.
- [21] S. Bhattacharya, J. Yoo, and A. Aksimentiev. “Water Mediates Recognition of DNA Sequence via Ionic Current Blockade in a Biological Nanopore”. *ACS Nano* 10 (2016), pp. 4644–51. DOI: 10.1021/acsnano.6b00940.
- [22] T. M. Haug, S. L. Sand, O. Sand, D. Phung, P. E. Granum, and S. P. Hardy. “Formation of very large conductance channels by *Bacillus cereus* Nhe in Vero and GH(4) cells identifies NheA + B as the inherent pore-forming structure”. *The Journal of Membrane Biology* 237.1 (2010), pp. 1–11. DOI: 10.1007/s00232-010-9298-6.

- [23] P. Meera, M. Wallner, and L. Toro. “A neuronal beta subunit (KCNMB4) makes the large conductance, voltage- and Ca²⁺-activated K⁺ channel resistant to charybdotoxin and iberiotoxin.” *Proceedings of the National Academy of Sciences* 97.10 (2000), pp. 5562–7. DOI: 10.1073/pnas.100118597.

Chapter 8

DNA-lipid channels



Parts of this work previously appeared in:

K. Göpfrich, C.-Y. Li, I. Mames, S. P. Bhamidimarri, M. Ricci, J. Yoo, A. Mames, A. Ohmann, M. Winterhalter, E. Stulz, A. Aksimentiev, U. F. Keyser, Ion channels made from a single membrane-spanning DNA duplex. *Nano Letters* 16, 4665-4669 (2016).

Abstract In this chapter, we present an integral membrane-spanning DNA duplex that induces the formation of DNA-lipid channels despite the lack of a physical pore. Decorated with six porphyrin tags, our duplex is designed to span the lipid bilayer. Combining electrophysiology measurements with all-atom MD simulations, we demonstrate that this construct induces ion conduction across lipid membranes. Ions flow at the DNA-lipid interface as the lipid head groups tilt towards the amphiphilic duplex forming a toroidal pore filled with water and ions. Ionic current traces produced by the DNA-lipid channel show well-defined insertion steps, closures and gating similar to those observed for traditional protein channels or synthetic pores. Ionic conductances obtained through simulations and experiments are in excellent quantitative agreement. With the smallest possible DNA-based ion channel, we elucidate the general microscopic conductance pathway of DNA pores and offer a route to design a new class of synthetic ion channels with maximum simplicity.

8.1 Introduction

In the previous chapters, we used DNA as a building block for synthetic transmembrane pores with tunable pore diameters. We started with a 2 nm wide prototype pore in Chapter 5, presented a structure with a sub-nanometre channel in Chapter 6, and finally built a large DNA origami porin with a 6 nm diameter in Chapter 7. In this chapter, we now present a radically different design: an integral membrane-spanning DNA duplex that lacks a central channel. For the past decades, ion channels have generally been conceived as hollow transmembrane proteins opening up a passage for ions within the channel lumen. This conductance mechanism is supported by crystal structures of channels like the potassium channel [1]. Yet another important class of transmembrane proteins, including single-pass α -helical proteins [2, 3] or G-protein coupled receptors [4, 5], lack such a physical channel. These integral proteins rely on extracellular signalling molecules to cause an intracellular response without exchanging ions or substrates between cellular compartments.

Here, we demonstrate a synthetic membrane-spanning construct that provides a direct ion pathway across the lipid membrane despite the lack of an internal physical channel. The idea for this study derived from MD simulations of the DNA origami porin presented in Chapter 7. These simulations have shown that while ions are transported through

the central channel lumen, it appears that a fraction of the current flows through gaps at the DNA-lipid interface. A similar interface should exist at the circumference of a single membrane-spanning DNA duplex. The challenge is thus to design a DNA duplex, which will actually span the lipid membrane and hence form a stable DNA-lipid channel (DLC).

8.2 Materials and methods

Design of the duplex. The design, synthesis and purification of the porphyrin DNA was carried out in collaboration with I. Mames and E. Stulz, University of Southampton. Two partially complementary 25-mers of single-stranded DNA contain three porphyrins each. The porphyrins form a stacked array upon hybridisation of the DNA [6]. In the assembled duplex, an eight nucleotide long single-stranded overhang persists on either side. These overhangs, which are located outside the bilayer, could help to orient the duplex in an orthogonal manner to the membrane. They may further be used as additional anchors. The DNA sequences of the porphyrin-tagged duplex are shown in Figure 8.1B.

Synthesis of the porphyrin monomers. The modified monomers were obtained according to procedures described previously [6]. Following this protocol, the porphyrins were transformed into the DMT-protected nucleosides. The first porphyrin with the rigid acetylene linker, labelled “1” in Figure 8.1B, was obtained via Sonogashira coupling [6]. The second porphyrin containing a flexible linker, labelled “2” in Figure 8.1B, was produced by coupling the monocarboxylic acid-functionalised porphyrin with the propargylamine derivative of 5-iodo-2'-deoxyuridine. The building blocks were phosphorylated and used immediately in solid phase DNA synthesis.

Synthesis and purification of the porphyrin oligonucleotides. The porphyrin oligonucleotides were synthesised using an Applied Biosystem Expedite synthesiser on solid phase support (SPS; Glen Research, pore size: 100 nm) on a 1.0 μ mol scale, using standard phosphoramidite chemistry. The unmodified nucleotides and reagents were obtained from Cambio or Tides Service Technology. For the porphyrin nucleosides, an extended coupling time of 6 min was used. Optionally, the DNA was additionally functionalised with a biotin at the 5' end using standard procedures for future modification. The purification of modified DNA was carried out by RP-HPLC using a Waters

XBridge OST C18, 2.5 μm 4.6 \times 55 mm² column; flow rates were set to 1 mL/min. The concentration of the DNA was determined from the optical absorbance at 260 nm by UV spectroscopy [7]. For some experiments, the DNA oligomers were treated with tetra butyl ammonium (Sigma Aldrich).

AFM imaging. AFM imaging was performed in air by absorbing 5 μL of the duplex suspended at a concentration of 5 μM in 10 mM Tris-HCl, 1 mM EDTA, 20 mM MgCl₂, pH 8.0 onto a freshly cleaved mica surface using the same procedure as described in Section 7.2.

Lipid vesicle preparation and confocal fluorescent imaging. Lipid vesicles were prepared as before in Section 7.2. For confocal imaging, we took advantage of the fluorescent properties of porphyrin itself. We prepared a porphyrin-free duplex, which carried two Cy3 tags (Integrated DNA Technologies) at its 3' ends instead for control experiments. Vesicles were suspended in 500 mM KCl, 10 mM MES, pH 6.0 in an incubation chamber (Grace Biolabs) and imaged using a Confocal Leica TCS SP5 microscope with a 60 \times oil immersion objective in bright field and fluorescence mode. While imaging, the duplex was added at a concentration of 5 nM. Porphyrin and Cy3 were excited at 514 nm using an argon laser and emission was collected above 530 nm. Images were processed using ImageJ.

Ionic current recordings. Ionic current recordings were carried out using solvent (n-decane, Alexis) containing DphPC membranes (Avanti Polar Lipids) following the detailed protocol by Gutschmann *et al.* [8, 9]. Three different samples were tested: (i) The porphyrin-tagged DNA duplex, (ii) the same DNA duplex with a cholesterol tag on one 3' end and (iii) the same DNA duplex with cholesterol-tags on both 3' ends. After a stable membrane was formed, the duplex was added to the cis side at concentrations between 1 and 3 nM in 1 M KCl, 10 mM MES, pH 6.0. Current data was acquired at a sampling rate of 1 kHz using an Axopatch 200B amplifier and analysed in Matlab and Clampfit.

MD simulations. MD simulations were carried out by C.-Y. Li and A. Aksimentiev, University of Illinois at Urbana-Champaign following the method described for the large DNA origami porin. For a detailed description of the MD methods see Appendix A4.

8.3 Results and discussion

8.3.1 Design and characterisation

With their hydrophobic transmembrane domains, proteins are generally believed to traverse the membrane by displacing lipids rather than reorganising the bilayer structure [10]. To favour a conformation where the two lipid bilayer leaflets form a toroidal pore with a DNA duplex at the centre, we positioned hydrophobic porphyrin tags on the

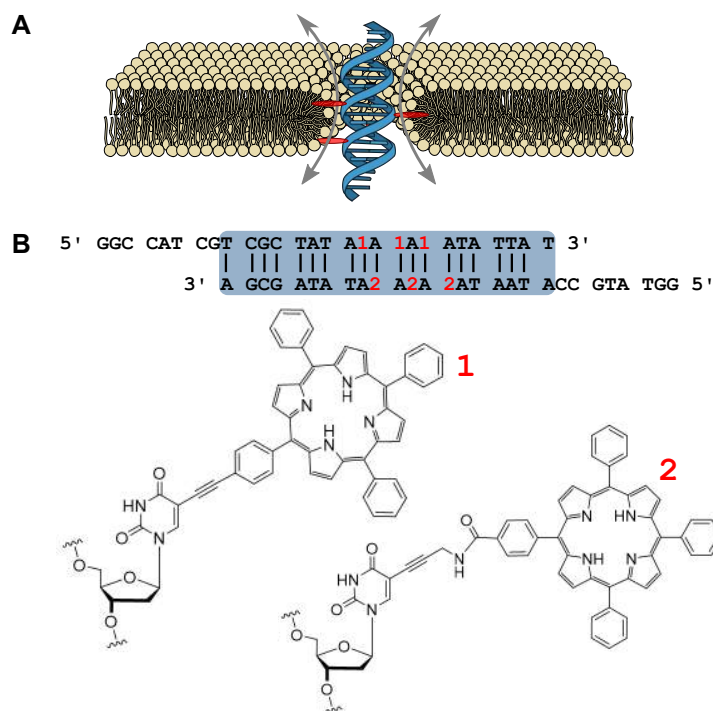


Figure 8.1: Design, shape and dimensions of the membrane-spanning DNA duplex.

A) Envisioned placement and conductance mechanism of the DNA duplex (blue) decorated with six porphyrin membrane anchors (red, only three are shown in the cross section) causing the formation of a toroidal lipid pore (yellow). The sketch is roughly drawn to scale. B) DNA sequence of the duplex. The locations of the porphyrin tags within the sequence are indicated in red. The bottom row shows the chemical structures of the tags labelled as “1” (with acetylene linker) and “2” (with amide linker) according to the target strand. The porphyrin-tagged DNA was synthesised by I. Mames and E. Stulz, University of Southampton.

duplex in such a way that their insertion into the lipid membrane is only possible when the charged duplex is penetrating the membrane. If the hydrophobic bilayer interior is in contact with the charged structure, this could cause reorganisation of the bilayer leaflet giving rise to a toroidal pore as illustrated in Figure 8.1A.

We chose a 19 base pair long duplex with six hydrophobic porphyrins attached to thymidine bases in a manner that they protrude the duplex and act as membrane anchors. The chemical structure of the porphyrin tags and the DNA sequence of the duplex are shown in Figure 8.1B [6, 7]. The porphyrins were attached to both complementary strands to form a zipper-like stable arrangement [11]. Eight bases of single-stranded DNA extensions were incorporated to protrude from the membrane on either end of the duplex. To highlight possibilities for future customisation, these “extramembranous domains” could serve for the attachment of complementary single-stranded DNA or signalling molecules. These design features were inspired by bitopic proteins which have a single transmembrane α -helix composed of around 20 amino acid molecules that connect two extra-membranous domains [2, 12].

With a molecular weight below 20 kDa, our duplex is almost an order of magnitude lighter than the four- (Chapter 6) and six-helix bundle (Chapter 5) and 250 times lighter than the DNA porin (Chapter 7). Despite its short length of only 6 nm, we were able to image the duplex using AFM as shown in Figure 8.2. Image analysis ($n = 33$) gave a length of 4.5 ± 0.1 nm and a width of 2.3 ± 0.02 nm. The apparent height of 0.8 ± 0.2 nm agrees well with literature values for a DNA duplex imaged in air [13]. It is reduced compared to the hydrated diameter of DNA, likely because the DNA is immersed in a salt layer [13].

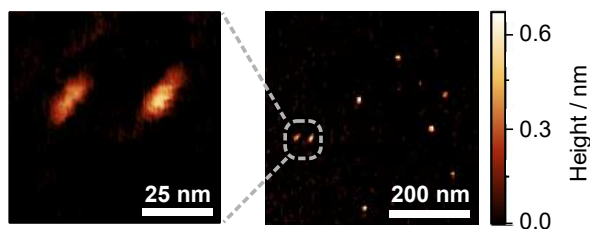


Figure 8.2: Zoom (left) and overview (right) AFM images of the duplex structures absorbed onto mica and imaged in air. AFM imaging was carried out by M. Ricci.

8.3.2 Confocal fluorescent imaging

To confirm the interaction of the porphyrin-tagged duplexes with lipid membranes, we demonstrated their binding to GUVs by confocal fluorescent imaging. For this purpose, we took advantage of the fluorescence of porphyrin itself [14]. After addition of the duplexes, bright rings appeared around the vesicles in the confocal plane as shown in Figure 8.3A, indicating their adhesion to the membranes. As a negative control, we prepared a duplex without porphyrin tags but with fluorescent Cy3 tags on both 3' ends. As expected from previous results with other DNA pores, the GUVs in Figure 8.3B appeared dark.

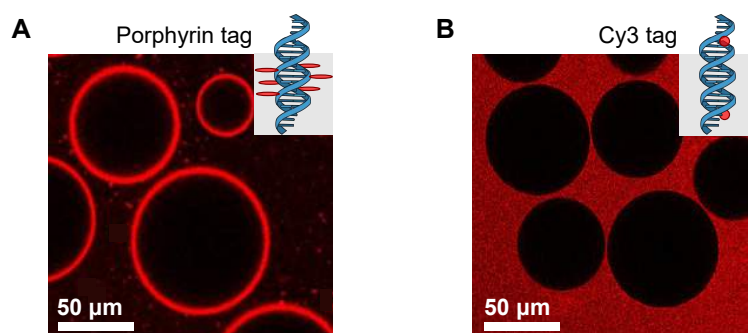


Figure 8.3: Fluorescent confocal images (excitation wavelength: 514 nm) of DphPC lipid vesicles after addition of A) the porphyrin-tagged duplexes, $c = 5$ nM and B) duplexes with two Cy3 tags but no porphyrin tags, $c = 5$ nM (negative control).

8.3.3 Ionic current recordings

To test whether the duplex is capable of inducing a passage for ions across the lipid membrane despite the lack of a physical pore, we carried out ionic current recordings in solvent containing membranes, see Section 4.4.3. As shown in Figure 8.4A, a stepwise increase in conductance (insertions steps) was observed in the presence of the duplex. Closure steps, as presented in Figure 8.4B, where the membrane returns to its native conductance, are often observed as a result of increasing the applied voltage. While the induced transmembrane current could be stable for hours, we also observed transient insertions and fluctuations between distinct conductance values. Figure 8.4C shows a representative trace reminiscent of gating observed for natural ion channels and for

DNA pores in previous chapters. It seems conceivable that the gating is produced by the single-stranded DNA overhangs of the duplex. They may be fluctuating in the electric field while stochastically blocking the conductance pathway. Alternatively, the gating could be produced by the repositioning of the duplex with respect to the membrane or by microscopic rearrangements of the lipid molecules themselves. The fact that the gating does not always occur is indicative of the inherent variability of the DLC formation.

Figure 8.4D presents a histogram obtained from conductance steps. The Gaussian fit of this histogram peaks at a conductance of 80 pS, the mean conductance is 120 pS. The rather broad distribution of conductances is likely to be caused by multiple factors. The orientation of insertion and the microscopic arrangement at the DNA-lipid interface might be variable. Bilayer thickness and tension changes with every new membrane and can potentially be influenced by duplexes that have been absorbed onto the membrane without penetrating it. Completely uniform conductances cannot be expected at sub-nanometre length scales. To obtain the I - V characteristics in Figure 8.4E, we only took stable insertions into account, where the DLC did not switch conductance state between -100 mV and $+100$ mV. While these traces exhibit nearly ohmic behaviour, deviations from ohmic behaviour, such as gating, closures or additional insertions, are often observed above ± 50 mV. For our subset of stable insertions, the linear fit of the I - V curve (dashed line) has a slope of 100 pS. The conductance of the duplex is lower than for all previous designs. The second-smallest pore, our four-helix bundle presented in Chapter 6, had a mean conductance of 440 pS. This suggests that we indeed measure ion flow via the DNA-lipid interface rather than clusters of duplexes forming a physical pore. Clusters of porphyrin-tagged DNA have previously been shown to disappear in the presence of organic solvents [6, 15] and are therefore not expected to occur in the lipid bilayer environment.

To elucidate the design principles required to obtain a transmembrane current inducing DNA duplex, we tested two additional designs, both using the same DNA sequences as the porphyrin-tagged duplex. A porphyrin-free duplex with a terminal cholesterol tag on the 3' end of one constituent single-strand (strand "1" in Figure 8.1B) did not induce any transmembrane currents, see Figure 8.5A. A duplex with two terminal cholesterol tags, one on each 3' end, caused occasional transient spike-like current signals, reminiscent of electroporation spikes at high voltages, as shown in Figure 8.5B. Yet stable transmembrane currents, as observed for the porphyrin-tagged duplex, were never seen for either of the two samples. This is likely because the cholesterol tags can insert without forcing the insertion of the charged duplex as illustrated in the bottom panel of Figure 8.5C. Since two cholesterol tags draw the duplex close to the surface of the bilayer, fluctuations

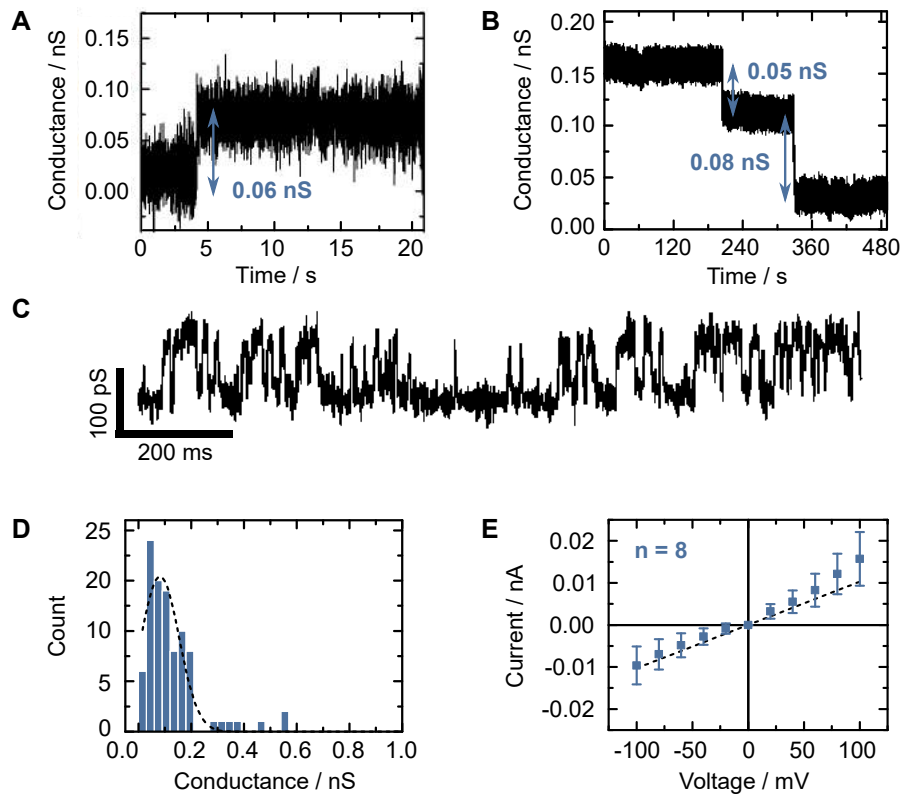


Figure 8.4: Ionic current recordings of the porphyrin-tagged duplex in 1 M KCl, 10 mM MES, pH 6.0. A) Exemplary current traces showing A) an insertion at 50 mV, B) two consecutive closure steps at 50 mV and C) gating behaviour at 100 mV. D) Histogram of conductance steps obtained from current traces of the duplex. The dashed line represents a Gaussian fit which peaks at 80 pS. E) I - V characteristics of stable insertions of the duplex. Error bars correspond to the standard deviation of eight independent recordings. The dashed line represents a linear fit.

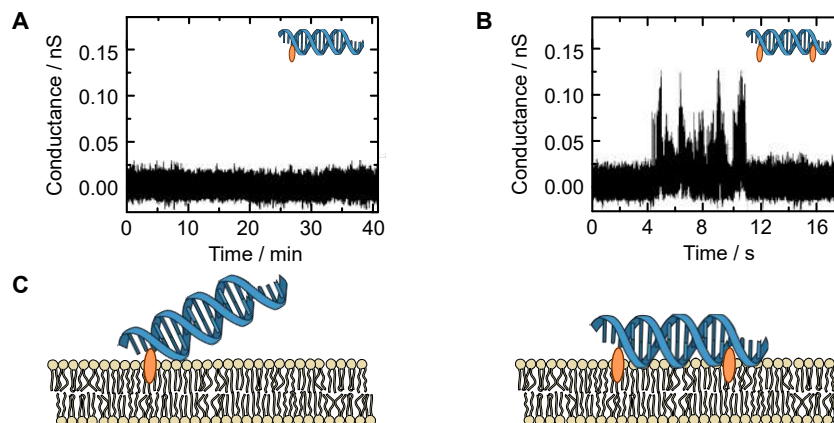


Figure 8.5: Control experiments with cholesterol-tagged DNA duplexes. A) A DNA duplex with a single terminal cholesterol tag does not induce transmembrane currents. B) A duplex with cholesterol tags on both ends causes occasional current bursts, but no stable transmembrane currents. C) Envisioned positioning of the cholesterol-tagged duplexes relative to the lipid membrane. In both cases, insertion of the cholesterol does not require the insertion of the charged DNA duplex. As a result, there is no reorganisation of the lipid bilayer sheet.

in the lipid bilayer structure may lead to the transient formation of lipid pores without well-defined conductance. Similar phenomena have been described previously [16].

8.3.4 Molecular dynamics simulations

To independently evaluate the DLC's ionic conductance, we built an all-atom model of the duplex as shown in Figure 8.6A. Analogous to the experimental conditions, the duplex was embedded in a DphPC lipid bilayer submerged in 1 M aqueous solution of KCl. The system was simulated by restraining the duplex to its initial coordinates in the membrane for the first 48 ns. The restraints were gradually removed over 15 ns, after which the duplex was simulated for 140 ns in the absence of any restraints. Because of the small dimensions of the duplex-lipid interface, a short equilibration simulation was sufficient for the bilayer to reach an equilibrium configuration around the duplex. During the equilibration simulation, lipid molecules rearranged around the transmembrane part of the duplex, forming a narrow water-filled passage in its circumference as visible in Figure 8.6B. The process of lipid rearrangement is shown in the time series in Figure 8.6C, where the lipid head groups are coloured in green. It happens within tens of

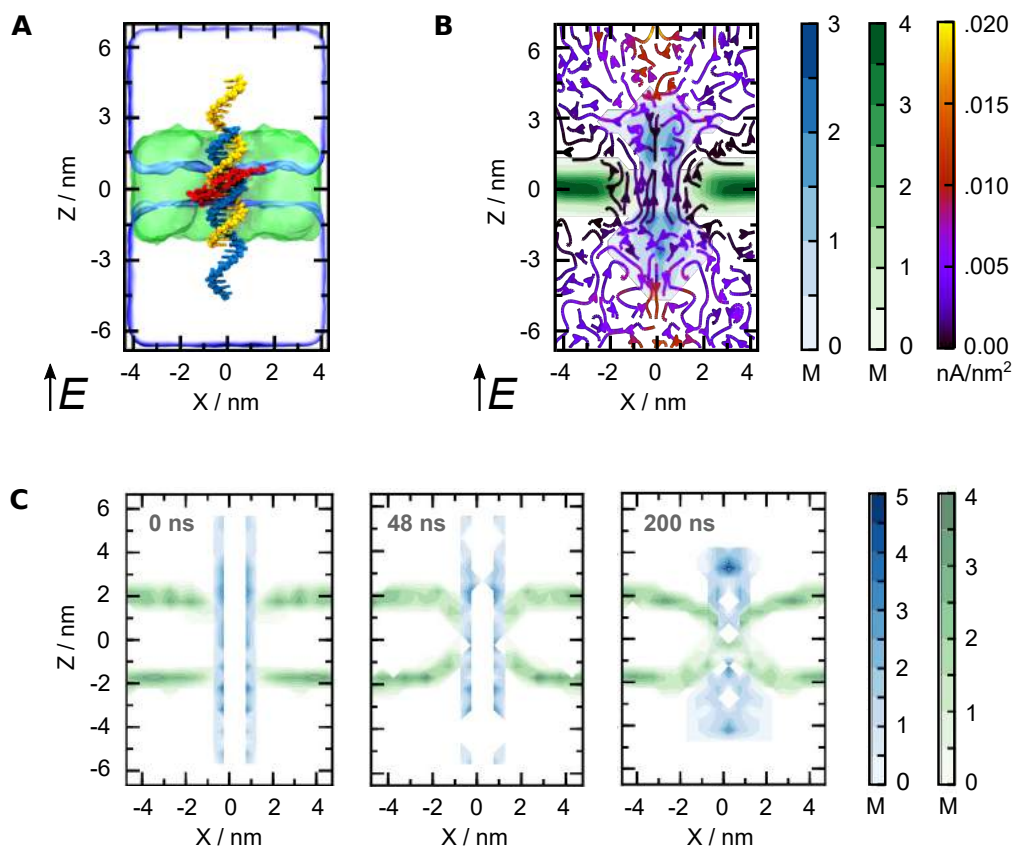


Figure 8.6: MD simulations of the duplex-induced DLC. A) All-atom models of the duplex with hydrophobic porphyrin tags (red) embedded in a lipid membrane (green) before equilibration. Total system size: 140,630 atoms. Electric field E in direction of positive transmembrane bias is indicated. B) Steady-state local densities of lipid chain (carbon atoms, green), DNA (phosphorus atoms, blue) and ionic current (streamlines). The arrows indicate the direction of the local ionic current flux, the colour the flux' magnitude. The maps were computed from a 672 ns MD trajectory at a +100 mV bias sampled with a frequency of 240 ps per frame; radially averaged about the z -axis of the duplex to improve the resolution. C) Local density of lipid head groups (carbon atoms, green) and DNA (phosphorus atoms, blue) at three time points of the MD simulation (from left to right: 0 ns, 48 ns and 200 ns) radially averaged about the z -axis. Each snapshot was computed by averaging the atomic coordinates over a 2 ns fragment of the 2.4 ps sampled trajectory nearest to the point of interest. Simulations were carried out by C.-Y. Li and A. Aksimentiev, University of Illinois at Urbana-Champaign.

nanoseconds during the equilibration simulation. A movie illustrating the formation of a toroidal lipid pore around the duplex was appended to our publication [17]. Figure 8.7 plots the cross section of the density of DNA (A), ions (B) and water molecules (C) across the lipid plane under an external electric field of +100 mV. The maximum density of DNA indicates the position of the DNA duplex. It lies in the centre of the overlapping torus-shaped density profiles of ionic current and water. Figure 8.7 directly compares these results with the previous simulations of the DNA origami porin from Chapter 7 (D-F). While the overall current is reduced in the case of the duplex, a passage for ions at the DNA-lipid interface exists in both systems. The ions are passing through the toroidal pore rather than following the groves of the DNA, which would cause helical currents. The local mobility of ions within the groves is considerably less than in the bulk. If an ion binds to the grove, it takes longer for it to pass through the membrane. So these ions do not contribute much to the current, or at least they do not follow the DNA helix as they move. This can be appreciated from the movie appended to our publication [17]. Approximately 100 water molecules were found on average surrounding the duplex within a 1 nm thick rectangular slab centred at the middle plane of the membrane. This number agrees with previous findings for the DNA origami porin in Chapter 7, which was surrounded by 900 water molecules in total, or equivalently 100 molecules per duplex. This is noteworthy because it shows that the type of membrane anchor (porphyrin for the duplex, cholesterol for the DNA origami porin) is not the primary factor determining the arrangement of the DLC. The formation of the toroidal lipid pore is predominantly shaped by the DNA itself. A continuous lipid sheet can fully shield the charged duplex from the hydrophobic lipid tails. Li and Aksimentiev have shown that the number of water molecules in the membrane is directly correlated with the DNA membrane pore conductance (private communication). It will be interesting to study a duplex where the phosphates are fully replaced by hydrophobic groups. Such a duplex should be incorporated into the lipid membrane whilst leaving the bilayer structure intact, like most integral proteins [2, 4] or, according to literature, carbon nanotubes with hydrophobic exterior [18].

The ionic conductance of the DLC was determined by applying an external electric field across the lipid bilayer and measuring the instantaneous displacement of ions within the MD trajectories as described in Appendix A4. Reproducing the experimental conditions, the system was simulated at +100, +30, -30, and -100 mV transmembrane biases for approximately 670 ns at each bias. Figure 8.8A displays the cumulative charge transmitted across the DLC as a function of the simulation time at different transmembrane voltages. The slope of each curve gives the average ionic current. The simulated ionic

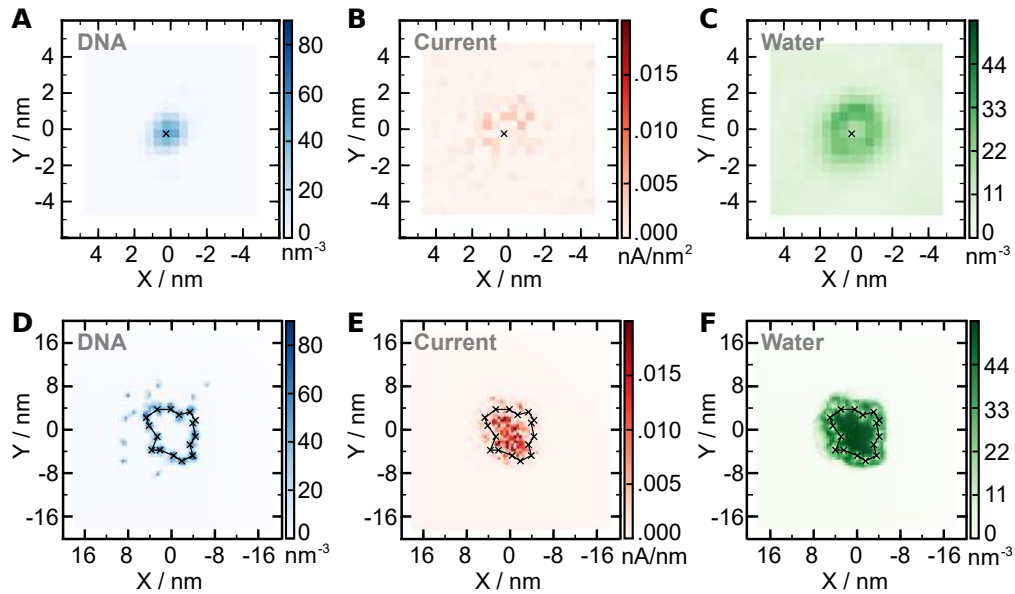


Figure 8.7: The local density of A) DNA (phosphorus atoms), B) ionic current and C) water molecules in the cross section of the lipid plane surrounding the DNA duplex. Applied bias: +100 mV. The density maps were calculated from a 672 ns MD trajectory. The data was averaged between $-1.75 \text{ nm} < Z < 1.75 \text{ nm}$ (see Figure 8.6B). The cross mark indicates the positions of the highest DNA density, approximately corresponding to the centre of the duplex. The data was averaged with a grid size of 0.5 nm and 240 ps per frame. D-F) For reasons of comparability, the corresponding cross sections for the DNA origami porin presented in Chapter 7 are plotted again. In both systems, ions and water molecules can pass at the DNA-lipid interface. Simulations were carried out by C.-Y. Li and A. Aksimentiev, University of Illinois at Urbana-Champaign.

currents exhibit considerable variations during individual MD trajectories, which we attribute to changing geometry of the interface between the DNA duplex and the lipid bilayer. The plot of the average current versus transmembrane voltage, Figure 8.8B, yields an average simulated conductance of 95 pS. The excellent quantitative agreement with the experimental conductance (100 pS) strongly suggests that the membrane-penetrating orientation of insertion explored by MD simulations represent the most likely experimental situation. Although spontaneous gating of the DLCs was not observed in MD simulations, the integrated current traces in Figure 8.8A show considerable variation of the ionic current over time produced by changing geometry of the interface between the DNA duplex and the lipid bilayer interface. While this could correspond to the gating seen in experiments, the different time scales of experiment and simulation preclude us from making a definite statement about the origin of the gating. In MD simulations, we explored the idealised case where the duplex is initially placed perpendicular to the membrane. Our experimental results, however, suggest that this may not always be the case. It is therefore not surprising that the MD simulations cannot fully explain the heterogeneity seen in experiments.

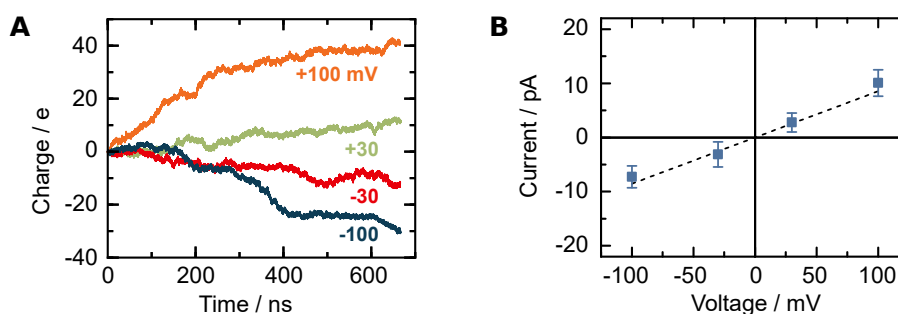


Figure 8.8: A) MD simulation of the cumulative charge transmitted across the lipid bilayer at +100 mV (orange), +30 mV (green), -30 mV (red) and -100 mV (blue) transmembrane biases. The instantaneous currents were sampled every 2.4 ps. The cumulative charge curves were obtained by integrating the respective instantaneous current curves versus simulation time. B) The simulated I - V characteristics. To compute the error, instantaneous ionic currents were block averaged with a block size of 9.6 ns. The error bars were computed as the standard error of the mean of the block averaged values. The dashed line represents a linear fit. Simulations were carried out by C.-Y. Li and A. Aksimentiev, University of Illinois at Urbana-Champaign.

8.4 Conclusion

Our membrane-inserting duplex is conceptually different from previous DNA-based membrane pores, since it lacks a central channel. Yet the insights gained from this chapter are essential for further development of all DNA pores as an emerging class of synthetic membrane channels. Our results settle the ongoing debate regarding the pathway of ions through DNA membrane pores [19–21]. DLCs are expected to contribute to the total conductance of all DNA-based pores that feature an amphiphilic transmembrane domain. The total conductance of DNA pores is thus the sum of the conductance through the central pore and through the toroidal lipid pore surrounding it. The relative contributions of these two conductance pathways will depend on the pore circumference relative to its area, as well as the hydrophobicity of its exterior and the lipid composition. In line with this argument, experiments and simulations yield lower conductances for the duplex-induced lipid channel (≤ 100 pS) compared to reports of previous DNA channels (0.44 – 1.6 nS [14, 19, 20, 22–24]). The ionic current characteristics of the duplex-induced DLCs show similarities with larger DNA pores, such as near-ohmic I - V behaviour in the lower voltage range [14, 19, 20, 22–24], closures at higher voltages [19, 23, 24] and relatively wide-spread conductance values [22, 24]. Amphiphilic peptides are known to destabilise lipid membranes [25] or change bilayer thickness [26]. However, our DLCs differ substantially from these peptide channels as they exhibit stable and higher magnitude currents. Toroidal lipid pores have been observed previously, for instance induced by a genetically engineered peripheral α -hemolysin pore with a truncated stem [10]. Here, we provide evidence that not only peripheral but also integral membrane components can cause the reorientation of lipids and thereby formation of ion pathways lined by the lipid head groups themselves. Although our DNA duplex-induced channel and the genetically engineered α -hemolysin protein are both man-made, they provide evidence that alternative conductance pathways without a physical channel may also exist in biological systems. Indeed, it has been suggested that toroidal lipid pores, transient or stable, can be induced by amphiphilic antimicrobial peptides [27, 28], by anion channels in the TMEM16/ANO superfamily [29], amyloid protein aggregates [30], the HIV-1 TAT peptide [31] and due to spontaneous density fluctuations within a membrane near its phase-transition observed in experiments [16] and simulations [32]. Our results are therefore of direct relevance to the ongoing debate on the physiological role of lipid channels, especially in the context of Alzheimer’s disease [30] and immune response [27, 28]. Furthermore, as a duplex is stable across a wider range of conditions compared to DNA origami, it is ideally suited for applications that re-

quire specific buffers, like cell culture. Single-stranded overhangs protruding from the membrane could serve as customisable extra-membranous domains for cellular targeting and stimuli-response. Extramembranous domains could be modified to target cellular receptors or serve as metastable binding sites for signalling molecules, highlighting the level of customisability of this versatile albeit minimalistic design. Substrate-induced oligomerisation will enable the creation of smaller and larger duplex-based assemblies in cellular environments. With this insightful combination of goal-oriented design, reverse-engineering, single-molecule experiments and all-atom simulations, we expect DLCs to contribute to our understanding of ion-conduction across lipid membranes and to our ability to control it.

Bibliography

- [1] D. A. Doyle, J. M. Cabral, R. A. Pfuetzner, A. Kuo, J. M. Gulbis, S. L. Cohen, B. T. Chait, and R. MacKinnon. “The structure of the potassium channel: molecular basis of K⁺ conduction and selectivity.” *Science* 280.5360 (1998), pp. 69–77. DOI: 10.1126/science.280.5360.69.
- [2] P. Hubert, P. Sawma, J.-P. Duneau, J. Khao, J. Hénin, D. Bagnard, and J. Sturgis. “Single-spanning transmembrane domains in cell growth and cell-cell interactions”. *Cell Adhesion & Migration* 4.2 (2010), pp. 313–24. DOI: 10.4161/cam.4.2.12430.
- [3] M. Zviling, U. Kochva, and I. T. Arkin. “How important are transmembrane helices of bitopic membrane proteins?” *Biochimica et Biophysica Acta* 1768.3 (2007), pp. 387–92. DOI: 10.1016/j.bbame.2006.11.019.
- [4] V. Cherezov et al. “High-resolution crystal structure of an engineered human β_2 -adrenergic G protein-coupled receptor”. *Science* 318 (2007), pp. 1258–65. DOI: 10.1126/science.1150577.
- [5] P. G. Strange. “G-protein coupled receptors: conformations and states”. *Biochemical Pharmacology* 58.7 (1999), pp. 1081–8. DOI: 10.1016/S0006-2952(99)00144-6.
- [6] A. Brewer, G. Siligardi, C. Neylon, and E. Stulz. “Introducing structural flexibility into porphyrin-DNA zipper arrays”. *Organic & Biomolecular Chemistry* 9 (2011), pp. 777–82.
- [7] L. A. Fendt, I. Bouamaied, S. Thöni, N. Amiot, and E. Stulz. “DNA as supramolecular scaffold for porphyrin arrays on the nanometer scale”. *Journal of the American Chemical Society* 129 (2007), pp. 15319–29.
- [8] P. Mueller, D. O. Rudin, H. T. Tien, and W. C. Wescott. “Reconstitution of cell membrane structure in vitro and its transformation into an excitable system.” *Nature* 194 (1962), pp. 979–80. DOI: 10.1038/194979a0.
- [9] T. Gutschmann, T. Heimburg, U. Keyser, K. R. Mahendran, and M. Winterhalter. “Protein reconstitution into freestanding planar lipid membranes for electrophysiological characterization.” *Nature Protocols* 10.1 (2015), pp. 188–98. DOI: 10.1038/nprot.2015.003.
- [10] D. Stoddart, M. Ayub, L. Höfler, P. Raychaudhuri, J. W. Klingelhoefer, G. Maglia, A. Heron, and H. Bayley. “Functional truncated membrane pores.” *Proceedings of the National Academy of Sciences* 111.7 (2014), pp. 2425–30. DOI: 10.1073/pnas.1312976111.

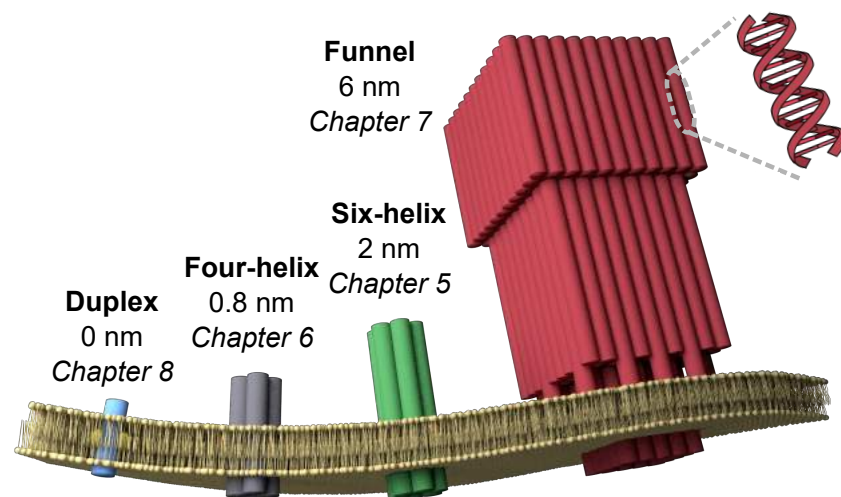
-
- [11] T. Nguyen, A. Brewer, and E. Stulz. “Duplex stabilization and energy transfer in zipper porphyrin-DNA”. *Angewandte Chemie International Edition* 48 (2009), pp. 1974–7.
- [12] F. Brandizzi, N. Frangne, S. Marc-Martin, C. Hawes, J.-M. Neuhaus, and N. Paris. “The Destination for Single-Pass Membrane Proteins Is Influenced Markedly by the Length of the Hydrophobic Domain”. *Plant Cell* 14.5 (2007), pp. 1077–92. DOI: 10.1105/tpc.000620.where.
- [13] T. Thundat, D. P. Allison, and R. J. Warmack. “Stretched DNA structures observed with atomic force microscopy.” *Nucleic Acids Research* 22.20 (1994), pp. 4224–8. DOI: 10.1093/nar/22.20.4224.
- [14] J. R. Burns, K. Göpfrich, J. W. Wood, V. V. Thacker, E. Stulz, U. F. Keyser, and S. Howorka. “Lipid-bilayer-spanning DNA nanopores with a bifunctional porphyrin anchor.” *Angewandte Chemie International Edition* 52.46 (2013), pp. 12069–72. DOI: 10.1002/anie.201305765.
- [15] T. Nguyen, P. Håkansson, R. Edge, D. Collison, B. a. Goodman, J. R. Burns, and E. Stulz. “EPR based distance measurement in Cu-porphyrin-DNA”. *New Journal of Chemistry* 38 (2014), pp. 5254–9. DOI: 10.1039/C4NJ00673A.
- [16] L. D. Mosgaard and T. Heimburg. “Lipid ion channels and the role of proteins.” *Accounts of Chemical Research* 46.12 (2013), pp. 2966–76. DOI: 10.1021/ar4000604.
- [17] K. Göpfrich et al. “Ion channels made from a single membrane-spanning DNA duplex”. *Nano Letters* 16.7 (2016), pp. 4665–9.
- [18] J. Geng et al. “Stochastic transport through carbon nanotubes in lipid bilayers and live cell membranes”. *Nature* 514.7524 (2014), pp. 612–5. DOI: 10.1038/nature13817.
- [19] A. Seifert, K. Göpfrich, J. R. Burns, N. Fertig, U. F. Keyser, and S. Howorka. “Bilayer-Spanning DNA Nanopores with Voltage-Switching between Open and Closed State.” *ACS Nano* 9.2 (2014), pp. 1117–26. DOI: 10.1021/mn5039433.
- [20] M. Langecker, V. Arnaut, T. G. Martin, J. List, S. Renner, M. Mayer, H. Dietz, and F. C. Simmel. “Synthetic lipid membrane channels formed by designed DNA nanostructures.” *Science* 338.6109 (2012), pp. 932–6. DOI: 10.1126/science.1225624.
- [21] V. Maingi, M. Lelimousi, S. Howorka, and M. S. P. Sansom. “Gating-like Motions and Wall Porosity in a DNA Nanopore Scaffold Revealed by Molecular Simulations.” *ACS Nano* 9.11 (2015), pp. 11209–17. DOI: 10.1021/acsnano.5b06357.
- [22] J. R. Burns, E. Stulz, and S. Howorka. “Self-Assembled DNA Nanopores That Span Lipid Bilayers.” *Nano Letters* 13.6 (2013), pp. 2351–6. DOI: 10.1021/nl304147f.

- [23] J.R. Burns, A. Seifert, N. Fertig, and S. Howorka. “A biomimetic DNA-based channel for the ligand-controlled transport of charged molecular cargo across a biological membrane”. *Nature Nanotechnology* 11.1 (**2016**), pp. 152–6. DOI: 10.1038/NNANO.2015.279.
- [24] K. Göpfrich, T. Zettl, A.E.C. Meijering, S. Hernández-Ainsa, S. Kocabey, T. Liedl, and U.F. Keyser. “DNA-tile structures lead to ionic currents through lipid membranes”. *Nano Letters* 15.5 (**2015**), pp. 3134–8. DOI: 10.1021/acs.nanolett.5b00189.
- [25] M. Ashrafuzzaman, M.A. Lampson, D.V. Greathouse, R.E. Koeppe, and O.S. Andersen. “Manipulating lipid bilayer material properties using biologically active amphipathic molecules”. *Journal of Physics: Condensed Matter* 18.28 (**2006**), pp. 1235–55. DOI: 10.1088/0953-8984/18/28/S08.
- [26] O.S. Andersen and R.E. Koeppe. “Bilayer Thickness and Membrane Protein Function: An Energetic Perspective”. *Annual Review of Biophysics and Biomolecular Structure* 36 (**2007**), pp. 107–30. DOI: 10.1146/annurev.biophys.36.040306.132643.
- [27] S.J. Ludtke, K. He, W.T. Heller, T.A. Harroun, L. Yang, and H.W. Huang. “Membrane pores induced by magainin”. *Biochemistry* 35.43 (**1996**), pp. 13723–8. DOI: 10.1021/bi9620621.
- [28] K. Matsuzaki, O. Murase, N. Fujii, and K. Miyajima. “An antimicrobial peptide, magainin 2, induced rapid flip-flop of phospholipids coupled with pore formation and peptide translocation”. *Biochemistry* 35.35 (**1996**), pp. 11361–8. DOI: 10.1021/bi960016v.
- [29] J.M. Whitlock and H.C. Hartzell. “A Pore Idea: the ion conduction pathway of TMEM16/ANO proteins is composed partly of lipid”. *Pflügers Archive* 468 (**2016**), pp. 455–73. DOI: 10.1007/s00424-015-1777-2.
- [30] A. Demuro, M. Smith, and I. Parker. “Single-channel Ca²⁺ imaging implicates A β 1-42 amyloid pores in Alzheimer’s disease pathology”. *The Journal of Cell Biology* 195.3 (**2011**), pp. 515–24. DOI: 10.1083/jcb.201104133.
- [31] H.D. Herce and A.E. Garcia. “Molecular dynamics simulations suggest a mechanism for translocation of the HIV-1 TAT peptide across lipid membranes.” *Proceedings of the National Academy of Sciences* 104.52 (**2007**), pp. 20805–10. DOI: 10.1073/pnas.0706574105.

- [32] W. F. D. Bennett, N. Sapay, and D. P. Tieleman. “Atomistic simulations of pore formation and closure in lipid bilayers”. *Biophysical Journal* 106.1 (2014), pp. 210–9. DOI: 10.1016/j.bpj.2013.11.4486.

Chapter 9

Conclusion



Parts of this chapter will be reprinted in:

K. Göpfrich & U. F. Keyser, DNA Sensors, Nanopores and Ion Channels, in Biological and Bio-inspired Nanomaterials: Assembly Mechanisms and Properties, Advances in Experimental Medicine and Biology (eds. T. Knowles, A. Buell & S. Perrett), Springer Nature (2017).

In this thesis, we have demonstrated the design of synthetic DNA-based membrane pores with a wide range of conductances and architectures, inspired by integral proteins, ion channels and large porins in nature. To evaluate our success, we will now test our pores against characteristics of protein pores. We will directly compare all existing DNA-based pores in terms of their structural and functional properties, including their gating behaviour. Finally, we will give an outlook for future directions in the rational design of DNA-based lipid membrane pores.

9.1 Comparative account of DNA membrane pores

Reiterating the characteristics introduced in Section 4.1, protein membrane pores should have versatile function-dependent structures while being anchored in the lipid membrane. They further mediate the flux of ions across the membrane and are responsive to stimulation. In the following, we will discuss to what extent our synthetic DNA-based membrane pores successfully mimic these properties of their natural counterparts.

Membrane pores can have a variety of function-dependent structures. Rapid prototyping of different nanoscale shapes is one of the most appreciated strengths of structural DNA nanotechnology. This is why it may seem surprising that the first DNA membrane pores all featured a 2 nm wide channel between six concentrically arranged DNA duplexes [1–4]. In this thesis, however, the structural variability of DNA membrane pores has been demonstrated with the creation of much smaller as well as much larger pores. An illustrative overview of the discussed architectures is presented in the figure at the beginning of this chapter. The DNA channel made from four DNA duplexes presented in Chapter 6 had a nominal diameter of 0.8 nm, approaching the dimensions of natural ion channels [5]. Due to its simple design, this DNA channel self-assembled within a minute at room temperature. On the other end of the spectrum, a membrane-inserting DNA origami funnel with a 6 nm construction was presented in Chapter 7 as the largest man-made pore to date [6]. It is wider than most natural porins and comparable to the electrical diameter of the nuclear pore complex [7]. Such large architectures are difficult to obtain with traditional chemical synthesis used to create artificial membrane pores. The realisation that this DNA porin had an effective electrical diameter of 11 nm due to ion flow at the DNA-lipid interface led to the design of the ultimately smallest DNA pore: a transmembrane-spanning duplex introduced in Chapter 8.

Table 9.1 compares all published DNA membrane pores. Until today, the pores presented in this thesis remain the only ones that do not follow the six-helix bundle architecture. Our pores, from the duplex to the funnel, span almost an order of magnitude in diameter and length, and over two orders of magnitude in molecular weight. They are built from 2 to 200 individual DNA strands, anchored via 2 to 19 hydrophobic tags. Even though the intriguing complexity of natural membrane components cannot be matched, our synthetic pores made from DNA span the biologically relevant scales.

Membrane pores span the lipid bilayer membrane. With confocal imaging of fluorescently labelled DNA nanopores we demonstrated their attachment to lipid vesicles via cholesterol or porphyrin anchors. Due to its fluorescent properties and its strong hydrophobicity, we used porphyrin for visualisation and membrane anchoring at the same time. An increase in the melting temperature and a shift in the fluorescence emission of porphyrin served as independent proofs of membrane insertion. It should be noted, however, that these techniques can only confirm membrane attachment – functional studies are required to demonstrate that the DNA pores actually span the lipid bilayer.

Membrane pores mediate the rapid flux of ions without moving themselves. By combining ionic current recordings with MD simulations, we not only demonstrated that DNA-based membrane pores induce transmembrane currents, but also revealed their microscopic conduction pathway. All DNA-based membrane pores exhibited ohmic I - V characteristics at lower voltages and a relatively broad spread of conductances. Ions flow through the central channel of the pores, but also through gaps at the DNA-lipid interface. The hydrophilic lipid head groups tilt to face the DNA, forming a toroidal DNA-lipid channel around the DNA structures as described in Chapters 7 and 8. This explains why even a membrane-spanning DNA duplex showed stable insertions with an average conductance of 0.1 nS, in good agreement with MD simulations, despite the lack of a physical channel.

Table 9.1 compares the mean open-pore conductance G of all DNA membrane pores. The conductance measured for the DNA origami porin is a factor of 300 larger than for the duplex. Generally, the conductance increases with the pore diameter, as expected. The ethane-modified six-helix pore by Burns *et al.*, however, does not follow this trend. There are multiple reasons why its conductance may be comparable to the smaller four-helix pore: First of all, unlike for all other pores ionic current recordings were performed on black lipid membranes, which are known to exert a high membrane

Table 9.1: Overview of structural and conductive properties of all published DNA membrane pores. G (measured) is the mean conductance determined from histograms of conductance steps in ionic current recordings. G (Eq. 4.8) denotes the conductance calculated from the Hille equation, Section 4.3.2, assuming a nominal helix diameter of 2 nm. All conductance values are given for an electrolyte solution of 1 M KCl.

DNA pore	Duplex	4-helix	6-helix “Ethane”	6-helix “Porphyrin”
Reference	Chapter 8	Chapter 6	[3], [8]	Chapter 5
Diameter [nm]	–	0.8	2.0	2.0
Length [nm]	6	11	14	15
MW [kDa]	20	92	165	180
# DNA strands	2	8	14	6
Hydrophobic tag	6 porphyrin	2 cholesterol	72 ethane	2 porphyrin
G (measured) [nS]	0.13	0.44	0.40	1.6
G (Eq. 4.8) [nS]	0	0.45	2.1	2.0
DNA pore	6-helix “Cholesterol”	6-helix “M1.3”	6-helix “Origami”	Funnel
Reference	[9]	[10]	[11]	Chapter 7
Diameter [nm]	2.0	2.0	2.0	6.8
Length [nm]	8	35	42	54
MW [kDa]	98	505	4970	4970
# DNA strands	6	37	390?	200
Hydrophobic tag	3 cholesterol	6 cholesterol	26 cholesterol	19 cholesterol
G (measured) [nS]	1.6	0.72	0.87	30
G (Eq. 4.8) [nS]	3.4	0.91	0.76	12.2

pressure [12]. This could reduce the effective pore diameter as MD simulations have shown [8] and thereby the conductance. In Section 5.3.4, we demonstrated that the membrane system can indeed influence the conductance behaviour of six-helix pores [4]. Furthermore, the membrane anchoring of the ethane pore is significantly different from all other designs. Instead of adding hydrophobic tags on the outside, the charged DNA backbone is replaced with uncharged groups. Therefore, there is a hydrophobic barrier on the inside of the pore resulting in a reduced electrostatic diameter. This hypothesis has been confirmed with MD simulations, where the same pore with charged phosphate groups on the inner channel walls had a three times higher conductance compared to the pore with ethane modifications all around [8].

Table 9.1 further shows the limitations of the Hille equation for the estimation of the conductances of DNA pores. Most prominently, the simple model assumes that the nominal channel diameter is equivalent to the electrical diameter. We observed, however, that the electrical diameter is larger due to ion flux at the DNA-lipid interface. On the other hand, the DNA structures are highly negatively charged so that potassium ions are the main charge carriers [8]. This reduces the overall conductance again. Equation 4.8 further assumes an ohmic cylindrical resistor with impermeable pore walls, which is not the case for DNA nanostructures [13]. Due to these cancelling effects, the estimate of Equation 4.8 is not as far off as one might expect. In all cases, the order of magnitude is in agreement with experiments – with the obvious exception of the DNA duplex.

MD simulations have described the conductance of the DNA origami porin and the duplex remarkably well, see Chapters 7 and 8. We thus establish how a comparison between MD simulations and experiments may inform the future design of DNA-based membrane pores in future studies: A significant mismatch between conductances obtained from MD simulations and experiments could point towards the fact that a considerable fraction of the pores does not penetrate the membrane in the simulated perpendicular orientation.

Membrane pores are often responsive to physical or chemical stimulation. All DNA membrane pores exhibited multiple conductance states reminiscent of gating observed for natural ion channels – independent of their architecture and the chemical nature of the membrane anchor. Example traces for a range of different pores are shown in Figure 9.1. Conductance steps can occur between different conductance levels or between the conductance of the plain bilayer and the pore conductance, potentially caused by DNA pores flipping in and out of the membrane (transient insertions). Not surprisingly for such highly charged pores, we showed in Chapter 5 that the conductance states are

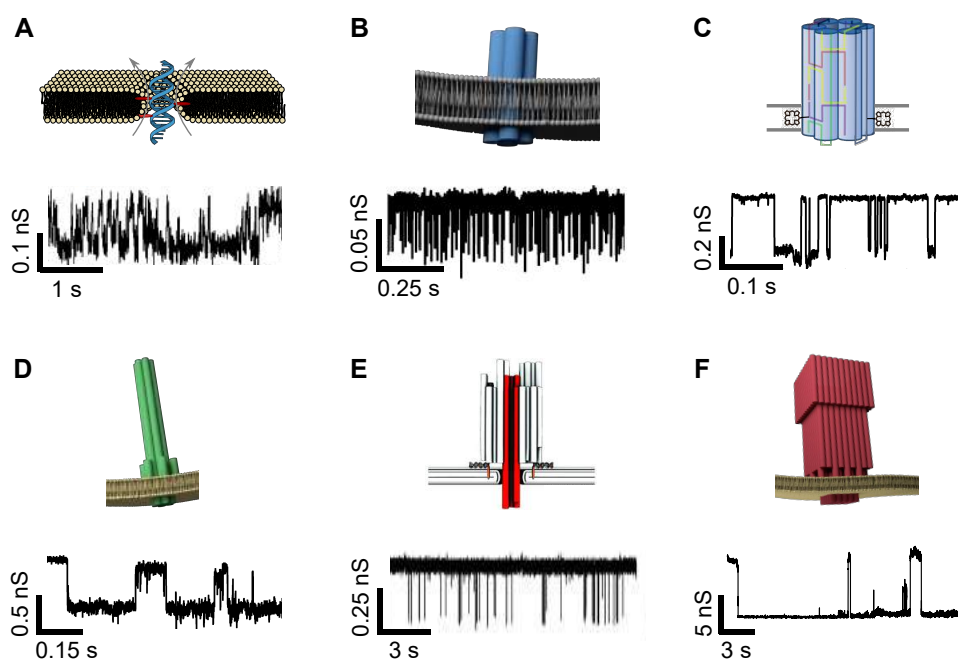


Figure 9.1: Gating of DNA-based membrane pores. Sketch of the pore (top row) and ionic current trace showing gating (bottom row) of A) the transmembrane spanning DNA duplex from Chapter 8; B) the four-helix bundle from Chapter 6; C) the scaffold-free six-helix pore from Chapter 5; D) the six-helix pore utilising the shorter M1.3 scaffold, adapted from [10]; E) the DNA origami six-helix pore. From [1]. Reprinted with permission from AAAS; F) the large DNA origami porin from Chapter 7.

voltage-dependent. At higher voltages, the pores were more likely to switch to a lower conductance state or to leave the membrane entirely [1, 4]. Experiments [1] and MD simulations [14] suggest that dynamic motion of the mouth regions could be the origin of the gating.

MD simulations further revealed mechanosensitivity of DNA pores [8], specifically of the six-helix bundle [3]. This could explain why we observed discrepancies in the relative abundance of conductance states on different membrane systems, which exert different membrane pressures on the pore, see Chapter 5.

9.2 Outlook

Having explored DNA nanotechnology as a radically new approach towards the design of synthetic membrane pores, we engineered channels that already show the four main characteristics of their natural counterparts. Some of the challenges in the field, like the lack of common building blocks for diverse architectures, have successfully been addressed. The largest DNA pore even outperforms most biological pores in terms of its dimensions and its conductance. The study of a membrane-spanning DNA duplex has revealed alternative conductance pathways through lipid membranes, which do not require the presence of a central physical channel – an observation that prompts questions about the role of such pathways in nature. Despite this significant progress, DNA membrane pores still fall a long way behind the natural benchmarks when considering their structural and functional complexity and specificity. While an in-depth study of the insertion efficiency of DNA pores is still missing, future emphasis should be put on achieving insertion rates comparable to long-studied model lipid membrane pores like α -hemolysin. Optimising the DNA membrane pore structure, its anchoring mechanism and the experimental conditions will be key. Apart from voltage, membrane pressure and ligands, protein pores can also be responsive to pH, light or temperature. The full exploitation of the available toolbox for chemical functionalisation of DNA provides a route towards custom-designed stimuli-responsive DNA membrane pores with the long-term goal of gaining the precision of nature. By modulating the electrostatic potential inside the channel, for instance by using nucleic acids with an uncharged backbone, it will be possible to gain control over the selectivity of the channel. If DNA membrane pores could one day be synthesised *in vivo*, this would certainly lead to exciting developments where DNA-based components could become part of the cellular machinery. The broad perspectives of applications of rationally designed pores, from sensing to drug delivery,

seem to make the efforts worthwhile and we may be curious to witness their development over the coming years – even if today, we may still be humble apprentices of nature.

“Origami may someday even save a life.”

Robert Lang, Mathematician and paper origami artist



Bibliography

- [1] M. Langecker, V. Arnaut, T. G. Martin, J. List, S. Renner, M. Mayer, H. Dietz, and F. C. Simmel. “Synthetic lipid membrane channels formed by designed DNA nanostructures.” *Science* 338.6109 (2012), pp. 932–6. DOI: 10.1126/science.1225624.
- [2] J. R. Burns, K. Göpfrich, J. W. Wood, V. V. Thacker, E. Stulz, U. F. Keyser, and S. Howorka. “Lipid-bilayer-spanning DNA nanopores with a bifunctional porphyrin anchor.” *Angewandte Chemie International Edition* 52.46 (2013), pp. 12069–72. DOI: 10.1002/anie.201305765.
- [3] J. R. Burns, E. Stulz, and S. Howorka. “Self-Assembled DNA Nanopores That Span Lipid Bilayers.” *Nano Letters* 13.6 (2013), pp. 2351–6. DOI: 10.1021/nl304147f.
- [4] A. Seifert, K. Göpfrich, J. R. Burns, N. Fertig, U. F. Keyser, and S. Howorka. “Bilayer-Spanning DNA Nanopores with Voltage-Switching between Open and Closed State.” *ACS Nano* 9.2 (2014), pp. 1117–26. DOI: 10.1021/nm5039433.
- [5] K. Göpfrich, T. Zettl, A. E. C. Meijering, S. Hernández-Ainsa, S. Kocabay, T. Liedl, and U. F. Keyser. “DNA-tile structures lead to ionic currents through lipid membranes”. *Nano Letters* 15.5 (2015), pp. 3134–8. DOI: 10.1021/acs.nanolett.5b00189.
- [6] K. Göpfrich, C.-Y. Li, M. Ricci, S. P. Bhamidimarri, J. Yoo, B. Gyenes, A. Ohmann, M. Winterhalter, A. Aksimentiev, and U. F. Keyser. “Large-Conductance Transmembrane Porin Made from DNA Origami”. *ACS Nano* 10.9 (2016), pp. 8207–14. DOI: 10.1021/acsnano.6b03759.
- [7] M. Mazzanti, J. O. Bustamante, and H. Oberleithner. “Electrical dimension of the nuclear envelope.” *Physiological Reviews* 81.1 (2001), pp. 1–19.
- [8] J. Yoo and A. Aksimentiev. “Molecular Dynamics of Membrane-Spanning DNA Channels: Conductance Mechanism, Electro-Osmotic Transport, and Mechanical Gating”. *Journal of Physical Chemistry Letters* 6.23 (2015), pp. 4680–7. DOI: 10.1021/acs.jpcllett.5b01964.
- [9] J. R. Burns, A. Seifert, N. Fertig, and S. Howorka. “A biomimetic DNA-based channel for the ligand-controlled transport of charged molecular cargo across a biological membrane”. *Nature Nanotechnology* 11.1 (2016), pp. 152–6. DOI: 10.1038/NNANO.2015.279.
- [10] K. Göpfrich. “Towards rational design of artificial membrane pores using DNA nanotechnology”. Master of Philosophy in Physics. University of Cambridge, 2013.

- [11] M. Langecker, V. Arnaut, T. G. Martin, J. List, S. Renner, M. Mayer, H. Dietz, and F. C. Simmel. “Synthetic Lipid Membrane Channels Formed by Designed DNA Nanostructures”. *Science* 338.6109 (**2012**), pp. 932–6. DOI: 10.1126/science.1225624.
- [12] T. Gutsmann, T. Heimburg, U. Keyser, K.R. Mahendran, and M. Winterhalter. “Protein reconstitution into freestanding planar lipid membranes for electrophysiological characterization.” *Nature Protocols* 10.1 (**2015**), pp. 188–98. DOI: 10.1038/nprot.2015.003.
- [13] J. Yoo and A. Aksimentiev. “In situ structure and dynamics of DNA origami determined through molecular dynamics simulations.” *Proceedings of the National Academy of Sciences* 110.50 (**2013**), pp. 20099–104. DOI: 10.1073/pnas.1316521110.
- [14] V. Maingi, M. Lelimousi, S. Howorka, and M. S. P. Sansom. “Gating-like Motions and Wall Porosity in a DNA Nanopore Scaffold Revealed by Molecular Simulations.” *ACS Nano* 9.11 (**2015**), pp. 11209–17. DOI: 10.1021/acs.nano.5b06357.

Appendix

A1. Methods for coarse-grained simulation of lipid pore formation

The MARTINI simulations were performed using the Gromacs 5.0.4 package with a 20 fs time step and 12 Å cut-offs for non-bonded forces [1]. The half harmonic potential was implemented using the MDRUN program of the Gromacs package [2]. First, we equilibrated a lipid bilayer membrane containing 8,192 dioleoyl-phosphatidylcholine (DOPC) lipid molecules and 96,000 water beads in a $50 \times 50 \times 9 \text{ nm}^3$ simulation box at zero surface tension under periodic boundary condition. We chose to simulate DOPC lipids over DphPC because the current MARTINI force field does not provide parameterisation for DphPC. DOPC is analogous to DphPC within the MARTINI's coarse-graining framework that maps four hydrocarbon atoms to one MARTINI bead. Following that, multiple systems, each containing a single pore of prescribed radius, were created by applying a half-harmonic cylindrical potential, $V_p(r)$, to all DOPC beads: $V_p(r) = 0.5k(r - R_p)^2$ for $r < R_p$ and 0 otherwise, where R_p is the pore radius and r is the distance from the pore centre. Each system was equilibrated for 300 ns; the average pressure was computed using the last 200 ns of equilibration. The error bars were estimated as the standard error of 10 ns block averages.

A2. Pathways of scaffold and staple strands of the DNA origami porin

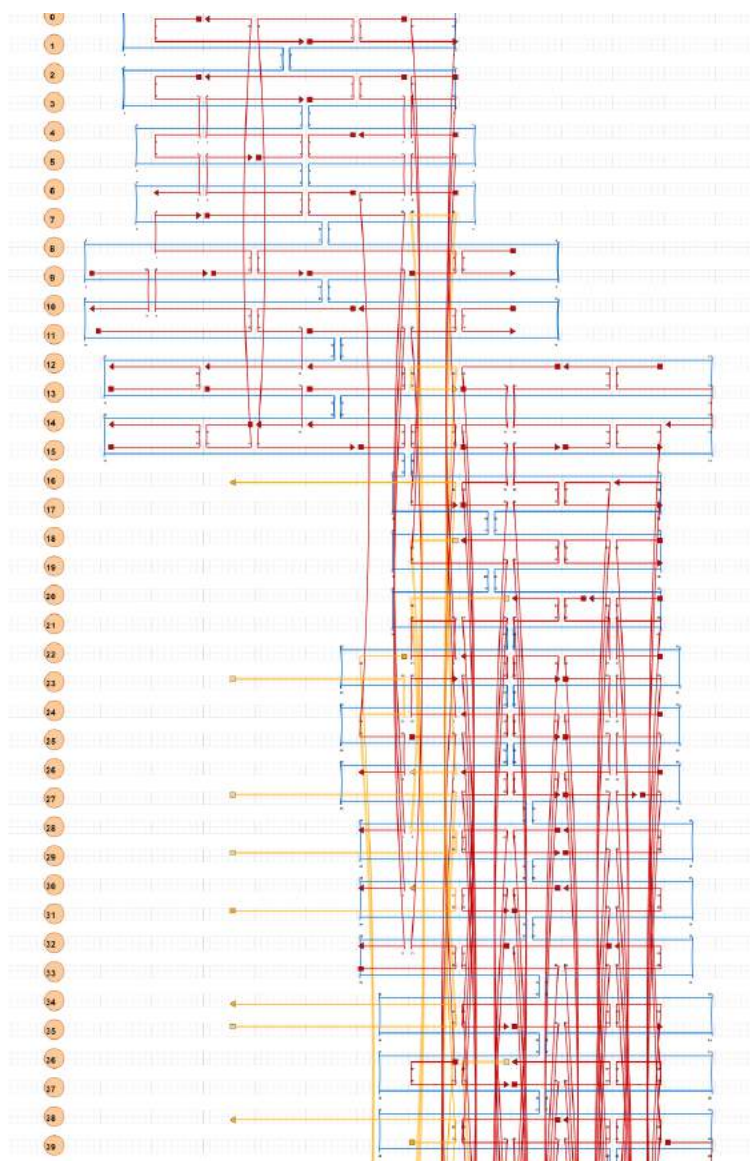


Figure 9.2: Pathways of the M13mp18 scaffold (blue) and the 179 staples (red) of the DNA origami porin. Single-stranded DNA overhangs for hybridisation with complementary cholesterol-tagged oligomers are shown in yellow.

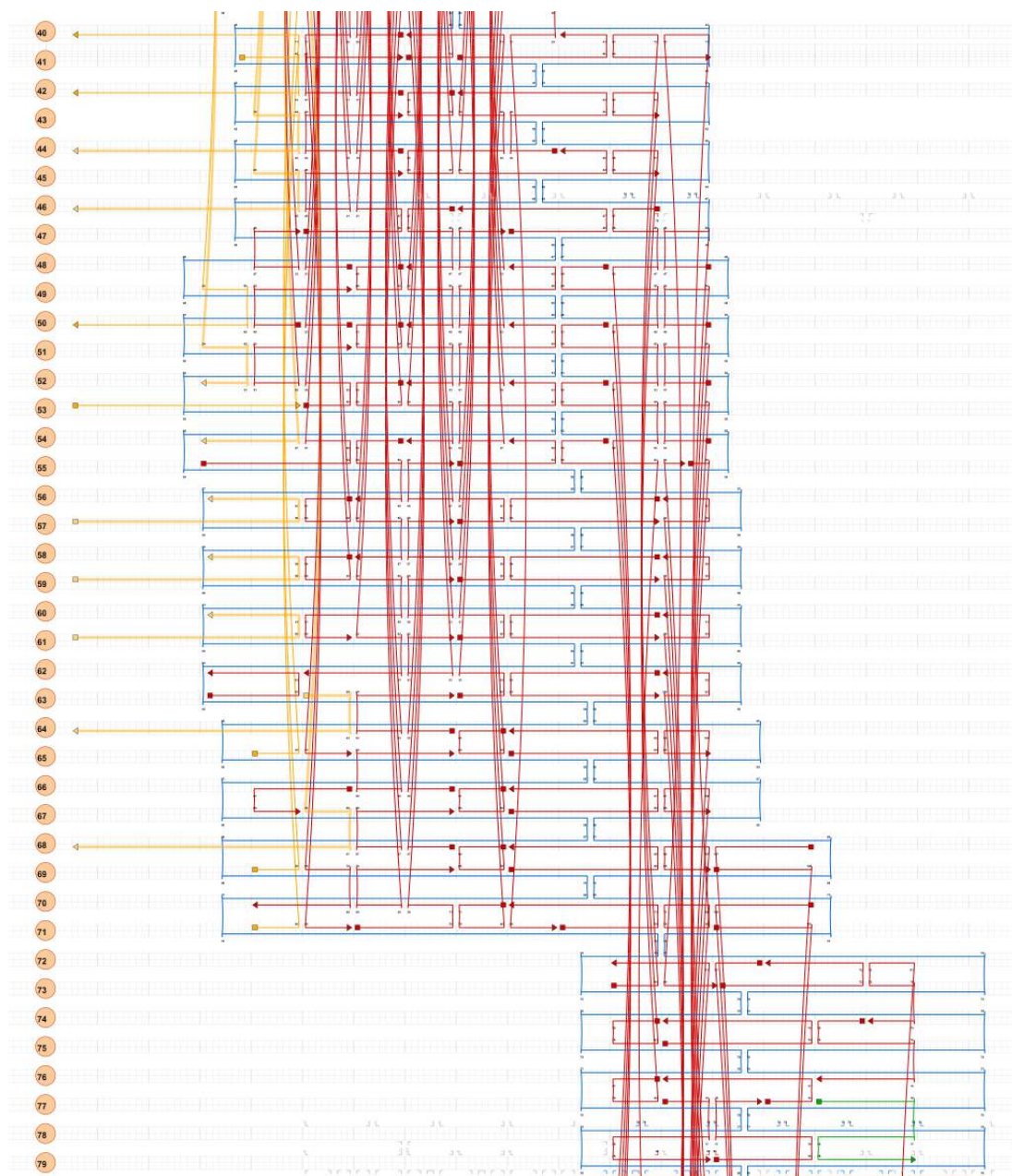


Figure 9.3: Continued: Pathways of the M13mp18 scaffold (blue) and the 179 staples (red) of the DNA origami porin. Single-stranded DNA overhangs for hybridisation with complementary cholesterol-tagged oligomers are shown in yellow, oligomers with optional Cy3 tags are shown in green.

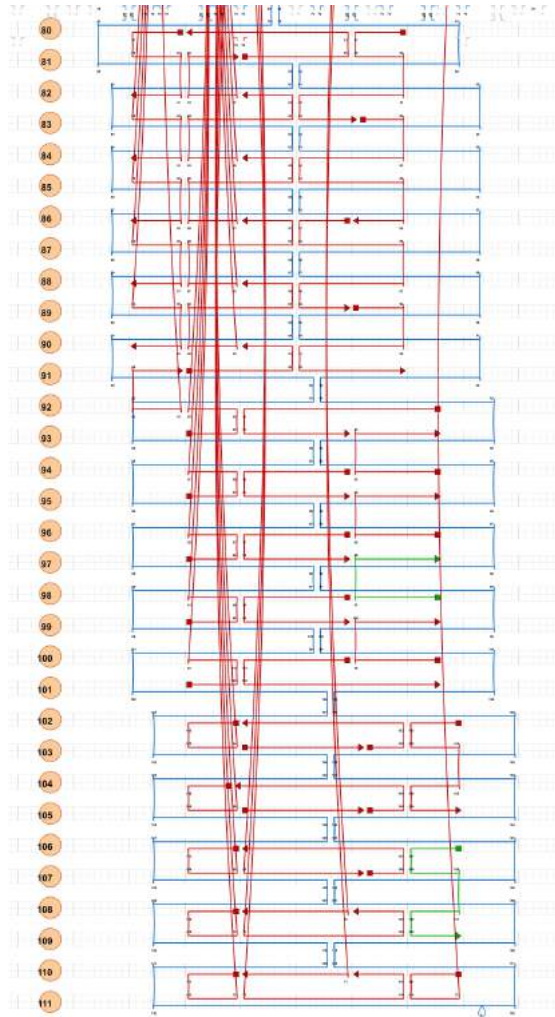


Figure 9.4: Continued: Pathways of the M13mp18 scaffold (blue) and the 179 staples (red) of the DNA origami porin. Oligomers with optional Cy3 tags are shown in green.

A3. DNA sequences for the DNA origami porin

Table 9.2: DNA sequences of the DNA origami porin (1).

Name	Sequence
Core1	ATAATTACTAAATAAGCCGACCGTCCGGCACCTTCGCCAT
Core2	AATTAGCAAGAACGGGTGCGAAATCCCAATTC
Core3	AGTATCGGCCGCCTGCAAAAATCTAAAATGGGCGCATCGT
Core4	GCCCCAGTCCTGTTTCAATAACGCAGTACCT
Core5	TGGCCTTCCTGTATGAGGATTTAGCGTTATTAATTTTTTAAACCAATAG
Core6	TGAAACCATCACCAGTAGCACCATATTAGAGCAGCGTAAACGTAAATGA
Core7	AGCTACAAAAGATTAGTAAAAACCTGCCAGAG
Core8	AAAGTGTAACACAACAGAATCCTTCGATAGCT
Core9	TTACCAACCAGTTACAGGCTCATTTTACCTTATGCGATTTAAGCTGCT
Core10	TCAGTGTCAAATTACAGTAGGGCTCATGTAATTTAAAAAGAATACT
Core12	AGACAGTCAAATCATATACAGTAAGATTCGCCTGATTTATTTCAACGC
Core13	CACACGACATTTACATTGGCAGATCCGCCTACATTTTGAC
Core15	GCCGCCACGCCACCCTCCACCACCGCCGCCAGTGGCCTTG
Core16	GTTTACCAAAAAGGAAGTTTTGTCTGTAGCAT
Core17	CTCAGAACACCCCCAGTGCCACTACGAAGGCA
Core18	AGCGTCATACCCTTGAGTAA
Core19	AAGGATAAAAGGCCGGGAAAAATACAACAATAGCCCTTTTAATAGCAA
Core20	CAGGACGTGTAGAAAGGCGTCTTTTTGCACCC
Core21	TGTAGGCATCACCTTGAGTTGAAAGGACGTGGTTCTCATT
Core22	CAGCAAAAGCCGAATTATCACCGTGAATAGAA
Core23	GTTGCAGCAAGCGATGGT
Core24	GAACGCCATTCGCGTCAACGCCAATAATTGAG
Core25	ATTTGGGATACCATTATCCACAGATACAAAT
Core26	TATCGGTTTCAGCTTGATACCGCCAAAATTAAGTCAATTCTACTAATAG
Core27	AAAACGCTCATGGAAATAAGCTCGAATTCATTGTTATCCGCAGAA
Core29	GATCTAAATTACGAGGAACAACATTATTACAG
Core30	TAGTAGCAGATACATTTATTAACAACACTCATCG
Core31	AGACAGGAACGGTCCTGAGAAGTGTT
Core32	CTTGCCCTCTTTAATCTCCCAATCCCAGAGCC
Core33	GAATGCCAAGCTCGACGTTGTA AACGAGGCGATTA
Core34	TGGATTATACTTCTGACGTGGACTCCAACGCCCCCGATTTGAGAAAGG
Core35	AAACCGTCATGGCCCATCAGATGAGTTAAAAT
Core37	GGCGGATACCGGAATACATCTTTT
Core38	CCGTCGGAGAACAAACGGCGGATTGGATAGGTCACGTTGG
Core39	TGATATAAGTATAGCAGTGCCGTCGAGAGG
Core42	GTATGTTAATGATTAAGACTCCTTTTACCGAA
Core44	ATATTTAAAGAACCCTAACATTATGACCCTGT
Core45	CTGGAGCAAACAACACTACCATATCAACGTCAGATGAACCATCAATATGA

Table 9.3: DNA sequences of the DNA origami porin (2).

Name	Sequence
Core46	CTTAAATCTTTTATCCCAACTAATGTTGAGATTTAGGAATTAAGAACT
Core47	CATCAATATAATCCTGGGAGTCAAAGGGCGAA
Core48	AATCGGCCCTGTTCGTTTTTCATTTTTTTAATG
Core49	TGCCCCGTATAAACAGTTAATGCCCTTTAACGGGGTCAGTGATGGCTTTT
Core50	GGAGGTTGAGAGCCGCCACCAGAACAGAGCCACCACCCTC
Core51	AGGTGAATTTCTTAAATATCAGCTACACCACGATTCATATGGTTTACC
Core52	GGGGTAATCATTGAATTCAGGTCT
Core53	AGCAAATGAACAGTGC GCGGTCAGTATTAACACCGAACGAA
Core54	GTTTAGAAGTTTAAAATAGCGAGAGGCTACCACATT
Core55	CATATATTTTAAATGCTAATGTGT
Core56	AGACTCCTCAAGAGAAAAGTATTAAGAGGC
Core58	ACAGCCATTTTTGTTTCATTCAGTCCAAATCA
Core59	GCGACATTCGGAAATTATTCATTAAGGTAGAATGGAAAGCAGGAGTG
Core60	ACGCTCAGCAGCGAAACTACAAAGAATCATATGTACCCCG
Core61	TTCTTTGATTAGTCTTGCCTGAGTAG
Core62	CATAGCCCCGCGTTTTTCATCGGCA
Core63	ATCAAGTTAGCACCGTGTCAACAA
Core64	TGCGAACGATAATGCTATCGTAGGGCGCCCAATAGCAAGC
Core65	GAGTCCAGTCGGGAAAAACGCGCGGGGAGAAT
Core66	AACCGTGCTTGAGGGGCTCCAGCC
Core67	GATGATACGCAGTCTCTGAATTTACAAACAA
Core68	GACTGTAGCCTTATTAGCGTTTGCGGTGTATCACCGTACT
Core69	AAATCTAAGATAAGAGACATGTTTTAAATATGCATATAAC
Core70	GCGACAGAGCCACCCTCAGAGTACACTTAGCCAAGTACAACGGAGATT
Core71	AAATCATATAGGTTGGAGTTGGGTGGGGATGTGCTGCAACGGTGCGG
Core72	ACGCCAGAGGCGGTTTACCAGTGAGACGGGAGCTAAACAGGAGGC
Core73	GACGAGAAAGCCCAATAGGCTGGCTCATAAGGGAACCGAA
Core74	CGACAATAGGTAAAGTTTAAATTG
Core75	AACGTCAACTTTGAAAGAGGATGTTTAGTATCGCCAACGC
Core76	GAGGAAGGGATAATACATTGCCAGCTTTCATC
Core78	CAGGAGGTACCAGAAGGAATTGCT
Core79	TCGATAGCTGCCTTTAGCGCGCCTCCCTCAGA
Core80	AATAAGCCTAATGAGTTGCCCGCTTCTGTCC
Core81	AAACGAAAGAGGCGGCAGAGGCATCGACAAAA
Core82	AGGATTAGGATTAGCGCAGTACCA
Core83	AGCGCTGGTAATAAGTCTGCCTATATTATTCTGAAACATG
Core84	TAGAAGGCCGAACCAGAAGCCCGA
Core85	GGGTTACCGAGGAAACAACATATAAAAAACCT

Table 9.4: DNA sequences of the DNA origami porin (3).

Name	Sequence
Core86	AACGGAATATAGCCGACGGGATCG
Core87	TGGGAAGAACAACGCCAGGAACCC
Core88	AAAACAAAATTAATTTGACCATTATTAACATCCAATATACCTGAGCAA
Core89	GAAACAGTACATAAATTGCTGAATAGTAGATTTAGTTACATTTAACAA
Core91	CAATAGAAAAGAATAAGTT
Core92	GTGATAAAAATTTTCATCTTCTGACCAAATATATGCGCAACGCTATTAC
Core95	GGCCTTGCTGGTACAATATTACCGCC
Core96	AAATTTTTTTTTACGAGTCCTTATCATTATAGTTGCGCCGAGTACCAAA
Core97	GCAAGTGTAAGGAGCAACGTGGCAGAGCTTG
Core98	AATGCTTTAAACAGTTTTTGC AAA
Core99	AACAATGATAAGAAAAGTAAGCAGACCCAAAAGA ACTGGCGCAAACGT
Core100	TTACCCTGCAAAAAGAAGTTTCAGATTGCGAATAAAGATA
Core101	CCGAAACAATCAGTAATGTACCGGGATAGCAACACCAGAAGTAATCT
Core102	TTATCTAAAATATCTTCAGTTGGCAAATCAACCTGAACCTCAAATATC
Core103	AGAAAATACATACATATAACCGAT
Core104	AAGACTTCGACCATAAGGAG
Core105	CATTTTAAAAGTTTGAGTAACATGAATTATCATCATATT
Core106	ATAAATCCTCATTAAAAGGCAGGTCAGACGATCATTGACA
Core107	CGAACAACTTAAGAGGACCGGAAG
Core109	TGCTTTAATCAGAGCGGGCAACAGCTGATT
Core110	AAC TTTTTCTAAATTTAAGCGCCAGCTTCTGGTGCCGGAACCTCAGGA
Core111	TGTGTGAAGTAATCATTAGT
Core112	TGCGGATGCTTCAAAGTTATCCGGACGCGAGGCGTTTTAG
Core113	TGACAAGAACCGGATAAGGCGCATCAAATAAGATAGCAGC
Core114	TCACCCGCCTGATAAAATTCAAAGGGTGAGA
Core115	AATAATAAACCCACAAGGCTACAGAAGTTTCCCCCAAAA
Core116	CCACCGAGTAAAAATCACGCAAATTA
Core117	GAAAAAACGATTATTATTTAATTGTGAAATACCAGT
Core118	AGGCAAAGAATACTTTGCTGTCTTCATGTAGA
Core120	TTGCAGGGCGCTTTTGACAAAGTTTAAAGCCCTTTTCGGTCCGCCACC
Core121	TAGATTAAGACGCAAAACGAGAATAAATATCGCGTTAATTTTCCCTTA
Core122	AAAATCTAGATGGTTTAATTTCAA
Core123	CCACCAGATCGCCATTA AAAATACTATTAGTCTTTAATGCAATATTT
Core125	CAGGAAGATTGTATAAGTAAACTAGGACTAAAATGCAGA
Core126	TACAGACCTTCATTACGAATAAGG
Core127	TAATTTGCGCTAACGAATTCATCAGCAGATAC
Core128	AAGCGCATCGCCTGATGAAATCCGCGACCTGCCTGACCAAAAAT
Core129	GTAACCGGGCGGTACTGTCCACGCTGGTTT
Core130	ACGTAACATAAGGCGTTAGAAAAAGCCCAGATGAACGGTG

Table 9.5: DNA sequences of the DNA origami porin (4).

Name	Sequence
Core131	TTCTTTTCGCGTATTGAAGAAGATACATCAAG
Core132	GACTTGCGATCAAAAACCCCCTCA
Core133	AAAACACTTGTATCATTAGACGGGTAACATAAAAACAGGG
Core134	GGGCGCGAGCTGAAAAGCTATATTTTCATT
Core136	AGACTACCCAGTGAGAAGAGTCAAGGTCATAGTCGACTCT
Core137	AATCGGAAAGTTTTTTAAGGAGCGTATCATTTAAATCCTT
Core138	ATATCCTCACAAATCCAAGCCTGGGGTCATCA
Core139	TACTGCGGAATCGTCATAAATATTAGTAAAATAAACAACACTGTCTTTCC
Core140	AACATTAAGTAACAACAGTATAAAATATGCGT
Core141	ATAACGCCGACGACGATTGCTATTTTCCTCCC
Core142	TAACTATAAAAGAACGGCCTCTTCTGTTGGGAAGGGCGATACCAGGCA
Core143	AAAGCGAGCGGTCACGCAAATCGGCCAAAAT
Core144	TGGAACAATTAAGAAATAATGGATGGCAATTAGAGAATAAAATCAGCT
Core145	TATTCAACCTGAGAGTGTTTCAGCTCCAGACGATTGAGCGC
Core146	CTCGTTAGGACGAGCACCGCTACAACCACACC
Core147	TCATGAGGAGGCTTTGAGCATGTGCGTATCAGGTCATTGC
Core148	AGAGGATCCCCGGGTACGGCCAGT
Core149	GCGCTCACGAGCTAACGAGTGAATCTGTAAAT
Core150	TACCAAAGACAAAAGGATCTCCAA
Core151	TGCACGTAAAACAGAAAAGTGTTGTTCCAGTT
Core152	TAACGTTTTTATTTTCGTAGCTCAGTCATTTT
Core153	CATCTTTGACCCTGAAGAGAGATAGAGCAAGA
Core154	CGGTAATCGCAAATATAATTCTGTAGACTTTT
Core155	CATAATCAAACCAGAGCCACCACCGGAACTCA
Core156	AAATTGCGTAGATTTTAGATAGGGTTGAGGGAAG
Core157	TCCATGTTAGAGAGAAAGAATTA ACTGAACCG
Core158	GATGGTGGTTCCGTGCGC
Core159	AAATATTGACAACCGATT
Core160	TTGAAATAAATAAACAAGATCGCAACGACGAC
Core161	CCCTTATAATAGCCCGCAGGTTTAAAATTATT
Core163	TAAACGTTAATATTTTAGGGTTAGAACGAGAATCGATGAA
Core164	CTGATGCATTTTAAACCTCCGGCTGGTCTGAGCCCAGTCATGCATGCC
Core165	TGCCCGAAAAGTATTAGACTTTACATTAGAGCCGTCAATA
Core166	CAAACCTCCCTCCTTTTTTTTTTTCAGGAGCCTT
Core167	TGCGGGAGAAGCCTTGCTTTGAATTTTCAATTTCAATAATCATACAGGCA
Core168	CCTGATTACTACGTGAACCATCACCCAAATCACCCATAAG
Core169	TTGAATGGCCCTTCTGACCTGAAAGCCAACAGAGATAGAATCACCAGT
Core170	CGTTCTAGCTGTTTATATATCCCATCCCGGTC

Table 9.6: DNA sequences of the DNA origami porin (5).

Name	Sequence
Core171	TTTTTGTTTAAAGTACTTTTCGAGCCAGTAATA
Core173	TTCGGGAAACGCAAAGTGCTTTTCG
Core174	AGAACAAGCAAGCTTGAGTTGATTGGTCAATAACCTGTTT
Core175	TTTTAGTTAATCCAATCGCAAGACTGTAAATGTGGCGAAAAACGCCAG
Core176	CCAACCTATAATATCACAAAGTCAGAGGGTAA
Core177	CGTCGCTATTAATTTTAATTCGAGGCTTAGAGCTTAATCAATATATGT
Core178	GCCCTTCACTGAGAGAGCGAATTAACCAAGTT

Table 9.7: DNA sequences of the DNA origami porin with single-stranded DNA overhangs for attachment of complementary cholesterol-tagged sequences.

Name	Sequence
Core14_01	TTCCTTCTATGCATCTTTTTTGGAAAGTTTCATTCCAACCTAAAGTACGGT
Core36_01	TTCCTTCTATGCATCTTCGTACCAGCAGCCCTCACTAACGGCATAGTAA
Core40_01	TTCCTTCTATGCATCTTACACTATCATAACCCTC
Core57_01	TTCCTTCTATGCATCTTTTTAGTACCTTTAATTGAACAGGTCAGGATTA
Core77_01	TTCCTTCTATGCATCTTTTTGAACAACCTAAAGGACGGAGTGACACCGA CTAGACGTTA
Core94_01	TTCCTTCTATGCATCTTTTTAAAAGGCTCCAAAACGTTGAAA
Core119_01	TTCCTTCTATGCATCTTCTGTATGGGATTTTGCTGTTTACTGGATAGC
Core172_01	TTCCTTCTATGCATCTTTTTTTTTTCGCCACGCAAAGGTGGCGCAATAAT
Core179_01	TTCCTTCTATGCATCTTTTTAAAGCGGATTGCATACTATTATAGTCAGA
Core11_01	GTAGCAACGAATTGAGTTTTTTTTTTTTTCAGCATGCTAGCTAG
Core28_01	CTTCCACCACCCTCATACGGTCAATGACCTTCATTTTTTTTTTTCAGCAT GCTAGCTAG
Core41_01	TGAGAGATGACAGCATCGGTTTTTTTTTTCAGCATGCTAGCTAG
Core43_01	CCACCCTCGCGAAACAGGAACGAGGTTTTTTTTTTCAGCATGCTAGCTAG
Core90_01	AGGTGGCACAATAAAGCCTCAGAGCATTTTTTTTTTTTCAGCATGCTAGCTAG
Core93_01	AGAAAAGCATTAAACGGTTTTTTTTTTTTTCAGCATGCTAGCTAG
Core108_01	AAATACGTAACGATTATACTTTTTTTTTTTCAGCATGCTAGCTAG
Core124_01	TAACACTGGGGCTTGACGTTAATAATTCAGCATGCTAGCTAG
Core135_01	GCTGAGGCAGGTAAAGTTAATGCCGAGAGGGTAGTTTTTTTTTTCAGCA TGCTAGCTAG
Core162_01	AATCGGTTCAATGACAACATTTTTTTTTTTCAGCATGCTAGCTAG
3'CholSequ.	GATGCATAGAAGGAA/3CholTEG/
5'CholSequ.	/5CholTEG/CTAGCTAGCATGCTG

A4. Methods for the molecular dynamics simulations

MD simulations were carried out by C.-Y. Li and A. Aksimentiev, University of Illinois at Urbana-Champaign. The methods are detailed in the following paragraphs.

General MD methods. All MD simulations were performed using the program NAMD2 [3], periodic boundary conditions, the CHARMM36 parameter set for water, ions and nucleic acids [4], CHARMM parameters for the DphPC lipid bilayer [5], custom parameterisation of ion-DNA and ion-ion interactions [6]. All simulations employed a 2–2–6-fs multiple time-stepping, SETTLE algorithm to keep water molecules rigid [7], RATTLE algorithm to keep all other covalent bonds involving hydrogen atoms rigid [8], a 8–10–12 Å cut-off for van der Waals and short-range electrostatic forces. Long-range electrostatic interactions were computed using the particle mesh Ewald (PME) method [9] over a 1.2 Å resolution grid [10].

Assembly of the simulation system. The caDNAno design of the DNA origami porin was converted to idealized all-atom structures using a previously described method [11]. Reproducing the experimental system, cholesterol groups were added to termini of selected DNA strands; the cholesterol groups were initially placed to orient normal to the plane of the lipid bilayer. Before inserting into the lipid membrane, the DNA origami structure was simulated using the all-atom MD method for 1 ns in vacuum under a network of elastic restraints which allowed the structure to globally relax its conformation [12]. The DphPC lipid membranes were prepared by replicating a small patch of a pre-equilibrated lipid bilayer. After merging the synthetic DNA porin with the DphPC lipid membrane, DphPC molecules located either within 3 Å of the DNA porin or inside the channel were removed. Mg²⁺-hexahydrates [6] were randomly placed near the DNA origami porin in the amount required to exactly compensate the electrical charge of the latter. Following that, water and 1 M KCl were added using the Solvate and Autoionize plugins of VMD.

Equilibration of the all-atom model. To equilibrate the DNA origami porin, we first cut away a 11-nm slab of the initial all-atom model containing the lipid membrane (5 nm thick) and the adjacent 6 nm-thick cross-section of the solvated DNA origami. The resulting system was energy-minimized for 1200 steps and equilibrated for 48 ns allowing the lipid bilayer and the solution to adopt equilibrium conformation around the struc-

ture; the DNA atoms were restrained to maintain their initial coordinates during this equilibration simulation (with the spring constant $k_{spring} = 1 \text{ kcal}/(\text{mol } \text{Å}^2)$). Following that, the equilibrated lipid bilayer and the surrounding solvent were combined with the full-length DNA origami porin. The resulting system was equilibrated under a network of harmonic restrains that maintained distances between atomic pairs at their initial values; such elastic restrains excluded hydrogen atoms, phosphate groups, atoms in the same nucleotide and pairs separated by more than 8 Å . The system was simulated under such elastic restrains for 14.4 ns; the spring constants of the restrains were decreased from 0.5 to 0.1 and then to 0.01 kcal/(mol Å^2) every 4.8 ns. All equilibration simulations were performed under the NPT condition, where the number of atoms (N), pressure (P) and temperature (T) were kept constant. The pressure was set to 1 atm using the Nosé-Hoover Langevin piston method [13, 14]. The temperature was maintained at 295 K using a Langevin thermostat [15]. The ratio of the system's dimensions along the x and y axis were constrained while the z axis was decoupled. Following that, the system was simulated in the absence of any restrains for 19.2 ns. During all MD simulations, the system's coordinates were recorded every 48 ps.

MD simulation of ionic current. All simulations of the ionic current were performed in the constant number of atom, volume and temperature ensemble. A voltage drop, V , across the system was produced by applying an external electric field E such that $V = -EL$, where L was the length of the simulation system in the direction of the applied field [16].

Ionic current calculations. Prior to calculations of the ionic current, frames of the MD trajectory were aligned [16] using a two-step process. First, we shifted the x and y coordinates of all atoms in the simulation system by the same amount to maintain the centre of mass coordinate of the DNA origami porin constant within the plane of the lipid bilayer. Next, the z -coordinates of all atoms in the system were shifted by the same amount to maintain the z -coordinate of the lipid bilayer centre of mass constant. To reduce thermal noise originating from stochastic displacements of ions in the bulk solution, the ionic current calculations were carried out within the $\ell/2 \leq z \leq \ell/2$ region of the system, where $\ell = 30 \text{ Å}$. The instantaneous current was computed as

$$I(t + \frac{\Delta t}{2}) = \frac{1}{\Delta t \ell} \sum_i^N q_i (\zeta_i(t + \Delta t) - \zeta_i(t)) \quad (9.1)$$

where

$$\zeta_i(t) = \begin{cases} z_i(t), & |z_i(t)| \leq \ell/2 \\ -\ell/2, & z_i(t) < -\ell/2 \\ \ell/2, & z_i(t) > \ell/2, \end{cases} \quad (9.2)$$

the sum over i indicates a sum over all ions, Δt is the time interval between two consecutive frames of the MD trajectory and q_i is the charge of ion i [17]. The average current of a trajectory was computed by summing up all instantaneous currents and dividing by the number of coordinate frames of the trajectory. To estimate the error, the ionic current trace was first block averaged with a block size of 2.88 ns. The reported standard errors of the mean were calculated from the block-averaged current traces.

Calculations of the local density and local ionic current flux. The local density and the local ionic current flux were computed as described previously [18]. We divided the simulation system into $5 \text{ \AA} \times 5 \text{ \AA} \times 5 \text{ \AA}$ grids and calculated the average density of the selected atom groups and average flux of each ion species in each grid using a sampling frequency of 240 ps. The local current in each grid in a given direction (x , y or z) was calculated by

$$I_j = \sum_i q_i \times f_{i,j}, (i = \text{K}^+, \text{Cl}^-, \text{Mg}^{2+}; j = x, y, z) \quad (9.3)$$

where i is the ion species (K^+ , Cl^- or Mg^{2+}), q_i is the charge of the ion and $f_{i,j}$ is the flux of the ion in the given direction. We averaged the 3-dimensional density and flux data in the cylindrical coordinate over the azimuthal angle to obtain the mean density and mean flux on the $r - z$ plane as described previously [19]. Following that, the 2D density and flux were made symmetric about the z axis by making a mirror image ($r \rightarrow -r$). Finally, we used the `contourf` and `streamplot` function in the python `matplotlib` package to generate the local density and flux plots, which were then assembled into the final figures.

Bibliography

- [1] B. Hess, C. Kutzner, D. van der Spoel, and E. Lindahl. “GROMACS 4: Algorithms for Highly Efficient, Load-Balanced, and Scalable Molecular Simulation”. *Journal of Chemical Theory and Computation* 4.3 (2008), pp. 435–447.
- [2] J. Yoo, M. B. Jackson, and Q. Cui. “A Comparison of Coarse-Grained and Continuum Models for Membrane Bending in Lipid Bilayer Fusion Pores”. *Biophysical Journal* 104.4 (2013), pp. 841–852. DOI: 10.1016/j.bpj.2012.12.043.
- [3] J. C. C. Phillips, R. Braun, W. Wang, J. Gumbart, E. Tajkhorshid, E. Villa, C. Chipot, R. D. D. Skeel, L. Kale, and K. Schulten. “Scalable Molecular Dynamics with NAMD”. *Journal of Computational Chemistry* 26 (16 2005), pp. 1781–1802.
- [4] A. D. MacKerell, Jr. et al. “All-Atom Empirical Potential for Molecular Modeling and Dynamics Studies of Proteins”. *Journal of Physical Chemistry B* 102 (1998), pp. 3586–3616.
- [5] J. B. Lim and J. B. Klauda. “Lipid Chain Branching at the Iso- and Anteiso-Positions in Complex Chlamydia Membranes: A Molecular Dynamics Study”. *Biochimica et Biophysica Acta* 1808.1 (2011), pp. 323–31. DOI: <http://dx.doi.org/10.1016/j.bbamem.2010.07.036>.
- [6] J. Yoo and A. Aksimentiev. “Improved Parametrization of Li⁺, Na⁺, K⁺, and Mg²⁺ Ions for All-Atom Molecular Dynamics Simulations of Nucleic Acid Systems”. *Journal of Physical Chemistry Letters* 3.1 (2012), pp. 45–50. DOI: <http://dx.doi.org/10.1021/jz201501a>.
- [7] S. Miyamoto and P. A. Kollman. “SETTLE: An Analytical Version of the SHAKE and RATTLE Algorithm for Rigid Water Molecules”. *Journal of Computational Chemistry* 13.8 (1992), pp. 952–962.
- [8] H. C. Andersen. “RATTLE: A “Velocity” Version of the SHAKE Algorithm for Molecular Dynamics Calculations”. *Journal of Chemical Physics* 52.1 (1983), pp. 24–34. DOI: [http://dx.doi.org/10.1016/0021-9991\(83\)90014-1](http://dx.doi.org/10.1016/0021-9991(83)90014-1).
- [9] P. F. Batcho, D. A. Case, and T. Schlick. “Optimized Particle-Mesh Ewald/Multiple-Time Step Integration for Molecular Dynamics Simulations”. *Journal of Chemical Physics* 115.9 (2001), pp. 4003–4018. DOI: <http://dx.doi.org/10.1063/1.1389854>.
- [10] R. D. Skeel, D. J. Hardy, and J. C. Phillips. “Correcting Mesh-Based Force Calculations to Conserve Both Energy and Momentum in Molecular Dynamics Simulations”. *Journal of Chemical Physics* 225.1 (2007), pp. 1–5.

-
- [11] J. Yoo and A. Aksimentiev. “In situ structure and dynamics of DNA origami determined through molecular dynamics simulations.” *Proceedings of the National Academy of Sciences* 110.50 (2013), pp. 20099–104. DOI: 10.1073/pnas.1316521110.
- [12] C. Maffeo, J. Yoo, and A. Aksimentiev. “*De Novo* Reconstruction of DNA Origami Structures through Atomistic Molecular Dynamics Simulation”. *Nucleic Acids Research* 44.7 (2016), pp. 3013–3019. DOI: 10.1093/nar/gkw155.
- [13] G. J. Martyna, D. J. Tobias, and M. L. Klein. “Constant Pressure Molecular Dynamics Algorithms”. *Journal of Chemical Physics* 101.5 (1994), pp. 4177–4189. DOI: <http://dx.doi.org/10.1063/1.467468>.
- [14] S. E. Feller, Y. H. Zhang, R. W. Pastor, and B. R. Brooks. “Constant Pressure Molecular Dynamics Simulation — the Langevin Piston Method”. *Journal of Chemical Physics* 103.11 (1995), pp. 4613–4621.
- [15] A. T. Brünger. *X-PLOR, Version 3.1: A System for X-ray Crystallography and NMR*. The Howard Hughes Medical Institute, Department of Molecular Biophysics, and Biochemistry, Yale University. 1992.
- [16] A. Aksimentiev and K. Schulten. “Imaging α -Hemolysin with Molecular Dynamics: Ionic Conductance, Osmotic Permeability and the Electrostatic Potential Map”. *Biophysical Journal* 88 (2005), pp. 3745–3761. DOI: <http://dx.doi.org/10.1529/biophysj.104.058727>.
- [17] A. Aksimentiev, J. B. Heng, G. Timp, and K. Schulten. “Microscopic Kinetics of DNA Translocation through Synthetic Nanopores”. *Biophysical Journal* 87 (2004), pp. 2086–2097. DOI: <http://dx.doi.org/10.1529/biophysj.104.042960>.
- [18] C. Y. Li, E. A. Hemmig, J. Kong, J. Yoo, U. F. Keyser, and A. Aksimentiev. “Ionic Conductivity , Structural Deformation and Programmable Anisotropy of DNA Origami in Electric Field”. *ACS Nano* 9.2 (2015), pp. 1420–33.
- [19] J. Yoo and A. Aksimentiev. “Molecular Dynamics of Membrane-Spanning DNA Channels: Conductance Mechanism, Electro-Osmotic Transport, and Mechanical Gating”. *Journal of Physical Chemistry Letters* 6.23 (2015), pp. 4680–7. DOI: 10.1021/acs.jpcllett.5b01964.

